

**A Thesis Submitted for the Degree of PhD at the University of Warwick**

**Permanent WRAP URL:**

<http://wrap.warwick.ac.uk/176897>

**Copyright and reuse:**

This thesis is made available online and is protected by original copyright.

Please scroll down to view the document itself.

Please refer to the repository record for this item for information to help you to cite it.

Our policy information is available from the repository home page.

For more information, please contact the WRAP Team at: [wrap@warwick.ac.uk](mailto:wrap@warwick.ac.uk)



# Mathematical Models of Aeroacoustics in Boundary Layers over Acoustic Linings:

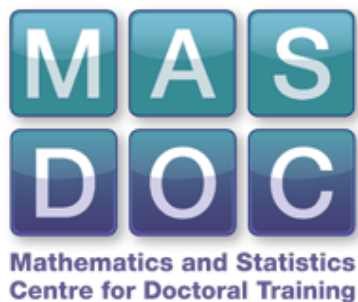
by

**Matthew John King**

A thesis submitted in partial fulfilment of the requirements for the degree of  
Doctor of Philosophy in Mathematics and Statistics.

University of Warwick, Mathematics Institute,  
Mathematics and Statistics Centre for Doctoral Training.

October 2022



# Contents

|           |  |           |
|-----------|--|-----------|
| <b>I</b>  | <b>Introduction</b>  | <b>1</b>  |
| 1         | Problem Background   | 1         |
| 2         | Notation   | 7         |
| 3         | Numerical Methods  | 7         |
| <b>II</b> | <b>The Critical Layer for a Point Mass Source</b>                      | <b>13</b> |
| 4         | Introduction   | 13        |
| 5         | Pridmore-Brown Equation  | 16        |
| 5.1       | Constructing the Pridmore-Brown Equation . . . . .                     | 16        |
| 5.2       | Additional Assumptions . . . . .                                       | 18        |
| 5.2.1     | Boundary Conditions . . . . .  | 18        |
| 5.2.2     | Non-dimensionalisation and Simplifying Assumptions . . . . .           | 19        |
| 6         | Solutions to the Pridmore-Brown Equation                               | 21        |
| 6.1       | Homogeneous Solutions Within the Region of Sheared Flow . . . . .      | 21        |
| 6.1.1     | Frobenius Series Expansions about $r = r_c^+$ . . . . .                | 22        |
| 6.1.2     | Expansion about $r = 1$ . . . . .                                      | 26        |
| 6.1.3     | A Homogeneous Solution Valid Across $[1 - h, 1]$ . . . . .             | 28        |
| 6.2       | Solutions to the Pridmore-Brown Equation Over $[0, 1]$ . . . . .       | 29        |
| 6.2.1     | Homogeneous Solutions Within the Region of Uniform Flow . . . . .      | 30        |
| 6.2.2     | Homogeneous Solutions Across the Full Domain . . . . .                 | 30        |
| 6.3       | The Wronskian $\mathcal{W}(r)$ . . . . .                               | 32        |
| 6.3.1     | Modal Solutions . . . . .  | 34        |
| 7         | The Green's Function for the Pridmore-Brown Equation                   | 35        |
| 7.1       | Inhomogeneous Solution to the Pridmore-Brown Equation . . . . .        | 35        |
| 7.2       | The $\alpha$ Square Root Branch Cut . . . . .                          | 37        |
| 7.3       | Analytic Continuation Behind the Critical Layer Branch Cut . . . . .   | 39        |
| 7.3.1     | The Jump in $\tilde{G}$ Across the Critical Layer Branch Cut . . . . . | 41        |
| 8         | Inverting the Fourier Transform  | 43        |
| 8.1       | Choosing an Inversion Contour . . . . .                                | 43        |
| 8.2       | Contribution from the Poles of $\tilde{G}$ . . . . .                   | 45        |
| 8.3       | Contribution from the Critical Layer Branch Cut . . . . .              | 46        |

|            |  |            |
|------------|--|------------|
| <b>9</b>   | <b>Asymptotic Analysis of the Solutions</b>  | <b>49</b>  |
| 9.1        | Behaviour as $k \rightarrow \frac{\omega}{M}$ . . . . .                              | 49         |
| 9.1.1      | Behaviour of the Homogenous Solutions . . . . .                                      | 50         |
| 9.1.2      | Behaviour of $\Delta\tilde{G}_{\frac{\omega}{M}}$ . . . . .                          | 53         |
| 9.1.3      | The Branch Point at $k = \frac{\omega}{M}$ . . . . .                                 | 54         |
| 9.2        | Behaviour as $k \rightarrow k_0$ . . . . .   | 55         |
| 9.2.1      | Behaviour of the Homogenous Solutions . . . . .                                      | 55         |
| 9.2.2      | Behaviour of $\Delta\tilde{G}_0$ . . . . .   | 56         |
| 9.2.3      | The Non-modal Pole at $k = k_0$ . . . . .  | 57         |
| 9.3        | Behaviour of $\Delta\tilde{G}_r$ as $k \rightarrow k_r$ . . . . .                    | 58         |
| 9.3.1      | The Branchpoint at $k = k_r$ . . . . .   | 58         |
| 9.4        | Far-Field Decay Rates of the Critical Layer Contribution . . . . .                   | 59         |
| 9.4.1      | Comparisons with Previous Far-Field Scalings . . . . .                               | 60         |
| <b>10</b>  | <b>Pole Locations</b>  | <b>61</b>  |
| <b>11</b>  | <b>Fourier Inversion Contributions</b>   | <b>66</b>  |
| 11.1       | Branch Cut Contributions . . . . .   | 66         |
| 11.2       | Full Fourier Inversion . . . . .   | 68         |
| <b>12</b>  | <b>The Critical Layer and the Stabilising of the <math>k^+</math> Surface Mode</b>   | <b>72</b>  |
| 12.1       | Poles of $\tilde{G}^+$ . . . . .   | 74         |
| 12.2       | Parameter Studies of the Hydrodynamic ‘Instability’ . . . . .                        | 74         |
| 12.2.1     | Variation of the Boundary Layer Thickness $h$ . . . . .                              | 75         |
| 12.2.2     | Variation of the Mach Number $M$ . . . . .   | 77         |
| 12.2.3     | Variation of the Frequency $\omega$ . . . . .  | 80         |
| 12.2.4     | Variation of the Impedance $Z$ . . . . .   | 84         |
| 12.3       | Hard Walled Ducts . . . . .  | 85         |
| 12.4       | Comparison to a Linear-Shear flow . . . . .  | 89         |
| <b>III</b> | <b>The Modified Myers Boundary Condition for a Quadratic Shear Flow</b>              | <b>97</b>  |
| <b>13</b>  | <b>Introduction</b>  | <b>97</b>  |
| <b>14</b>  | <b>Construction of the Brambley Boundary Condition</b>                               | <b>99</b>  |
| 14.1       | The Quadratic-Brambley Boundary Condition . . . . .                                  | 105        |
| 14.2       | The Critical Layer Branch Cut in the Quadratic-Brambley Boundary Condition . . . . . | 107        |
| <b>15</b>  | <b>Mode Locations</b>  | <b>109</b> |

|   |            |
|---|------------|
| <b>16 Fourier Inversion for a Point Mass Source</b>   | <b>126</b> |
| 16.1 Construction of the Green's Function . . . . .   | 126        |
| 16.2 Contribution of the Modal Poles . . . . .  | 127        |
| 16.3 Branch Points of the Critical Layer Branch Cut . . . . .                                 | 128        |
| 16.4 Contribution of the Critical Layer Branch Cut and the Stabilised $k^+$<br>Mode . . . . . | 131        |
| 16.5 Fourier Inversion under the Quadratic-Brambley Boundary Condition                        | 132        |
| <b>17 Numerical Comparisons of the Fourier Inversion</b>                                      | <b>133</b> |
| 17.1 Contribution of the Critical Layer Branch Cut . . . . .                                  | 133        |
| 17.2 Full Fourier Inversion . . . . .   | 134        |
| 17.3 Comparison to other Boundary conditions and the Full Solution . . .                      | 139        |
| <br>  |            |
| <b>IV Wave Scattering due to a Change in Boundary Con-<br/>ditions</b>                        | <b>141</b> |
| <b>18 Introduction</b>  | <b>141</b> |
| 18.1 Half Range Transforms . . . . .  | 145        |
| <b>19 Problem Formulation and Solutions</b>   | <b>146</b> |
| 19.1 Asymptotic Behaviour in the Strip $D$ . . . . .  | 150        |
| 19.2 Asymptotic Behaviour of the Entire Function . . . . .                                    | 154        |
| <b>20 Scattering due to Change in Boundary Condition for a Modal<br/>Source</b>               | <b>155</b> |
| 20.1 Modal Scattering for $x < 0$ . . . . .   | 156        |
| 20.2 Scattering for $x > 0$ . . . . .   | 156        |
| 20.2.1 Modal Scattering for $x > 0$ . . . . .   | 156        |
| 20.2.2 Non-modal Scattering for $x > 0$ . . . . .   | 157        |
| 20.2.3 Total Scattering for $x > 0$ . . . . .   | 160        |
| <b>21 Scattering of an Incoming Wave from a Non-Modal Pole</b>                                | <b>161</b> |
| <b>22 Scattering of a <math>k^+</math> Modal Incoming Wave</b>                                | <b>164</b> |
| <b>23 Interpretation of Results</b>   | <b>167</b> |
| <b>24 Construction of the Matrix Wiener-Hopf Problem</b>                                      | <b>169</b> |
| <br>  |            |
| <b>V Conclusions</b>  | <b>174</b> |

|  |            |
|--|------------|
| <b>25 Summary of Key Results</b>   | <b>174</b> |
| <b>26 Extensions</b>   | <b>182</b> |
| 26.1 Extension to Other Sheared Flow Profiles . . . . .  | 184        |
| 26.1.1 Differences Between the Results for Linear and Quadratic Shear<br>Flow Problems . . . . . | 184        |
| 26.1.2 Generalising the Decay Rates . . . . .  | 185        |
| 26.1.3 Stabilisation of the Hydrodynamic Instability . . . . .                                   | 187        |
| 26.2 Extending the Brambley Boundary Condition . . . . .   | 188        |
| 26.3 Other Flow Profiles . . . . .   | 190        |
| 26.4 Extensions to the Scattering Problem . . . . .  | 191        |

# List of Figures

|   |   |    |
|---|---|----|
| 1 | A cylindrical duct containing an axial mean flow $U(r)$ . . . . .   | 4  |
| 2 | A cross sectional view of a cylindrical duct with lined walls containing sheared axial flow. $\rho_0(r)$ is the mean flow density (here taken constant), and $U(r)$ is the mean flow velocity, here taken to be uniform outside a boundary layer of width $h$ . $Z$ is the boundary impedance and defines the boundary condition at the wall of the duct. . . . .   | 20 |
| 3 | Schematic of possible locations of the $r_c^+$ branch cut in the complex $r$ -plane. (a) A possible choice of branch cut when $\text{Im}(r_c^+) > 0$ . (b) The other choice of branch cut is needed when $\text{Im}(r_c^+) < 0$ . . . . .   | 25 |
| 4 | Schematic of possible locations of the $r_c^\pm$ critical points in the complex $r$ -plane. (a) The radius of convergence of the expansion about $r_c^+$ covers the region of interest $r \in [1 - h, 1]$ . (b) The radius of convergence about $r_c^+$ is insufficient to cover $r \in [1 - h, 1]$ (as $k$ is too close to $\frac{\omega}{M}$ ). . . . .   | 27 |
| 5 | As for figure 4(b) with the radius of convergence for $\tilde{p}_{11}$ and $\tilde{p}_{12}$ added.  | 28 |
| 6 | Illustration of the inversion contours taken when an unstable $k^+$ pole is present. The inversion contour for $\tilde{G}$ is labelled $\mathcal{C}$ . (Left) For $x < 0$ , the contour is closed in the upper half plane along the $\mathcal{C}_<$ contour. (Right) For $x > 0$ , the contour is closed in the lower half plane along the $\mathcal{C}_>$ contour, and around the critical layer branch cut along the $\mathcal{C}_b$ contour. Contributing modal poles are indicated in blue. . . . .   | 44 |
| 7 | (Top Left) The integration contour required for the computation of the contribution from the critical layer branch cut, understood by integrating above and below the branch cut. Possible poles of $\tilde{G}^-$ and $\tilde{G}^+$ are denoted $k^-$ and $k^+$ respectively. (Top Right) The integration contour after being transformed onto the steepest descent contour. Red lines behave as if evaluated below $\frac{\omega}{M}$ (using $\tilde{G}^-$ ); blue as if having been analytically continued around the $\frac{\omega}{M}$ branch point; green as if having been analytically continued around the $\frac{\omega}{M}$ and $k_<$ branch points; and purple as if analytically continued around all branch points, giving $\tilde{G}^+$ . (Bottom) As top right but with the relative locations of the $k^+$ and $k^-$ poles to $k_<$ and $k_>$ varied. Note that while the $k^-$ pole is only picked up by the red contour ( $\tilde{G}^-$ ) the $k^+$ pole is picked up by the first contour to its left, and its contribution will vary accordingly. . . . . | 47 |

|    |  |    |
|----|--|----|
| 8  | Location of the poles in the complex $k$ plane for two sub-parameter sets from each of the parameter sets A-D. The usual acoustic modal poles have been marked with an ( $\times$ ). The critical layer branch cut, ( $-$ ), and any $k^+$ modal poles ( $+$ ). Modes that are coloured red are unstable under the Briggs-Bers criterion. Stable $k^+$ modes located in the lower half plane are ‘hidden’ behind the branch cut. . . . .   | 62 |
| 9  | Location of the poles in the complex $k$ plane for two sub-parameter sets from each of the parameter sets $E - H$ . As figure 8 with the Briggs-Bers trajectories as $\text{Im}(\omega)$ is varied from 0 to $-50$ ( $- \cdot -$ ), with locations at $\text{Im}(\omega) = 0$ marked as a pole. . . . .  | 63 |
| 10 | The mode shapes of five modes from parameter sets $B1, D3, E4$ and $F4$ . Rows 1 and 2 show the mode shapes for upstream propagating, ( $x < 0$ ), modes, Rows 3,4,5 show the mode shapes for downstream propagating ( $x > 0$ ) modes, with the bottom row (5) illustrating the mode shape of either unstable ( $D3$ and $F4$ ) or hidden ( $B1$ and $E4$ ) $k^+$ surface modes. The first and third rows correspond to the acoustic mode with the smallest imaginary part. . . . .   | 65 |
| 11 | Plotting the real (solid lines), and imaginary part (dashed lines), of the residue of the stabilised $k^+$ pole, $R^+(k^+)$ (red) and $R^+(k^+) + I_r$ (blue) for parameter sets $B1, D4$ and $E4$ . This is plotted for $r_0 = 1$ , $x = 0.1$ , for $r$ values near the discontinuity. . . . .  | 66 |
| 12 | A comparison of the terms that contribute to the critical layer, for $r_0 = 1 - \frac{4h}{5}$ . Plotted are the absolute values on a $\log_{10}$ scale. Left to right: parameter sets $B4, C4$ and $E2$ . Top to bottom: (i) the sum of the three steepest descent contours, $I_{\frac{\omega}{M}} + I_r + I_0$ ; (ii) the non-modal $k_0$ pole; (iii) the contribution of the $k^+$ pole located behind the branch cut; and (iv) the total contribution from integrating around the critical layer branch cut, obtained by summing (i)–(iii). . . . . | 67 |
| 13 | Plots of the real part of the contribution from integrating around the branch cut ( $\text{Re}(p(x, r))$ ) for parameter sets $A1, C3, H3$ Each of these parameter sets do not have a $k^+$ pole behind the branch cut. Solid lines indicate positive values, dashed lines indicate negative values. i): $r_0 = 1 - 2h$ ; ii): $r_0 = 1 - \frac{11h}{10}$ ; iii): $r_0 = 1 - \frac{9h}{10}$ ; iv): $r_0 = 1 - \frac{h}{5}$ . . . . .   | 69 |

- 14 Plotted for parameter sets *A3*, *D2*, *E3* and *H1* are the three steepest descent contours  $|I_{\frac{\omega}{M}}|$  (i) and (ii),  $|I_r|$  (iii), and  $|I_0|$  (iv), under a  $\log_{10}$  scale. The point mass source is located at  $r_0 = 1 - \frac{11h}{10}$  (i) and  $r_0 = 1 - \frac{4h}{5}$  (ii-iv). Solid lines correspond to radial locations  $r = 1 - 4h, 1 - 2h, 1 - \frac{h}{2}$ , and  $1 - \frac{h}{4}$ . The dashed line is the predicted far-field rate of decay. Note that for  $r < 1 - h$ ,  $|I_r| = 0$  and so these ‘decay rates’ are not given. . . . . 70
- 15 Plotting the real values of the different contributions. (a) just the contribution for the stable modal poles. (b) the full Fourier inversion, which also includes the  $k^+$  pole. The parameter sets used from top to bottom are *A4*, *C1*, *E1* and *F1*, with  $r_0 = 1 - \frac{4h}{5}$  in each case. In case *F1*, the  $k^+$  pole is a convective instability. In cases *A4*, *C1* and *E1*, the  $k^+$  pole is located behind the branch cut. . . . . 71
- 16 The absolute value of pressure on a log scale ( $10 \log_{10}(|p|)$ ) over a longer range of axial distances downstream of the point source. (a) just the contribution for the modal poles. (b) modal poles plus the three steepest descent contours and the  $k_0$  non-modal pole. (c) the Full Fourier Inversion, which also includes the  $k^+$  pole. The parameter sets used from top to bottom are *B3*, *D4*, *E3* and *G1*, with  $r_0 = 1 - \frac{4h}{5}$  in each case. In each case, the  $k^+$  pole is located behind the branch cut. . . . . 73
- 17 Location of the modal poles as the boundary layer thickness  $h$  is varied between 0.1 and  $5 \times 10^{-4}$ . Plotted are parameter sets, *C2*, *F1*, *G2* and *H3*. Blue lines indicate stable poles, while a red line indicates an instability. Dashed lines (—) indicate a pole is hidden behind the critical layer branch cut. Note that for parameter sets *C* and *G*, since these only vary in  $h$ , their tracks are uniform between the sub-parameter sets. The  $k^+$  pole associated with each sub-parameter set are indicated as; 1 (+), 2 (\*), 3 ( $\Delta$ ), 4 ( $\star$ ) with the usual acoustic modal poles indicated just for the highlighted given parameter set. Arrows indicate the direction of increasing boundary layer thickness  $h$ . 76

|    |  |    |
|----|--|----|
| 18 | Locations of the modal poles as the Mach number is varied between $M = 0.1$ and $M = 0.9$ , scaled by $\frac{M}{\omega}$ . Blue trajectories indicate stable modal poles, while red trajectories represent instabilities. Dashed lines (--) indicate poles located behind the critical layer branch cut. Plotted are parameter sets $B2$ , $D3$ , $G1$ and $H3$ . Note that the sub-parameter sets of sets $D$ and $E$ only vary by Mach number and so there trajectories are consistent. The $k^+$ pole associated with each sub-parameter set are indicated as; 1 (+), 2 (*), 3 ( $\Delta$ ), 4 ( $\star$ ) with only the acoustic modal poles indicated for the named sub-parameter set. Only modal poles with Imaginary part $\text{Im}(k) < \frac{3\omega}{M}$ have been tracked. Arrows indicate the direction of increasing Mach number $M$ . | 78 |
| 19 | Values of $h_c$ (blue) (left subplots) and $k^+(h_c)$ (red) (right subplots) as the Mach number $M$ is varied. Plotted for parameter sets $A1$ , $C$ , $F3$ and $H$ . Note that parameter set $C$ only varies in boundary layer thickness $h$ and parameter set $H$ in Mach number $M$ and so these plots are consistent between the sub-parameter sets. Note that unlike figure 18 we have not scaled our values of $k^+$ .   | 79 |
| 20 | As figure 18, as the frequency $\omega$ is varied from 1 to 50 for parameter sets $A1$ , $D4$ , $E2$ and $F4$ . Arrows indicate the direction of increasing frequency $\omega$ .   | 81 |
| 21 | As figure 19, for varying the frequency $\omega$ for parameter sets $A$ , $B1$ , $F2$ and $G$ . Note that parameter set $A$ only varies in the frequency $\omega$ and parameter set $G$ in boundary layer thickness $h$ and so these plots are consistent between the sub-parameter sets. Impedance $Z = Z(\omega)$ is given by the Mass-Spring-Damper model.  | 82 |
| 22 | As figure 21, for a fixed impedance as given in table 3 (solid lines), and a varied impedance (dashed lines). Plotted are parameter sets $B4$ , $C$ , $D1$ and $E$ .   | 83 |
| 23 | As figure 17, as the reactance $\text{Im}(Z)$ is varied from $-\infty$ to $\infty$ for parameter sets $A2$ , $D1$ , $F4$ and $G3$ . Location of the $k^+$ mode at $ Z  = \infty$ is indicated with a circled cross, $\otimes$ .  | 84 |
| 24 | Contour plot of $h_c$ against $\text{Re}(Z)$ and $\text{Im}(Z)$ for parameter sets $A2$ , $B4$ , $D3$ and $F4$ . Values of $h_c$ as given by the colour bar are indicated on a $\log_{10}$ scale. The poorly resolved outermost contours are due to a loss of numerical precision resulting from large $k^+(h_c)$ .  | 86 |

|    |  |     |
|----|--|-----|
| 25 | Contour plots of $h_c$ (on a $\log_{10}$ scale) as the frequency and impedance are varied, performed for parameter sets $A$ , $C$ , $F3$ and $H4$ , with the impedance mass $\mu$ , spring $K$ and damper $R$ terms being varied between 0 and 10 times their original value. Black dashed lines (--) indicate lines of constant impedance $Z = Z(\omega)$ with the value of $\text{Im}(Z)$ indicated. Note that parameter set $A$ only varies in the frequency $\omega$ and parameter set $C$ in boundary layer thickness $h$ and so these plots are consistent between the sub-parameter sets. . . . . | 87  |
| 26 | Plotting the real values of the full solution for a quadratic boundary layer flow profile (a) and a linear boundary layer flow profile (b) [from Brambley et al., 2012a]. Plotted for parameter sets $A1$ , $C4$ , $F2$ and $G1$ with $r_0 = 1 - \frac{4h}{5}$ in each case. Positive values are marked with a solid line (-), while negative real parts are indicated with a dashed line (--). . . . .  | 90  |
| 27 | As figure 17 varying boundary layer thickness $h$ , for a linear shear flow profile. . . . .   | 92  |
| 28 | As figure 18 varying the Mach number $M$ , for a linear shear flow profile. . . . .  | 93  |
| 29 | As figure 20, varying the frequency $\omega$ , for a linear shear flow profile.  | 94  |
| 30 | As figure 23, varying the impedance, $\text{Im}(Z)$ , for a linear shear flow profile. . . . .   | 95  |
| 31 | Location of the poles in the complex $k$ plane for a Uniform flow under the Quadratic-Brambley boundary condition. Plotted for two sub-parameter sets from each of the parameter sets $A - D$ . The usual acoustic modal poles have been marked with an ( $\times$ ). The critical layer branch cut, (-), and any $k^+$ modal poles (+). Modes that are coloured red are unstable under the Briggs-Bers criterion. Stable $k^+$ modes located in the lower half plane are ‘hidden’ behind the branch cut. . . . .  | 110 |
| 32 | Location of the poles in the complex $k$ plane for two sub-parameter sets from each of the parameter sets $E - H$ . As figure 31 with the Briggs-Bers trajectories as $\text{Im}(\omega)$ is varied from 0 to $-50$ (-.-), with locations at $\text{Im}(\omega) = 0$ marked as a pole. . . . .   | 111 |

- 33 Location of the contributing modes for a uniform flow under each of the Ingard-Myers boundary condition (\*), the Linear-Brambley boundary condition ( $\times$ ), and the Quadratic-Brambley boundary condition (+). Stable modes are coloured blue, while unstable modes are red. Any hydrodynamic instabilities, or modes hidden behind the branch cut are circled ( $\otimes, \oplus$ ). Plotted for parameter sets *B3, B4, D2, D4, G3, G4, H1* and *H4* . . . . . 113
- 34 Location of the modes for a uniform flow under the Ingard-Myers boundary condition (\*), the Linear-Brambley boundary condition ( $\times$ ), and the Quadratic-Brambley boundary condition (+). Any hydrodynamic instabilities, or modes hidden behind the branch cut are circled ( $\otimes, \oplus$ ). Plotted for parameter sets *B2, C2, F1* and *G2* with trajectories as the boundary layer thickness *h* is varied from  $h = 0.3$  to  $h = 10^{-6}$ . Tracks for the Linear-Brambley boundary condition are marked ( $-\cdot-$ ), while tracks for the Quadratic-Brambley boundary condition are solid lines ( $---$ ), except when the mode is behind the branch cut, where a dashed line ( $---$ ) is used for a mode below the branch cut, with  $\text{Re}(k) > \frac{\omega}{M}$ , and a green dotted line ( $\cdots$ ) when  $\text{Re}(k) < \frac{\omega}{M}$ . Arrows indicate the direction of increasing boundary layer thickness *h*. . . . . 114
- 35 Location of the modes for a uniform flow under the Ingard-Myers boundary condition (\*), the Linear-Brambley boundary condition ( $\times$ ), and the Quadratic-Brambley boundary condition (+) on a scaled complex *k* plane. Any hydrodynamic instabilities, or modes hidden behind the branch cut are circled ( $\otimes, \oplus$ ). Plotted for parameter sets *B2, F4,* and *G4* with trajectories as the Mach number *M* is varied from  $M = 0.05$  to  $M = 0.95$ . Tracks of the Ingard-Myers boundary condition, using thick solid lines, tracks for the Linear-Brambley boundary condition are marked ( $-\cdot-$ ), while tracks for the Quadratic-Brambley boundary condition are solid lines ( $---$ ), except when the mode is behind the branch cut, where a dashed line ( $---$ ) is used for a mode below the branch cut, with  $\text{Re}(k) > \frac{\omega}{M}$ , and a green dotted line ( $\cdots$ ) when  $\text{Re}(k) < \frac{\omega}{M}$ . Arrows indicate the direction of increasing boundary layer thickness *M*. . . . . 116
- 36 As figure 35, while tracking the frequency number from  $\omega = 0.5$  to  $\omega = 75$ . Arrows indicate the direction of increasing frequency  $\omega$ . . . . 117

|    |  |     |
|----|--|-----|
| 37 | As figure 34, tracking the Reactance $\text{Im}(Z)$ for $\text{Im}(Z) = -\infty$ to $\text{Im}(Z) = \infty$ . Including tracks of the Ingard-Myers boundary condition with thick solid lines. Arrows indicate the direction of increasing $\text{Im}(Z)$ . . . . .   | 119 |
| 38 | Tracks of the modal locations of the full Frobenius series solution against the Quadratic-Brambley boundary condition as the boundary layer thickness $h$ is varied from $10^{-5}$ to 0.1. Modes of the full solution are marked with a cross ( $\times$ ), and tracked on dot-dash lines ( $-\cdot-$ ), except when behind the critical layer branch cut where they are tracked on dotted line ( $\cdots$ ). Modes of the Quadratic-Brambley boundary condition are marked with a plus ( $+$ ) and are tracked on solid lines ( $-$ ), or on dashed lines ( $--$ ) when behind the branch cut, irrespective is to the left or right. Stable modes are coloured blue, unstable modes are red, any $k^+$ modes are circled $\circ$ . Arrows indicate the direction of increasing boundary layer thickness $h$ . . . . . | 121 |
| 39 | Tracks of the modal locations on a scaled complex $k$ plane of the full Frobenius series solution against the Quadratic-Brambley boundary condition as the Mach number $M$ is varied from 0.1 to 0.9. Modes of the Full solution are marked with a cross ( $\times$ ) and tracked on dot-dash lines ( $-\cdot-$ ), except when behind the critical layer branch cut where they are tracked on dotted line ( $\cdots$ ). Modes of the Quadratic-Brambley boundary condition are marked with a plus ( $+$ ) and are tracked on solid lines ( $-$ ), or on dashed lines ( $--$ ) when behind the branch cut, irrespective is to the left or right. Stable modes are coloured blue, unstable modes are red, any $k^+$ modes are circled $\circ$ . Arrows indicate the direction of increasing Mach number $M$ . . . . .    | 122 |
| 40 | As figure 39, but for varying the frequency $\omega$ from 1 to 50. . . . .   | 123 |
| 41 | As figure 38 but for varying the Reactance from $\text{Im}(Z) = -\infty$ to $\text{Im}(Z) = \infty$ in the complex $k$ plane. . . . .  | 124 |
| 42 | Mode shapes, $\frac{J_m(\alpha r)}{J_m(\alpha)}$ against the radial location $r$ , of the $k^+$ modes for the; Quadratic-Brambley boundary condition ( <i>i</i> ). Linear-Brambley boundary condition ( <i>ii</i> ) and the Ingard-Myers boundary condition ( <i>iii</i> ). Real parts are solid lines coloured red, imaginary parts are dashed lines coloured blue. . . . .   | 125 |

|    |   |     |
|----|---|-----|
| 43 | Illustration of the integration contour used for inverting the Fourier transform for a uniform flow under the Quadratic-Brambley boundary condition, both when a hydrodynamic instability is present (Left), and when it has been stabilised by the critical layer (Right). The $k^+$ modal pole is hollow when behind the critical layer branch cut to indicate that it would not contribute as a usual modal pole. Note that these are the same contours as given in figure 6, and the integration around the critical layer Branch cut $\mathcal{C}_b$ is only present when closing the contour in the lower half plane. . . . .   | 128 |
| 44 | As figure 7, for the Quadratic-Brambley boundary condition; (Left) The integration contour $\mathcal{C}_b$ around the critical layer branch cut. (Right) The integration contour transformed onto the steepest descent contour. Note we have illustrated three differently located $k^+$ poles, $k_1^+$ is located directly below the branch cut and contributes as part of the steepest descent contour, while the hydrodynamic instability mode $k_2^+$ , or hidden mode to the left of the steepest descent contour do not contribute to the critical layer branch cut. Note that the hydrodynamic instability mode $k_2^+$ would contribute as part of the modal sum. . . . . | 131 |
| 45 | Contribution of $ I_{\frac{\omega}{M}}(x, r; r_0) $ for parameter sets $D1$ , $F2$ and $H4$ normalised by the value at $x = 1$ . Plotted are $r = 0.1$ (red) $r = 0.5$ (blue) and $r = 0.995$ (green), and $r_0 = 0.1$ (—) $r_0 = 0.5$ (— · —) and $r_0 = 0.995$ (···). Also indicated with a solid black line is the predicted decay rate $x^{-\frac{5}{2}}$ . . . . .   | 133 |
| 46 | Plotting the real values of the different contributions. (i) just the contribution for the stable modal poles. (ii) the contribution of the critical layer branch cut. (iii) the Full Fourier Inversion, which also includes an unstable $k^+$ pole. The parameter sets used from top to bottom are $B1$ , $C3$ and $F4$ , with $r_0 = 1 - 4h/5$ in each case. Solid lines indicate positive real parts while dashed lines are negative. Colour bars are given on a $\log_{10}$ scale. . . . .  | 135 |
| 47 | Plotting the real values of the different contributions. (i) just the contribution for the stable modal poles. (ii) the contribution of the steepest descent contour of the critical layer branch cut. (iii) the Full Fourier Inversion, which also includes a stable $k^+$ pole hidden behind and contributing as part of the critical layer branch cut. Plotted for parameter sets $E1$ and $G1$ with $r_0 = 1 - 4h/5$ in each case. Solid lines indicate positive real parts, while dashed lines are negative. Colour bars are given on a $\log_{10}$ scale. . . . .   | 136 |

|    |   |
|----|---|
| 48 | Plotting the absolute values of the different contributions for large values of $x > 0$ . (i) just the contribution for the stable modal poles. (ii) the contribution of the steepest descent contour of the critical layer branch cut. (iii) the Full Fourier Inversion, which also includes a stable $k^+$ pole hidden behind and contributing as part of the critical layer branch cut. Plotted for parameter sets <i>A4</i> , <i>C1</i> and <i>E2</i> with $r_0 = 1 - 4h/5$ in each case. Solid lines indicate positive real parts, while dashed lines are negative. Colour bars are given in a $\log_{10}( p )$ . <i>C1</i> (i) is left blank due to the modal sum having magnitude $\log_{10}( p ) < -78$ . . . . . 137 |
| 49 | Plots of the real part of the Fourier inversion for parameter sets <i>B3</i> , <i>E3</i> and <i>H3</i> . Solid lines indicate positive values, dashed lines indicate negative values with the colour bars given on a $\log_{10}( Re(p) )$ scale. i): $r_0 = 0.1$ ; ii): $r_0 = 0.7$ ; iii): $r_0 = 0.99$ ; iv): $r_0 = 0.9995$ . . . . . 138  |
| 50 | Comparisons of the real part of the Fourier inversion for parameter sets <i>B4</i> , <i>C4</i> , <i>E2</i> and <i>F2</i> . For a uniform flow under the Quadratic-Brambley (i), Linear-Brambley (ii) and Ingard-Myers (iii) boundary conditions, and the full quadratic sheared flow solution (iv). Solid lines indicate positive values, while dashed lines indicate negative values with the colour bars given in $\log_{10}( Re(p) )$ . . . . . 140  |
| 51 | Illustration of the complex $k$ plane illustrating how the strip $D$ may be constructed through considering the Briggs-Bers criterion. (a) shows the pole locations and the upper and lower bound of the strip for large $-\text{Im}(\omega)$ , while (b) shows the pole locations and the strip $D$ for real $\omega$ , having been deformed in order to maintain the poles in the correct half planes. This illustration is not representative of any particular parameter set and does not include effects of a branch cut singularity. Later we refer to the blue lines as $\Gamma_-$ and the red line as $\Gamma_+$ . . . . . 143  |
| 52 | A cross sectional view of a cylindrical duct with lined walls containing sheared axial flow. $\rho_0(r)$ is the mean flow density (here taken constant), and $U(r)$ is the mean flow velocity, here taken to be uniform outside a boundary layer of width $h$ . $Z$ is the boundary impedance and defines the boundary condition at the wall of the duct. . . . . 144   |
| 53 | A cross sectional view of a cylindrical duct with lined walls containing sheared axial flow. $\rho_0(r)$ is the mean flow density (here taken constant), and $U(r)$ is the mean flow velocity, here taken to be uniform outside a boundary layer of width $h$ . $Z$ is the boundary impedance and defines the boundary condition at the wall of the duct. . . . . 144   |

|    |  |     |
|----|--|-----|
| 54 | Illustration of $\Gamma_{\pm}$ and the strip $D$ . Blue poles, located in the upper half plane, would correspond to a hard walled duct. While the red mode poles including a hydrodynamic instability are associated with the lined wall. Note that $\Gamma_{+}$ has been taken above the critical layer branch cut. . . . .   | 146 |
| 55 | The steepest decent contours deformed for the Wiener-Hopf equation for an incoming wave from a non-modal pole at $k = k_0$ as in figure 7, although no $k^{\pm}$ pole have been included. (Left) For $r < r_0$ we evaluate the integral around $k_0$ as if we are above at $1 - h$ and $r$ , while for (Right) $r > r_0$ , we evaluate as if we are above at $1 - h$ but below at $r$ . . . . .  | 163 |
| 56 | Illustration of the residues that contribute to the closure of $\Gamma$ in the lower half plane. Red lines indicate evaluation as below the branch cut, blue lines as if above the branch cut at $1 - h$ , but below at $r$ , and green if above at both $1 - h$ and $r$ . Note that $k_{in}^{+}$ is integrated around three times in each illustration, once as a usual pole, which is removed by the first steepest descent contour, and then a new contribution is given by either the blue ( $k_r > \text{Re}(k_{in}^{+})$ , bottom) or green ( $k_r > \text{Re}(k_{in}^{+})$ , top) steepest decent contour depending on the value of $r$ , this cancels exactly with the incoming wave in the total pressure perturbation. . . . . | 166 |

## List of Tables

|   |  |    |
|---|--|----|
| 1 | Commonly occurring parameters. . . . .   | 8  |
| 2 | Commonly used functions, superscripts, subscripts and diacritics used within this thesis. $f$ is used as a dummy variable. . . . .   | 9  |
| 3 | Parameter sets used for any following numerical results sections. The impedance is of mass-spring-damper type, $Z(\omega) = R + i\mu\omega - iK/\omega$ . The impedance has been given in each case to 3 decimal places. . . .                     | 12 |
| 4 | Comparison of the different decay rates given for a general flow profile by Swinbanks [1975] and for a linear boundary layer flow profile by Brambley et al. [2012a] against those given here for a quadratic boundary layer flow profile. . . . . | 60 |

## Acknowledgements

I would like to express my deepest gratitude to my supervisor Dr. Ed Brambley, for your guidance, support and friendship throughout not just the PhD, but everything around it. Your insights, encouragement and optimism have brought out the best in me as a person and a mathematician.

I am extremely grateful to my family for their unwavering support and encouragement throughout not just the last couple years but my whole life.

To my friends old and new. Thank you for continually listening to me ramble on about much of this work, for your patience with me, and for the welcome distraction you have provided.

Thank you Daphne for your kind support and smile, as well as for all your encouragement and patience.

Thank you to my Dad. You inspire me. Thank you for everything you have done for me. For your support, your sacrifices, your guidance and your advice. You have truly been there for me no matter what.

I also express my sincerest thanks to Stephen. Your unconditional love, patience and support throughout these years has been instrumental to where I am today. Although you may not have been able to help with the workload, you have filled every moment with happiness, I will always treasure each moment we share. I love you.

And finally to those who have passed.

My Mums.

Thank you.

Thank you also to the University of Warwick and the MASDOC program for the funding and the opportunity to complete this PhD.

# Declaration

This thesis is submitted to the University of Warwick in support of my application for the degree of Doctor of Philosophy. It has been composed by myself and has not been submitted in any previous application for any degree.

The work presented (including data generated and data analysis) was carried out by myself.

Parts of this thesis have been published by myself:

- The Critical Layer in Quadratic Flow Boundary Layers over Acoustic Linings, by; **Matthew J.King**, Edward J.Brambley, Renan Liupekevicius, Miren Radia, Paul Lafourcade and Tauqeer H.Shah. In press in the Journal of Fluid Mechanics. [King et al., 2022]
- Stabilisation of the Hydrodynamic Instability by the Critical Layer, by; **Matthew J.King** and Edward J.Brambley. AIAA 2022-3096 Conference paper, Presented as part of the 28th AIAA/CEAS Aeroacoustics 2022 Conference, June 14-17, 2022, Southampton, UK. [King and Brambley, 2022]
- Stabilisation of the Hydrodynamic Instability by the Critical Layer, by; **Matthew J.King** and Edward J.Brambley. Submitted for review in the AIAA Journal.

The analysis presented within these publications has been adapted and is contained within part II of this thesis, with; The Critical Layer in Quadratic Flow Boundary Layers over Acoustic Linings [King et al., 2022], contained in sections 5.1-11.2, and section 26.1. Stabilisation of the Hydrodynamic Instability [King and Brambley, 2022], contained in section 12.

The contributions of Renan Liupekevicius, Miren Radia, Paul Lafourcade and Tauqeer H.Shah is contained within the analysis of sections 5.1, 6 and 9.1. Their contributions took place prior to the start of the PhD. Given was: The construction of the Pridmore-Brown equation, (5.15); The form and coefficients of the  $\tilde{p}_c$  solutions (6.3) through a Frobenius series including the jump in  $\tilde{p}_{c2}$  although corrections were required; The radius of convergence of these solutions and the issues that presented was understood but not resolved with the Frobenius series solutions about  $r = 1$  being constructed; The Wronskian  $W(r)$  (6.26c); And an outline of the approach to be taken, to construct the Green's function solution, analysis the jump across the branch cut, and predict the decay rates using Watson's lemma. Each of the results

given were confirmed independently, and any extensions and conclusions given was carried out without further collaboration with Renan Liupekevicius, Miren Radia, Paul Lafourcade or Tauqeer H.Shah.

The contributions of Edward J.Brambley is that of a PhD supervisor across all of the work presented as part of this thesis.

# Abstract

Throughout this document we will study the linearised Euler equations within a cylindrical duct. We assume a mean flow that is uniform within most of the duct, except for a region near the wall, where the flow is sheared to retrieve a non-slip boundary. For these flow profiles, under Fourier series and transform, the linearised Euler equations become the Pridmore-Brown equation, which contains a regular singularity known as the critical layer.

When inverting the Fourier transform the resulting pressure perturbation consists of various contributions; the modal sum, the integration around a branch cut which occurs because of the critical layer, and a mode known as the hydrodynamic instability. The branch cut, which we refer to as the critical layer branch cut, is more commonly known as the continuous spectrum.

We consider a mean flow profile that has a boundary layer following a quadratic curve. It is found that in our case hydrodynamic instability mode can interact with the critical layer branch cut and be stabilised. As a result, the mode contributes as part of the critical layer branch cut and the far-field pressure perturbation changes considerably.

This thesis is split into three main topics. Firstly, we solve the Pridmore-Brown equation for the mean flow profile mentioned above, including the appropriate analytic continuations, to examine the behaviour of the critical layer branch cut. We make use of the Green's function to understand the contributions to the Fourier inversion. This includes studying how the hydrodynamic instability may be stabilised, and the resulting far-field effects. This is followed by an extension to the Brambley boundary condition for a uniform mean flow to account for the sheared flow effects and observe similar behaviours. Finally, we examine the contributions of the critical layer under the scattering due to a change in the duct wall.

# Part I

## Introduction

### 1 Problem Background

The propagation of sound through an otherwise steady mean flow has many important applications including the prediction and optimisation of noise within aircraft engines. With aircraft noise being subjected to ever increasing restrictions, being able to successfully model this noise becomes increasingly important. In particular, aircraft engine noise at takeoff depends critically on the sound absorbing performance of acoustic liners. Unfortunately, acoustic liner performance in the presence of a steady mean flow is poorly predicted by existing theory, as demonstrated by comparisons to laboratory experiments [Renou and Aurégan, 2011, Spillere et al., 2020]. The theory is equally applicable to any situation with small perturbations to an otherwise steady mean flow along a non-rigid boundary: for example, the stability analysis of flow over a deformable surface.

The behaviour of sound in air within an otherwise steady mean flow is usually modelled using the linearized Euler equations, although the Navier-Stokes equations with a high Reynolds number may also be used. In order to model non-rigid boundaries, such as the acoustic liners used in aircraft engines, an impedance boundary condition is used. [Watson et al., 1999, Rienstra and Peake, 2005].

Considering a disturbance that leads to an oscillating pressure, with frequency  $\omega$ , given by  $\text{Re}(p \exp\{i\omega t\})$ . Evaluating the governing equations at the boundary leads to an oscillating normal boundary velocity with the same frequency,  $\text{Re}(v \exp\{i\omega t\})$  with the relation  $p = Z(\omega)v$ .  $Z(\omega)$  is considered the impedance and is generally complex with real part often called the resistance, and imaginary part known as the reactance. Models for the impedance include; a fixed constant, a Mass-Spring-Damper model, or a Helmholtz Resonator model [Rienstra, 2006]. Other more general examples, and conditions for physical relevance are also provided in [Rienstra, 2006]. Such impedance boundary conditions are well understood for mean flows that have ‘no-slip’ at the boundary. A mean flow profile  $U$  is characterised as being no-slip if  $U = 0$  when evaluated anywhere along duct wall. Often within the literature however, in order to construct a simplified model, mean flows that do not satisfy no-slip at the boundary are used: for example, uniform axial flow in a duct. For these slipping mean flows, it is known that the impedance boundary condition must

be modified, introducing an effective impedance that accounts for the slipping effects.

Most acousticians investigate the interaction of sound and acoustic linings by considering the duct modes in the frequency domain [e.g. Campos and Kobayashi, 2009, Marx and Aurégan, 2013, Nørtoft et al., 2015] found by considering the Fourier transformed problem. The modes occur, for a fixed frequency, at an axial wavenumber that leads to a solution that satisfies the boundary conditions at the walls. Mathematically these are eigenvalues in the axial wavenumber and have associated eigenfunctions.

Each mode may be categorised in two ways which depend on their axial wavenumber. The first is their direction of propagation. This may be either upstream (travelling against the flow) or downstream (travelling with the flow). This is decided through the consideration of causality arguments which we will discuss later. The other way to categorise the modes is if the mode is 'cut-off' or not, (referred to as being 'cut-on'). A mode is considered as cut-off when the associated eigenfunction decays in their propagating direction. This decay is exponential with exponent related to the axial wavenumber. Cut-on modes instead are neutrally stable and have a constant amplitude in the far-field. These cut-on modes are only typically present for hard walled duct and non-energy absorbing walls. Since these modes are not typically present in other cases, we instead identify 'nearly cut-on' modes which still decay exponentially in the far-field but with a small exponent, resulting in their contribution being long-lived compared to the cut-off modes.

A reasonably general solution is given by a linear sum of these modes, with amplitudes fitted to emulate a particular sound source. This is the basis of techniques such as mode-matching [e.g. Gabard and Astley, 2008, Yang et al., 2018], although, since the modes also occur as poles in complex analytic methods, other methods such as the Wiener-Hopf technique [e.g. Rienstra, 2007, Jiang et al., 2017, Sobolev and Yakovets, 2017] may also be applied.

As previously mentioned, each mode may either propagate upstream or downstream. Determining this is one complication of considering duct modes in the frequency domain. This can be achieved using the Briggs-Bers criterion [Briggs, 1964, Bers, 1983], which can further be extended into the time domain. Other methods for determining the direction of propagation for the modes have been used in the literature, although within Brambley [2009b] it is shown that there are cases where these fail to correctly predict the stability. Hence, we only consider the directions of propagation under the Briggs-Bers criterion here.

Under the Briggs-Bers criterion most of the modes are stable and decay in their

direction of propagation, but a number of modes exist with interesting properties [Rienstra, 2003]. Known as surface modes, these modes typically contribute to the pressure field with a contribution contained near the boundary, giving them their name. One such surface mode is known as the hydrodynamic instability. Hydrodynamic instabilities only exist in the presence of a mean flow and correspond to a mode with an exponentially growing contribution. In this way these modes, despite being surface modes, will dominate the resulting pressure profile across the entire domain in the far-field. Mathematically this would lead to a break down of the linearisation assumptions, with the perturbation terms becoming comparable to the mean flow solutions. This would result in the solutions not being valid in the far-field, and additionally is when viewed in the context of sound.

There is also some experimental evidence of instabilities [e.g. Aurégan and Leroux, 2008], although the hydrodynamic instability is in most cases the least well theoretically-predicted duct mode using the various impedance boundary conditions. Further, previous mathematical models have found the hydrodynamic instability to always be present, which would not be expected physically. For this reason some previous work has elected to explicitly remove the hydrodynamic instability mode which can be done by either directly ignoring the mode and its contribution as unphysical [Rienstra and Tester, 2008, Sobolev and Yakovets, 2017], or by neglecting what may be otherwise physically relevant terms, modifying the differential equation through gradient term suppression within the linearised Euler equations [e.g. Deng et al., 2021, Hu and Nark, 2022]. Within either approach to removing the hydrodynamic instability validation can be made against experiments. However, neither result in a model that captures all of the physical properties of the linearised Euler equations.

One commonly used model, that in some cases does not present a hydrodynamic instability is a uniform mean flow with the Ingard–Myers boundary condition [Ingard, 1959, Myers, 1980] applied. This is a modified impedance boundary condition used in order to account for the slipping flow. This boundary condition is known to be the correct limiting behaviour for an inviscid mean flow boundary layer in the limit that the boundary layer thickness tends to zero [Eversman and Beckemeyer, 1972, Tester, 1973]. However, this boundary condition, when applied in the time domain may be ill-posed [Brambley, 2009b]. This is due to the unbounded growth rate of the absolute instabilities under the Briggs-Bers criterion. For this reason, and the ongoing pursuit of experimentally accurate models, an improved model is still being actively sought.

Several alternative boundary conditions have been suggested for a uniform flow [Brambley, 2011b, Schulz et al., 2017, Khamis and Brambley, 2017a, Aurégan, 2018],

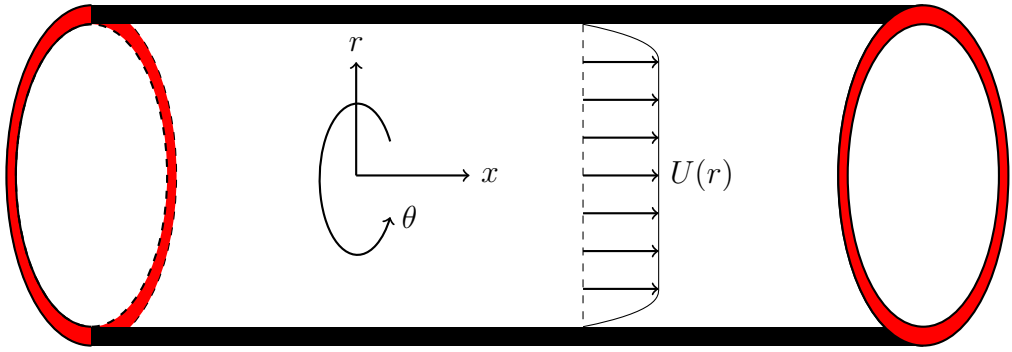


Figure 1: A cylindrical duct containing an axial mean flow  $U(r)$ .

with each attempt to include more relevant physics, including the effect of the mean flow boundary layer and the effect of viscosity. However, these boundary conditions come with their own complications, including the need to fit further free parameters, and as yet none have been made to agree with laboratory experiments [Spillere et al., 2020] and varying agreement with the full solutions they intend to model has been found [Gabard, 2013, Khamis and Brambley, 2017b].

In light of this difficulty with boundary conditions in slipping mean flow, one may instead only consider mean flows  $U(r)$  that satisfy no-slip at the boundary [e.g. Weng et al., 2017]. Doing so, however, involves solving for the sound in a strongly varying mean flow, which is especially taxing when the boundary layers are particularly thin. Numerically resolving the sound in thin boundary layers requires a fine resolution, which then also requires a small time step owing to the Courant–Friedrichs–Lewy condition [Courant et al., 1967]. Despite this, as computers become more powerful, direct numerical simulation is more regularly being used to resolve the boundary layer, solving the governing equations numerically near a wall that is not described by the Impedance but rather by cavities that the Impedance represents. This allows us to check the assumptions of the use of an Impedance boundary condition, with comparisons made against analytic solutions. Other uses including the reproduction of sound and flow fields near the wall. Tam and Kurbatskii [2000], Tam et al. [2010], Zhang and Bodony [2016], Chen et al. [2020]. Alternatively, progress may be made analytically by considering the simplified situation of a straight rectilinear or cylindrical duct containing axial mean flow as depicted in figure 1. By linearising the Euler equations about this steady mean flow and assuming the solutions act are waves in both when considered both in time and along the length of the duct, i.e. their  $t$  and  $x$  dependencies are contained within an  $\exp\{i\omega t - ikx\}$  term, one eventually arrives at the Pridmore-Brown equation (5.1), a second-order linear ordinary differential equation for the pressure perturbation within the duct due to Pridmore-Brown [1958]. The Pridmore-Brown equation has been the sub-

jected of much analysis [e.g. Mungur and Gladwell, 1969, Ko, 1972, Swinbanks, 1975, Nagel and Brand, 1982, Brambley et al., 2012a, Rienstra, 2020], owing to its complexity. One complexity is that, for any known frequency when solving for the axial wavenumber  $k$  as the eigenvalue, the Pridmore-Brown equation is not Sturm–Liouville and results in a nonlinear eigenvalue problem for  $k$ . A second complexity is that the Pridmore-Brown equation possesses a regular singularity, referred to as the critical layer or the continuous spectrum. Despite these difficulties, eigen expansions using eigenfunctions of the Pridmore-Brown equation are frequently used, with the eigenfunctions assumed to form a complete basis, despite the problem not being self-adjoint, and the effect of the critical layer ignored [e.g. Brooks and McAlpine, 2007, Olivieri et al., 2010, Oppeneer et al., 2016, Khavaran, 2019, Rienstra, 2021]. In the time domain, it is known that these problems will lead to a well-posed problem, due to the bounded growth rate of any absolute instabilities, moreover, it is known that increasing the boundary layer thickness will lead to the removal of the absolute instabilities, which become hydrodynamic instabilities [Rienstra and Darau, 2011].

The critical layer, or continuous spectrum, is a singularity of the linearized Euler equations occurring when the phase velocity of the perturbation,  $\omega/k$ , and is equal to the local fluid velocity of the steady flow,  $U(r_c)$ , for some critical radius  $r_c$ . Because the phase speed is equal to the flow speed, the effect of the critical layer may be thought of as being convected with the mean flow, and therefore as hydrodynamic in nature [Case, 1960, Rienstra et al., 2013]. For swirling flows, the critical layer is known to lead to algebraically growing instabilities [Golubev and Atassi, 1996, Tam and Auriault, 1998, Heaton and Peake, 2006]. For the Pridmore-Brown equation however the critical layer branch cut leads to algebraically decaying disturbances [Swinbanks, 1975, Félix and Pagneux, 2007, Brambley et al., 2012a]. The rate of this decay varies when considering different sheared flow profiles. However, this has only been previously given in full detail for a linear shear mean flow profile.

The lack of completeness of the modal solutions of the Pridmore-Brown equation motivates the investigation of the Green’s function solution. The Green’s function is the solution of the governing equations subject to a point forcing; for example, a point mass source leads to the right-hand-side of equation (5.1). The Green’s function may be used to construct the solution of the governing equations subject to any arbitrary forcing; hence, the Green’s function is capable of being used to express any solution to the governing equations, in contrast to a modal eigenvalue expansion which can only express an arbitrary solution if the modal basis is com-

plete. The Green's function is also worth considering on its own merits without reference to a particular forcing, since if the governing equations are capable of exhibiting a particular feature (such as instability, focusing, perfect reflection, etc), then the Green's function must also exhibit that feature. The Green's function is also used in various approximation techniques [e.g. Brambley et al., 2012b, Posson and Peake, 2013, Mathews and Peake, 2018b]. For this reason, the Green's functions has been constructed for a variety of acoustical situations [e.g. Rienstra and Tester, 2008, Brambley et al., 2012a, Mathews and Peake, 2017, 2018a]. In particular, the Green's function solution to the Pridmore-Brown equation naturally includes the critical layer, allowing us to identify the decay rate. The Pridmore-Brown equation and its Green's function are both found and studied in part II, we will then account for the same setting within a boundary condition for a slipping flow in part III.

Due to the algebraic decay of the critical layer, it is often considered to be negligible in comparison with the modal sum of the acoustics modes. This is particularly true in the presence of a hydrodynamic instability. Although even if the hydrodynamic instability is removed or ignored the critical layer is still often neglected. This may not be justified however, with cases in the works such as that given by Brambley, Darau and Rienstra [2012a] where the critical layer has been seen to be comparable in magnitude to the acoustic modes.

Considering the applications, and the experiments used to test impedance linings, it is worthwhile considering problems with not just an impedance boundary condition down an entire duct, but also problems that experience a change in the boundary condition, going from hard walled to lined, and then back to hard walled. These lead to scattering problems, which are typically approached using the aforementioned mode-matching technique [Regan and Eaton, 1999, Gabard and Astley, 2008, Openeer et al., Yang et al., 2018]. However, this is only applicable for an assumed modal solution, which as discussed is not the case here. Not wanting to neglect these terms it is also possible to approach these problems using the Wiener-Hopf technique [Koch and Mohring, 1983, Rienstra and Peake, 2005], which can then account for the critical layer. Despite this, the inclusion of the critical layer and non-modal effects is not present within the literature to date. When making use of the Wiener-Hopf technique, which is considered in part IV, we can draw from the Green's function solution to an infinite lined duct considered in part II under a single boundary condition, in order to correctly identify the form of the incoming wave modes, allowing for a greater range of incoming waves than that used for mode-matching.

## 2 Notation

Throughout this thesis we will be making use of various notations in order to show-case different behaviours. While efforts have been made where ever possible to maintain consistency in the notation, some letters and symbols are re-used depending on context. Table 1 summarises most of the commonly used notation.

In addition to this, we often make use of the functions, superscripts, sub-scripts and diacritics summarised in table 2.

Notation that is either re-used, is temporary, or redefined throughout the main body of this work is highlighted at the point of use.

## 3 Numerical Methods

In addition to the analytic results which are constructed and given across the following work, effort has been made to provide numerical confirmations and examples of specific behaviours. All of the code generated and figures produced has been completed within MATLAB, with large portions of the code having been made accessible as supplementary material alongside [King et al., 2022].

The use of the code can be largely broken down into three processes: The evaluation of the analytic solutions, the location of modal poles, and the evaluation of the Fourier inversion. Of the solutions constructed some require the evaluation of special infinite power series, known as Frobenius series. In order to maintain accuracy where possible these have always been summed using appropriate scaling between each power and its corresponding coefficients. The series is then summed until a relative error of order  $10^{-16}$  is achieved, while tracking any potential numerical error introduced by summing a large number of terms. Additionally, where possible the series have only been evaluated away from the edge of their radii of convergence in order help keep the errors small. This has been done by tactfully choosing what forms to express solutions as accordingly.

When seeking roots of expressions, as will be done to locate and track modal poles, a variant of the Secant method has been used. This has then been confirmed against results using a finite-difference [Brambley, 2011b] and Runge-Kutta methods applied to the Pridmore-Brown equation.

Finally when summing residues in order to retrieve Fourier Inversions, only poles with imaginary part  $|\text{Im}(k)| < 400$  have been included. Additional poles could have been included which would increase accuracy of the resulting Fourier Inversion, par-

| Symbol            | Description   |
|-------------------|---|
| $r$               | Radial location in the duct, $r = 0$ indicates the centre line of the duct, which is taken to be cylindrical throughout. Prior to non-dimensionalisation of lengths by the duct radius $a$ , we consider $0 < r < a$ .                    |
| $r_0$             | A specific radial location, detailing the location of a point mass forcing.   |
| $x$               | The axial location within the duct, $x = 0$ is chosen in order to examine upstream, $x < 0$ , and downstream, $x > 0$ , generated by specific stimulus located at $x = 0$ .   |
| $k$               | The axial wave number, found by Fourier transform $x \rightarrow k$ .   |
| $t$               | Time.   |
| $\omega$          | The frequency of the assumed time harmonic solutions, following the $e^{i\omega t}$ convention.   |
| $\theta$          | The azimuthal co-ordinate within the cylindrical duct, with $\theta = 0$ taken fixed, but arbitrary.  |
| $m$               | Azimuthal wave number, found by performing a Fourier series in $\theta \rightarrow m$ .   |
| $U(x, r, \theta)$ | The mean flow profile. Assumed to be only varying radially, and flowing parallel to the duct throughout, $U(r)\mathbf{e}_x$ .   |
| $c$               | The speed of sound within the duct.   |
| $M$               | The Mach number of the mean flow at the centre-line of the duct.<br>$M = \frac{U(0)}{c(0)}$   |
| $h$               | The boundary layer thickness, within which the flow profile considered varies; $\frac{U(r)}{c} = M$ for $r < a(1 - h)$ , where $a$ is the radius of the duct.   |
| $h_c$             | A critical value of the boundary layer thickness, for which different behaviours are observed for $h < h_c$ and $h > h_c$ .   |
| $Z$               | The duct wall impedance, prescribed by the acoustic lining being considered, in general, $Z = Z(\omega)$ . We considered $Z(\omega)$ to follow a Mass-Spring-Damper model. $Z(\omega) = R + i\left(\mu\omega - \frac{K}{\omega}\right)$ . |
| $\mu$             | Impedance Mass.   |
| $K$               | Impedance Spring.   |
|                   | $K = K(k)$ ; The Wiener-Hopf kernel. In part IV only.   |
| $R$               | Impedance Damper.   |
|                   | Dummy variable used for a change of the radial variable.  |
|                   | $R = R(k)$ Residue of a modal pole located at axial wave number $k$ .   |
| $\rho$            | The flow density.   |
| $p$               | The flow pressure.  |
|                   | The recovered linearised pressure perturbation for a single azimuthal wave mode $m$ .   |
| $\psi$            | Alternative variable used for the flows pressure perturbation.  |
| $G$               | Alternative variable used for the flow pressure perturbation, relating to the pressure wave as a result of a point mass source, representing the resulting Green's function solution.   |
| $\mathbf{u}$      | The flow velocity with components, $\mathbf{u} = (u, v, w)$ , in the $(x, r, \theta)$ directions respectively.  |
| $r_c^\pm$         | $= 1 - h \pm Q$ The complex radial locations, following non-dimensionalisation, for which the critical layer singularity occurs within the Pridmore-Brown equation.   |

Table 1: Commonly occurring parameters.

| Symbol                     | Description  |
|----------------------------|--|
| $\delta(f)$                | The delta function, takes value 1 when $f = 0$ , or 0 otherwise.   |
| $H(f)$                     | The Heaviside function, takes value 1 for $f > 0$ , and 0 for $x < 0$ . It is only defined for real inputs.  |
| $\text{Re}(f)$             | The real part of a complex variable $f$ .  |
| $\text{Im}(f)$             | The imaginary part of a complex variable $f$ .   |
| $ f $                      | The absolute value of $f$ , making use of the complex modulus.   |
| $f'$                       | The derivative of $f$ , often with respect to the radial variable $r$ unless otherwise stated.   |
| $\mathcal{W}(f_1, f_2; r)$ | The Wronskian operator between two functions $f_1(r)$ and $f_2(r)$ .   |
| $\Delta f$                 | The change in evaluation of $f$ for crossing a branch cut from above to below.   |
| $f^+$                      | When $f$ is a function, $f^+$ is the analytic continuation of that function through a branch cut as if we are located above the branch cut, $f^+ = f + \Delta f$ .                                   |
| $k^+$                      | A mode of the function $f^+(k)$ , but not necessarily $f(k)$ .   |
| $f^-$                      | When $f$ is a function, $f^-$ is the analytic continuation of that function through a branch cut as if we are located below the branch cut, $f^- = f - \Delta f$ .                                   |
| $k^-$                      | A mode of the function $f^-(k)$ , but not necessarily $f(k)$ .   |
| $f_0$                      | The mean flow equivalent of $f$ . Relating to the linearised Euler equations.  |
| $\hat{f}$                  | The linear perturbation of $f = f_0 + \epsilon \hat{f} + O(\epsilon^2)$ .<br>Applied to coefficients within linear combinations of functions to indicate there association to larger values of $r$ . |
| $\check{f}$                | Applied to coefficients within linear combinations of functions to indicate there association to smaller values of $r$ .   |
| $f_{<}$                    | Considers the evaluation of $f$ due to the smaller of $r$ and $r_0$ , $r_{<} = \min(r, r_0)$ .   |
| $f_{>}$                    | Considers the evaluation of $f$ due to the greater of $r$ and $r_0$ , $r_{>} = \max(r, r_0)$ .   |
| $\tilde{f}$                | The function $f$ , relating to the linear perturbation having undergone a Fourier series in $\theta \rightarrow m$ and a Fourier transform in $x \rightarrow k$ .                                    |
| $f_{in}$                   | A specific value or function $f$ corresponding to an incoming wave.  |
| $f_{\pm}$                  | The terms of an additive decomposition of the function $f = f_+ + f_-$ .   |
| $f_{\pm}$                  | The terms of an multiplicative decomposition of the function $f = f_+ f_-$ .   |

Table 2: Commonly used functions, superscripts, subscripts and diacritics used within this thesis.  $f$  is used as a dummy variable.

ticularly for very small values of  $x$ ; however due to the large value of  $k$  our solutions are less accurate and we may be introducing further errors through the summing of many terms in the Frobenius Series and the large scaling required for the evaluation of the Bessel functions, or otherwise failing to locate poles.

Throughout we show results from eight parameter sets detailed in table 3. These parameter sets have been broken down into four different sub-parameter sets, changing only a single variable in each for a total of 31 parameter sets considered. These are indicated within the text as  $A1$ ,  $B3$  and  $E4$  etc. The table of parameter sets may be read as each row remaining largely consistent for each parameter given, while the subscripts denote the effects of changing only one parameter. For example; parameter set  $A1$  in the text refers to  $A$ , with  $m = 0$ ,  $h = 0.02$ ,  $M = 0.5$ ,  $\mu = 0.15$ ,  $K = 1.15$ ,  $R = 3$ . Additionally with  $\omega = 5$ , as indicated by the subscript (1) in table 3, resulting in  $Z(\omega) = 3 + i(0.15\omega - \frac{1.15}{\omega}) = 3 + 0.52i$ . It should be noted that parameter set  $D3 = G3$ .

We have chosen these parameters in order to showcase a variety of different behaviours throughout the main text. While some parameter sets have been drawn from the literature, as detailed below, we have specifically chosen  $A4$ ,  $C4$  and  $D4$  in order to locate poles in the complex  $k$  plan near the critical layer branch cut.

The impedance model used for parameter set  $A$  has been drawn from [Khamis and Brambley, 2016], while parameter sets  $B1$  and  $B2$  are used in [Brambley et al., 2012a], with parameter sets  $C2$  and  $G2$ , and the impedance model of both parameter set  $D$ , are given in [Brambley and Gabard, 2016].

While the code has been carefully constructed for the accurate numerical evaluations of the solutions given throughout this thesis, some numerical errors remain observable. These correspond particularly to our Fourier inversions near  $x = 0$  such as in figure 26. Additionally, any integrals around the critical layer branch cut have been performed using the steepest descent contours described in the main text, which have not been numerically compared to the true integral around the branch cut. This has not been performed due to the highly oscillatory behaviour and large amounts of cancellation as a result of integrating around the critical layer branch cut, which is avoided for an exponentially decaying integral as a result. Moreover, even when evaluating the steepest descent contours we have chosen to only consider a finite integral, assuming contributions for large  $|k|$  to be negligible, which is once again not necessarily true for  $x$  near 0.

Despite these difficulties it is our belief that the resulting plots are accurate within

the majority of the near-field and the far-field. In addition the conclusions drawn are not expected to be impacted by these errors.

|          | A                                       | B   | C   | D  |
|----------|---|---|---|--|
| $\omega$ | $5^{(1)}$<br>$31^{(3)}$                 | 10<br>$20.4^{(4)}$                                  | 31  | 10   |
| $m$      | 0                                       | $0^{(1)}$ $5^{(2)}$<br>$10^{(3)}$ $24^{(4)}$        | 24  | 24   |
| $h$      | 0.02                                    | 0.05  | $0.01^{(1)}$ $0.001^{(2)}$<br>$0.0001^{(3)}$ $0.0075^{(4)}$ | 0.005  |
| $M$      | 0.5                                     | 0.5   | 0.4   | $0.3^{(1)}$ $0.4^{(2)}$<br>$0.5^{(3)}$ $0.433^{(4)}$ |
| $\mu$    | 0.15                                    | 0.2   | 0.08  | 0.01   |
| $K$      | 1.15                                    | 10  | 6   | 10   |
| $R$      | 3                                       | 2   | 1.6   | 0.75   |
| $Z$      | $3 + 0.52i^{(1)}$<br>$3 + 4.613i^{(3)}$ | $2 + i$<br>$3 + 1.385i^{(2)}$<br>$3 + 3.004i^{(4)}$ | $1.6 + 2.286i$  | $0.75 - 0.013i$                                      |

|          | E                                    | F   | G  | H  |
|----------|--------------------------------------|---|--|--|
| $\omega$ | $2^{(1)}$<br>$10^{(3)}$              | 10<br>$5^{(2)}$<br>$31^{(4)}$                         | 31   | 10   |
| $m$      | 5                                    | $0^{(1)}$ $5^{(2)}$<br>$10^{(3)}$ $24^{(4)}$<br>0.005 | 24   | 24   |
| $h$      | 0.05                                 | 0.005   | $0.01^{(1)}$ $0.001^{(2)}$<br>$0.005^{(3)}$ $0.0005^{(4)}$ | 0.005  |
| $M$      | 0.3                                  | 0.5   | 0.5  | $0.3^{(1)}$ $0.4^{(2)}$<br>$0.5^{(3)}$ $0.7^{(4)}$ |
| $\mu$    | 0.2                                  | 0.1   | 0.01   | 0.06   |
| $K$      | 5                                    | 5   | 10   | 3  |
| $R$      | 1                                    | 0.75  | 0.75   | 0.75   |
| $Z$      | $1 - 2.1i^{(1)}$<br>$1 + 1.5i^{(3)}$ | $0.75 + 0.5i$<br>$1 + 6.038i^{(4)}$                   | $0.75 - 0.013i$  | $0.75 + 0.3i$                                      |

Table 3: Parameter sets used for any following numerical results sections. The impedance is of mass–spring–damper type,  $Z(\omega) = R + i\mu\omega - iK/\omega$ . The impedance has been given in each case to 3 decimal places.

## Part II

# The Critical Layer for a Point Mass Source

## 4 Introduction

Throughout the following part we will be considering a specific mean flow profile that follows a uniform flow near the centre line of the duct, and is then sheared quadratically within some boundary layer to retrieve non-slip at the duct wall. We will be making use of the linearised Euler equations to do so, performing a Fourier series and transform in order to retrieve the Pridmore-Brown equation, which is then solved using a Frobenius series. Exciting the system by considering the case of a point mass source, we then proceed to study the effect of the acoustic modes and the critical layer under the Fourier inversion of the Fourier transform.

When considering the modes as eigenvalues of the linearised Euler equations it has been observed that the critical layer branch cut, in this scenario considered to be a continuous spectrum, can be considered as separating distinct sets of eigenfunctions; that is, for each point in the continuous spectrum there is an associated value of  $r_c$ , and the evaluations for  $r < r_c$  and  $r > r_c$  are constructed using these distinct sets of eigenfunctions [Campos and Oliveira, 2011]. Although we do not give further details of this here, it is clear that even when considering just the eigenvalue problem, great care must be taken when considering these values of the axial wavenumber  $k$ .

When taking a Green's function approach, as the one that will be used here, the critical layer has been observed to have an algebraically decaying contribution. For different flow profiles the approaches and results for the specific rate of decay given have varied. For example, Swinbanks [1975] predicted a disturbance of constant amplitude plus a disturbance with  $O(x^{-3})$  decay for a point source, and  $O(x^{-1})$  decay for a distributed source, although exact formulae for these disturbances are not given. Swinbanks [1975, p. 62] goes on to argue that the constant amplitude disturbance would not be present when the disturbance is caused "by moving the surface of a solid body". Despite the work of Swinbanks being analytic in approach no details on the process to reproduce these results are given. Félix and Pagneux [2007] demonstrated numerically, for a point source in a parabolic mean flow, a de-

cay rate of  $O(x^{-1})$  appearing to contradict Swinbanks. This result is only produced through a line of best fit to numerically generated data points, and may not be accurate. This led to Brambley, Darau and Rienstra [2012a] investigating the problem further, despite the large differences in setting between Swinbanks [1975], Félix and Pagneux [2007] and their own work. Brambley et al. proceeded to construct an explicit analytic solution for the critical layers' far-field effect for a mean flow  $U(r)$  that is constant in the centre of the duct, and then varies linearly in boundary layer to zero at the duct walls, thus retrieving non-slip  $U(a) = 0$ . Locating a point mass source at a radius  $r_0$ , they found the pressure perturbation from the critical layer at a radius  $r$  consisted of three distinct components with phase velocities  $U(0)$ ,  $U(r)$  and  $U(r_0)$ , each with different decay rates. However, Brambley, Darau and Rienstra [2012a] chose a rather special mean flow profile. In particular, as observed by Swinbanks, the critical layer is usually caused by a nonzero second derivative of the mean flow profile,  $U''(r)$ , but for the constant-then-linear mean flow  $U''(r)$  is either identically zero or has a delta function discontinuity suggesting it would not be present for such a flow profile. Instead, the critical layer may also occur as a consequence of the ducts cylindrical geometry, which Swinbanks would not have observed, considering a rectilinear duct.

Since the critical layer is a singularity of the Pridmore-Brown equation, traditional numerical methods, such as finite differences, are particularly inaccurate near the critical layer. This often manifests as a collection of spurious numerical modes being located along values of the axial wavenumber  $k$  of which  $\omega = U(r)k$  for some  $r$  within the duct. This leads to this line of critical values being interpreted as the continuous spectrum with finite meshes in the radial axis leading to the appearance of a discrete set of modes. In contrast, previous analytic studies have used a Frobenius expansion about the singular point  $r = r_c$  for which  $\omega = U(r_c)k$  for each fixed axial wavenumber  $k$  [e.g. Heaton and Peake, 2006, Campos and Kobayashi, 2009, Brambley et al., 2012a]. One advantage of the Frobenius series is that we can locate the series around specific points, such as the  $r_c$ . In this way we can guarantee accuracy around this specific point. On the other hand one complication of the Frobenius series is that, much like a power series, it has an associated radius of convergence. For the constant-then-linear mean flow Frobenius expansion [Brambley et al., 2012a], this did not prove a problem, as the radius of convergence covered the region of interest in all cases that were considered. For general flow profiles this will not be the case, and a solution covering the entire region of interest will involve multiple Frobenius expansions with overlapping radii of convergence; this will turn out to be the case here. By matching two different expansions in a region where

both converge, a hybrid solution may be constructed that spans the whole region of interest.

Irrespective of the effects of the critical layer, in the downstream far-field it is dominated by any hydrodynamic instabilities. When considering a mean flow profile that was uniform except with a boundary layer where a tanh curve was followed [Brambley, 2013], it was found that the hydrodynamic instability could move behind the critical layer branch cut for certain parameters; this then would have resulted in a stable situation. However, this was not investigated further due to the numerical method being unable to track the hydrodynamic instability surface wave mode behind the critical layer. Fortunately, the Frobenius method is capable of tracking the mode behind the branch cut by analytic continuation. In the case of a linear-shear flow profile in Brambley, Darau and Rienstra [2012a] the hydrodynamic instability was not observed to move behind the branch cut. Rather, it was argued that this could not occur, believing it would result in a discontinuity in the residue of the mode. A different pole was observed to contribute as part of the critical layer in this case however. Brambley [2013] clearly demonstrates that this is an incorrect conclusion and further, in section 8.3, it is shown that in the event that a hydrodynamic instability moves behind the critical layer branch cut then not only would the solution then stabilise, but that the contribution of this hidden pole is included in the Fourier inversion integral around the critical layer which accounts for the expected discontinuity resulting in a continuous solution, This further results in the possibility that this integral could be dominant in the far-field, particularly for a sound source close to the wall. In cases such as this ignoring the critical layer would give inaccurate results.

As previously stated here we will construct the Pridmore-Brown equation, which is then solved using the Frobenius expansion method as described by Brambley, Darau and Rienstra [2012a], applying it to a mean flow that is constant in the centre of the duct and then varies quadratically within a boundary layer to satisfy non-slip at the wall. As well as being more realistic than the constant-then-linear profile considered by Brambley, Darau and Rienstra [2012a], this mean flow profile is twice differentiable, allowing  $U''(r)$  to enter the analysis, and as such we expect the results to be more representative of an arbitrary mean flow profile. This is following the aforementioned observation made by Swinbanks, that the effect of the critical layer, which was in that work examined for an arbitrary mean flow profile within a rectilinear duct, varies depending on if the sound source is located at a point in the flow where  $U''(r) = 0$  or otherwise.

In the case of a linear shear flow the effect of the critical layer is due not to the flow being present, since  $U''(r) = 0$  almost everywhere, but instead due to the problem geometry. In the quadratic shear flow case within a cylindrical duct we are instead able to observe both the critical layer within  $U''(r)$  but also the geometry of the problem, unlike either of these previous papers.

We will observe the resulting effect of the critical layer on the pressure perturbation, predicting and numerically verifying the decay rates. Further we will observe cases where the hydrodynamic instability is stabilised by moving behind the critical layer branch cut, and explore how this may occur in each of our parameters.

## 5 Pridmore-Brown Equation

### 5.1 Constructing the Pridmore-Brown Equation

At all points in this work we will be making use of the Euler equations as our governing equations, with viscous effects assumed to be zero.

$$\frac{\partial \rho}{\partial t} + \nabla \cdot (\rho \mathbf{u}) = 0, \quad \rho \frac{D\mathbf{u}}{Dt} = -\nabla p, \quad \frac{Dp}{Dt} = c^2 \frac{D\rho}{Dt}. \quad (5.1a)$$

These are the equations of conservation of mass, conservation of momentum and conservation of energy respectively with the variables;  $\rho$  the flow density,  $\mathbf{u} = (u, v, w)$  the flow velocity in cylindrical coordinates  $(x, r, \theta)$ ,  $p$  the flow pressure and  $c^2 = \left. \frac{\partial p}{\partial \rho} \right|_s$  the square of the speed of sound. This assumes the flow is adiabatic, and does not produce or lose any heat or mass into the duct walls.

In addition, throughout parts II and III we will excite the system with a mass source  $q$ , with our conservation of mass becoming

$$\frac{\partial \rho}{\partial t} + \nabla \cdot (\rho \mathbf{u}) = q. \quad (5.1b)$$

$q$  is assumed to be a small time-harmonic point mass source, which in cylindrical co-ordinates, with a suitable choice of origin takes the form

$$q = \text{Re} \left( \frac{\epsilon}{r_0} \delta(x) \delta(\theta) \delta(r - r_0) \exp\{i\omega t\} \right), \quad (5.2)$$

$\epsilon$  is the small amplitude,  $\omega$  is the frequency, and the  $1/r_0$  term comes from writing a unit amplitude point source in cylindrical coordinates. This form explicitly locates the mass source at  $(x, r, \theta) = (0, r_0, 0)$ .

In addition to this, we expand each variable in powers of  $\epsilon$ , with the assumptions

that each of the perturbed variables are time harmonic.

$$\begin{aligned} \rho &= \rho_0(r) + \text{Re}(\epsilon \hat{\rho} e^{i\omega t}) + O(\epsilon^2), & p &= p_0 + \text{Re}(\epsilon \hat{p} e^{i\omega t}) + O(\epsilon^2), \\ \mathbf{u} &= U(r) \mathbf{e}_x + \text{Re}(\epsilon (\hat{u}, \hat{v}, \hat{w}) e^{i\omega t}) + O(\epsilon^2), & c^2(r) &= c_0^2(r) + O(\epsilon), \end{aligned} \quad (5.3)$$

where  $p_0$  is necessarily a constant in order that the steady state should satisfy the Euler equations. Note that we have made the assumption here that our mean flow,  $U(r) \mathbf{e}_x$ , is a parallel, non-swirling flow and travelling in the  $x$  direction with only radial dependence.

These assumptions lead to the linearised Euler equations being written, to first order as,

$$i\omega \hat{\rho} + U(r) \frac{\partial \hat{\rho}}{\partial x} + \rho_0 \frac{\partial \hat{u}}{\partial x} + \frac{1}{r} \frac{\partial}{\partial r} (r \rho_0 \hat{v}) + \frac{\rho_0}{r} \frac{\partial \hat{w}}{\partial \theta} = q, \quad (5.4a)$$

$$i\omega \hat{p} + U \frac{\partial \hat{p}}{\partial x} = c_0^2 \left( i\omega \hat{\rho} + U \frac{\partial \hat{\rho}}{\partial x} + \hat{v} \rho_0' \right), \quad (5.4b)$$

$$i\omega \rho_0 \hat{u} + \hat{v} U' + U \frac{\partial \hat{u}}{\partial x} = - \frac{\partial \hat{p}}{\partial x}, \quad (5.4c)$$

$$i\omega \rho_0 \hat{v} + U \frac{\partial \hat{v}}{\partial x} = - \frac{\partial \hat{p}}{\partial r}, \quad (5.4d)$$

$$i\omega \rho_0 \hat{w} + U \frac{\partial \hat{w}}{\partial x} = - \frac{1}{r} \frac{\partial \hat{p}}{\partial \theta}. \quad (5.4e)$$

The time harmonic dependence can also be thought of as having taken a Fourier transform in time into the frequency  $\omega$ , however we will not consider the time domain in any detail throughout the work contained within this document.

It should further be noted that our choice of writing  $c^2$  only to leading order with order  $\epsilon$  corrections is due to the first order term not appearing within the first order linearised Euler equations. If you were to instead consider the quadratic terms this would require additional description.

Without loss of generality, each of the perturbed variables can be expanded using a Fourier series in  $\theta$  into the azimuthal wavenumber  $m$  and a Fourier Transform in  $x$  to the axial wavenumber  $k$ . As a result, the pressure perturbation is given as

$$\hat{p}(x, r, \theta) = \frac{1}{2\pi} \sum_{m=-\infty}^{\infty} e^{-im\theta} \int_{-\infty}^{\infty} \tilde{p}(r; k, m, \omega) e^{-ikx} dk, \quad (5.5)$$

and similarly for the density  $\hat{\rho}$  and the velocity components  $\hat{u}$ ,  $\hat{v}$  and  $\hat{w}$ . Substituting these into the Euler equations (5.4), each of  $\tilde{\rho}$ ,  $\tilde{u}$ ,  $\tilde{w}$ , and finally  $\tilde{v}$  may be eliminated. In particular, we make use of each of the following expressions constructed from

equations (5.4)(b-e), and substitute them into (5.4a);

$$i(\omega - U(r)k)\tilde{\rho} - ik\rho_0\tilde{u} + \frac{\rho_0}{r}\tilde{v} + \rho_0\tilde{v}' + \rho_0'\tilde{v} + \frac{im}{r}\rho_0\tilde{w} = \frac{1}{2\pi r_0}\delta(r - r_0), \quad (5.6a)$$

$$i(\omega - U(r)k)\tilde{p} = c_0^2 i(\omega - U(r)k)\tilde{\rho} + c_0^2 \tilde{v}\rho_0', \quad (5.6b)$$

$$i(\omega - U(r)k)\rho_0\tilde{u} = ik\tilde{p} - U'(r)\rho_0\tilde{v}, \quad (5.6c)$$

$$\tilde{v} = \frac{i\tilde{p}'}{\rho_0(\omega - Uk)}, \quad (5.6d)$$

$$\rho_0\tilde{w} = \frac{m}{r} \frac{1}{(\omega - U(r)k)}\tilde{p}, \quad (5.6e)$$

where a prime denotes the derivative with respect to  $r$ . Multiplying through by a factor of  $-i(\omega - U(r)k)$  gives the following equation for  $\tilde{p}$ .

$$\begin{aligned} \tilde{p}'' + \left( \frac{2kU'(r)}{\omega - U(r)k} + \frac{1}{r} - \frac{\rho_0'(r)}{\rho_0(r)} \right) \tilde{p}' + \left( \frac{(\omega - U(r)k)^2}{c_0^2(r)} - k^2 - \frac{m^2}{r^2} \right) \tilde{p} \\ = \frac{\omega - U(r_0)k}{2i\pi r_0} \delta(r - r_0). \end{aligned} \quad (5.7)$$

This is the Pridmore-Brown [1958] equation for a point mass source, written in cylindrical co-ordinates. Throughout the remainder of this work we will be seeking the Fourier inversion for a single azimuthal wavenumber  $m$

$$p(x, r; m) = \frac{1}{2\pi} \int_{-\infty}^{\infty} \tilde{p}(r; k, m, \omega) e^{-ikx} dk \quad (5.8)$$

making note of the abuse of notation between the total pressure field,  $p(x, r, \theta)$  and Fourier series co-efficient  $p(x, r; m)$ .

Considering a single azimuthal wavenumber is physically relevant to aeroengine rotor noise, where the sound typically has a known frequency, and a few known values of  $m$  dominate the total contribution from the Fourier series.

## 5.2 Additional Assumptions

### 5.2.1 Boundary Conditions

In order to model a lined duct we require two boundary conditions. These are located at the duct's centre-line and the duct wall.

At  $r = 0$ , the centre-line of the duct, we assume that both the pressure and it's derivative are some finite constant at  $r = 0$  as we vary  $\theta$ . In order to impose this boundary condition we need only that we can invert the Fourier series and Fourier transform. We therefore take the boundary condition at  $r = 0$  for equation (5.1) to be regularity. This is found as follows;

Considering  $m \neq 0$ , for small  $r$ , the Pridmore-Brown equation reduces to leading order,

$$\tilde{p}'' + \left(\frac{1}{r}\right)\tilde{p}' + \left(-\frac{m^2}{r^2}\right)\tilde{p} = 0, \quad (5.9)$$

which will have two solutions; a singular solution that behaves as  $O(r^{-|m|})$  and a regular solution behaving as  $O(r^{|m|})$ .

For  $m = 0$  we instead have,

$$\tilde{p}'' + \left(\frac{1}{r}\right)\tilde{p}' = 0 \quad (5.10)$$

Which can be solved to give  $\tilde{p}' = O(\frac{1}{r})$  or  $\tilde{p}' = 0$  that is, for  $m = 0$ , the singular solution behaves as  $O(\log r)$  while the regular solution behaves as  $O(1)$ . Since we are imposing regularity we choose to eliminate the singular solutions, which is possible taking the boundary conditions at  $r = 0$  to be;

$$\tilde{p}(0) = 0 \quad \text{for } m \neq 0 \quad (5.11a)$$

$$\tilde{p}'(0) = 0 \quad \text{for } m = 0. \quad (5.11b)$$

For our second boundary condition, since we wish to model sound within a straight cylindrical lined duct of some radius  $r = a$ , we take the other boundary condition to be the impedance boundary condition at  $r = a$ ,

$$\tilde{p}(a) = Z(\omega)\tilde{v}(a). \quad (5.12)$$

This can be rewritten using (5.6d) as

$$\tilde{p}'(a) = \frac{-i(\omega - U(a)k)\rho_0(a)}{Z(\omega)}\tilde{p}(a). \quad (5.13)$$

In each of these  $Z(\omega)$  is the impedance of the duct wall. With a hard wall corresponding to  $Z \rightarrow \infty$  and hence  $\tilde{v}(a) = 0$ .

### 5.2.2 Non-dimensionalisation and Simplifying Assumptions

In order to further simplify the Pridmore-Brown equation (5.1) we apply the additional assumption of constant density  $\rho_0(r)$ . This is a homentropic assumption and implies that  $c_0(r)$  is also constant. Physically this can be interpreted as constant temperature within the duct. In addition to this we can non-dimensionalise the problem. We choose to scale speeds by the sound speed  $c_0$ , densities by  $\rho_0$ , and distances by the duct radius  $a$ .

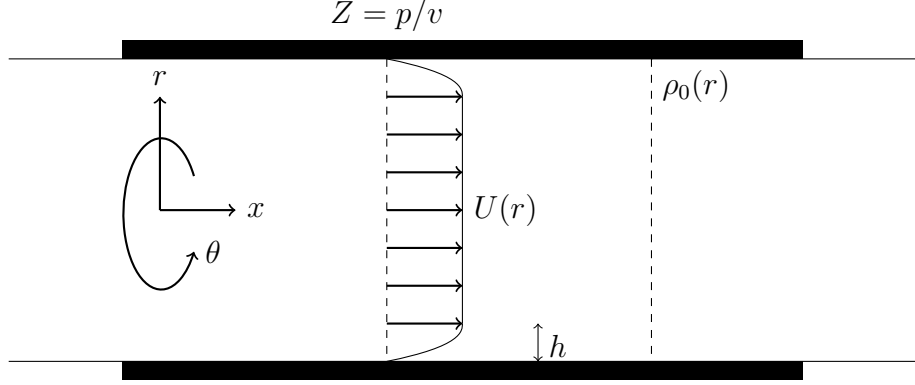


Figure 2: A cross sectional view of a cylindrical duct with lined walls containing sheared axial flow.  $\rho_0(r)$  is the mean flow density (here taken constant), and  $U(r)$  is the mean flow velocity, here taken to be uniform outside a boundary layer of width  $h$ .  $Z$  is the boundary impedance and defines the boundary condition at the wall of the duct.

It is important to note that this places the impedance boundary condition in non-dimensional terms at  $r = 1$ .

We will also assume a flow profile  $U(r)$  that is uniform, except within a boundary layer of thickness  $h$  where it varies quadratically:

$$U(r) = \begin{cases} M & 0 \leq r \leq 1 - h \\ M(1 - (1 - \frac{1-r}{h})^2) & 1 - h \leq r \leq 1 \end{cases}. \quad (5.14)$$

With the non-dimensionalisation of velocities by  $c_0$ ,  $M$  is the duct centreline Mach number. This situation is depicted schematically in figure 2. Applying the above assumptions and scalings to the Pridmore-Brown equation (5.1) we now seek to solve the inhomogeneous Pridmore-Brown equation (5.15) subjected to a harmonic point mass source.

$$\tilde{p}'' + \left( \frac{2kU'}{\omega - U(r)k} + \frac{1}{r} \right) \tilde{p}' + \left( (\omega - U(r)k)^2 - k^2 - \frac{m^2}{r^2} \right) \tilde{p} = \frac{(\omega - U(r_0)k)}{2i\pi r_0} \delta(r - r_0), \quad (5.15)$$

with boundary condition at the duct wall

$$\tilde{p}'(1) = \frac{-i\omega}{Z(\omega)} \tilde{p}(1). \quad (5.16)$$

To solve this we first consider solutions to the homogeneous form

$$\tilde{p}'' + \left( \frac{2kU'}{\omega - U(r)k} + \frac{1}{r} \right) \tilde{p}' + \left( (\omega - U(r)k)^2 - k^2 - \frac{m^2}{r^2} \right) \tilde{p} = 0, \quad (5.17)$$

With the intention of then constructing a Green's function solution to (5.15).

Equation (5.17) can be broken down into two further cases according to (5.14) depending on if we are within the uniform or sheared flow regions.

When  $r \in [0, 1 - h]$ , we are in the uniform flow region, investigated in section 6.2.1

$$\tilde{p}'' + \frac{1}{r}\tilde{p}' + \left( (\omega - Mk)^2 - k^2 - \frac{m^2}{r^2} \right) \tilde{p} = 0. \quad (5.18)$$

While in the sheared flow region, for  $r \in [1 - h, 1]$ , investigated in section 6.1

$$\tilde{p}'' + \left( \frac{1}{r} - \frac{2}{r - r_c^-} - \frac{2}{r - r_c^+} \right) \tilde{p}' + \left( \frac{M^2 k^2}{h^4} (r - r_c^+)^2 (r - r_c^-)^2 - k^2 - \frac{m^2}{r^2} \right) \tilde{p} = 0. \quad (5.19)$$

Where  $r_c^\pm$  are the solutions in  $r$  to  $\omega - U(r)k = 0$ .

$$r_c^\pm = 1 - h \pm Q \quad Q = h\sqrt{1 - \frac{\omega}{Mk}}. \quad (5.20)$$

In what follows we will take  $\text{Re}(Q) \geq 0$  such that  $\text{Re}(r_c^+) \geq 1 - h$ .

## 6 Solutions to the Pridmore-Brown Equation

The work contained within this section has been previously presented within [King et al., 2022, sections 2.2-2.5, Appendix A]. In the current work additional detail has been provided at each step.

### 6.1 Homogeneous Solutions Within the Region of Sheared Flow

In order to solve the homogeneous Pridmore-Brown equation (5.19), where  $U(r)$  varies following a quadratic polynomial, we propose Frobenius expansions about strategically chosen points in the complex  $r$  plane.

First, we observe that equation (5.19) has three regular singularities,  $r = 0$ , and  $r = r_c^\pm$ . Of these, only  $r_c^+$  may occur in  $(1 - h, 1)$ , which is the region where we require the solutions to be valid, since we took  $Q$  to have a positive real part. When  $r_c^+$  is either real or has a small imaginary part, numerical methods of approximating the solutions such as finite difference, would be inaccurate for  $r$  near  $r_c^+$ . Since we seek accuracy near  $r_c^+$ , we choose to propose our first Frobenius series solution about this point.

### 6.1.1 Frobenius Series Expansions about $r = r_c^+$

Following Brambley, Darau and Rienstra [2012a], we propose a Frobenius expansion [Teschl, 2012, Section 4.2] about the regular singularity  $r_c^+$ ,

$$\tilde{p}(r) = \sum_{n=0}^{\infty} a_n (r - r_c^+)^{n+\sigma} \quad \text{with} \quad a_0 \neq 0. \quad (6.1)$$

Where the  $a_n$  and  $\sigma$  are complex, constants, to be found.

We begin by expanding equation (5.19) as sums in  $(r - r_c^+)$ . In what follows, for compactness, we have denoted  $(r - r_c^+) = R$ ;

$$\frac{1}{r} = \sum_{j=0}^{\infty} (-1)^j \frac{R^j}{(r_c^+)^{j+1}}, \quad |R| < |r_c^+| \quad (6.2a)$$

$$\frac{1}{r - r_c^-} = \sum_{j=0}^{\infty} (-1)^j \frac{R^j}{(2Q)^{j+1}}, \quad |R| < 2|Q| \quad (6.2b)$$

$$\frac{1}{r^2} = \sum_{j=0}^{\infty} (-1)^j \frac{R^j (j+1)}{(r_c^+)^{j+2}}, \quad |R| < |r_c^+| \quad (6.2c)$$

$$\tilde{p}'' = \sum_{n=0}^{\infty} a_n (n + \sigma)(n + \sigma - 1) R^{n+\sigma-2}, \quad (6.2d)$$

$$\tilde{p}' = \sum_{n=0}^{\infty} a_n (n + \sigma) R^{n+\sigma-1}. \quad (6.2e)$$

These transform the Pridmore-Brown equation into a sum in  $a_n$

$$\begin{aligned} & \sum_{n=0}^{\infty} a_n \left[ R^{n+\sigma-2} (n + \sigma) ((n + \sigma - 1) - 2) \right. \\ & \quad + (n + \sigma) \sum_{j=0}^{\infty} (-1)^j R^{n+\sigma-1+j} \left( \frac{1}{(r_c^+)^{j+1}} - \frac{2}{(2Q)^{j+1}} \right) \\ & \quad + \frac{M^2 k^2}{h^4} (R^{n+\sigma+4} + 4QR^{n+\sigma+3} + 4Q^2 R^{n+\sigma+2}) - k^2 R^{n+\sigma} \\ & \quad \left. - m^2 \sum_{j=0}^{\infty} (-1)^j \frac{(j+1) R^{n+\sigma+j}}{(r_c^+)^{j+2}} \right] = 0, \quad (6.2f) \end{aligned}$$

or equivalently as a sum in powers of  $R$ ,

$$\begin{aligned} & \sum_{n=0}^{\infty} R^{n+\sigma-2} \left[ a_n (n + \sigma) (n + \sigma - 3) \right. \\ & \quad + \sum_{j=0}^{\infty} (-1)^j a_{n-1-j} (n - j - 1 + \sigma) \left( \frac{1}{(r_c^+)^{j+1}} - \frac{2}{(2Q)^{j+1}} \right) \\ & \quad \left. + \frac{M^2 k^2}{h^4} (a_{n-6} + 4Q a_{n-5} + 4Q^2 a_{n-4}) - k^2 a_{n-2} \right] \end{aligned}$$

$$-m^2 \sum_{j=0}^{\infty} (-1)^j a_{n-2-j} \frac{(j+1)}{(r_c^+)^{j+2}} \Big] = 0. \quad (6.2g)$$

Specifying that  $a_n = 0$  for  $n < 0$  and  $a_0 \neq 0$  results in a condition on  $\sigma$  by considering  $n = 0$ . That is,

$$a_0 \sigma (\sigma - 3) = 0 \quad (6.2h)$$

and we find that  $\sigma = 0, 3$ . By Fuchs' theorem [Teschl, 2012, Theorem 4.5], this gives a pair of linearly independent solutions of the form

$$\tilde{p}_{c1}(r) = \sum_{n=0}^{\infty} a_n (r - r_c^+)^{n+3}, \quad (6.3a)$$

$$\tilde{p}_{c2}(r) = A \tilde{p}_{c1}(r) \log(r - r_c^+) + \sum_{n=0}^{\infty} b_n (r - r_c^+)^n. \quad (6.3b)$$

The coefficients  $a_n$  are then found by setting  $\sigma = 3$  and each power of co-efficient of  $(r - r_c^+) = R$  to be 0.

$$a_0 = 1, \quad (6.4a)$$

$$\begin{aligned} a_n = \frac{1}{n(n+3)} \Big[ & k^2 a_{n-2} - \frac{k^2 M^2}{h^4} (a_{n-6} + 4Q a_{n-5} + 4Q^2 a_{n-4}) \\ & - \sum_{j=0}^{n-1} (-1)^j (n+2-j) a_{n-1-j} \left( \frac{1}{(r_c^+)^{j+1}} - \frac{2}{(2Q)^{j+1}} \right) \\ & + m^2 \sum_{j=0}^{n-2} \frac{(-1)^j}{(r_c^+)^{j+2}} (j+1) a_{n-2-j} \Big], \quad (6.4b) \end{aligned}$$

In order to find  $A$  and the  $b_n$  which correspond to  $\sigma = 0$  the same process is repeated with the form given in (6.3b) observing that any remaining log terms are cancelled by  $\tilde{p}_{c1}$  being a solution of (5.19). We once again assume that  $b_0 = 1$  and  $b_n = 0$  for  $n < 0$ . For  $n = 3$ , since any multiple of  $\tilde{p}_{c1}$  remains a solution, we are further required to set  $b_3$ . We choose this to be zero, and can further retrieve  $A$ .

It is found,

$$\begin{aligned} & \sum_{n=0}^{\infty} A a_n \left[ (2n+3) R^{n+1} + \sum_{j=0}^{\infty} (-1)^j R^{n+2+j} \left( \frac{1}{(r_c^+)^{j+1}} - \frac{2}{(2Q)^{j+1}} \right) \right] \\ & + b_n \left[ n(n-3) R^{n-2} + \sum_{j=0}^{\infty} (-1)^j n R^{n-1+j} \left( \frac{1}{(r_c^+)^{j+1}} - \frac{2}{(2Q)^{j+1}} \right) \right] \\ & + \frac{M^2 k^2}{h^4} (R^{n+4} + 4Q R^{n+3} + 4Q^2 R^{n+2}) - k^2 R^n \end{aligned}$$

$$- m^2 \sum_{j=0}^{\infty} (-1)^j R^{n+j} \frac{j+1}{(r_c^+)^{j+2}} \Big] = 0, \quad (6.4c)$$

which leads to

$$\begin{aligned} \sum_{n=0}^{\infty} R^{n-2} \Big[ & A \left( (2n-3)a_{n-3} + \sum_{j=0}^{\infty} (-1)^j a_{n-4-j} \left( \frac{1}{(r_c^+)^{j+1}} - \frac{2}{(2Q)^{j+1}} \right) \right) \\ & + \left( n(n-3)b_n - k^2 b_{n-2} + \frac{M^2 k^2}{h^4} (b_{n-6} + 4Qb_{n-5} + 4Q^2 b_{n-4}) \right. \\ & + \sum_{j=0}^{\infty} (-1)^j (n-1-j)b_{n-1-j} \left( \frac{1}{(r_c^+)^{j+1}} - \frac{2}{(2Q)^{j+1}} \right) \\ & \left. - m^2 \sum_{j=0}^{\infty} (-1)^j b_{n-2-j} \frac{j+1}{(r_c^+)^{j+2}} \right] = 0. \end{aligned} \quad (6.4d)$$

and so;

$$b_0 = 1, \quad b_1 = 0, \quad b_2 = -\frac{1}{2} \left( k^2 + \left( \frac{m}{r_c^+} \right)^2 \right), \quad b_3 = 0, \quad (6.4e)$$

$$\begin{aligned} b_n = -\frac{1}{n(n-3)} \Big[ & A \left( (2n-3)a_{n-3} + \sum_{j=0}^{n-4} a_{n-4-j} (-1)^j \left( \frac{1}{(r_c^+)^{j+1}} - \frac{2}{(2Q)^{j+1}} \right) \right) \\ & - k^2 b_{n-2} + \frac{k^2 M^2}{h^4} (b_{n-6} + 4Qb_{n-5} + 4Q^2 b_{n-4}) \\ & + \sum_{j=0}^{n-1} (-1)^j (n-1-j)b_{n-1-j} \left( \frac{1}{(r_c^+)^{j+1}} - \frac{2}{(2Q)^{j+1}} \right) \\ & \left. - m^2 \sum_{j=0}^{n-2} \frac{(-1)^j}{(r_c^+)^{j+2}} (j+1)b_{n-2-j} \right], \end{aligned} \quad (6.4f)$$

and

$$A = -\frac{1}{3} \left( \frac{1}{Q} - \frac{1}{r_c^+} \right) \left( k^2 + \left( \frac{m}{r_c^+} \right)^2 \right) - \frac{2m^2}{3r_c^{+3}}. \quad (6.5)$$

Where  $A$  comes from considering the  $n = 3$  case. Equations (6.3) and (6.5) are in agreement with equations (2.3)–(2.5) of Brambley, Darau and Rienstra [2012a] for a general sheared flow profile.

$$A = -\frac{1}{3} \left( \frac{\omega^2}{M^2} + \frac{m^2}{r_c^2} \right) \left( \frac{U''(r_c)}{U(r_c)} - \frac{1}{r_c} \right) - \frac{2m^2}{3r_c^3} \quad (6.6)$$

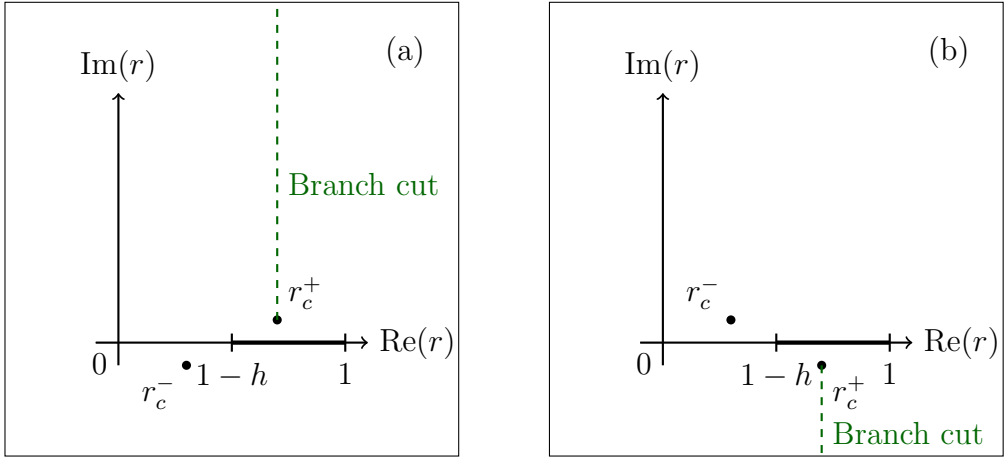


Figure 3: Schematic of possible locations of the  $r_c^+$  branch cut in the complex  $r$ -plane. (a) A possible choice of branch cut when  $\text{Im}(r_c^+) > 0$ . (b) The other choice of branch cut is needed when  $\text{Im}(r_c^+) < 0$ .

For any flow profile  $U(r)$ , expanded about the critical layer,  $\omega - U(r_c)k = 0$ .

Due to the log term in  $\tilde{p}_{c2}$  in (6.3), a branch cut is necessary in the complex  $r$  plane originating from the branch point  $r = r_c^+$ . This branch cut is taken such that the solutions remain continuous for the real values of  $r \in [1-h, 1]$ , and so the branch cut must avoid crossing the real  $r$  axis between  $1-h$  and  $1$ . In the following, we achieve this by choosing the branch cuts parallel to the imaginary axis and away from the real axis, as depicted in figure 3. However, when  $r_c^+$  is real and  $1-h < r_c^+ < 1$ , no suitable choice of branch cut exists, and as a result, any solution  $\tilde{p}(r)$  with  $\tilde{p}(r_c^+) \neq 0$  necessarily has a singular third derivative at  $r_c^+$ . Mapping the corresponding values of the axial wavenumber  $k$  for which this behaviour occurs it is found that this is exactly the half line  $[\frac{\omega}{M}, \infty)$ ; this range of excluded values of  $k$  we refer to as the critical layer branch cut.

As  $r_c^+$  becomes real, the value of  $\tilde{p}_{c2}(r_c^+)$  is different depending on whether we approach from positive or negative imaginary part. Thinking of  $r_c^+$  as a function of  $k$ , making use of (5.20), this corresponds to approaching the critical layer branch cut  $[\frac{\omega}{M}, \infty)$  in  $k$  from above or below respectively. This re-enforces the consideration of the critical layer appearing as a branch cut in the complex  $k$  plane, taken along the real line from  $k = \frac{\omega}{M}$ . The change in  $\tilde{p}_{c2}$  when crossing the critical layer branch cut from below to above is described as

$$\Delta\tilde{p}_{c2}(r) = \lim_{\text{Im}(k) \searrow 0^+} \tilde{p}_{c2}(r) - \lim_{\text{Im}(k) \nearrow 0^-} \tilde{p}_{c2}(r) = -2\pi i A \tilde{p}_{c1}(r) H(r_c^+ - r) \quad (6.7)$$

Where  $H(r)$  is the Heaviside function.

$$H(r) = \begin{cases} 0 & r < 0, \\ 1 & r > 0. \end{cases} \quad (6.8)$$

In order to retrieve this result we need only consider the  $\log(r - r_c^+)$  term of  $\tilde{p}_{c2}$ . Note that  $\partial r_c^+ / \partial k > 0$  for real  $k$  and real positive  $\omega$ . Hence, if  $k$  is nearly real and  $\text{Im}(k) > 0$ , then  $\text{Im}(r_c^+) > 0$ , and we must take the branch cut of  $\log(r - r_c^+)$  upwards towards  $+i\infty$ . Similarly, for  $\text{Im}(k) < 0$  then  $\text{Im}(r_c^+) < 0$ , and the branch cut for  $\log(r - r_c^+)$  must be taken downwards to  $-i\infty$ .

When  $r_c^+$  is located on the real line,  $(r - r_c^+)$  is negative for  $r < r_c^+$ . When we choose the branch cut into the upper half plane, this corresponds to an angle of  $-\pi$ . When we choose the branch cut into the lower half plane, this corresponds to an angle of  $\pi$ . This difference results in the jump of  $2\pi i$  given. If we instead consider  $r > r_c^+$ , the same argument is retrieved regardless of which direction we take the branch-cuts, and so no jump is observed. This is the reason for the presence of the Heaviside function.

In addition to the presence of the branch cut in the complex  $r$  plane the Frobenius series solutions (6.3) are limited by a radius of convergence, in that the series converge if  $|r - r_c^+| < \bar{R}$  for some radius of convergence  $\bar{R}$ . In this way  $\bar{R}$  is the distance between  $r_c^+$  and the next nearest singularity of the Pridmore-Brown equation, which is either at  $r = 0$  or at  $r = r_c^-$ , and hence

$$\bar{R} = \min \{|1 - h + Q|, 2|Q|\}. \quad (6.9)$$

This radius is additionally viewed as minimum radius of convergence corresponding to the expansions (6.2 *a - c*) in Fuchs' theorem. [Teschl, 2012]

The choice of  $r_c^+$  as the singularity to expand around means that this expansion maximizes the region of  $[1 - h, 1]$  contained within the radius of convergence while specifically maintaining convergence at the points  $r = 1 - h$  and near  $r = r_c^+$ , where these solutions are additionally highly accurate. This is shown schematically in figure 4. It can be observed that these solutions are not always valid for all of  $r \in [1 - h, 1]$ . In particular, in the case of  $k \rightarrow \frac{\omega}{M}$  we observe  $r_c^\pm \rightarrow (1 - h)$  and the radius of convergence  $\bar{R} \rightarrow 0$ . To this end we seek a second pair of solutions such that we may cover the remainder of the domain.

### 6.1.2 Expansion about $r = 1$

In order to cover the remainder of the domain  $[1 - h, 1]$ , we construct a second series solution about  $r = 1$ . We choose this point as it is the first value within  $[1 - h, 1]$

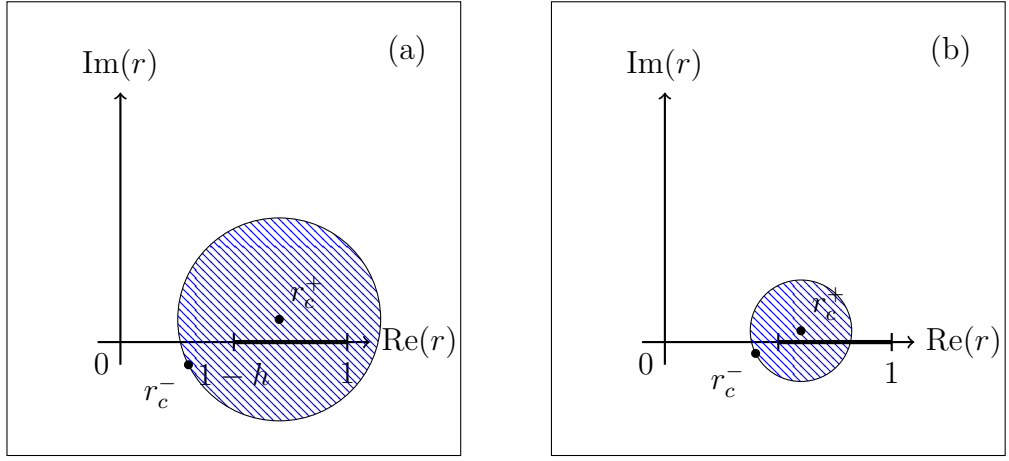


Figure 4: Schematic of possible locations of the  $r_c^\pm$  critical points in the complex  $r$ -plane. (a) The radius of convergence of the expansion about  $r_c^+$  covers the region of interest  $r \in [1 - h, 1]$ . (b) The radius of convergence about  $r_c^+$  is insufficient to cover  $r \in [1 - h, 1]$  (as  $k$  is too close to  $\frac{\omega}{M}$ ).

that is not contained within the radius of convergence of the  $\tilde{p}_c$  solutions as  $k \rightarrow \frac{\omega}{M}$ , which will be important later, but also results in solutions that are at their most accurate at the duct wall, allowing for accurate implementation of the boundary condition. The solutions are found in the same way as in section 6.1.1 and find that  $\sigma = 0, 1$  and;

$$\tilde{p}_{11}(r) = \sum_{n=0}^{\infty} \alpha_n (r-1)^{(n+1)}, \quad \tilde{p}_{12}(r) = \sum_{n=0}^{\infty} \beta_n (r-1)^n. \quad (6.10)$$

These values of  $\sigma$  would typically give a log term in  $\tilde{p}_{12}$  as we had before, however in this case we find that the coefficient is zero.

Specifying that  $\alpha_0 = \beta_0 = 1$ , and  $\beta_1 = 0$  results in the recurrence relations;

$$\begin{aligned} \alpha_n = -\frac{1}{n(n+1)} \left[ -k^2 \alpha_{n-2} + \frac{k^2 M^2}{h^4} \left( \alpha_{n-6} + 4h \alpha_{n-5} + 2(3h^2 - Q^2) \alpha_{n-4} \right. \right. \\ \left. \left. + 4h(h^2 - Q^2) \alpha_{n-3} + (h^2 - Q^2)^2 \alpha_{n-2} \right) \right. \\ \left. + \sum_{j=0}^{n-1} (-1)^j (n-j) \alpha_{n-j-1} \left( 1 - \frac{2}{(h+Q)^{j+1}} - \frac{2}{(h-Q)^{j+1}} \right) \right. \\ \left. - m^2 \sum_{j=0}^{n-2} (-1)^j (j+1) \alpha_{n-j-2} \right]. \quad (6.11a) \end{aligned}$$

$$\begin{aligned} \beta_n = -\frac{1}{n(n-1)} \left[ -k^2 \beta_{n-2} + \frac{k^2 M^2}{h^4} \left( \beta_{n-6} + 4h \beta_{n-5} + 2(3h^2 - Q^2) \beta_{n-4} \right. \right. \\ \left. \left. + 4h(h^2 - Q^2) \beta_{n-3} + (h^2 - Q^2)^2 \beta_{n-2} \right) \right. \end{aligned}$$

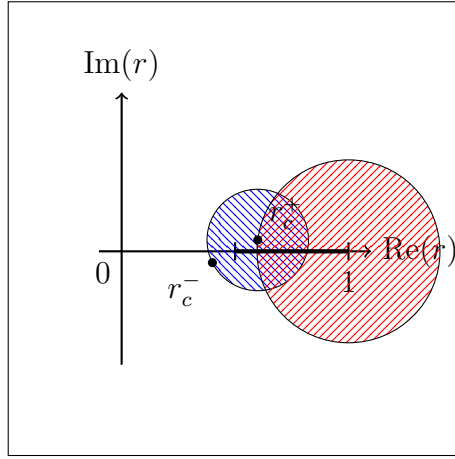


Figure 5: As for figure 4(b) with the radius of convergence for  $\tilde{p}_{11}$  and  $\tilde{p}_{12}$  added.

$$\begin{aligned}
& + \sum_{j=0}^{n-1} (-1)^j (n-j-1) \beta_{n-j-1} \left( 1 - \frac{2}{(h+Q)^{j+1}} - \frac{2}{(h-Q)^{j+1}} \right) \\
& - m^2 \sum_{j=0}^{n-2} (-1)^j (j+1) \beta_{n-j-2} \Big]. \tag{6.11b}
\end{aligned}$$

with  $\alpha_n = \beta_n = 0$  for  $n < 0$ . These solutions do not experience a branch cut but also have a radius of convergence also limited by the distance from  $r = 1$  to the next closest singularity, either  $r = r_c^+$  or  $r = 0$ . Although in either case there will always exist a region of overlap between the  $\tilde{p}_c$  and the  $\tilde{p}_1$  solutions as can be seen in figure 5.

### 6.1.3 A Homogeneous Solution Valid Across $[1-h, 1]$

Making use of the solutions derived in sections 6.1.1 and 6.1.2 we construct solutions to the homogeneous Pridmore-Brown equation  $\tilde{p}_1(r)$  and  $\tilde{p}_2(r)$  such that they are valid across the whole of  $[1-h, 1]$ , accounting for the radii of convergence of both sets of solutions. We set

$$\tilde{p}_1(r) = \begin{cases} \tilde{p}_{c1}(r) & |r - r_c^+| < \bar{R}, \\ A_1 \tilde{p}_{11}(r) + B_1 \tilde{p}_{12}(r) & \text{otherwise,} \end{cases} \tag{6.12a}$$

$$\tilde{p}_2(r) = \begin{cases} \tilde{p}_{c2}(r) & |r - r_c^+| < \bar{R}, \\ A_2 \tilde{p}_{11}(r) + B_2 \tilde{p}_{12}(r) & \text{otherwise.} \end{cases} \tag{6.12b}$$

With  $\bar{R}$  given in equation (6.9). First of all, we note from figure 5 that the regions of convergence of the  $\tilde{p}_c$  solutions and the  $\tilde{p}_1$  solutions almost always overlap. There are two exceptions, when  $k = 0$  and when  $k = \frac{\omega}{M}$ . At these values of  $k$ ,  $r_c^\pm(k)$  is ill-defined, and  $r_c^+ = r_c^- = 1 - h$  respectively. We exclude these cases here as it will turn out that neither is required for our final Fourier inverted solutions. For any

other values of  $k$ , we can always construct a uniformly valid solution using these expansions. For any real  $\bar{r} > \text{Re}(r_c^+)$  contained within both regions of convergence, we may find the coefficients  $A_1$ ,  $A_2$ ,  $B_1$  and  $B_2$  by requiring continuity and continuous derivatives at  $r = \bar{r}$ :

$$\begin{bmatrix} A_1 & A_2 \\ B_1 & B_2 \end{bmatrix} = \begin{bmatrix} \tilde{p}_{11}(\bar{r}) & \tilde{p}_{12}(\bar{r}) \\ \tilde{p}'_{11}(\bar{r}) & \tilde{p}'_{12}(\bar{r}) \end{bmatrix}^{-1} \begin{bmatrix} \tilde{p}_{c1}(\bar{r}) & \tilde{p}_{c2}(\bar{r}) \\ \tilde{p}'_{c1}(\bar{r}) & \tilde{p}'_{c2}(\bar{r}) \end{bmatrix} \quad (6.13)$$

These coefficients are independent of the specific choice of  $\bar{r}$ , and the resulting solutions  $\tilde{p}_1$  and  $\tilde{p}_2$  have not only  $C^1$  continuity but  $C^\infty$ , since both are solutions to the Pridmore-Brown equation. In effect,  $\tilde{p}_1$  analytically continues  $\tilde{p}_{c1}$  beyond its radius of convergence, and similarly  $\tilde{p}_2$  analytically continues  $\tilde{p}_{c2}$ .

As described in section 6.1.1, there is a jump in  $\tilde{p}_{c2}$  across the critical layer branch cut due to the log term in (6.3). If the radius of convergence  $\bar{R}$  is sufficiently large that  $r = 1$  is within the radius of convergence, then no matching coefficients are needed, and this jump in  $\tilde{p}_{c2}$  obviously carries through to  $\tilde{p}_2$ . In the other case, that  $\bar{R}$  is sufficiently small that matching is needed, it follows that  $\bar{r} < 1$ . In addition to this, for  $\bar{R}$  sufficiently small, we also have that the radius of convergence for  $\tilde{p}_{11}$  and  $\tilde{p}_{12}$  will be limited by  $r = r_{c^+}$ , resulting in values of  $\bar{r} > \text{Re}(r_c^+)$ . Thus,  $\Delta\tilde{p}_2(\bar{r}) = 0$  and there is no jump in the matching coefficients  $A_1$ ,  $A_2$ ,  $B_1$  and  $B_2$  as  $\bar{r} > \text{Re}(r_c^+)$ , and hence

$$\Delta\tilde{p}_2(r) = -2i\pi A\tilde{p}_1(r)H(r_c^+ - r). \quad (6.14)$$

This is analogous to the jump in  $\tilde{p}_{c2}$  given in (6.7), and shows that the jump in  $\tilde{p}_2$  carries through the analytic continuation, as might have been expected a priori.

When evaluating these solutions numerically, as has been done for the production of the figures in section 11, in order to reduce the computational cost and error in summing many terms within each of the Frobenius series solutions, we deliberately prevent the evaluation of the  $\tilde{p}_c$  and  $\tilde{p}_1$  solutions near their radii of convergence. Instead we choose which expansions to use based on which are, as a proportion of the whole radius, greatest within the radius of convergence. Matching is performed at the mid-point between the two edges of radii of convergence on the real line following exactly as in equation (6.13).

## 6.2 Solutions to the Pridmore-Brown Equation Over $[0, 1]$

In order to construct a solution across the whole duct,  $[0, 1]$  we are first required to solve the Pridmore-Brown equation within the region of uniform flow (5.18). We will then continue these solutions into the sheared flow region, making use of both  $\tilde{p}_1(1 - h)$  and  $\tilde{p}_2(1 - h)$ .

### 6.2.1 Homogeneous Solutions Within the Region of Uniform Flow

Within the uniform flow region we are required to solve

$$\tilde{p}'' + \frac{1}{r}\tilde{p}' + \left( (\omega - Mk)^2 - k^2 - \frac{m^2}{r^2} \right) \tilde{p} = 0. \quad (5.18)$$

This is Bessel's equations of order  $m$  rescaled by  $\alpha$ , where

$$\alpha^2 = (\omega - Mk)^2 - k^2; \quad (6.15)$$

With  $\alpha$  defined by its square it is important to note that a square root branch cut is required. It will turn out later that the branch chosen for  $\alpha$  does not matter as discussed below. For definiteness we choose  $\text{Im}(\alpha) \geq 0$ .

Bessel's equation has two pairs of linearly independent solutions that we shall make use of: the Bessel functions of the first and second kind,  $J_m(\alpha r)$  and  $Y_m(\alpha r)$ ; and the Hankel functions of the first and second kind;  $H_m^{(1)}(\alpha r)$  and  $H_m^{(2)}(\alpha r)$ . More information regarding these can be found in [Abramowitz and Stegun, 1964, chapter 9]. It is worth noting that only  $J_m(\alpha r)$  is regular at  $r = 0$ , with the other solutions all requiring a branch cut along  $\alpha r < 0$  with a singularity at  $\alpha r = 0$ . Fortunately, due to  $\alpha$  requiring a square root branch cut we have been able to remove this branch from our solutions. Instead we are required to consider the square root branch cuts along  $\alpha^2 \in \mathbb{R}^-$ . It additionally turns out that in our case these branch cuts are removable, with more information on this given in section 7.2.

### 6.2.2 Homogeneous Solutions Across the Full Domain

In order to construct a full solution in  $r \in [0, 1]$ , we now construct two solutions  $\tilde{\psi}_1(r)$  and  $\tilde{\psi}_2(r)$  that solve (5.1) across  $r \in [0, 1]$ . By matching the solutions derived above in sections 6.2.1 and 6.1, we construct  $\tilde{\psi}_1(r)$  to satisfy the boundary condition at  $r = 0$  (5.11), therefore, we take

$$\tilde{\psi}_1(r) = \begin{cases} J_m(\alpha r) & 0 \leq r \leq 1 - h \\ C_1 \tilde{p}_1(r) + D_1 \tilde{p}_2(r) & 1 - h \leq r \leq 1, \end{cases} \quad (6.16)$$

where the matching coefficients  $C_1$  and  $D_1$  ensure  $C^1$  continuity, and are given by

$$C_1 = \frac{J_m(\alpha(1-h))\tilde{p}_2'(1-h) - \alpha J_m'(\alpha(1-h))\tilde{p}_2(1-h)}{W(1-h)}, \quad (6.17a)$$

$$D_1 = -\frac{J_m(\alpha(1-h))\tilde{p}_1'(1-h) - \alpha J_m'(\alpha(1-h))\tilde{p}_1(1-h)}{W(1-h)}, \quad (6.17b)$$

and  $W(r) = \mathcal{W}(\tilde{p}_1, \tilde{p}_2; r)$  is the Wronskian of  $\tilde{p}_1$  and  $\tilde{p}_2$

$$W(r) = \mathcal{W}(\tilde{p}_1, \tilde{p}_2; r) = \tilde{p}_1(r)\tilde{p}_2'(r) - \tilde{p}_2(r)\tilde{p}_1'(r) = -\frac{3r_c^+(r-r_c^+)^2(r-r_c^-)^2}{4rQ^2}. \quad (6.18)$$

More details on the Wronskian and its derivation are given in section 6.3.

In order to satisfy the boundary condition at  $r = 0$  (5.11), we have chosen  $J_m$  and  $Y_m$  as our independent solutions to the Pridmore-Brown equation within uniform flow (5.18) to construct  $\tilde{\psi}_1(r)$ . It can be noted that  $J_m$  satisfies the boundary condition (5.11) exactly, while  $Y_m$  would grow unbounded as  $r \rightarrow 0$  and so only the Bessel function the first kind is present within our final solution.

We now proceed to construct  $\tilde{\psi}_2$  which satisfies the boundary condition (5.16) at  $r = 1$ . Writing  $\tilde{\psi}_2$  in terms of the homogeneous solutions,

$$\tilde{\psi}_2(r) = \begin{cases} \check{C}_2 H_m^{(1)}(\alpha r) + \check{D}_2 H_m^{(2)}(\alpha r) & 0 \leq r \leq 1-h \\ \hat{C}_2 \tilde{p}_1(r) + \hat{D}_2 \tilde{p}_2(r) & 1-h \leq r \leq 1, \end{cases} \quad (6.19)$$

we choose  $\hat{C}_2$  and  $\hat{D}_2$  to satisfy  $\tilde{\psi}_2(1) = 1$  and  $\tilde{\psi}_2'(1) = -\frac{i\omega}{Z}$ .

This forces a non-zero normalized solution to  $\tilde{\psi}_2$ , and satisfies the boundary condition (5.16) at  $r = 1$ . This leads to

$$\hat{C}_2 = \frac{\tilde{p}_2'(1) + \frac{i\omega}{Z}\tilde{p}_2(1)}{W(1)}, \quad \hat{D}_2 = -\frac{\tilde{p}_1'(1) + \frac{i\omega}{Z}\tilde{p}_1(1)}{W(1)}. \quad (6.20)$$

The coefficients  $\check{C}_2$  and  $\check{D}_2$  are chosen such that our solution is  $C^1$  continuous at  $r = 1-h$ , giving

$$\begin{pmatrix} \check{C}_2 \\ \check{D}_2 \end{pmatrix} = \frac{i\pi(1-h)}{4} \begin{pmatrix} \alpha H_m^{(2)'}(\alpha(1-h)) & -H_m^{(2)}(\alpha(1-h)) \\ -\alpha H_m^{(1)'}(\alpha(1-h)) & H_m^{(1)}(\alpha(1-h)) \end{pmatrix} \begin{pmatrix} \tilde{p}_1(1-h) & \tilde{p}_2(1-h) \\ \tilde{p}_1'(1-h) & \tilde{p}_2'(1-h) \end{pmatrix} \begin{pmatrix} \hat{C}_2 \\ \hat{D}_2 \end{pmatrix} \quad (6.21)$$

where the factor at the beginning comes from the Wronskian of  $H_m^{(1)}$  and  $H_m^{(2)}$  as given in [Abramowitz and Stegun, 1964, formula 9.1.17].

We will also require later the jump in behaviour of  $\tilde{\psi}_1$  and  $\tilde{\psi}_2$  as  $k$  crosses the critical layer branch cut from below to above. Since any jump comes from the log term in

$\tilde{p}_2(r)$  when  $r < r_c^+$ , we have,

$$\Delta C_1 = 2i\pi AD_1, \quad \Delta \widehat{C}_2 = \Delta D_1 = \Delta \widehat{D}_2 = 0, \quad (6.22a)$$

$$\begin{pmatrix} \Delta \check{C}_2 \\ \Delta \check{D}_2 \end{pmatrix} = \frac{\pi^2(1-h)A\widehat{D}_2}{2} \begin{pmatrix} \alpha H_m^{(2)'}(\alpha(1-h)) & -H_m^{(2)}(\alpha(1-h)) \\ -\alpha H_m^{(1)'}(\alpha(1-h)) & H_m^{(1)}(\alpha(1-h)) \end{pmatrix} \begin{pmatrix} \tilde{p}_1(1-h) \\ \tilde{p}_1'(1-h) \end{pmatrix}, \quad (6.22b)$$

resulting in

$$\Delta \tilde{\psi}_1(r) = 2i\pi AD_1 \tilde{p}_1 H(r - r_c^+), \quad (6.23a)$$

$$\Delta \tilde{\psi}_2(r) = \begin{cases} \Delta \check{C}_2 H_m^{(1)}(\alpha r) + \Delta \check{D}_2 H_m^{(2)}(\alpha r) & 0 \leq r \leq 1-h \\ -2i\pi A \tilde{p}_1(r) \widehat{D}_2 H(r_c^+ - r) & 1-h \leq r \leq 1. \end{cases} \quad (6.23b)$$

Note that, if  $r_c^+ > 1$ , then  $\Delta \tilde{\psi}_1 = \Delta \tilde{\psi}_2 = 0$ , since the  $\tilde{\psi}_1$  and  $\tilde{\psi}_2$  solutions are uniquely defined by their boundary conditions and no branch point occurs on the interval  $r \in [1-h, 1]$  to cause a jump.

### 6.3 The Wronskian $\mathcal{W}(r)$

Consider a second order ODE, with two linearly independent solutions,  $\tilde{p}_1$  and  $\tilde{p}_2$

$$\tilde{p}''(r) + f(r)\tilde{p}'(r) + g(r)\tilde{p}(r) = 0. \quad (6.24a)$$

Defining the Wronskian of the two solutions to be

$$\mathcal{W}(\tilde{p}_1, \tilde{p}_2; r) = \tilde{p}_1(r)\tilde{p}_2'(r) - \tilde{p}_1'(r)\tilde{p}_2(r), \quad (6.24b)$$

then it can be shown that the Wronskian satisfies the first order ODE

$$\mathcal{W}'(r) = f(r)\mathcal{W}(r). \quad (6.24c)$$

That is,

$$\mathcal{W}(r) = e^{\int_{s_0}^r f(s)ds}, \quad (6.24d)$$

For some  $s_0$ . In our case we find that

$$f(r) = \frac{1}{r} - \frac{2}{r - r_c^+} - \frac{2}{r - r_c^-}, \quad (6.25a)$$

$$W(r) = \mathcal{W}(\tilde{p}_1, \tilde{p}_2; r) = C \frac{(r - r_c^+)^2 (r - r_c^-)^2}{r} \quad (6.25b)$$

for some  $C$ . Considering  $r = r_c^+ + \epsilon$  it can be found that, to leading order, noting that in any case we can make use of the  $\tilde{p}_c$  expansions

$$\tilde{p}_1(r) = \epsilon^3 + O(\epsilon^4), \quad (6.25c)$$

$$\tilde{p}_2(r) = 1 + O(\epsilon^2), \quad (6.25d)$$

$$\tilde{p}'_1(r) = 3\epsilon^2 + O(\epsilon^3), \quad (6.25e)$$

$$\tilde{p}'_2(r) = 2b_2\epsilon + O(\epsilon^2), \quad (6.25f)$$

$$W(r) = -3\epsilon^2 + O(\epsilon^3), \quad (6.25g)$$

$$= C \left( \frac{4Q^2\epsilon^2}{r_c^+} + O(\epsilon^3) \right). \quad (6.25h)$$

Taking  $\epsilon \rightarrow 0$  then gives

$$C = -\frac{3r_c^+}{4Q^2} \quad W(r) = -\frac{3r_c^+(r - r_c^+)^2(r - r_c^-)^2}{4rQ^2}. \quad (6.25i)$$

It is worth noting that any  $r$  dependence in the Wronskian is defined not by the solutions being considered but rather the ODE being solved, that is, if two other linearly independent solutions to the same problem were considered, for example  $\tilde{p}_{11}$  and  $\tilde{p}_{12}$ , then their Wronskian will only differ by the constant  $C$ . We will later make use of the fact that

$$\mathcal{W}(\tilde{p}_{11}, \tilde{p}_{12}; r) = -\frac{(r - r_c^+)^2(r - r_c^-)^2}{r(1 - r_c^+)^2(1 - r_c^-)^2}. \quad (6.25j)$$

Which comes from the knowledge  $\tilde{p}_{11}(1) = 0$ ,  $\tilde{p}_{12}(1) = 1$ ,  $\tilde{p}'_{11}(1) = 1$  and  $\tilde{p}'_{12}(1) = 0$  and considering the Wronskian at  $r = 1$ . We will later require,  $\mathcal{W}(\tilde{\psi}_1, \tilde{\psi}_2; r)$ . Making use of the form given in equation (6.24b), considering  $r < 1 - h$ , and  $r > 1 - h$  it can be found that,

$$\mathcal{W}(\tilde{\psi}_1, \tilde{\psi}_2; r) = \alpha\check{C}_2\mathcal{W}(J_m, H_m^{(1)}; r) + \alpha\check{D}_2\mathcal{W}(J_m, H_m^{(2)}; r) \quad (6.26a)$$

$$= \alpha(\check{C}_2 - \check{D}_2)\frac{2i}{\pi r}, \quad r < 1 - h, \quad (6.26b)$$

$$\mathcal{W}(\tilde{\psi}_1, \tilde{\psi}_2; r) = (C_1\hat{D}_2 - \hat{C}_2D_1)W(r) \quad r > 1 - h. \quad (6.26c)$$

where we have made use of the Bessel function identities (9.1.3), (9.1.4) and (9.1.16) from Abramowitz and Stegun [1964]. Note in particular that  $r\mathcal{W}(\tilde{\psi}_1, \tilde{\psi}_2; r)$  is a constant independent of  $r$  for  $0 \leq r \leq 1 - h$ . Since  $\mathcal{W}(\tilde{\psi}_1, \tilde{\psi}_2; r)$  is continuous in  $r$  across  $r = 1 - h$ , since  $\tilde{\psi}_1$  and  $\tilde{\psi}_2$  are both  $C^1$  continuous, it follows that for  $0 \leq r \leq 1 - h$  we can set  $r\mathcal{W}(\tilde{\psi}_1, \tilde{\psi}_2; r) = (1 - h)\mathcal{W}(\tilde{\psi}_1, \tilde{\psi}_2; 1 - h)$ . We therefore

arrive at the conclusion that

$$\mathcal{W}(\tilde{\psi}_1, \tilde{\psi}_2; r) = (C_1 \widehat{D}_2 - \widehat{C}_2 D_1) \begin{cases} W(r) & 1-h \leq r \leq 1 \\ \frac{1-h}{r} W(1-h) & 0 \leq r \leq 1-h, \end{cases} \quad (6.27)$$

In addition to solving a first order ODE (6.24c), the Wronskian, having been constructed from linearly independent solutions, is additionally able to be used to identify when this independence between the solutions is lost. This occurs exactly when  $\mathcal{W}(\tilde{p}_1, \tilde{p}_2; r) = 0$ , and in our work leads to modal solutions as discussed below.

### 6.3.1 Modal Solutions

Modal solutions of the homogeneous Pridmore-Brown equation (5.17) are nonzero solutions  $\tilde{p}(r)$  that satisfy both the boundary conditions at  $r = 0$  and at  $r = 1$  (5.11, 5.16).

In general, satisfying both boundary conditions would force the solution  $\tilde{p}(r) \equiv 0$ , so non-zero solutions exist only for particular modal eigenvalues  $k$  (assuming  $\omega$  is given and fixed). In contrast, the solution  $\tilde{\psi}_1(r)$  is never identically zero and always satisfies the homogeneous Pridmore-Brown equation and the boundary condition at  $r = 0$ ; indeed, any solution satisfying the boundary condition at  $r = 0$  is necessarily a multiple of  $\tilde{\psi}_1(r)$ . Likewise, the solution  $\tilde{\psi}_2(r)$  is never identically zero and always satisfies the homogeneous Pridmore-Brown equation and the boundary condition at  $r = 1$ , and any solution satisfying the boundary condition at  $r = 1$  is necessarily a multiple of  $\tilde{\psi}_2(r)$ .

In general,  $\tilde{\psi}_1$  and  $\tilde{\psi}_2$  are linearly independent, and so their Wronskian  $\mathcal{W}(\tilde{\psi}_1, \tilde{\psi}_2; r)$  is not identically zero. However, if  $\tilde{p}(r)$  is nonzero and satisfies both boundary conditions at  $r = 0$  and  $r = 1$ , then  $\tilde{p}(r) = a\tilde{\psi}_1(r) = b\tilde{\psi}_2(r)$  for some nonzero coefficients  $a, b$ . In other words, a modal solution is one where  $\tilde{\psi}_1$  and  $\tilde{\psi}_2$  are linearly dependent, and so  $\mathcal{W}(\tilde{\psi}_1, \tilde{\psi}_2; r) \equiv 0$ .

Considering the Wronskian between  $\tilde{\psi}_1$  and  $\tilde{\psi}_2$  (6.24b), if  $\mathcal{W}(\tilde{\psi}_1, \tilde{\psi}_2; r) = 0$  then it must be that either  $W(r) = 0$  (6.18), or,  $C_1 \widehat{D}_2 - \widehat{C}_2 D_1 = 0$ . Since  $\tilde{p}_1$  and  $\tilde{p}_2$  were constructed to be linearly independent, we expect  $W(r)$  not to be identically zero, and indeed (6.18) shows that  $W(r) \neq 0$  except at the critical layer  $r = r_c^+$ . Since this varies as  $r$  varies this is not considered a modal solution, thus, any modal solutions are given by the condition that  $C_1 \widehat{D}_2 - \widehat{C}_2 D_1 = 0$ . We refer to this as the dispersion relation. It can not only be observed that this is independent of  $r$  but also implies that  $C_1/D_1 = \widehat{C}_2/\widehat{D}_2$  and so that  $\tilde{\psi}_1$  and  $\tilde{\psi}_2$  are indeed multiples of one another.

In the next section, we see how these modal solutions occur naturally as poles in the solution of the non-homogeneous Pridmore-Brown equation.

## 7 The Green's Function for the Pridmore-Brown Equation

The work contained within this section has been previously presented within [King et al., 2022, sections 3.1-3.2, Appendix B]. In the current work additional detail has been provided at each step.

### 7.1 Inhomogeneous Solution to the Pridmore-Brown Equation

While previously we have only been solving the homogeneous form (5.17), our original problem was to solve the inhomogeneous Pridmore-Brown equation (5.15) subjected to a harmonic point mass source.

$$\tilde{p}'' + \left( \frac{2kU'}{\omega - U(r)k} + \frac{1}{r} \right) \tilde{p}' + \left( (\omega - U(r)k)^2 - k^2 - \frac{m^2}{r^2} \right) \tilde{p} = \frac{\omega - U(r_0)k}{2i\pi r_0} \delta(r - r_0), \quad (5.15)$$

Due to the right hand side of equation (5.15) being a scalar multiple of a delta function, located at  $r = r_0$ , we seek the Green's function of equation (5.15) multiplied by the same constant. This solution will be denoted  $\tilde{G}$ .

We require  $\tilde{G}$  to satisfy the boundary condition at  $r = 0$  and  $r = 1$ , and solve the homogeneous Pridmore-Brown equation for  $r < r_0$  and  $r > r_0$ ; hence,  $\tilde{G}$  may be written as a multiple of the homogeneous solution  $\tilde{\psi}_1$  for  $r < r_0$  and as a multiple of the homogeneous solution  $\tilde{\psi}_2$  for  $r > r_0$  and all that is required is to join the two solutions at  $r = r_0$  such that they are continuous, and their derivative is discontinuous with a jump exactly matching the amplitude of the delta function. To this end,  $\tilde{G}$  is given by;

$$\tilde{G} = \frac{\omega - U(r_0)k}{2\pi i r_0} \frac{\tilde{\psi}_1(\tilde{r})\tilde{\psi}_2(\hat{r})}{\mathcal{W}(\tilde{\psi}_1, \tilde{\psi}_2; r_0)}, \quad (7.1a)$$

where

$$\hat{r} = \max(r, r_0), \quad \tilde{r} = \min(r, r_0), \quad (7.1b)$$

and we have once again used  $\mathcal{W}(\tilde{\psi}_1, \tilde{\psi}_2; r)$  as the Wronskian of  $\tilde{\psi}_1$  and  $\tilde{\psi}_2$ . Using (6.27), this may be rewritten as

$$\tilde{G} = \frac{\omega - U(r^*)k}{2\pi i r^* W(r^*)} \frac{\tilde{\psi}_1(\tilde{r})\tilde{\psi}_2(\hat{r})}{C_1 \hat{D}_2 - \hat{C}_2 D_1} \quad \text{where } r^* = \max(1 - h, r_0), \quad (7.2)$$

as described in section 6.3.1 it can be observed any modal solution, solving  $C_1 \widehat{D}_2 - \widehat{C}_2 D_1 = 0$ , will be poles of our Green's function.

It is important to note that, in addition to the modal poles, there are poles of  $\widetilde{G}$  when  $W(r^*) = 0$ . Recalling

$$W(r) = -\frac{3 r_c^+ (r - r_c^+)^2 (r - r_c^-)^2}{4 r Q^2}. \quad (6.18)$$

$W(r^*) = 0$  only when  $r^* = r_c^+$ . When  $r_0 \leq 1 - h$  this could only occur at  $k = \frac{\omega}{M}$ , which we will see later in section 9.1.3 does not lead to a pole. However, we do observe a pole when  $r_0 > 1 - h$ , section 9.2.3, and it lies on the critical layer branch cut. We will refer to this pole as the  $k_0$  non-modal pole as its location depends on the location of the source.

$$k_0 = \frac{\omega}{U(r_0)} \quad r_0 > 1 - h \quad (7.3)$$

When considering  $k$  near  $k_0$  in  $\widetilde{G}$ , because we are evaluating  $\widetilde{\psi}_1$  or  $\widetilde{\psi}_2$  at  $r_0$  which are linear combinations of  $\widetilde{p}_1$  and  $\widetilde{p}_2$ , at  $k = k_0$

$$\widetilde{p}_1(r_0, k_0) = 0 \quad \widetilde{p}_1'(r_0, k_0) = 0 \quad (7.4)$$

and due to the  $\log(r_0 - r_c^+)$  term in  $\widetilde{p}_2(r_0)$  our Green's function is undefined.

In similar ways, upon close inspection of  $\widetilde{G}$ , through  $\widetilde{\psi}_1$  and  $\widetilde{\psi}_2$  one will find that we are also required to evaluate  $\widetilde{p}_1$  and  $\widetilde{p}_2$  at  $r > 1 - h$ ,  $1 - h$  and  $1$ . If at any of these locations we lost independence between  $\widetilde{p}_1$  and  $\widetilde{p}_2$ , i.e.  $W(r) = 0$ , then we would be unable to construct  $\widetilde{\psi}_1$  and  $\widetilde{\psi}_2$ . Hence,  $\widetilde{G}$  can not be evaluated at these points. Fortunately we are not required to consider  $r = 1$ , where  $|k| = \infty$ . However, for  $r_c^+ = 1 - h$ ,  $k = \frac{\omega}{M}$ , and

$$r_c^+ = r > 1 - h, \quad k_r = \frac{\omega}{U(r)}, \quad (7.5)$$

we must take greater care. Since both of these occur on the critical layer branch cut they act as branch points, however unlike like  $k_0$  they do not act as non-modal poles.

In addition to the critical layer branch cut we additionally have two branch cuts from  $\alpha$ , within both  $\widetilde{\psi}_1$ ,  $\widetilde{\psi}_2$  and the dispersion relation.

## 7.2 The $\alpha$ Square Root Branch Cut

Recall

$$\alpha = \sqrt{(\omega - Mk)^2 - k^2}. \quad (7.6)$$

With  $\text{Im}(\alpha) \geq 0$ . This leads to two branch cuts in the complex  $k$  along the lines  $(\omega - Mk)^2 - k^2 \in \mathbb{R}^+$ , which locates the branches on  $[-\frac{\omega}{1-M}, \frac{\omega}{1+M}]$  for real  $\omega$ . It will turn out that the Green's function does not see a jump for crossing this branch cut which corresponds to a change in evaluation of  $\alpha = ze^{i\pi}$  to  $\alpha = z$  for real positive  $z$ . Since the Green's function does not see a jump across the branch cut, when we close the contour in the upper and lower half planes, where we would typically have to deform the contour around the alpha branch cuts, the contribution of going around these branch cuts is exactly zero. This is shown in the following way;

Within  $\tilde{G}$ ,  $\alpha$  is evaluated within the terms

$$\frac{\psi_1(r_<) \psi_2(r_>)}{C_1 D_2 - C_2 D_1} \quad (7.7)$$

with the denominator displaying  $\alpha$  dependence within  $C_1$  and  $D_1$  only, and within  $\psi_2(r_>)$  if  $r_> < 1-h$ . Since the  $\alpha$  dependence is always present in both  $\psi_1(r_<)$  and the denominator, we consider the jumps in  $\psi_2(r)$  separately to the rest of the expression.

Let us first assume that  $r_< < 1-h$ ,

$$\frac{\psi_1(r_<)}{C_1 D_2 - C_2 D_1} = \frac{J_m(\alpha r_<) W(1-h)}{J_m(\alpha(1-h)) \psi_2'(1-h) - \alpha J_m'(\alpha(1-h)) \psi_2(1-h)}. \quad (7.8)$$

In Abramowitz and Stegun [1964] it is given that

$$J_m(ze^{i\pi}) = (-1)^m J_m(z) \quad J_m'(ze^{i\pi}) = (-1)^{m-1} J_m'(z). \quad (7.9a)$$

Taking  $\alpha = ze^{i\pi}$ , it follows that each term will contribute exactly a factor  $(-1)^m$  as we rewrite the problem in terms of  $\alpha = z$ . And so,

$$\begin{aligned} & \frac{J_m(ze^{i\pi} r_<) W(1-h)}{J_m(ze^{i\pi}(1-h)) \psi_2'(1-h) + ze^{i\pi} J_m'(ze^{i\pi}(1-h)) \psi_2(1-h)} \\ &= \frac{J_m(z r_<) W(1-h)}{J_m(z(1-h)) \psi_2'(1-h) - z J_m'(z(1-h)) \psi_2(1-h)}. \end{aligned} \quad (7.9b)$$

Thus, no jump is seen in these terms for crossing the branch cut.

For the case  $r_< > 1-h$ , expanding the  $C_1$  and  $D_1$  found in  $\psi_1(r_<)$  in terms of the

Bessel functions gives;

$$\frac{\psi_1(r_<)}{C_1 D_2 - C_2 D_1} = \frac{J_m(\alpha r_<) (\tilde{p}'_2(1-h)\tilde{p}_1(r_<) - \tilde{p}'_1(1-h)\tilde{p}_2(r_<))}{J_m(\alpha(1-h)\psi'_2(1-h) - \alpha J'_m(\alpha(1-h)\psi_2(1-h))} - \frac{\alpha J'_m(\alpha r_<) (\tilde{p}_2(1-h)\tilde{p}_1(r_<) - \tilde{p}_1(1-h)\tilde{p}_2(r_<))}{J_m(\alpha(1-h)\psi'_2(1-h) - \alpha J'_m(\alpha(1-h)\psi_2(1-h))}, \quad (7.10)$$

and it follows identically that we do not see a jump across the  $\alpha$  branch cuts as in (7.9b).

Considering instead,  $\psi_2(r_>)$  for  $r_> < 1-h$ .

$$\begin{aligned} \psi_2(r_>) = & - \frac{(H_m^{(2)}(\alpha(1-h))\psi'_2(1-h) - \alpha H_m^{(2)'}(\alpha(1-h))\psi_2(1-h))H_m^{(1)}(r_>)}{\frac{4}{i\pi(1-h)}} \\ & + \frac{(H_m^{(1)}(\alpha(1-h))\psi'_2(1-h) - \alpha H_m^{(1)'}(\alpha(1-h))\psi_2(1-h))H_m^{(2)}(r_>)}{\frac{4}{i\pi(1-h)}}, \end{aligned} \quad (7.11)$$

We have the analytic continuations

$$H_m^{(1)}(ze^{i\pi}) = (-1)^{m-1} H_m^{(2)}(z) \quad (7.12a)$$

$$H_m^{(1)'}(ze^{i\pi}) = (-1)^m H_m^{(2)'}(z) \quad (7.12b)$$

$$H_m^{(2)}(ze^{i\pi}) = (-1)^m (H_m^{(1)}(z) + 2H_m^{(2)}(z)) \quad (7.12c)$$

$$H_m^{(2)'}(ze^{i\pi}) = (-1)^{m-1} (H_m^{(1)'}(z) + 2H_m^{(2)'}(z)) \quad (7.12d)$$

we can then expand equation (7.11) for  $\alpha = ze^{i\pi}$  as before and find,

$$\begin{aligned} \psi_2(r_>, ze^{i\pi}) = & - \frac{(H_m^{(2)}(ze^{i\pi}(1-h))\psi'_2(1-h))H_m^{(1)}(ze^{i\pi}r_>)}{\frac{4}{i\pi(1-h)}} \\ & + \frac{(H_m^{(2)}(ze^{i\pi}H_m^{(2)'}(ze^{i\pi}(1-h))\psi_2(1-h))H_m^{(1)}(ze^{i\pi}r_>)}{\frac{4}{i\pi(1-h)}} \\ & + \frac{(H_m^{(1)}(ze^{i\pi}(1-h))\psi'_2(1-h))H_m^{(2)}(ze^{i\pi}r_>)}{\frac{4}{i\pi(1-h)}} \\ & - \frac{(H_m^{(1)}(ze^{i\pi}H_m^{(1)'}(ze^{i\pi}(1-h))\psi_2(1-h))H_m^{(2)}(ze^{i\pi}r_>)}{\frac{4}{i\pi(1-h)}}, \end{aligned} \quad (7.13a)$$

$$\begin{aligned}
&= + \frac{(H_m^{(2)}(ze^{i\pi}(1-h))\psi_2'(1-h))H_m^{(2)}(zr_>)(-1)^n}{\frac{4}{i\pi(1-h)}} \\
&+ \frac{(H_m^{(2)}(zH_m^{(2)'}(ze^{i\pi}(1-h))\psi_2(1-h))H_m^{(2)}(zr_>)(-1)^n}{\frac{4}{i\pi(1-h)}} \\
&+ \frac{(-H_m^{(2)}(z(1-h))\psi_2'(1-h))H_m^{(2)}(ze^{i\pi}r_>)(-1)^n}{\frac{4}{i\pi(1-h)}} \\
&+ \frac{(-H_m^{(2)}(zH_m^{(2)'}(z(1-h))\psi_2(1-h))H_m^{(2)}(ze^{i\pi}r_>)(-1)^n}{\frac{4}{i\pi(1-h)}}, \quad (7.13b)
\end{aligned}$$

$$\begin{aligned}
&= + \frac{(H_m^{(1)}(z(1-h))\psi_2'(1-h) - zH_m^{(1)'}(z(1-h))\psi_2(1-h))H_m^{(2)}(zr_>)}{\frac{4}{i\pi(1-h)}} \\
&- \frac{(H_m^{(2)}(z(1-h))\psi_2'(1-h) - zH_m^{(2)'}(z(1-h))\psi_2(1-h))H_m^{(1)}(zr_>)}{\frac{4}{i\pi(1-h)}} \\
&+ 2 \frac{(H_m^{(2)}(z(1-h))\psi_2'(1-h) - zH_m^{(2)'}(z(1-h))\psi_2(1-h))H_m^{(2)}(zr_>)}{\frac{4}{i\pi(1-h)}} \\
&- 2 \frac{(H_m^{(2)}(z(1-h))\psi_2'(1-h) - zH_m^{(2)'}(z(1-h))\psi_2(1-h))H_m^{(2)}(zr_>)}{\frac{4}{i\pi(1-h)}}, \quad (7.13c)
\end{aligned}$$

$$\begin{aligned}
&= - \frac{(H_m^{(2)}(z(1-h))\psi_2'(1-h) - zH_m^{(2)'}(z(1-h))\psi_2(1-h))H_m^{(1)}(zr_>)}{\frac{4}{i\pi(1-h)}} \\
&+ \frac{(H_m^{(1)}(z(1-h))\psi_2'(1-h) - zH_m^{(1)'}(z(1-h))\psi_2(1-h))H_m^{(2)}(zr_>)}{\frac{4}{i\pi(1-h)}}. \quad (7.13d)
\end{aligned}$$

It therefore can be seen that,  $\psi_2(r_>, ze^{i\pi}) = \psi_2(r_>, z)$  and we do not observe the  $\alpha$  square root branch cut in the  $\psi_2(r)$  terms.

Since none of the  $\alpha$  terms observe a jump across the branch cut, it can be said that the  $\alpha$  square root branch cut is removable and we do not need to consider its contribution to the Fourier inversion, which would evaluate to be 0. Thus we only need to consider the effects of the modal poles and the critical layer branch cut on  $\tilde{G}$ .

### 7.3 Analytic Continuation Behind the Critical Layer Branch Cut

The solution for  $\tilde{G}$  in (7.2) above contains a branch cut along the critical layer  $k \in [\frac{\omega}{M}, \infty)$ . This is because not only do  $\tilde{\psi}_1$  and  $\tilde{\psi}_2$  depend on  $\tilde{p}_2$ , but so too does  $C_1$ . We now introduce the following additional notation: When evaluating a

function  $f(k)$  on the branch cut, for  $k \in [\frac{\omega}{M}, \infty)$ , we denote

$$f^+(k) = \lim_{\varepsilon \rightarrow 0} f(k + i\varepsilon) \quad f^-(k) = \lim_{\varepsilon \rightarrow 0} f(k - i\varepsilon) \quad \Delta f(k) = f^+(k) - f^-(k) \quad (7.14)$$

Note that the definition of  $\Delta f$  agrees with the use of  $\Delta$  in equations (6.7), (6.14), (6.22), (6.23) above. By using these equations, we find that

$$\begin{aligned} \Delta \tilde{G} = & - \frac{\omega - U(r^*)k}{2i\pi r^* W(r^*)} \frac{1}{C_1^- \widehat{D}_2 - \widehat{C}_2 D_1 + 2i\pi A D_1 \widehat{D}_2} \\ & \times \left[ \frac{2i\pi A D_1 \widehat{D}_2 \tilde{\psi}_1^-(\check{r}) \tilde{\psi}_2^-(\hat{r})}{C_1^- \widehat{D}_2 - \widehat{C}_2 D_1} - \tilde{\psi}_1^-(\check{r}) \Delta \tilde{\psi}_2(\hat{r}) \right. \\ & \left. - \Delta \tilde{\psi}_1(\check{r}) \tilde{\psi}_2^-(\hat{r}) - \Delta \tilde{\psi}_1(\check{r}) \Delta \tilde{\psi}_2(\hat{r}) \right] \end{aligned} \quad (7.15)$$

A typical branch cut, such as the branch cut in  $\sqrt{z - z_0}$ , may be taken in any direction from the branch point  $z_0$ . This was previously used to set  $\text{Im}(\alpha) \geq 0$ . The critical layer branch cut in the complex  $k$ -plane is different, in that the choice of branch cut was forced upon us by the requirement that the solution be continuous in  $r$  for  $r \in [1 - h, 1]$ . None-the-less, noting from (7.15) that  $\Delta \tilde{G}$  is well defined function for general complex  $k$ , we may use equation (7.15) to analytically continue  $\tilde{G}$  behind the critical layer branch cut. For real  $\omega$ , we therefore define the analytic continuation of  $\tilde{G}$  behind the branch cut into the lower-half  $k$ -plane as

$$\tilde{G}^+(k) = \begin{cases} \tilde{G}(k) & \text{Im}(k) > 0 \text{ or } \text{Re}(k) < \frac{\omega}{M}, \\ \tilde{G}(k) + \Delta \tilde{G}(k) & \text{Im}(k) < 0 \text{ and } \text{Re}(k) > \frac{\omega}{M}. \end{cases} \quad (7.16)$$

Similarly, we may rewrite (7.15) as

$$\begin{aligned} \Delta \tilde{G} = & - \frac{\omega - U(r^*)k}{2i\pi r^* W(r^*)} \frac{1}{C_1^+ \widehat{D}_2 - \widehat{C}_2 D_1 - 2i\pi A D_1 \widehat{D}_2} \\ & \times \left[ \frac{2i\pi A D_1 \widehat{D}_2 \tilde{\psi}_1^+(\check{r}) \tilde{\psi}_2^+(\hat{r})}{C_1^+ \widehat{D}_2 - \widehat{C}_2 D_1} - \tilde{\psi}_1^+(\check{r}) \Delta \tilde{\psi}_2(\hat{r}) \right. \\ & \left. - \Delta \tilde{\psi}_1(\check{r}) \tilde{\psi}_2^+(\hat{r}) + \Delta \tilde{\psi}_1(\check{r}) \Delta \tilde{\psi}_2(\hat{r}) \right], \end{aligned} \quad (7.17)$$

which allows the analytic continuation of  $\tilde{G}^-$  into the upper-half  $k$ -plane,

$$\tilde{G}^-(k) = \begin{cases} \tilde{G}(k) & \text{Im}(k) < 0 \text{ or } \text{Re}(k) < \frac{\omega}{M}, \\ \tilde{G}(k) - \Delta \tilde{G}(k) & \text{Im}(k) > 0 \text{ and } \text{Re}(k) > \frac{\omega}{M}. \end{cases} \quad (7.18)$$

The utility of these analytic continuations is not readily apparent. However, their

use allows for poles of  $\tilde{G}$ , corresponding to modal solutions to the homogeneous Pridmore-Brown equation, to be tracked behind the branch cut, and in particular a possible hydrodynamic instability mode will later be found to be hidden behind the critical layer branch cut in certain cases. More information on this is given in section 12.1 Their use also allows the deformation of integral contours behind the critical layer branch cut, as will be needed for the steepest descent contours needed for the large- $x$  asymptotic evaluation of the inverse Fourier transform.

In what follows  $k^+$  and  $k^-$  denote modal poles, see section 6.3.1, of only  $\tilde{G}^+$  or  $\tilde{G}^-$  respectively. These coincide with usual modal poles when they are located above or below the branch cut respectively. Outside of these regions however they can only be found by specifically considering  $\tilde{G}^+$  or  $\tilde{G}^-$  respectively.

In the same way, as will be required for later, we can also define;  $C_1^\pm$ ,  $\tilde{\psi}_1^+$  and  $\tilde{p}_2^+$ ,

$$C_1^+(k) = \begin{cases} C_1(k) + \Delta C_1(k) & \text{Im}(k) < 0 \text{ or } \text{Re}(k) < \frac{\omega}{M}, \\ C_1(k) & \text{Im}(k) > 0 \text{ and } \text{Re}(k) > \frac{\omega}{M}. \end{cases} \quad (7.19)$$

$$C_1^-(k) = \begin{cases} C_1(k) & \text{Im}(k) < 0 \text{ or } \text{Re}(k) < \frac{\omega}{M}, \\ C_1(k) - \Delta C_1(k) & \text{Im}(k) > 0 \text{ and } \text{Re}(k) > \frac{\omega}{M}. \end{cases} \quad (7.20)$$

$$\tilde{\psi}_1^+(k, r) = \begin{cases} \tilde{\psi}_1(k, r) + \Delta \tilde{\psi}_1(k, r) & \text{Im}(k) < 0 \text{ or } \text{Re}(k) < \frac{\omega}{M}, \\ \tilde{\psi}_1(k, r) & \text{Im}(k) > 0 \text{ and } \text{Re}(k) > \frac{\omega}{M}. \end{cases} \quad (7.21)$$

$$\tilde{\psi}_2^+(k, r) = \begin{cases} \tilde{\psi}_2(k, r) + \Delta \tilde{\psi}_2(k, r) & \text{Im}(k) < 0 \text{ or } \text{Re}(k) < \frac{\omega}{M}, \\ \tilde{\psi}_2(k, r) & \text{Im}(k) > 0 \text{ and } \text{Re}(k) > \frac{\omega}{M}. \end{cases} \quad (7.22)$$

### 7.3.1 The Jump in $\tilde{G}$ Across the Critical Layer Branch Cut

Considering  $\Delta \tilde{G}$  given by equation (7.15) with  $\Delta \tilde{\psi}_1$  and  $\Delta \tilde{\psi}_2$  given in (6.23) as

$$\Delta \tilde{\psi}_1(r) = \begin{cases} 0 & r < r_c^+ \\ 2i\pi A D_1 \tilde{p}_1 & r \geq r_c^+, \end{cases} \quad (6.23a)$$

$$\Delta \tilde{\psi}_2(r) = \begin{cases} \Delta \check{C}_2 H_m^{(1)}(\alpha r) + \Delta \check{D}_2 H_m^{(2)}(\alpha r) & 0 \leq r \leq 1 - h \\ -2i\pi A \tilde{p}_1(r) \hat{D}_2 & 1 - h \leq r \leq r_c^+ \\ 0 & r_c^+ < r \leq 1. \end{cases} \quad (6.23b)$$

It has previously been noted in section 7 that we can have up to three branch points on the critical layer branch cut, one always occurs at  $k = \frac{\omega}{M}$ , while the others,  $k_0$  (7.3) and  $k_r$  (7.5) occur only when  $r_0$  or  $r > 1 - h$  respectively. Thus we have three

cases to consider.

When  $r, r_0 < 1 - h$  then for any  $k$  on the branch cut we have that  $\Delta\tilde{\psi}_1 = 0$  and  $\Delta\tilde{\psi}_2 \neq 0$ . Thus for any  $k$  on the critical layer branch cut we have the same formula for  $\Delta\tilde{G}$  and  $\frac{\omega}{M}$  is the only branch point of  $\Delta\tilde{G}$ . Hence, we write  $\Delta\tilde{G} = \Delta\tilde{G}_{\frac{\omega}{M}}$ , where

$$\begin{aligned}\Delta\tilde{G}_{\frac{\omega}{M}} &= -\frac{\omega - U(r^*)k}{2i\pi r^*W(r^*)} \frac{1}{C_1^- \widehat{D}_2 - \widehat{C}_2 D_1 + 2i\pi AD_1 \widehat{D}_2} \\ &\quad \times \left[ \frac{2i\pi AD_1 \widehat{D}_2 \tilde{\psi}_1^-(\check{r}) \tilde{\psi}_2^-(\hat{r})}{C_1^- \widehat{D}_2 - \widehat{C}_2 D_1} - \tilde{\psi}_1^-(\check{r}) \Delta\tilde{\psi}_2(\hat{r}) \right], \\ &= -\frac{\omega - U(r^*)k}{r^*W(r^*)} \frac{1}{C_1^- \widehat{D}_2 - \widehat{C}_2 D_1 + 2i\pi AD_1 \widehat{D}_2} \frac{A\widehat{D}_2^2 \tilde{\psi}_1^-(\check{r}) \tilde{\psi}_1^-(\hat{r})}{C_1^- \widehat{D}_2 - \widehat{C}_2 D_1}.\end{aligned}\quad (7.23a)$$

When  $\check{r} < 1 - h < \hat{r}$  then the formula for  $\Delta\tilde{G}$  depends on whether  $\frac{\omega}{M} < k < k_>$  or  $k > k_>$ . In this case, we set  $\Delta\tilde{G} = \Delta\tilde{G}_{\frac{\omega}{M}}$  for  $\frac{\omega}{M} < k_>$ , and  $\Delta\tilde{G} = \Delta\tilde{G}_{\frac{\omega}{M}} + \Delta\tilde{G}_>$  for  $k > k_>$ , so that  $\Delta\tilde{G}_>$  is the correction required for  $k > k_>$ . In effect,  $\Delta\tilde{G}$  has two overlapping branch cuts, one at  $\frac{\omega}{M}$  and one at  $k_>$  in this case, and by making this definition we may write, as will be required later,

$$\int_{\frac{\omega}{M}}^{\infty} \Delta\tilde{G} e^{-ikx} dk = \int_{\frac{\omega}{M}}^{\infty} \Delta\tilde{G}_{\frac{\omega}{M}} e^{-ikx} dk + \int_{k_>}^{\infty} \Delta\tilde{G}_> e^{-ikx} dk.\quad (7.23b)$$

By considering (7.15) in this case, we find that

$$\Delta\tilde{G}_{\frac{\omega}{M}} = -\frac{\omega - U(r^*)k}{r^*W(r^*)} \frac{1}{C_1^- \widehat{D}_2 - \widehat{C}_2 D_1 + 2i\pi AD_1 \widehat{D}_2} \frac{AD_1 \widehat{D}_2 \tilde{\psi}_1^-(\check{r}) \tilde{\psi}_2^-(\hat{r})}{C_1^- \widehat{D}_2 - \widehat{C}_2 D_1},\quad (7.23c)$$

$$\begin{aligned}\Delta\tilde{G}_> &= \frac{\omega - U(r^*)k}{2i\pi r^*W(r^*)} \frac{1}{C_1^- \widehat{D}_2 - \widehat{C}_2 D_1 + 2i\pi AD_1 \widehat{D}_2} \tilde{\psi}_1^-(\check{r}) \Delta\tilde{\psi}_2(\hat{r}), \\ &= -\frac{\omega - U(r^*)k}{r^*W(r^*)} \frac{A\widehat{D}_2 \tilde{\psi}_1^-(\check{r}) \tilde{p}_1(\hat{r})}{C_1^- \widehat{D}_2 - \widehat{C}_2 D_1 + 2i\pi AD_1 \widehat{D}_2}.\end{aligned}\quad (7.23d)$$

Finally, when we have  $1 - h < \check{r}$  we must consider three cases:  $\frac{\omega}{M} < k < k_<$ ,  $k_< < k < k_>$  and  $k_> < k$ . Similarly to the previous case, we consider  $\Delta\tilde{G}_{\frac{\omega}{M}} = \Delta\tilde{G}$  for  $\frac{\omega}{M} < k < k_<$ , and take  $\Delta\tilde{G}_<$  and  $\Delta\tilde{G}_>$  to be correction terms as  $k$  crosses  $k_<$  and  $k_>$  respectively. This leads to

$$\begin{aligned}\Delta\tilde{G}_{\frac{\omega}{M}} &= -\frac{\omega - U(r^*)k}{2i\pi r^*W(r^*)} \frac{1}{C_1^- \widehat{D}_2 - \widehat{C}_2 D_1 + 2i\pi AD_1 \widehat{D}_2} \\ &\quad \times \left[ \frac{2i\pi AD_1 \widehat{D}_2 \tilde{\psi}_1^-(\check{r}) \tilde{\psi}_2^-(\hat{r})}{C_1^- \widehat{D}_2 - \widehat{C}_2 D_1} - \Delta\tilde{\psi}_1^-(\check{r}) \tilde{\psi}_2(\hat{r}) \right],\end{aligned}$$

$$= - \frac{\omega - U(r^*)k}{r^*W(r^*)} \frac{1}{C_1^- \widehat{D}_2 - \widehat{C}_2 D_1 + 2i\pi AD_1 \widehat{D}_2} \frac{AD_1^2 \tilde{\psi}_2^-(\tilde{r}) \tilde{\psi}_2^-(\hat{r})}{C_1^- \widehat{D}_2 - \widehat{C}_2 D_1}. \quad (7.23e)$$

$$\begin{aligned} \Delta \tilde{G}_< &= - \frac{\omega - U(r^*)k}{2i\pi r^*W(r^*)} \frac{1}{C_1^- \widehat{D}_2 - \widehat{C}_2 D_1 + 2i\pi AD_1 \widehat{D}_2} \Delta \tilde{\psi}_1^-(\tilde{r}) \tilde{\psi}_2^-(\hat{r}), \\ &= - \frac{\omega - U(r^*)k}{r^*W(r^*)} \frac{AD_1 \tilde{p}_1(\hat{r}) \tilde{\psi}_2^-(\hat{r})}{C_1^- \widehat{D}_2 - \widehat{C}_2 D_1 + 2i\pi AD_1 \widehat{D}_2}. \end{aligned} \quad (7.23f)$$

$$\begin{aligned} \Delta \tilde{G}_> &= \frac{\omega - U(r^*)k}{2i\pi r^*W(r^*)} \frac{1}{C_1^- \widehat{D}_2 - \widehat{C}_2 D_1 + 2i\pi AD_1 \widehat{D}_2} \tilde{\psi}_1^-(\tilde{r}) \Delta \tilde{\psi}_2^-(\hat{r}), \\ &= - \frac{\omega - U(r^*)k}{r^*W(r^*)} \frac{A \widehat{D}_2 \tilde{\psi}_1^-(\tilde{r}) \tilde{p}_1(\hat{r})}{C_1^- \widehat{D}_2 - \widehat{C}_2 D_1 + 2i\pi AD_1 \widehat{D}_2}. \end{aligned} \quad (7.23g)$$

## 8 Inverting the Fourier Transform

The work contained within this section has been previously presented within [King et al., 2022, section 3.3]. In the current work additional detail has been provided at each step.

Having formulated  $\tilde{G}$  as the solution to the inhomogeneous Pridmore-Brown equation (5.15), to recover the actual pressure perturbation  $\hat{p}(x, r, \theta)$ , we are required to invert the Fourier transform and sum the Fourier series. For a fixed azimuthal mode  $m$  we invert the Fourier transform using the formula

$$G(x, r; r_0, m) = \frac{1}{2\pi} \int_{\mathcal{C}} \tilde{G}(r, r_0, k, m) e^{-ikx} dk. \quad (8.1)$$

Typically,  $\mathcal{C}$  would be taken along the real  $k$  axis, however, the critical layer branch cut is located along the real- $k$  half line  $k \in [\frac{\omega}{M}, \infty)$ . Therefore, we are required to be careful in choosing a suitable inversion contour  $\mathcal{C}$  in order to correctly invert the Fourier transform.

### 8.1 Choosing an Inversion Contour

In order to choose the correct Fourier inversion contour  $\mathcal{C}$ , we appeal to the Briggs-Bers criterion [Briggs, 1964, Bers, 1983]. The Briggs-Bers criterion, summarised below, invokes the notion of causality; that the cause of the disturbance (the delta function forcing) should occur before the effect (the disturbance  $\hat{p}$ ), which is otherwise lost when considering a time-harmonic forcing, as we do here. Typically the Briggs-Bers criterion is used to invert both the space and time Fourier transforms, bringing the problem out of the frequency domain and into the time domain. This does not prevent us however from acknowledging the requirements for the Briggs-Bers criterion, and only applying one of the Fourier inversions.

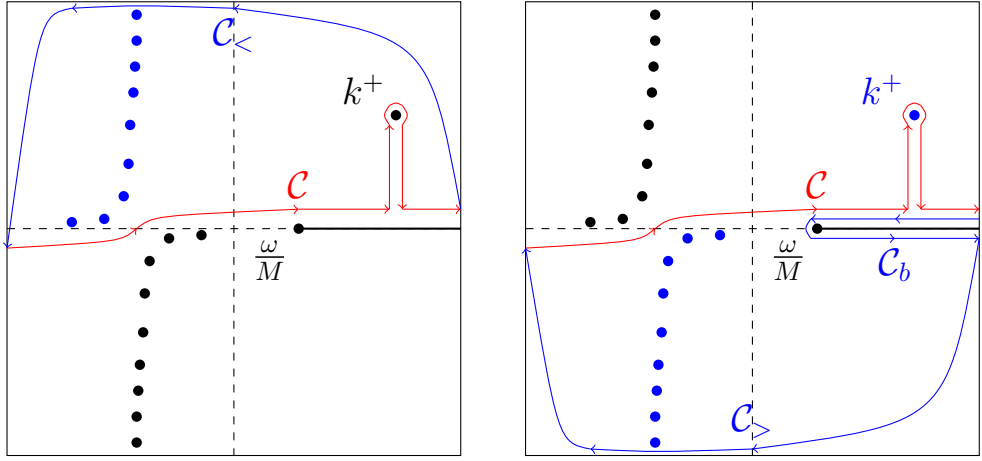


Figure 6: Illustration of the inversion contours taken when an unstable  $k^+$  pole is present. The inversion contour for  $\tilde{G}$  is labelled  $\mathcal{C}$ . (Left) For  $x < 0$ , the contour is closed in the upper half plane along the  $\mathcal{C}_<$  contour. (Right) For  $x > 0$ , the contour is closed in the lower half plane along the  $\mathcal{C}_>$  contour, and around the critical layer branch cut along the  $\mathcal{C}_b$  contour. Contributing modal poles are indicated in blue.

In order to make use to the Briggs-Bers criterion, the rate of exponential growth of the solution must be bounded; that is, there must exist  $\Omega, K > 0$  such that, if  $\text{Im}(\omega) < -\Omega$ , then  $\tilde{G}$  is analytic for  $|\text{Im}(k)| < K$ . For a given  $\omega$  with  $\text{Im}(\omega) < -\Omega$ , we take the  $k$ -inversion contour  $\mathcal{C}$  in (8.1) along the real- $k$  axis, and map the locations of any singularities (e.g. poles, branch points, etc). In order to find a correct integration contour for the real values of  $\omega$  that are of interest, the imaginary part of  $\omega$  is smoothly increased to 0, and the locations of any singularities tracked throughout this process. During this process, the  $k$ -inversion contour  $\mathcal{C}$  must be smoothly deformed in order to maintain analyticity; that is, no singularities must cross the  $k$ -inversion contour. Assuming this process may be completed and  $\text{Im}(\omega)$  increased to zero, then the resulting  $k$ -inversion contour  $\mathcal{C}$  is the correct causal contour.

One complication to this process is the presence of absolute instabilities. These occur when two poles from opposite half planes for large  $-\text{Im}(\omega)$  collide as  $\text{Im}(\omega)$  is taken to zero. These are of greater interest in the time domain, as the time integration must be deformed around the value of  $\omega$  for which this occurs. When an absolute instability may be present, then the stability of the poles involved after the contour has been deformed is somewhat artificial, as their half plane of origin will vary depending on how  $\text{Im}(\omega)$  is taken to zero, and if  $\text{Re}(\omega)$  is varied also.

Once we have the integration contour  $\mathcal{C}$ , we need only close the the contour and the Fourier inversion can be given by the method of residues. Since for  $x < 0$  the  $\exp\{-ikx\}$  term is exponentially small as  $|k| \rightarrow \infty$  in the upper-half  $k$ -plane, for  $x < 0$  we may close the contour with a large semi-circular arc at infinity in the upper-half  $k$ -plane, denoted  $\mathcal{C}_>$ . The resulting contours are illustrated in figure 6.

In this illustration, the majority of singularities of  $\tilde{G}$  are poles which do not cross the real  $k$  axis as  $\text{Im}(\omega)$  is varied, and hence correspond to exponentially decaying disturbances away from the point mass source at  $x = 0$ . The exception to these poles is the pole labelled  $k^+$ , which for this illustration originates in the lower-half  $k$ -plane for  $\text{Im}(\omega)$  sufficiently negative, and therefore belongs below the  $k$ -inversion contour. This implies that this pole is seen downstream of the point mass source, for  $x > 0$ , despite having  $\text{Im}(k) > 0$ , and therefore corresponds to an exponentially growing instability and is identified with as a hydrodynamic instability. The critical layer, as described earlier, exists when  $k/\omega = 1/U(r_c) \in [1/M, \infty]$  for some critical radius  $r_c$ , and so is found in the lower-half  $k$ -plane for  $\text{Im}(\omega) < 0$ . Thus, as shown in figure 6, for  $x > 0$  in order to close  $\mathcal{C}$  in the lower-half  $k$ -plane, we must pass around the critical layer branch cut, denoted by the contour  $\mathcal{C}_b$ , before closing in the lower-half  $k$ -plane with a semi-circular arc denoted  $\mathcal{C}_>$ . The contribution from integrating around the critical layer branch cut,  $\mathcal{C}_b$ , leads to the non-modal contribution of the critical layer, and is discussed in detail below in section 8.3.

As  $-\text{Im}(\omega)$  is increased it might be observed that the  $k^+$  modal pole will cross the critical layer branch cut. It will turn out that this does not effect the resulting contour of Fourier inversion, since this is merely a consequence of the choice of how to vary  $\omega$  and the impedance modal  $Z(\omega)$  being used.

Actual trajectories or the mode locations under the Briggs-Bers criterion are given later in figure 9 within section 10.

## 8.2 Contribution from the Poles of $\tilde{G}$

We may now write the integral around the closed contour as a sum of residues of poles:

$$\frac{1}{2\pi} \int_{\mathcal{C} \cup \mathcal{C}_<} \tilde{G}(r, r_0, k, m) e^{-ikx} dk = G(x, r; r_0, m) = \sum_{j: \text{Im}(k_j) > \text{Im}(\mathcal{C})} R(k_j) \quad \text{for } x < 0, \quad (8.2a)$$

$$\frac{1}{2\pi} \int_{\mathcal{C} \cup \mathcal{C}_b \cup \mathcal{C}_>} \tilde{G}(r, r_0, k, m) e^{-ikx} dk = G(x, r; r_0, m) - I(x) = \sum_{j: \text{Im}(k_j) < \text{Im}(\mathcal{C})} R(k_j) \quad \text{for } x > 0, \quad (8.2b)$$

where  $I(x)$  is the contribution from integrating around the critical layer branch cut contour  $\mathcal{C}_b$  discussed in the next section,  $R(k_j)$  is the residue from a pole at  $k_j$  discussed below, and the notation  $\text{Im}(k_j) > \text{Im}(\mathcal{C})$  is used to denote poles  $k_j$  lying above the inversion contour  $\mathcal{C}$ .

The poles of  $\tilde{G}$  correspond to zeros of the denominator of  $\tilde{G}$ , as given in (7.2). They

can occur in two ways as already highlighted: these were as modal or non-modal poles. We consider the modal poles first. The modal poles occur as zeros of the term  $C_1\widehat{D}_2 - \widehat{C}_2D_1 = 0$ . As discussed in section 6.3.1, this occurs when both  $\psi_1$  and  $\psi_2$  satisfy both boundary conditions at  $r = 0$  and  $r = 1$ . These modal poles can be further classified into acoustic modes and surface modes: acoustic modes are those for which  $\alpha$  in equation (6.15) has a small imaginary part, and correspond to functions which are oscillatory in  $r$ ; and surface modes are those for which  $\alpha$  has a significant imaginary part, and correspond to functions which decay exponentially away from the duct walls at  $r = 1$ . For different parameters, we may find a variety of surface modes, and two with which we will be particularly interested here will be denoted  $k^-$  and  $k^+$ .

Since the modal poles occur as zeros of  $C_1\widehat{D}_2 - \widehat{C}_2D_1 = 0$ , which we shall assume are simple zeros, the contribution from the residues of these poles are given by

$$R(k) = -\text{sgn}(x) \frac{\omega - U(r^*)k}{2\pi r^* W(r^*)} \frac{\psi_1(\tilde{r})\psi_2(\hat{r})}{\frac{\partial}{\partial k}(C_1\widehat{D}_2 - \widehat{C}_2D_1)} e^{-ikx}. \quad (8.3)$$

The second type of poles are the non-modal poles, which occur when  $W(r^*) = 0$ . These occur when we lose independence between  $\tilde{p}_1$  and  $\tilde{p}_2$  at  $r^*$ . Since  $1 - h \leq r^* \leq 1$  this can only occur when  $k$  is located on the critical layer branch cut. Note that the  $k_0$  is a function of the radial location of the point source  $r_0$  (through  $r^*$ ), which is unlike the modal poles for which  $k_j$  is independent of the value of  $r_0$ ; this is one reason this  $k_0$  pole is referred to as a non-modal pole. However, since our closed contour goes around the critical layer branch cut (along contour  $\mathcal{C}_b$ ), this pole is always excluded from the sum of residues in (8.2) above, and only occurs within the calculation of  $I(x)$ , which we consider in section 8.3.

### 8.3 Contribution from the Critical Layer Branch Cut

The contribution from the critical layer branch cut, including any non-modal pole  $k_0$  along the branch cut, is contained solely within the integral around the critical layer branch cut denoted  $\mathcal{C}_b$  in figure 6,

$$I(x) = \frac{-1}{2\pi} \int_{\mathcal{C}_b} \tilde{G} e^{-ikx} dk. \quad (8.4)$$

However, as it stands, this integral for  $I(x)$  is oscillatory, owing to the  $e^{-ikx}$  factor in the integrand, and so is difficult to accurately compute numerically. This is especially true for large values of  $x$ . Instead, it is helpful to deform the integral onto the Steepest Descent contour, for which  $e^{-ikx}$  is exponentially decaying along

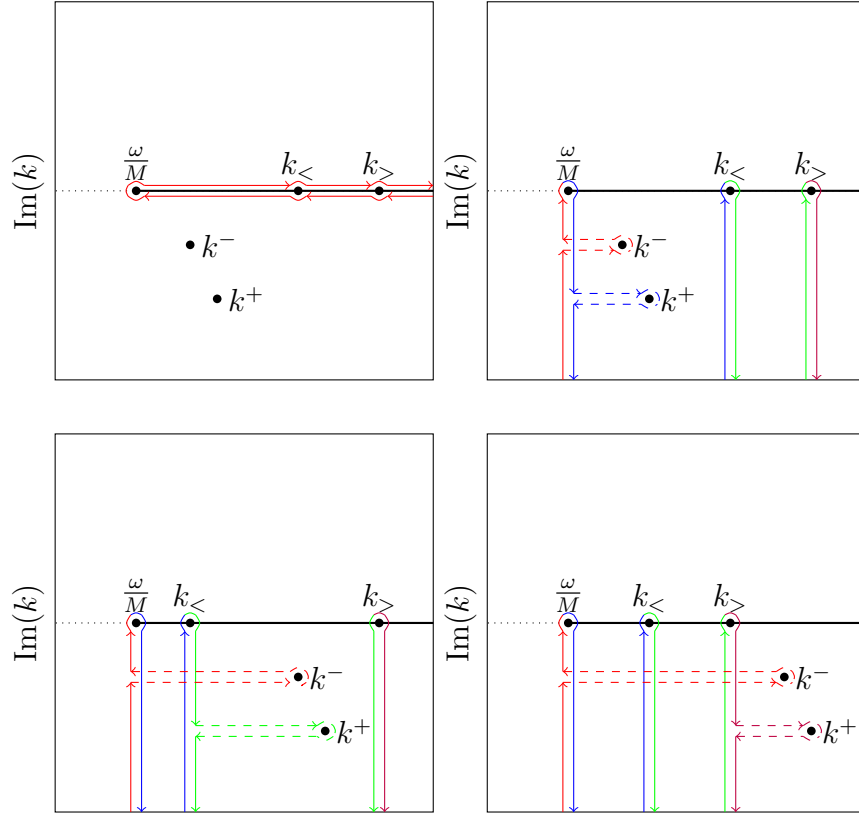


Figure 7: (Top Left) The integration contour required for the computation of the contribution from the critical layer branch cut, understood by integrating above and below the branch cut. Possible poles of  $\tilde{G}^-$  and  $\tilde{G}^+$  are denoted  $k^-$  and  $k^+$  respectively. (Top Right) The integration contour after being transformed onto the steepest descent contour. Red lines behave as if evaluated below  $\frac{\omega}{M}$  (using  $\tilde{G}^-$ ); blue as if having been analytically continued around the  $\frac{\omega}{M}$  branch point; green as if having been analytically continued around the  $\frac{\omega}{M}$  and  $k_<$  branch points; and purple as if analytically continued around all branch points, giving  $\tilde{G}^+$ . (Bottom) As top right but with the relative locations of the  $k^+$  and  $k^-$  poles to  $k_<$  and  $k_>$  varied. Note that while the  $k^-$  pole is only picked up by the red contour ( $\tilde{G}^-$ ) the  $k^+$  pole is picked up by the first contour to its left, and its contribution will vary accordingly.

the contour. This contour deformation has three benefits: firstly, it allows accurate numerical calculation of the integral; secondly, it allows the derivation of large- $x$  asymptotics using the method of steepest descents; and thirdly, it brings insight into the various contributions that make up  $I(x)$ . In deforming the integration contour, however, we must analytically continue  $\tilde{G}$  behind the branch cut, as described in section 7.3, and carefully deform around any poles and branch points. This is illustrated schematically in figure 7. It should be noted that the integration contour taken in figure 7 is in the opposite direction to that of  $\mathcal{C}_b$ . This is accounted for by the introduction of a negative sign. Note also that poles and branch points of  $\tilde{G}$  may exist behind the critical layer branch cut, and we must therefore use analytic continuations of  $\tilde{G}$ ; the reader is reminded that  $\tilde{G}^+$  is the analytic continuation of  $\tilde{G}$  down behind the branch cut from above, while  $\tilde{G}^-$  is the analytic continuation of  $\tilde{G}$

up behind the branch cut from below. Here, we use the notation that a pole of  $\tilde{G}^+$  with  $\text{Re}(k) > \frac{\omega}{M}$  is denoted  $k^+$ , and a pole of  $\tilde{G}^-$  with  $\text{Re}(k) > \frac{\omega}{M}$  is denoted  $k^-$ . Thus, a  $k^+$  pole with  $\text{Im}(k^+) < 0$  or a  $k^-$  pole with  $\text{Im}(k^-) > 0$  are considered as being hidden behind the critical layer branch cut. In the schematic in figure 7, one  $k^-$  and one  $k^+$  pole are present, both with  $\text{Im}(k) < 0$ , although this is not always the case. In fact, in each case investigated for a quadratic shear flow no  $k^-$  poles have been found below the critical layer branch cut. Despite this, the appropriate analysis for their inclusion is still given, such that this work may be used as a basis for other flow profiles, such as the linear shear flow, where they may be observed.

The steepest descent contours are where  $e^{-ikx}$  is exponentially decaying; i.e. towards  $-i\infty$  in the complex  $k$  plane. There is no difficulty deforming the contour at infinity, since  $e^{-ikx}$  is exponentially small, (provided  $x > 0$ , which is the only case in which the critical layer branch cut contributes) so has negligible contribution. As previously mentioned along the branch cut there are up to three branch points, see section 7.1, denoted  $\frac{\omega}{M}$ ,  $k_<$  and  $k_>$  in figure 7, that must be deformed around.

The total integral around the branch cut can therefore be found by summing these three integrals, subtracting any  $k^-$  contributions below the branch cut and adding any  $k^+$  contributions below the branch cut, and adding the pole residue at  $k_0$  calculated as if it was located above the branch cut. This results in

$$I(x) = I_{\frac{\omega}{M}}(x) + I_0(x) + I_r(x) + R_0^+(k_0) + \sum_{\text{Im}(k^+) < 0} R^+(k^+) - \sum_{\text{Im}(k^-) < 0} R(k^-), \quad (8.5)$$

where  $R^\pm$  is the residue given by

$$R^+(k^+) = -\frac{\omega - U(r^*)k^+}{2\pi r^* W(r^*)} \frac{\tilde{\psi}_1^+(k^+, \tilde{r}) \tilde{p}_2^+(k^+, \hat{r})}{\frac{\partial}{\partial k} (C_1^+ \hat{D}_2 - \hat{C}_2 D_1)_{k=k^+}} e^{-ik^+ x} \quad (8.6)$$

and  $R_0^+(k_0)$  is the residue of the non-modal pole  $k_0$  evaluated as if approached from above the branch cut, given by

$$R_0^+(k_0) = \frac{2Mk_0^2(\omega - Mk_0)e^{-ik_0 x}}{3\pi r_0 h^2 \omega (C_1^+ \hat{D}_2 - \hat{C}_2 D_1)} \begin{cases} \hat{D}_2 \psi_1(r) & r < r_0, \\ D_1 \psi_2(r) & r > r_0. \end{cases} \quad (8.7)$$

In addition to this, the steepest descent integrals are defined as

$$I_q(x) = \frac{1}{2i\pi} \int_0^\infty \Delta \tilde{G}_q(k_q - i\xi) e^{-i(k_q - i\xi)x} d\xi, \quad (8.8)$$

and the jumps across each of the steepest descent branch cuts have been calculated

in section 7.3.1 to be

$$\Delta\tilde{G}_{\frac{\omega}{M}} = \frac{-(\omega - U(r^*)k)A}{r^*W(r^*)(C_1^-\hat{D}_2 - \hat{C}_2D_1 + 2i\pi AD_1\hat{D}_2)} \times \begin{cases} \frac{\hat{D}_2^2\psi_1^-(\check{r})\psi_1^-(\hat{r})}{(C_1^-\hat{D}_2 - \hat{C}_2D_1)} & \hat{r} < 1-h \\ \frac{D_1\hat{D}_2\psi_1^-(\check{r})\psi_2^-(\hat{r})}{(C_1^-\hat{D}_2 - \hat{C}_2D_1)} & \check{r} < 1-h < \hat{r} \\ \frac{D_1^2\psi_2^-(\check{r})\psi_2^-(\hat{r})}{(C_1^-\hat{D}_2 - \hat{C}_2D_1)} & 1-h < \check{r}, \end{cases} \quad (8.9a)$$

$$\Delta\tilde{G}_{<} = \frac{-(\omega - U(r^*)k)}{r^*W(r^*)} \frac{AD_1\tilde{p}_1(\check{r})\psi_2^-(\hat{r})}{C_1^-\hat{D}_2 - \hat{C}_2D_1 + 2i\pi AD_1\hat{D}_2} H(\check{r} - (1-h)), \quad (8.9b)$$

$$\Delta\tilde{G}_{>} = \frac{-(\omega - U(r^*)k)}{r^*W(r^*)} \frac{A\hat{D}_2\psi_1^-(\check{r})\tilde{p}_1(\hat{r})}{C_1^-\hat{D}_2 - \hat{C}_2D_1 + 2i\pi AD_1\hat{D}_2} H(\hat{r} - (1-h)). \quad (8.9c)$$

Note that  $\Delta\tilde{G}_{\frac{\omega}{M}} + \Delta\tilde{G}_{<} + \Delta\tilde{G}_{>} = \Delta\tilde{G} = \tilde{G}^+ - \tilde{G}^-$ . While these integrals are now amenable to numerical integration, additional understanding of the contribution from the three steepest descent contours may be gained by considering the large- $x$  limit. To this end we shall consider various asymptotic behaviours of  $\tilde{G}$  and  $\Delta\tilde{G}$ .

## 9 Asymptotic Analysis of the Solutions

The work presented as this section has previously been given in [King et al., 2022, Appendix C], although greater detail regarding the leading order expansions and the branch points on the critical layer branch cut are given.

In order to predict the far-field behaviour of each of the three steepest descent contours we are required to observe how they behave as we approach the branch points in  $k$ . Further we will confirm here which of the branch points are poles and when.

### 9.1 Behaviour as $k \rightarrow \frac{\omega}{M}$

The branch point located at  $k = \frac{\omega}{M}$  is always present. As has been previously mentioned in this limit we have  $r_c^+ \rightarrow 1-h$ , which will result in a decreasing radius of convergence for the  $\tilde{p}_c$  solutions, and so when considering  $r > 1-h$  we will be

required to consider the matched solutions.

### 9.1.1 Behaviour of the Homogenous Solutions

First note that;

$$\left(k - \frac{\omega}{M}\right) = \xi, \quad Q = h\sqrt{\frac{M\xi}{\omega}}, \quad (9.1)$$

and so we shall consider leading orders of  $Q$ ,

$$\left(k - \frac{\omega}{M}\right) = O(Q^2). \quad (9.2)$$

As already suggested, we must consider the leading order of  $\tilde{p}_1$  and  $\tilde{p}_2$  separately for  $r = 1 - h$  and  $r > 1 - h$ . We shall first consider the leading order behaviours of  $\tilde{p}_{c1}(r)$  and  $\tilde{p}_{c2}(r)$  near  $r = 1 - h$ . That is, we consider

$$r = 1 - h + RQ, \quad R \leq O(1). \quad (9.3)$$

such that taking  $R = 0$  retrieves  $r = 1 - h$  and we can also use these solutions for matching in the small  $Q$  limit.

Consider the following leading order approximation of the  $a_n$

$$a_n = \sum_{j=0}^{n-1} a_{n-1-j} \left[ \frac{(-1)^j 2(n+2-j)}{n(n+3)(2Q)^{j+1}} + O(1) \right]. \quad (9.4a)$$

Then it follows that we can express the  $a_n$  as

$$a_n = a_n^{(0)} \frac{1}{Q^n} + O(Q^{-n+1}), \quad (9.4b)$$

$$a_n^{(0)} = \sum_{j=0}^{n-1} a_{n-1-j}^{(0)} \left( \frac{-1}{2} \right)^j \frac{(n+2-j)}{n(n+3)}. \quad (9.4c)$$

$$(9.4d)$$

This yields,

$$a_0^{(0)} = 1, \quad a_1^{(0)} = \frac{3}{4}, \quad (9.4e)$$

$$a_2^{(0)} = \frac{3}{20}, \quad a_n^{(0)} = 0 \quad n \geq 3, \quad (9.4f)$$

and it follows that

$$\tilde{p}_{c1}(1-h + RQ) = Q^3(R-1)^3 \left( 1 + \frac{3}{4}(R-1) + \frac{3}{20}(R-1)^2 \right) + O(Q^4), \quad (9.5a)$$

$$\tilde{p}_{c1}(1-h+RQ) = 3Q^2(R-1)^2 \left( 1 + (R-1) + \frac{1}{4}(R-1)^2 \right) + O(Q^3). \quad (9.5b)$$

Doing the same for the  $b_n$  it can be found

$$A = -\frac{1}{3Q} \left( \frac{\omega^2}{M^2} + \frac{m^2}{r_c^{+2}} \right) + O(1), \quad (9.6)$$

and,

$$b_0 = 1, \quad b_1 = 0, \quad (9.7a)$$

$$b_2 \approx \frac{1}{2} \left( \frac{\omega^2}{M^2} - \frac{m^2}{(1-h)^2} \right), \quad b_3 = 0, \quad (9.7b)$$

where each of these is of order  $O(1)$ . For  $n \geq 4$ , to leading order,

$$b_n = \sum_{j=0}^{n-3} \frac{(-1)^j 2(n-1-j)}{n(n-3)(2Q)^{j+1}} + O(Q^{n-4}), \quad (9.7c)$$

$$b_n = b_n^{(0)} \frac{1}{Q^{n-2}}, \quad (9.7d)$$

$$b_n^{(0)} = \sum_{j=0}^{n-3} \left( \frac{-1}{2} \right)^j \frac{(n-1-j)}{n(n-3)}. \quad (9.7e)$$

This results in

$$\tilde{p}_{c2}(1-h+RQ) = 1 + O(Q^2 \log(Q)), \quad (9.8a)$$

$$\begin{aligned} \tilde{p}'_{c2}(1-h+RQ) &= -Q \log(Q) \left( \frac{\omega^2}{M^2} + \frac{m^2}{(1-h)^2} \right) (R-1)^2 \left( 1 + (R-1) + \frac{(R-1)^2}{4} \right) \\ &\quad + O(Q) \end{aligned} \quad (9.8b)$$

Further, considering the same values of  $r$  for  $\tilde{p}_{11}$  and  $\tilde{p}_{12}$  gives,

$$\tilde{p}_{11}(1-h+RQ) = \sum_{n=0}^{\infty} (RQ)^n \tilde{p}_{11}^{(n)}, \quad \tilde{p}_{12}(1-h+RQ) = \sum_{n=0}^{\infty} (RQ)^n \tilde{p}_{12}^{(n)}, \quad (9.9a)$$

$$\tilde{p}'_{11}(1-h+RQ) = \sum_{n=0}^{\infty} (RQ)^n \tilde{p}'_{11}^{(n)}, \quad \tilde{p}'_{12}(1-h+RQ) = \sum_{n=0}^{\infty} (RQ)^n \tilde{p}'_{12}^{(n)}. \quad (9.9b)$$

While for  $r > 1-h$  and away from  $1-h$  we find that each of these expansions are order 1. That is, the leading order expansions of  $\tilde{p}_1(r)$  and  $\tilde{p}_2(r)$  away from  $r = 1-h$  is dictated by the leading orders of the matching coefficients  $A_1$ ,  $B_1$ ,  $A_2$  and  $B_2$  (6.13).

In order to understand the matching coefficients we must consider that we require the matching to be valid for each value of  $r$  in the overlapping region of convergence.

That is, we are required to find a polynomial in  $R$  that matches in orders of  $Q$ , not just matching at leading orders of  $Q$ . Note that to leading  $R$ , when considering  $\tilde{p}_1$  and  $\tilde{p}_2$  we have

$$\tilde{p}_{c1} \approx \frac{3}{20}R^5Q^3, \quad \tilde{p}'_{c1} \approx \frac{3}{4}R^4Q^2, \quad (9.10a)$$

$$\tilde{p}_{c2} \approx 1, \quad \tilde{p}'_{c2} \approx -\left(\frac{\omega^2}{M^2} + \frac{m^2}{(1-h)^2}\right)R^4Q \log Q. \quad (9.10b)$$

Which, to the same order of  $R$  is

$$\tilde{p}_{11} \approx R^5Q^5\tilde{p}_{11}^{(5)}, \quad \tilde{p}'_{11} \approx R^4Q^4\tilde{p}'_{11}^{(4)}, \quad (9.10c)$$

$$\tilde{p}_{12} \approx R^5Q^5\tilde{p}_{12}^{(5)}, \quad \tilde{p}'_{12} \approx R^4Q^4\tilde{p}'_{12}^{(4)}. \quad (9.10d)$$

Since we require at  $R$ ,  $\tilde{p}_{c1} = A_1\tilde{p}_{11} + B_1\tilde{p}_{12}$ , it follows that

$$A_1 = O(Q^{-2}), \quad B_1 = O(Q^{-2}). \quad (9.11a)$$

Doing similar for  $\tilde{p}_{c2}$  gives

$$A_2 = O(Q^{-3} \log Q), \quad B_2 = O(Q^{-3} \log Q). \quad (9.11b)$$

We will later require  $A_1B_2 - A_2B_1$ . This can be considered through the Wronskians, that is

$$W(r) = (A_1B_2 - A_2B_1)\mathcal{W}(\tilde{p}_{11}, \tilde{p}_{12}, r) \quad (9.12)$$

With  $W(r)$  given in equation (6.26c) and

$$\mathcal{W}(\tilde{p}_{11}, \tilde{p}_{12}, r) = \frac{(r - r_c^+)^2(r - r_c^-)}{r(1 - r_c^+)^2(1 - r_c^-)^2} \quad (9.13)$$

which results in;

$$A_1B_2 - A_2B_1 = \frac{3(h - Q)^2(h + Q)^2(1 - h + Q)}{4Q^2} = O(Q^{-2}). \quad (9.14)$$

This is smaller than might have been anticipated from the individual scalings of  $A_1$ ,  $B_1$ ,  $A_2$  and  $B_2$  given above, but this is expected as, when the critical point  $r_c^+$  is approached, the two linearly independent solutions lose their linear independence, and so there is significant cancellation between  $A_1B_2$  and  $A_2B_1$ .

Note also from (6.26c) that, as  $|Q| \rightarrow 0$ , we have

$$W(r^*) = \begin{cases} -\frac{3Q^2}{4} \left(1 + \frac{Q}{1-h}\right) & r_0 \leq 1-h \\ -\frac{3(1-h-r_0)^4}{4r_0} \left(\frac{(1-h)}{Q^2} + \frac{1}{Q} + O(1)\right) & r_0 > 1-h. \end{cases} \quad (9.15)$$

With each of these, in addition to that  $\alpha = O(1)$ , and the Bessel Functions will also be of order 1, it then follows that

$$C_1 = \frac{4\alpha J'_m(\alpha(1-h))}{3Q^2} + O(Q^{-1}) = O(Q^{-2}), \quad (9.16a)$$

$$D_1 = J_m(\alpha(1-h)) + O(Q) = O(1), \quad (9.16b)$$

$$\widehat{C}_2 = -\frac{4Q^2}{3} \frac{A_2 + \frac{i\omega}{Z} B_2}{(1-h+Q)(h-Q)^2(h+Q)^2} = O(Q^{-1} \log(Q)), \quad (9.16c)$$

$$\widehat{D}_2 = \frac{4Q^2}{3} \frac{A_1 + \frac{i\omega}{Z} B_1}{(1-h+Q)(h-Q)^2(h+Q)^2} = O(1), \quad (9.16d)$$

$$\check{C}_2 = \frac{\pi i(1-h)\alpha}{4} \widehat{D}_2 H_m^{(2)'}(\alpha(1-h)) = O(1), \quad (9.16e)$$

$$\check{D}_2 = -\frac{\pi i(1-h)\alpha}{4} \widehat{D}_2 H_m^{(1)'}(\alpha(1-h)) = O(1). \quad (9.16f)$$

We can use the above to establish that  $\psi_1$  and  $\psi_2$  are both order 1 quantities for particular values of  $r$ ;

$$\psi_1(r) = J_m(\alpha r) = O(1) \quad \text{for } r < 1-h, \quad (9.17)$$

$$\psi_2(r) = \widehat{C}_2 \widetilde{p}_1 + \widehat{D}_2 \widetilde{p}_2 = \widetilde{p}_{12} - \frac{i\omega}{Z} \widetilde{p}_{11} = O(1) \quad \text{for } r > 1-h. \quad (9.18)$$

We also note that  $\omega - U(r^*)k = -M(k - \frac{\omega}{M}) = -\omega Q^2/h^2 + O(Q^4) = O(Q^2)$  for  $r_0 \leq 1-h$  and is  $O(1)$  for  $r_0 > 1-h$ .

### 9.1.2 Behaviour of $\Delta \widetilde{G}_{\frac{\omega}{M}}$

We now substitute all of the above into the equation for  $\Delta \widetilde{G}_{\frac{\omega}{M}}$  given in equation (8.9a). First of all, we rewrite (8.9a) exactly as

$$\Delta \widetilde{G}_{\frac{\omega}{M}} = \frac{4A(\widehat{D}_2 \psi_1^-(1-h))^2 f(r) f(r_0) j(r^*)}{3(1-h)Q^3 \left(C_1^- \widehat{D}_2 - \widehat{C}_2 D_1 + 2i\pi A D_1 \widehat{D}_2\right) \left(C_1^- \widehat{D}_2 - \widehat{C}_2 D_1\right)}, \quad (9.19a)$$

$$\text{where } j(r_0) = -\frac{3}{4}(1-h)Q^3 \frac{\omega - U(r_0)k}{r_0 W(r_0)} \quad \text{and} \quad f(r) = \begin{cases} \frac{\psi_1^-(r)}{\psi_1^-(1-h)} & r < r_0 \\ \frac{D_1 \psi_2^-(r)}{\widehat{D}_2 \psi_1^-(1-h)} & r > r_0. \end{cases} \quad (9.19b)$$

Taking now the leading order terms as  $k \rightarrow \frac{\omega}{M}$ , we find that

$$\Delta \widetilde{G}_{\frac{\omega}{M}} \sim -\frac{\left(\frac{\omega^2}{M^2} + \frac{m^2}{(1-h)^2}\right)}{4(1-h)} \frac{J_m(\alpha(1-h))^2}{\alpha^2 J'_m(\alpha(1-h))^2} f(r) f(r_0) j(r_0), \quad (9.20a)$$

$$\text{where } f(r) = \begin{cases} \frac{J_m(\alpha r)}{J_m(\alpha(1-h))} & r < r_0 \\ \frac{\psi_2^-(r)}{\widehat{D}_2} & r > r_0. \end{cases} \quad (9.20b)$$

$$\text{and } j(r_0) = \begin{cases} -\frac{\omega}{h^2} Q^3 & r_0 < 1-h \\ \frac{\omega(1-U(r_0)/M)}{(r_0-1+h)^4} Q^5 & r_0 > 1-h. \end{cases} \quad (9.20c)$$

And since we are intending to evaluate  $\Delta \widetilde{G}_{\frac{\omega}{M}}$  as  $k = \frac{\omega}{M} - i\xi$ , so that  $Q = (1-i)h\sqrt{M\xi/2\omega} + O(\xi^{3/2})$  (recalling that  $\text{Re}(Q) \geq 0$ ), we find that  $j(r_0)$  may be written to leading order as

$$j(r_0) = \begin{cases} \frac{1+i}{\sqrt{2}} \frac{hM^{3/2}}{\omega^{1/2}} \xi^{3/2} & r_0 < 1-h \\ -\frac{1-i}{\sqrt{2}} \frac{h^5 M^{5/2}}{\omega^{3/2}} \frac{1-U(r_0)/M}{(r_0-1+h)^4} \xi^{5/2} & r_0 > 1-h. \end{cases} \quad (9.21)$$

It is then found that  $\Delta \widetilde{G} = O(\xi^{3/2})$  for  $r_0 < 1-h$  and  $\Delta \widetilde{G} = O(\xi^{5/2})$  for  $r_0 > 1-h$ .

### 9.1.3 The Branch Point at $k = \frac{\omega}{M}$

We may also use the above scalings to consider the branch point of  $\widetilde{G}$  at  $k = \frac{\omega}{M}$ , with the aim of showing that  $\widetilde{G}$  does not experience a pole at  $k = \frac{\omega}{M}$  for any value

of  $r_0$ . Recall from (7.2) that

$$\tilde{G} = \frac{(\omega - U(r^*)k)}{2\pi i r^* W(r^*)} \frac{\psi_1(\tilde{r})\psi_2(\hat{r})}{C_1 \hat{D}_2 - \hat{C}_2 D_1}. \quad (7.2)$$

Using the results above, if  $k = \frac{\omega}{M} + \xi e^{i\theta}$ , as would be the case for integrating around a branch point, then for  $r_0 \leq 1 - h$ , since  $\psi_1$  and  $\psi_2 = O(1)$ ,

$$\tilde{G} \sim \frac{M\xi e^{i\theta}}{2\pi i(1-h)} \frac{\psi_1(\tilde{r})\psi_2(\hat{r})}{\alpha J'_m(\alpha(1-h))\hat{D}_2} = O(\xi). \quad (9.22)$$

If instead  $r_0 > 1 - h$ , we find that

$$\tilde{G} \sim \frac{-Mh^4 \xi^2 e^{2i\theta} (M - U(r_0))}{2\pi i \omega (1-h)(1-h-r_0)^4} \frac{\psi_1(\tilde{r})\psi_2(\hat{r})}{\alpha J'_m(\alpha(1-h))\hat{D}_2} = O(\xi^2). \quad (9.23)$$

In particular, in either case there is no pole of  $\tilde{G}$  at  $k = \frac{\omega}{M}$ . Hence, we have that

$$I_\xi(x) = \frac{-1}{2\pi} \int_0^{2\pi} \tilde{G}\left(\frac{\omega}{M} + \xi e^{i\theta}\right) \exp\left\{-ix\left(\frac{\omega}{M} + \xi e^{i\theta}\right)\right\} i\xi e^{i\theta} d\theta \rightarrow 0 \quad \text{as } \xi \rightarrow 0. \quad (9.24)$$

Confirming that  $k = \frac{\omega}{M}$  is indeed a branch point but not a pole when  $r_0 \neq 1 - h$ .

We consider the case that  $r_0 = 1 - h$  in section 9.2.3 and will find that we may identify it with equation (9.22).

## 9.2 Behaviour as $k \rightarrow k_0$

It is worth noting that we only need to consider this limit when  $r_0 \geq 1 - h$ , that is, the source is located in the boundary layer. In addition, we need only consider  $\Delta\tilde{G}_0$  when  $r_0 > 1 - h$  since for  $r_0 = 1 - h$  it is absorbed into  $\Delta\tilde{G}_{\frac{\omega}{M}}$ , we shall also show here that when  $r_0 = 1 - h$  we do not have a pole at  $k = \frac{\omega}{M}$ .

### 9.2.1 Behaviour of the Homogenous Solutions

Consider  $k \rightarrow k_0$  with  $r_0 > 1 - h$ . We have that

$$r_0 - r_c^+ = -\frac{\omega h^2 (k - k_0)}{2Mk_0^2 Q_0} + O((k - k_0)^2), \quad \text{where} \quad Q_0 = h\sqrt{1 - \frac{\omega}{Mk_0}}. \quad (9.25)$$

Hence, in this limit,  $\tilde{p}_1(r_0)$  and  $\tilde{p}_2(r_0)$  may always be evaluated in terms of  $\tilde{p}_{c1}$  and  $\tilde{p}_{c2}$ , as we are always eventually within their radius of convergence. Hence, in this

limit,

$$\tilde{p}_1(r_0) = \left( \frac{-\omega h^2(k - k_0)}{2Mk_0^2 Q_0} \right)^3 + O((k - k_0)^4), \quad \tilde{p}_2(r_0) = 1 + O((k - k_0)^2). \quad (9.26)$$

For  $r \neq r_0$ , the Bessel function, Hankel functions, and  $\tilde{p}_1$  and  $\tilde{p}_2$  all behave as  $O(1)$  quantities when evaluated at  $1 - h$ ,  $r$ , and  $1$ , resulting in  $O(1)$  behaviour for  $C_1, D_1, \check{C}_2, \check{D}_2, \hat{C}_2$  and  $\hat{D}_2$ . It can further be shown that  $A = O(1)$  and

$$W(r_0) = -\frac{3h^4 \omega^2 (k - k_0)^2}{4Q_0^2 M^2 k_0^4} + O((k - k_0)^3). \quad (9.27)$$

### 9.2.2 Behaviour of $\Delta\tilde{G}_0$

Moreover, we may substitute all the above into  $\Delta\tilde{G}_0$ , where,

$$\Delta\tilde{G}_0 = \begin{cases} \Delta\tilde{G}_< & r_0 < r, \\ \Delta\tilde{G}_> & r_0 > r. \end{cases} \quad (9.28)$$

From equations (8.9b) and (8.9c) respectively, and the leading order contribution to  $\Delta\tilde{G}_0$  as  $k \rightarrow k_0$  can be found. First of all, we find the exact expression for  $\Delta\tilde{G}_0$  to be;

$$\Delta\tilde{G}_0 = -\frac{\omega - U(r_0)k}{r_0 W(r_0)} \frac{A\tilde{p}_1(r_0)}{C_1^- \hat{D}_2 - \hat{C}_2 D_1 + 2i\pi A D_1 \hat{D}_2} \times \begin{cases} \hat{D}_2 \psi_1^-(r) & r_0 > r \\ D_1 \psi_2^-(r) & r_0 < r. \end{cases} \quad (9.29)$$

Using asymptotics above, to leading order we find that

$$\Delta\tilde{G}_0 = \frac{A\omega h^2 U(r_0)}{6r_0 M k_0^2 (r_0 - 1 + h)} \frac{(k - k_0)^2}{C_1^- \hat{D}_2 - \hat{C}_2 D_1 + 2\pi i A D_1 \hat{D}_2} \times \begin{cases} \hat{D}_2 \psi_1^-(r) & r_0 > r \\ D_1 \psi_2^-(r) & r_0 < r. \end{cases} \quad (9.30)$$

That is, for  $k = k_0 - i\xi$ ,

$$\Delta\tilde{G}_0 = -\frac{A\omega h^2 U(r_0)}{6r_0 M k_0^2 (r_0 - 1 + h)} \frac{\xi^2}{C_1^- \hat{D}_2 - \hat{C}_2 D_1 + 2\pi i A D_1 \hat{D}_2} \times \begin{cases} \hat{D}_2 \psi_1^-(r) & r_0 > r \\ D_1 \psi_2^-(r) & r_0 < r \end{cases} = O(\xi^2). \quad (9.31)$$

### 9.2.3 The Non-modal Pole at $k = k_0$

When  $r_0 > 1 - h$ , substituting all the above into  $\tilde{G}$  (7.2) (as  $k \rightarrow k_0$  from above) result in

$$\tilde{G}^+(k) = \frac{-2Mk_0^2(\omega - Mk_0)}{3\pi i r_0 h^2 \omega (k - k_0)} \frac{1}{C_1^+ \hat{D}_2 - \hat{C}_2 D_1} \begin{cases} \hat{D}_2 \psi_1(r) & r < r_0 \\ D_1 \psi_2(r) & r > r_0 \end{cases} + O(1), \quad (9.32)$$

confirming a pole at  $k = k_0$ . We Integrate around the non-modal pole;

$$R_0^+(k_0) = \frac{1}{2\pi} \int_{\frac{3\pi}{2}}^{\frac{\pi}{2}} \tilde{G}^+(k_0 + \epsilon e^{i\theta}) e^{-i(k_0 + \epsilon e^{i\theta})x} i \epsilon e^{i\theta} d\theta \quad (9.33a)$$

We make use of the knowledge that  $\tilde{G}^+$  has a simple pole at  $k_0$ , (9.32), in order to make use of the residue formula,

$$Res(f, c) = \frac{1}{2\pi i} \oint_{\gamma} f(z) dz = \lim_{z \rightarrow c} (z - c) f(z) \quad (9.33b)$$

For some anticlockwise contour around  $z = c$  which does not contain any other poles.

Observing that we are considering a clockwise contour we make use of equation (9.32) to give us,

$$R_0^+(k_0) = -2i\pi \lim_{k \rightarrow k_0} \frac{-2Mk_0^2(\omega - Mk_0)e^{-ik_0x}}{6\pi^2 i r_0 h^2 \omega (C_1^+ \hat{D}_2 - \hat{C}_2 D_1)} \begin{cases} \hat{D}_2 \psi_1(r) & r < r_0 \\ D_1 \psi_2(r) & r > r_0 \end{cases} \quad (9.33c)$$

that gives a residue contribution of

$$R_0^+(k_0) = \frac{2Mk_0^2(\omega - Mk_0)e^{-ik_0x}}{3\pi r_0 h^2 \omega (C_1^+ \hat{D}_2 - \hat{C}_2 D_1)} \begin{cases} \hat{D}_2 \psi_1(r) & r < r_0 \\ D_1 \psi_2(r) & r > r_0. \end{cases} \quad (9.34)$$

However if we instead consider  $r_0 = 1 - h$ ,  $k_0 = \frac{\omega}{M}$  equation (7.2) has leading order,

$$\tilde{G}(k) = \frac{-M(k - \frac{\omega}{M})}{2\pi i (1 - h)} \frac{1}{\alpha J'_m(\alpha(1 - h)) \hat{D}_2} \begin{cases} \hat{D}_2 \psi_1(r) & r < 1 - h \\ J_m(\alpha(1 - h)) \psi_2(r) & r > 1 - h \end{cases} + O((k - k_0)^2), \quad (9.35)$$

which does not have a pole, but in fact a zero at  $k = k_0 = \frac{\omega}{M}$ , and can be identified with the case of  $r_0 < 1 - h$  as in section 9.1.3.

### 9.3 Behaviour of $\Delta\tilde{G}_r$ as $k \rightarrow k_r$

Analogously to the derivation above for  $k \rightarrow k_0$ , we consider here the limit  $k \rightarrow k_r$ . In this case, the only difference is that both  $W(r^*)$  and  $(\omega - U(r^*)k)$  remain  $O(1)$  quantities whenever  $r \neq r^*$ , unlike for the limit  $k \rightarrow k_0$ . Otherwise, the same procedure is applicable, with, in particular,

$$r - r_c^+ = -\frac{\omega h^2(k - k_r)}{2Mk_r^2 Q_r} + O((k - k_r)^2), \quad \text{where} \quad Q_r = h\sqrt{1 - \frac{\omega}{Mk_r}}, \quad (9.36)$$

and similarly

$$\tilde{p}_1(r) = \left(\frac{-\omega h^2(k - k_r)}{2Mk_r^2 Q_r}\right)^3 + O((k - k_r)^4), \quad \tilde{p}_2(r) = 1 + O((k - k_r)^2). \quad (9.37)$$

Equation (8.9b) and (8.9c) for  $r > 1 - h$  give  $\Delta G_r$  as

$$\Delta\tilde{G}_r = -\frac{\omega - U(r^*)k}{r^*W(r^*)} \frac{A\tilde{p}_1(r)}{C_1^-\widehat{D}_2 - \widehat{C}_2D_1 + 2i\pi AD_1\widehat{D}_2} \times \begin{cases} D_1\psi_2^-(r_0) & r < r_0 \\ \widehat{D}_2\psi_1^-(r_0) & r > r_0 \end{cases} \quad (9.38)$$

Substituting the above asymptotics into this equation gives

$$\begin{aligned} \Delta\tilde{G}_r \sim & \frac{A(\omega - U(r^*)k_r)\omega^3 h^6}{8r^*W(r^*)M^3k_r^6(r - 1 + h)^3} \frac{(k - k_r)^3}{C_1^-\widehat{D}_2 - \widehat{C}_2D_1 + 2i\pi AD_1\widehat{D}_2} \\ & \times \begin{cases} \widehat{D}_2\psi_1^-(r_0) & r_0 < r \\ D_1\psi_2^-(r_0) & r_0 > r. \end{cases} + O(k - k_r)^4 \end{aligned} \quad (9.39)$$

and we observe  $\tilde{G}_r$  behaves like an order  $\xi^3$  quantity for  $k = k_r - i\xi$ .

#### 9.3.1 The Branchpoint at $k = k_r$

Substituting all the above into (7.2) as  $k \rightarrow k_r$  gives, to leading order,

$$\tilde{G} \sim \frac{\omega - U(r^*)k_r}{2\pi i r^* W(r^*)} \frac{1}{C_1\widehat{D}_2 - \widehat{C}_2D_1} \begin{cases} D_1\psi_2(r_0) & r < r_0 \\ \widehat{D}_2\psi_1(r_0) & r > r_0 \end{cases} = O(1), \quad (9.40)$$

confirming no singular behaviour at  $k = k_r$ , and in particular no pole at  $k = k_r$ .

## 9.4 Far-Field Decay Rates of the Critical Layer Contribution

The critical layer branch cut contribution (8.5) contains integrals  $I_q(x)$  given by (8.8) which are amenable to asymptotic analysis in the limit  $x \rightarrow \infty$ , using the method of steepest descent. Having already deformed the integration contours onto the steepest descent contours, so that the integrands have had their  $x$ -dependent oscillation removed and are now exponentially decaying along the contour, we may directly apply Watson's lemma [Watson, 1918].

If some function  $f(k)$  satisfies  $f(k_q - i\xi) \sim B\xi^\nu + O(\xi^{\nu+1})$  to leading order for small  $\xi$  with  $\nu > -1$ , then Watson's lemma gives us that, for large  $x$ ,

$$\frac{1}{2i\pi} \int_0^\infty f(k_q - i\xi) e^{-i(k_q - i\xi)x} d\xi \sim \frac{B\Gamma(\nu + 1)e^{-ik_q x}}{2i\pi x^{\nu+1}} + O(x^{-(\nu+2)}), \quad (9.41)$$

where  $\Gamma$  is the Gamma function, and in particular,  $\Gamma(\nu + 1) = \nu!$  for integer  $\nu$ . For each of the  $I_q(x)$  integrals, this can then be interpreted as an algebraically decaying wave of phase velocity  $\frac{\omega}{k_q}$ .

As was observed above, for  $k = \frac{\omega}{M} - i\xi$ , as  $\xi \rightarrow 0$  with  $\xi > 0$ , we find that

$$\Delta\tilde{G}_{\frac{\omega}{M}} \sim \begin{cases} \xi^{3/2} & r_0 \leq 1 - h \\ \xi^{5/3} & r_0 > 1 - h. \end{cases} \quad (9.42)$$

By Watson's lemma, this results in a wave convected with the flow speed  $M = U(1 - h)$  and algebraically decaying like  $x^{-\frac{5}{2}}$  when the source is within the region of uniform flow, and  $x^{-\frac{7}{2}}$  for a source located in the sheared flow; the pre-factor in each case is different, and is also governed by the above expressions.

In the case  $r_0 > 1 - h$ , the leading order contribution to  $\Delta\tilde{G}_0$  as  $k \rightarrow k_0$  is given as

$$\Delta\tilde{G}_0 = \frac{A\omega h^2 U(r_0)}{6r_0 M k_0^2 (r_0 - 1 + h)} \frac{(k - k_0)^2}{C_1^- \widehat{D}_2 - \widehat{C}_2 D_1 + 2\pi i A D_1 \widehat{D}_2} \times \begin{cases} \widehat{D}_2 \psi_1^-(r) & r_0 > r \\ D_1 \psi_2^-(r) & r_0 < r. \end{cases} \quad (9.43)$$

By Watson's lemma, this results in a wave convected with the flow speed at the point source,  $U(r_0)$ , and decaying algebraically like  $x^{-3}$ .

Finally, considering  $\Delta\tilde{G}_r$  as  $k \rightarrow k_r$ ,

|              | $I_{\frac{\omega}{M}}$ |                    | $I_r$       | $I_0$         |
|--------------|------------------------|--------------------|-------------|---------------|
|              | $r_0 \leq 1 - h$       | $r_0 > 1 - h$      | $r > 1 - h$ | $r_0 > 1 - h$ |
| Swinbanks    | –                      | –                  | –           | $x^{-3}$      |
| Linear BL    | $x^{-4}$               | $x^{-5}$           | $x^{-4}$    | $x^{-3}$      |
| Quadratic BL | $x^{-\frac{5}{2}}$     | $x^{-\frac{7}{2}}$ | $x^{-4}$    | $x^{-3}$      |

Table 4: Comparison of the different decay rates given for a general flow profile by Swinbanks [1975] and for a linear boundary layer flow profile by Brambley et al. [2012a] against those given here for a quadratic boundary layer flow profile.

$$\Delta\tilde{G}_r \sim \frac{A(\omega - U(r^*)k_r)\omega^3 h^6}{8r^*W(r^*)M^3k_r^6(r-1+h)^3} \frac{(k - k_r)^3}{C_1^- \hat{D}_2 - \hat{C}_2 D_1 + 2i\pi A D_1 \hat{D}_2} \times \begin{cases} \hat{D}_2 \psi_1^-(r_0) & r_0 < r \\ D_1 \psi_2^-(r_0) & r_0 > r. \end{cases} \quad (9.44)$$

By Watson’s lemma, this results in a wave convected with the flow speed  $U(r)$  and decaying algebraically like  $x^{-4}$ .

We now proceed to compare these results with previous literature.

#### 9.4.1 Comparisons with Previous Far-Field Scalings

Our results for the large- $x$  decay of the various components of the critical layer are compared to those predicted by Swinbanks [1975] for a general flow profile, and those predicted by Brambley et al. [2012a] for a constant-then-linear flow profile, in table 4. The  $I_0$  integral gives a wave with phase velocity equal to that of the mean flow at the location of the point mass source,  $U(r_0)$ , provided the point mass source is in a region of sheared flow,  $r_0 > 1 - h$ . It can be observed in table 4 that agreement is seen in all three works for  $r_0 > 1 - h$ . While Swinbanks did not consider the other cases in detail, this work finds further agreement for the  $I_r$  contribution with Brambley et al.. In both the linear and quadratic shear flow cases, when the source is located within the region of sheared flow, the  $I_0$  contribution is the slowest decaying term. When the source is located within the uniform flow region, the  $I_{\frac{\omega}{M}}$  contribution is the slowest decaying term, although this is matched by  $I_r$  contribution for linear shear. It should be noted, however, that when  $r_0 > 1 - h$  we have in addition the contribution of the non-modal  $k_0$  pole, which does not decay. It may additionally be observed that there is a discrepancy between the decay rates of the wave travelling with phase velocity equal to that of the uniform flow region between the linear and quadratic boundary layer profiles with each case differing by a factor of  $x^{-\frac{3}{2}}$ . This difference can be understood as coming from two factors. The

first is a result of the boundary layer how the factor  $Q$  scales in terms of  $k - \frac{\omega}{M}$ , and additionally on the factor  $A$  which has leading order depending on the second derivative of the flow profile. More information on this is given in section 26.1.1.

## 10 Pole Locations

Within this section we will cover the material contained with [King et al., 2022, section 4.2], although the plots produced are unique to this work, and were not all present within the cited paper.

As previously discussed there are several factors that contribute to the Fourier inversion of the Green's function, namely the modal poles, and the critical layer branch cut. For a selection of the parameter sets given in table 3 the locations of the poles in the complex  $k$  plane and the critical layer branch cut are plotted in figure 8. In addition to the usual acoustic modes (denoted as  $\times$  in figure 8), at least one  $k^+$  is found for each parameter set. For parameter sets  $A3, B1, B4, C1$  and  $D2$ , the  $k^+$  pole is located behind the critical layer branch cut, and so would not be found using conventional numerical methods, although the  $k^+$  pole does still contribute to the total pressure field through the critical layer branch cut contribution, as described in section 8.3 above. In contrast, for parameter sets  $A1$  and  $D3$ , the  $k^+$  pole is not behind the branch cut and takes the form of a standard modal pole, in this case a hydrodynamic instability surface wave. The stability of the modal poles is verified from the movement of the poles in the  $k$  plane as  $\text{Im}(\omega)$  is decreased from zero, following the Briggs-Bers criterion. Equivalent tracks indicating the unstable behaviour are shown for parameter sets  $E1, F1$  and  $G3$  in figure 9, where the equivalent pole locations may also be observed. Finally in the cases of parameter sets  $C2, E4$  and  $F4$ , two  $k^+$  poles are observed, while only one acts as a hydrodynamic instability mode. As the imaginary part of  $\omega$  is varied the other mode merges with the other acoustic modes. As will be observed later in section 12.2, these modes may become unstable as the other system parameters are varied, and so are associated with the hydrodynamic instability. In fact it can be further observed that the presence of these modes suggests the potential of absolute instability in the time domain, with the two  $k^+$  poles colliding and forming a double root as  $\text{Im}(\omega)$  is varied. This will not be further investigated however in this work.

Note that the critical layer branch cut also moves as a function of  $\text{Im}(\omega)$ . Of particular note is that  $k^+$  poles, hidden behind the critical layer branch cut, may emerge from behind the critical layer branch cut as  $\text{Im}(\omega)$  is reduced from zero, becoming a standard modal pole provided  $\text{Im}(\omega)$  is taken sufficiently negative. The effect of this,

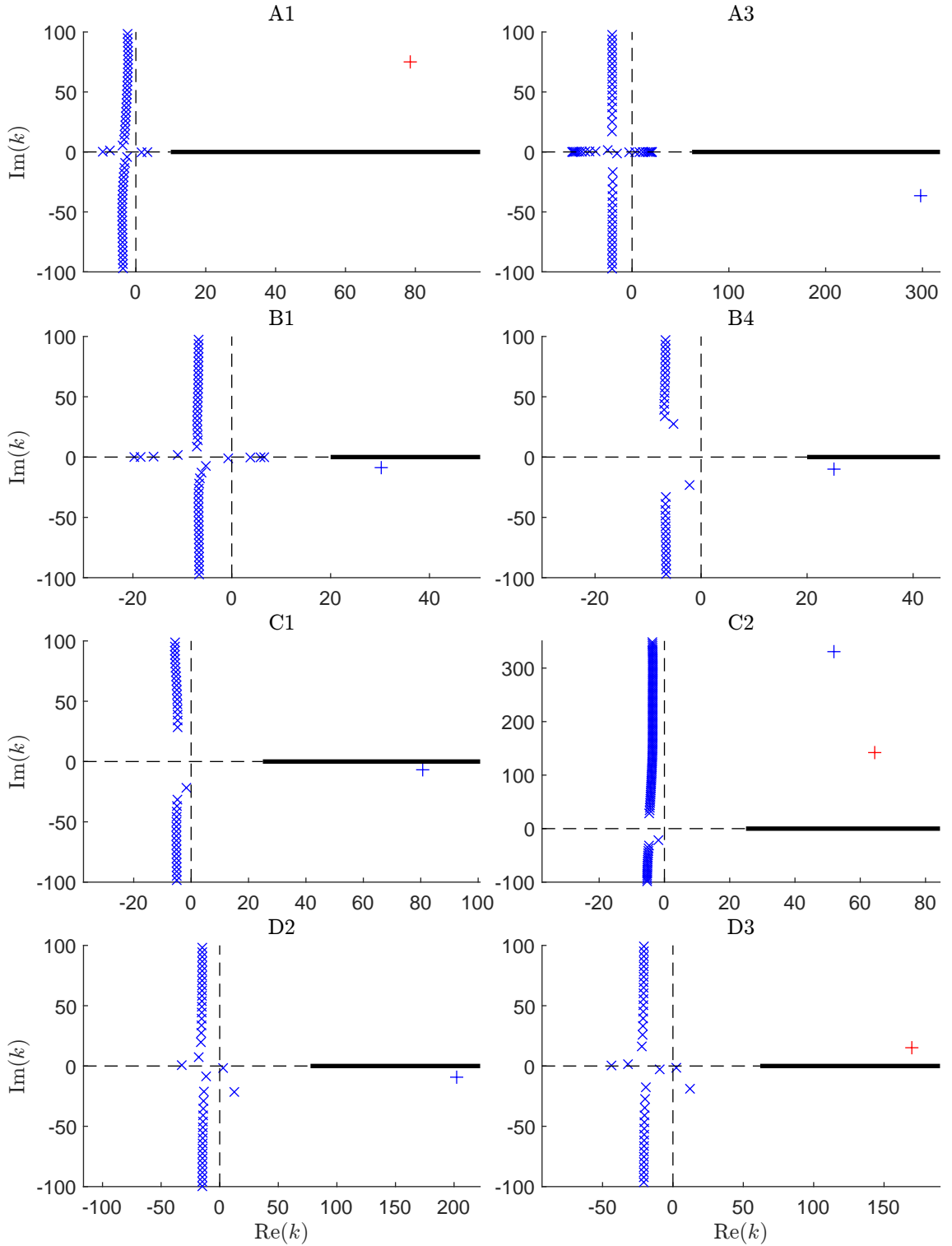


Figure 8: Location of the poles in the complex  $k$  plane for two sub-parameter sets from each of the parameter sets A-D. The usual acoustic modal poles have been marked with an ( $\times$ ). The critical layer branch cut, ( $-$ ), and any  $k^+$  modal poles ( $+$ ). Modes that are coloured red are unstable under the Briggs-Bers criterion. Stable  $k^+$  modes located in the lower half plane are ‘hidden’ behind the branch cut.

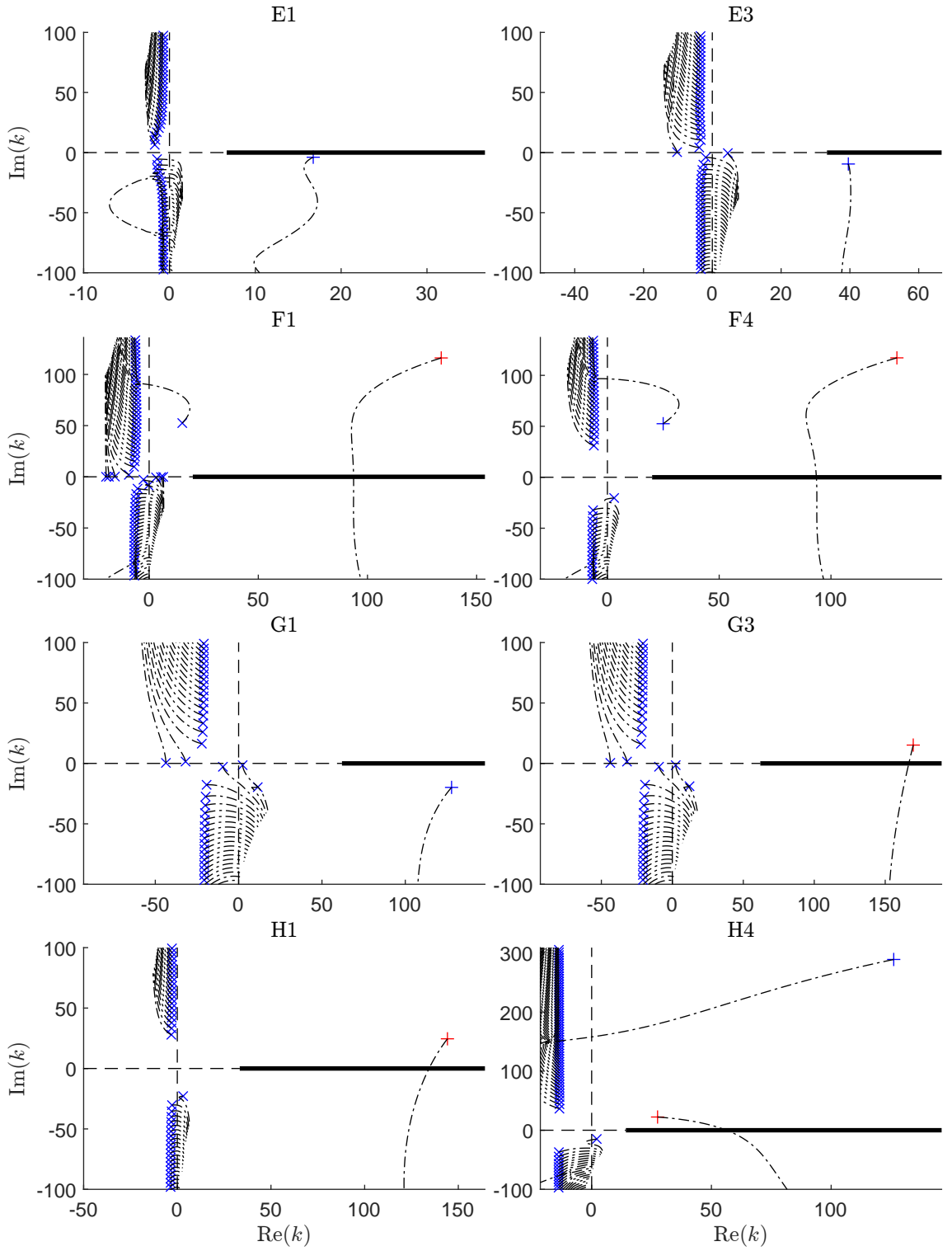


Figure 9: Location of the poles in the complex  $k$  plane for two sub-parameter sets from each of the parameter sets  $E - H$ . As figure 8 with the Briggs-Bers trajectories as  $\text{Im}(\omega)$  is varied from 0 to  $-50$  ( $- \cdot -$ ), with locations at  $\text{Im}(\omega) = 0$  marked as a pole.

however, does not impact the overall Fourier inversion contour or the contribution of the critical layer branch cut or  $k^+$  pole. How this occurs will in addition vary based on the model being used for the Impedance  $Z$ , which is also a function of the frequency  $\omega$ .

As discussed in section 8.3, when a  $k^+$  pole is located above the branch cut it may be unstable, with a contribution growing exponentially in  $x$ . In general we only observe one  $k^+$  pole above the critical layer branch cut, which is always unstable. However, in some cases there may be two  $k^+$  poles present, only one of which is observed to unstable for any particular parameter set. When the  $k^+$  pole is located below the critical layer branch cut (noting that in all observed cases there is only one such  $k^+$  mode, with no  $k^+$  above the critical layer branch cut) we do not see its contribution to the modal sum directly. Instead it contributes as part of the branch cut integral, as seen when deforming onto the steepest descent contour. In this latter case, we would observe a contribution that decays in  $x$ . For each parameter set investigated, in addition to the modal poles, as plotted in figures 8 and 9, there also exists a  $k^-$  pole located above, and behind, the critical layer branch cut and so does not contribute towards the Fourier inversion. In the event that any  $k^-$  poles were located below the branch cut, its contribution would almost exactly cancel the critical layer branch cut contribution, again seen by deforming onto the steepest descent contour. This pole has not been included in these plots due to its absence from the Fourier inversion.  $k^-$  poles located below the critical layer branch cut, despite not being seen here, were observed in the case of a linear shear boundary layer profile, which is investigated further in section 11.2 below.

Each mode, hidden behind the branch cut or otherwise, has an associated mode shape. This can be considered as the solution  $\tilde{\psi}_1(k, r)$ , for each fixed  $k$ . A selection of these are plotted in figure 10. From figure 10 the behaviour of the  $k^+$  pole as a surface mode can be observed, with a contribution contained near the duct wall at  $r = 1$ .

When the  $k^+$  pole is located behind the branch cut its mode shape contains a discontinuity at  $r = \text{Re}(r_c^+(k^+))$ , although this can not be observed in figure 10, since the jump is small and contained near the wall. The Jump in  $\tilde{\psi}_1(k^+, r)$  is not seen in the final Fourier inversion as an equal and opposite jump is contained within the integral  $I_r$ . This may be observed in figure 11, particularly for parameter sets B1 and E4, although is still present whenever the  $k^+$  pole is located behind the critical layer branch cut.

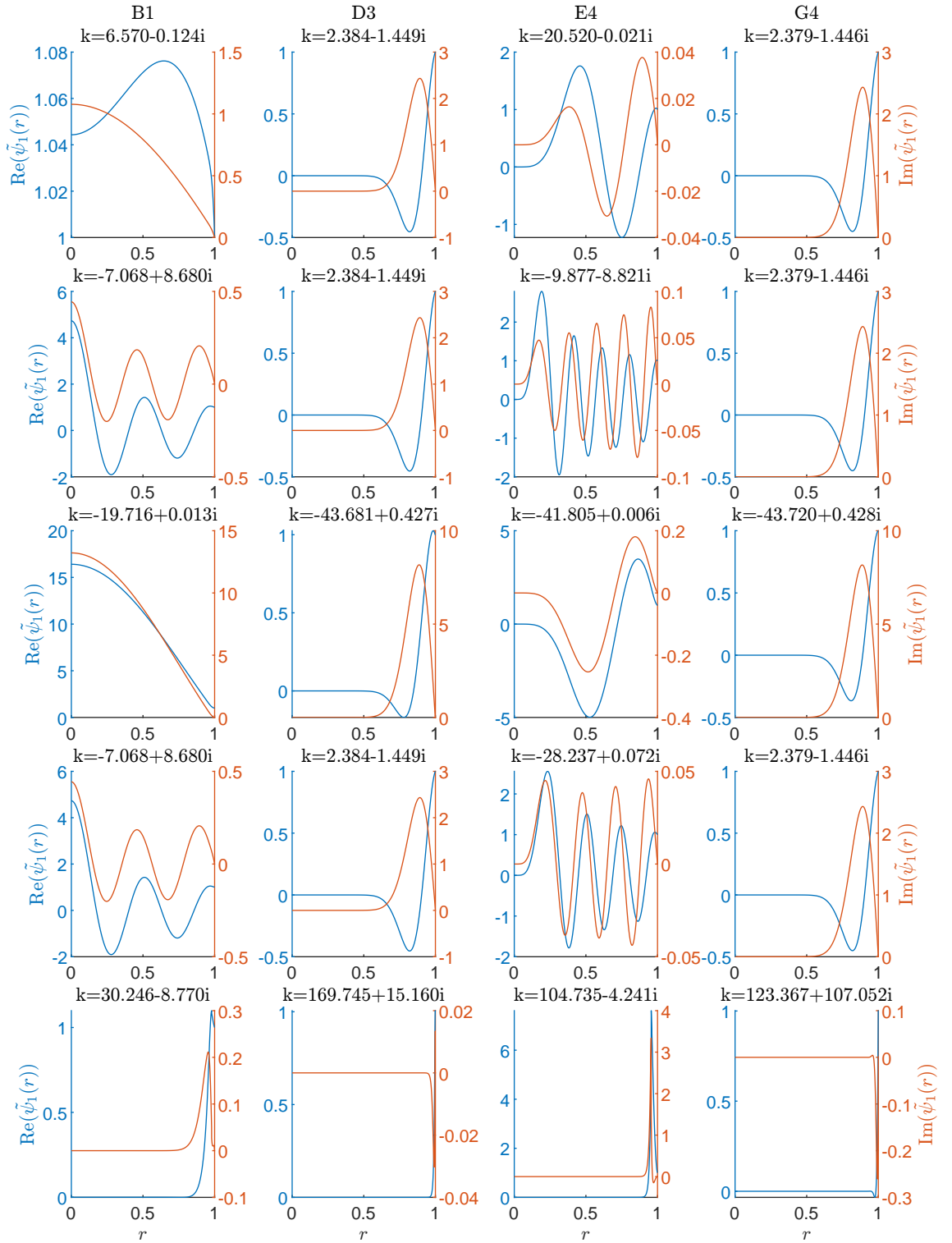


Figure 10: The mode shapes of five modes from parameter sets  $B1$ ,  $D3$ ,  $E4$  and  $F4$ . Rows 1 and 2 show the mode shapes for upstream propagating, ( $x < 0$ ), modes, Rows 3,4,5 show the mode shapes for downstream propagating ( $x > 0$ ) modes, with the bottom row (5) illustrating the mode shape of either unstable ( $D3$  and  $F4$ ) or hidden ( $B1$  and  $E4$ )  $k^+$  surface modes. The first and third rows correspond to the acoustic mode with the smallest imaginary part.

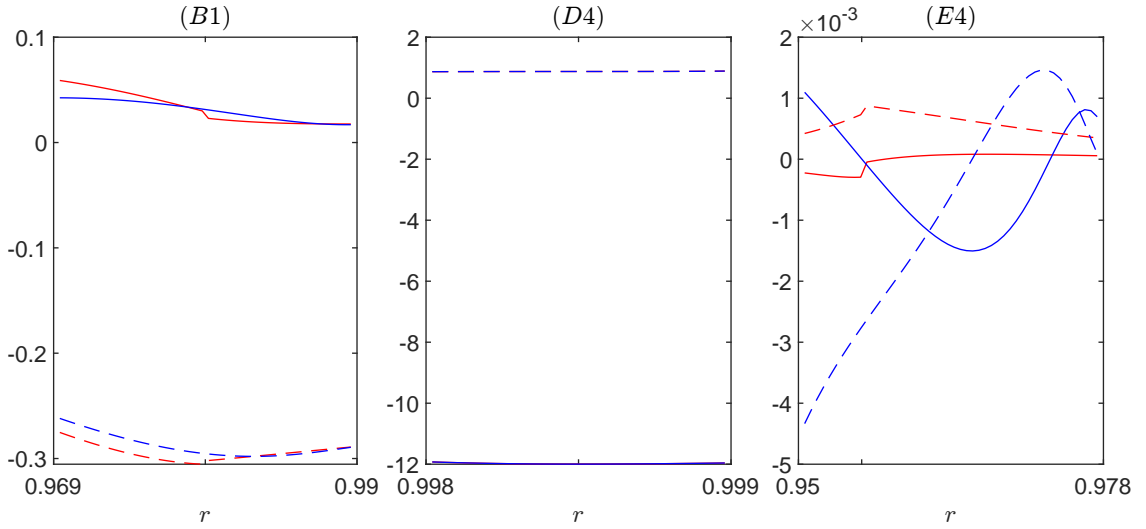


Figure 11: Plotting the real (solid lines), and imaginary part (dashed lines), of the residue of the stabilised  $k^+$  pole,  $R^+(k^+)$  (red) and  $R^+(k^+) + I_r$  (blue) for parameter sets  $B1$ ,  $D4$  and  $E4$ . This is plotted for  $r_0 = 1$ ,  $x = 0.1$ , for  $r$  values near the discontinuity.

## 11 Fourier Inversion Contributions

Within this section we will cover the material contained with [King et al., 2022, section 4.2-4.3], although the plots produced are unique to this work, and were not all present within the cited paper.

### 11.1 Branch Cut Contributions

Figure 12 illustrates the differences between the three types of contributions occurring due to the presence of the boundary layer: the three steepest descent contour integrals (figure 12(i)); the  $k_0$  non-modal pole (figure 12(ii)); and the  $k^+$  modal pole when it is located below the branch cut and therefore does not appear in the modal sum (figure 12(iii)). From each of the parameter sets, the far-field behaviour will be dominated by the  $k_0$  non-modal pole for larger values of  $x$ , as can be seen by looking for similarities between rows (ii) and (iv) which plots the sum of the three terms. Although in each case the  $k^+$  hidden modal pole, which is present for all three of the parameter sets given, may be comparable in size, or larger than the contribution of the  $k_0$  non modal pole. This can particularly be seen for parameter set C4, where the behaviour near the duct wall is nearly identical between rows (iii) and (iv), with the  $k_0$  pole becoming comparable near  $r = 0.9$ . For that particular case the  $k^+$  pole is 'nearly cut-on'. For smaller values of  $x$  by comparing rows (i), (ii) and (iv) it can additionally be observed that the three steepest descent are comparable to the stabilised  $k^+$ , or larger, such as for parameter set B4, while for both parameter sets B4 and H2, the decaying behaviour of the steepest descent contours and the  $k^+$

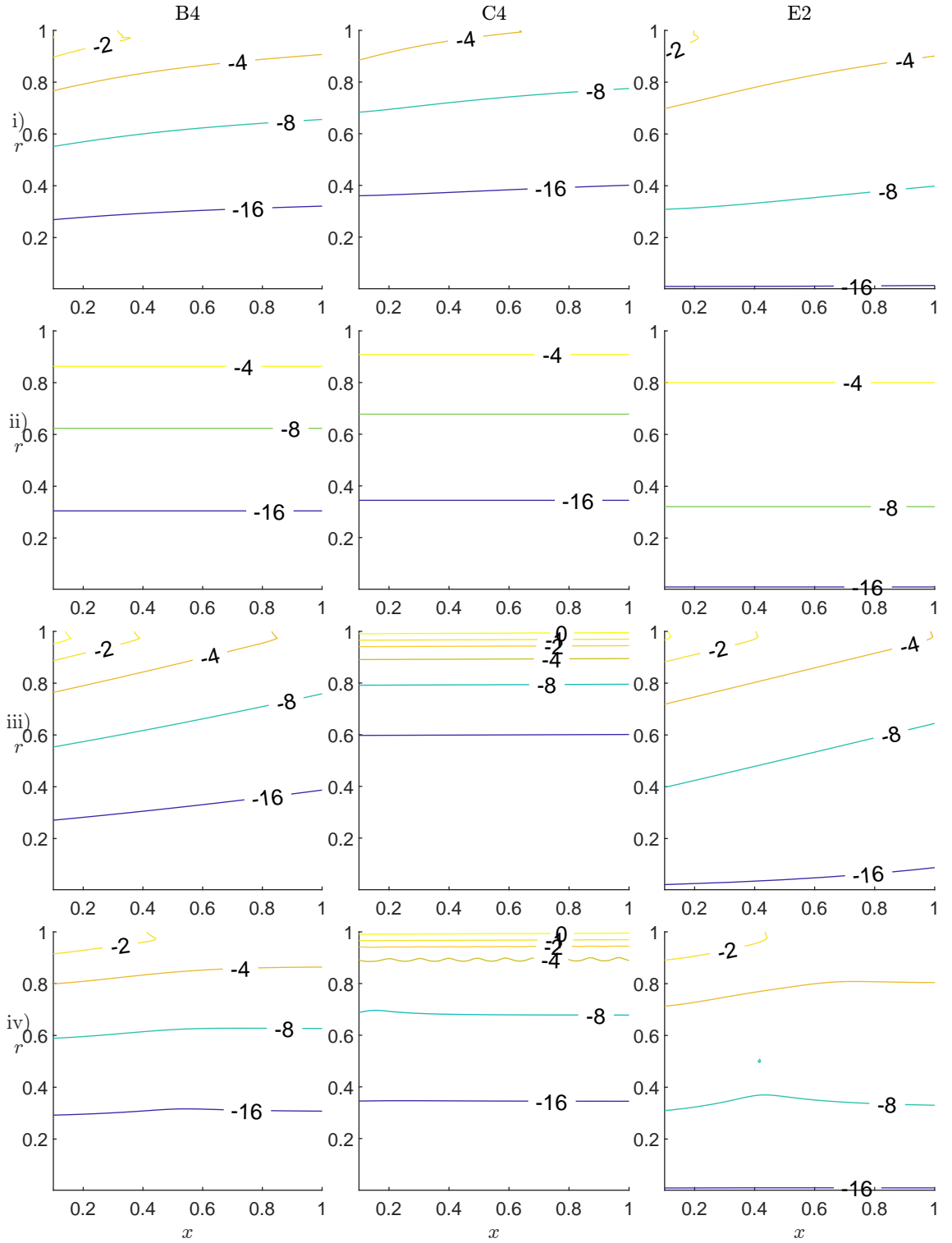


Figure 12: A comparison of the terms that contribute to the critical layer, for  $r_0 = 1 - \frac{4h}{5}$ . Plotted are the absolute values on a  $\log_{10}$  scale. Left to right: parameter sets  $B4, C4$  and  $E2$ . Top to bottom: (i) the sum of the three steepest descent contours,  $I_{\frac{\omega}{M}} + I_r + I_0$ ; (ii) the non-modal  $k_0$  pole; (iii) the contribution of the  $k^+$  pole located behind the branch cut; and (iv) the total contribution from integrating around the critical layer branch cut, obtained by summing (i)–(iii).

modal pole can clearly be seen within the full contribution.

It should be noted that unlike the modal poles and the other contributions, the behaviour of the  $k_0$  non-modal pole will extend into the far-field. With all other terms decaying, either exponentially, albeit with a small exponent for the ‘nearly cut-on’ modes, or algebraically for the three steepest descent contours. So when we have a stable  $k^+$  pole hidden behind the critical layer branch cut, the  $k_0$  non-modal pole will be the dominant contribution to the far-field.

Since this  $k_0$  pole will dominant for stable  $k^+$  but varies with  $r_0$  we can further look at how these contributions as the location of the source is adjusted, shown in figure 13. The contribution of the critical layer branch cut may be seen to increase as  $r_0$  increases, as can be observed by observing down each of the rows. This is particularly true for the  $k_0$  non-modal pole, which is only present in rows (iii) and (iv), having a zero contribution otherwise. Although the stability can be observed in row (iii), see parameter sets *C3* and *E3*, in row (iv) the non-modal pole dominates the contribution, with an amplitude comparable to the that of the sound source. Additionally, the effects of the surface modes are being felt further away from the wall as  $r_0$  approaches the duct wall although the contribution continues to decay radially. Note that although *C3* (i) appears blank the contributions of the critical layer branch cut are still present, however they are smaller than  $10^{-6}$  in magnitude and so have not been included, further highlighting that the growth of the critical layer branch cut can be observed even for  $r_0 < 1 - h$ . Finally, comparing rows (iii) and (iv) we can additionally observed the increasing phase velocity  $\frac{\omega}{U(r_0)}$ .

Figure 14 compares the numerically-computed steepest descent integrals with their predicted far-field rates of decay given in section 9.4, although we have not included the corresponding pre-factors. In each case a good agreement can be seen, particularly for the larger values of  $x$ . Note that for  $r_0 < 1 - h$  we would have also retrieved that  $|I_0| = 0$  for any value of  $r$ , while the decay rates of  $|I_r|$  would remain the same.

## 11.2 Full Fourier Inversion

We now consider the full Fourier inversion, including the contribution from all the modal poles as well as the critical layer branch cut contribution considered above. Figure 15 compares a snapshot in the near-field (for small  $x$  values) of the wave field generated by only the stable modal poles (left) with the full solution including the critical layer and any unstable  $k^+$  pole (right). The unstable mode may only be observed in parameter set *F1* of the parameter sets plotted in figure 15. When the  $k^+$  pole is a hydrodynamic instability it clearly dominates the solution sufficiently far downstream, as it grows exponentially in  $x$ . Additionally, the contribution of this unstable mode is felt further away from the duct wall, despite the hydrodynamic

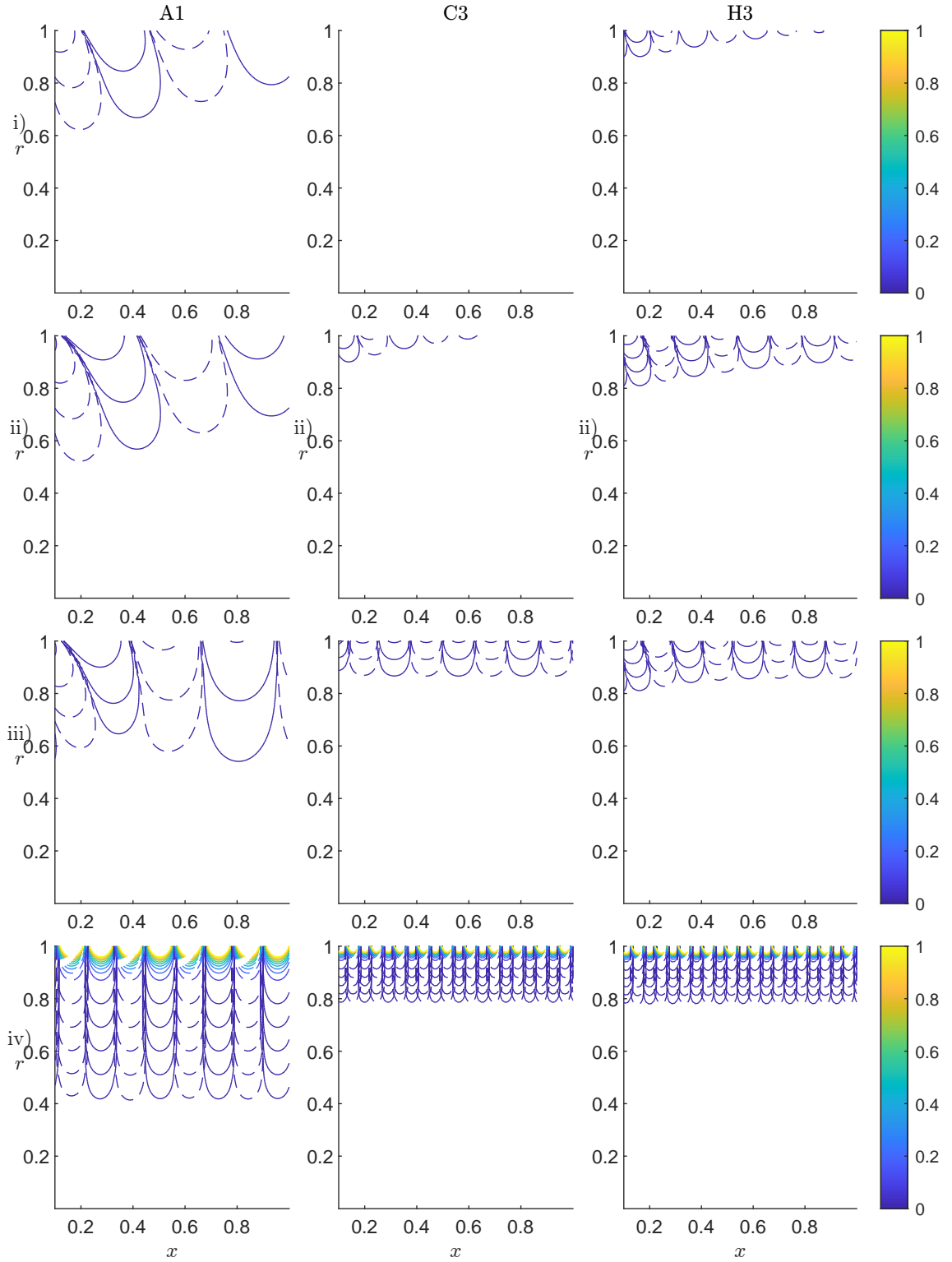


Figure 13: Plots of the real part of the contribution from integrating around the branch cut ( $\text{Re}(p(x, r))$ ) for parameter sets  $A1$ ,  $C3$ ,  $H3$ . Each of these parameter sets do not have a  $k^+$  pole behind the branch cut. Solid lines indicate positive values, dashed lines indicate negative values. i):  $r_0 = 1 - 2h$ ; ii):  $r_0 = 1 - \frac{11h}{10}$ ; iii):  $r_0 = 1 - \frac{9h}{10}$ ; iv):  $r_0 = 1 - \frac{h}{5}$ .

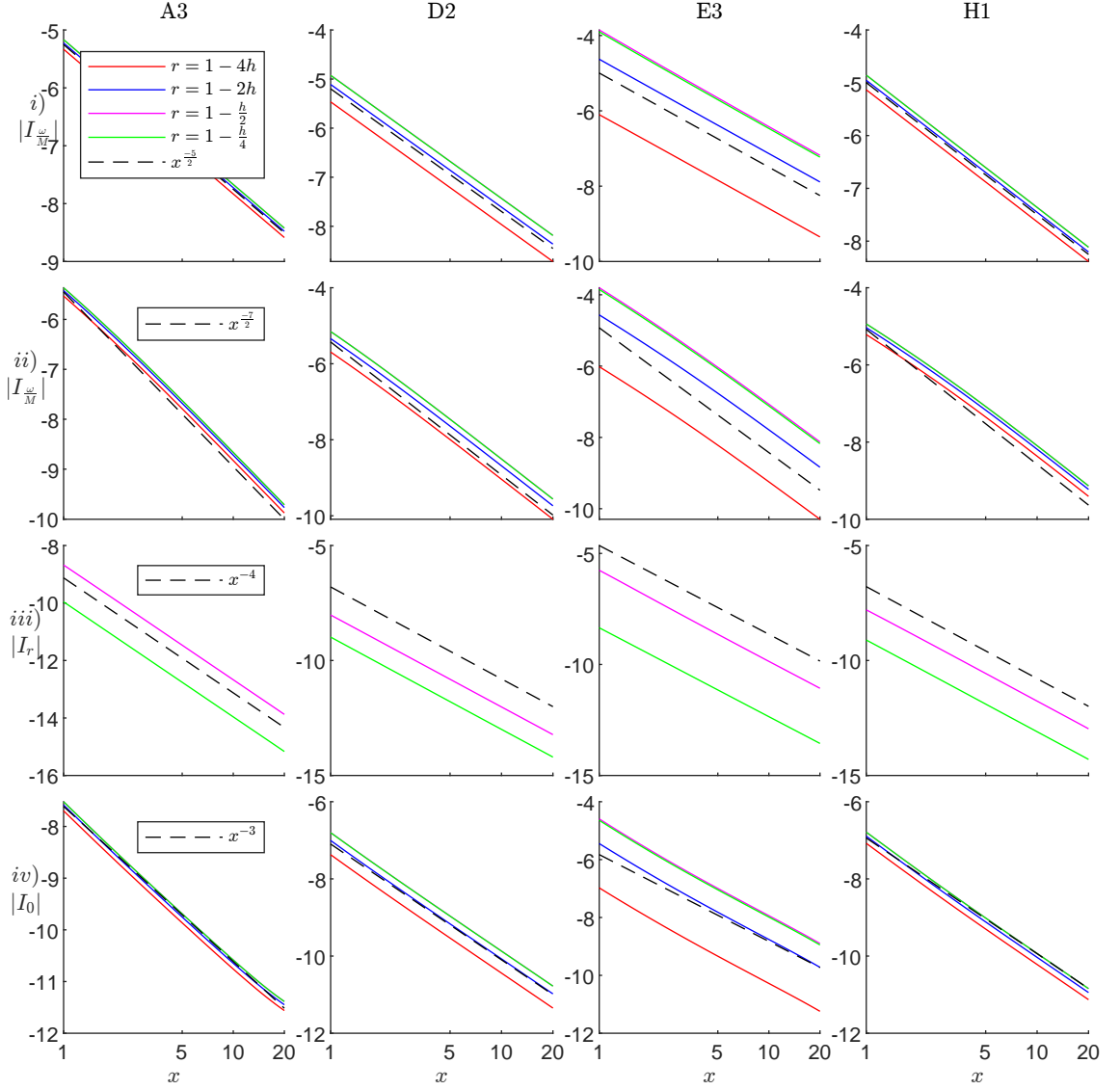


Figure 14: Plotted for parameter sets  $A3$ ,  $D2$ ,  $E3$  and  $H1$  are the three steepest descent contours  $|I_{\frac{\omega}{M}}|$  (i) and (ii),  $|I_r|$  (iii), and  $|I_0|$  (iv), under a  $\log_{10}$  scale. The point mass source is located at  $r_0 = 1 - \frac{11h}{10}$  (i) and  $r_0 = 1 - \frac{4h}{5}$  (ii-iv). Solid lines correspond to radial locations  $r = 1 - 4h, 1 - 2h, 1 - \frac{h}{2}$ , and  $1 - \frac{h}{4}$ . The dashed line is the predicted far-field rate of decay. Note that for  $r < 1 - h$ ,  $|I_r| = 0$  and so these ‘decay rates’ are not given.

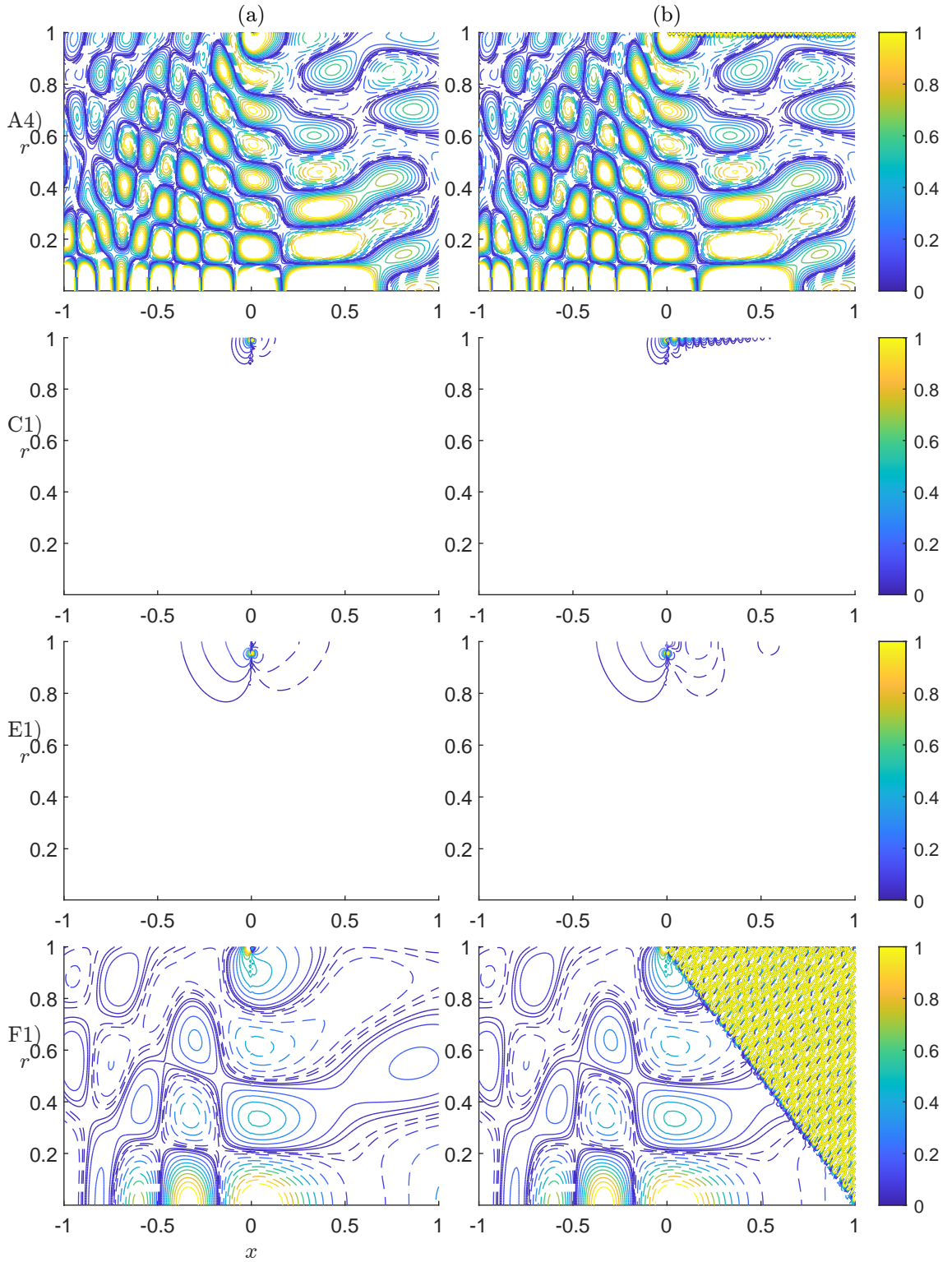


Figure 15: Plotting the real values of the different contributions. (a) just the contribution for the stable modal poles. (b) the full Fourier inversion, which also includes the  $k^+$  pole. The parameter sets used from top to bottom are  $A4$ ,  $C1$ ,  $E1$  and  $F1$ , with  $r_0 = 1 - \frac{4h}{5}$  in each case. In case  $F1$ , the  $k^+$  pole is a convective instability. In cases  $A4$ ,  $C1$  and  $E1$ , the  $k^+$  pole is located behind the branch cut.

instability otherwise being a surface mode. In these near-field plots, the critical layer often appears negligible compared with the modal sum, as can be observed away from the duct walls within each of the plots, various other effects may be observed: For parameter set *C1* the critical layer is comparable in size in the near field. While for parameter sets *A4* and *F1* we instead observe the critical layer dominating the behaviour near the wall, with the effects being much longer lived in the case of parameter set *A4*. Note that these effects would only be increased as  $r_0$  is increased, although this is not plotted here, instead we refer the reader back to figure 13.

In comparison, figure 16 shows the behaviour outside the near field for four additional stable cases. Plotting the amplitude of oscillations  $|p|$  on a logarithmic scale. In all cases, since the modal sum decays exponentially, in the far field the dominant contribution is from the critical layer. For parameter set *B3* this may be observed as early as two radial distances down from the sound source. For parameter set *D4* in the region 0 plotted we do not observe either the modal poles or the non-modal pole in the full Fourier Inversion plot, rather we are seeing the effects of the nearly cut on  $k^+$  pole located behind the branch cut. Although in both this case and for parameter set *H3* where the modal sum is felt further into the duct, it remains true that this will indeed decay to leave only the effects of the non-modal pole which are neutrally stable.

Throughout this section it can be observed that the change in nature of the  $k^+$  pole in the case of a quadratic sheared flow from a hydrodynamic instability to being stable and contributing as part of the critical layer branch cut is clearly of significant importance. With consequences not just limited to the far-field but rather throughout the length of the duct. We will, therefore, consider the variation of the solution as various parameters of interest are varied within the next section.

## 12 The Critical Layer and the Stabilising of the $k^+$ Surface Mode

The contained within the following section as previously been presented in light detail within [King et al., 2022, section 4.4] and was covered in similar detail to that presented here within [King and Brambley, 2022]. All of the plots given have been reproduced specifically for the purpose of this thesis highlighting additional behaviours. Additionally, section 12.3 has not been previously presented within any work published or unpublished.

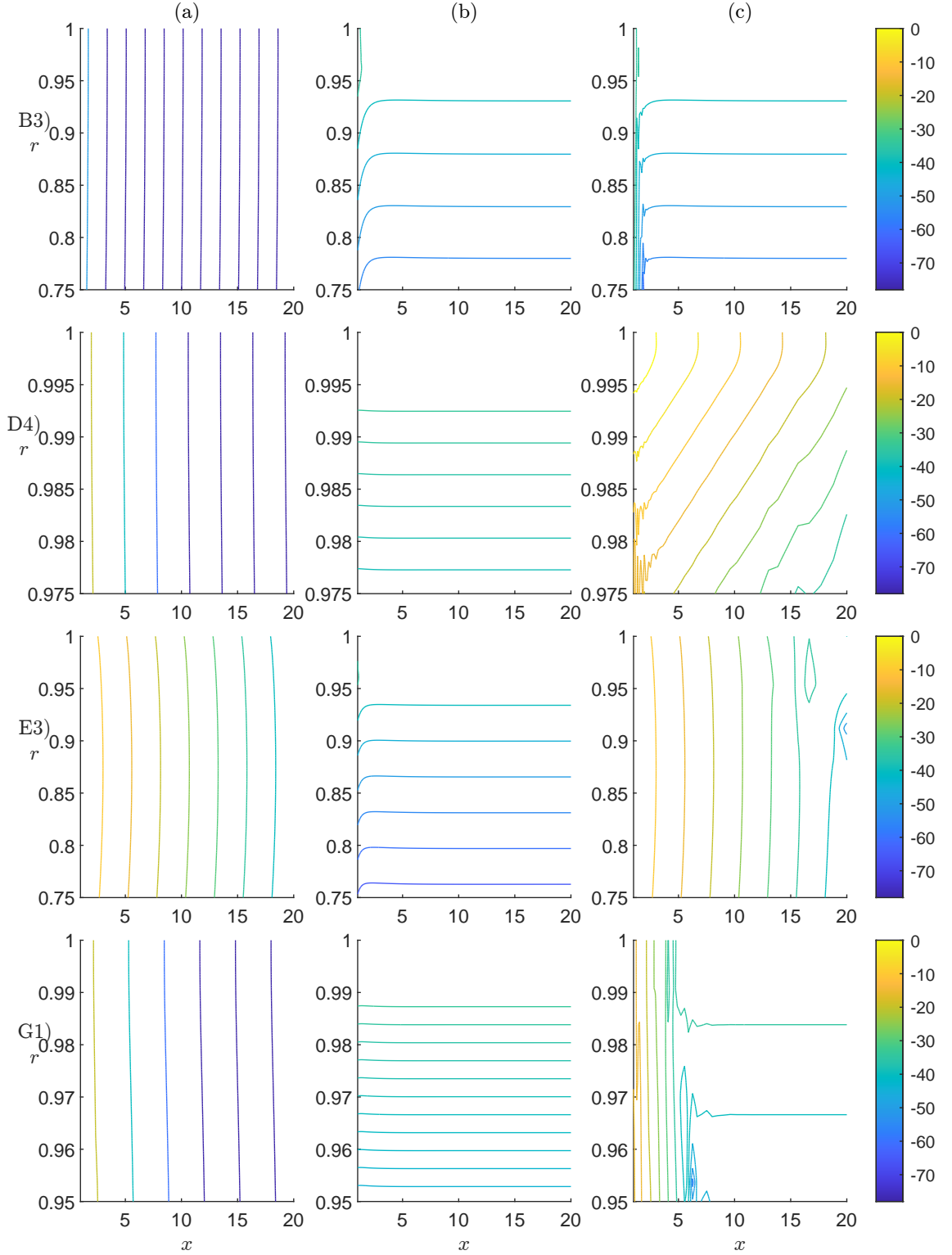


Figure 16: The absolute value of pressure on a log scale ( $10 \log_{10}(|p|)$ ) over a longer range of axial distances downstream of the point source. (a) just the contribution for the modal poles. (b) modal poles plus the three steepest descent contours and the  $k_0$  non-modal pole. (c) the Full Fourier Inversion, which also includes the  $k^+$  pole. The parameter sets used from top to bottom are  $B3$ ,  $D4$ ,  $E3$  and  $G1$ , with  $r_0 = 1 - \frac{4h}{5}$  in each case. In each case, the  $k^+$  pole is located behind the branch cut.

## 12.1 Poles of $\tilde{G}^+$ .

When Fourier inverting  $\tilde{G}$  we sought its poles, which occur as zeros of the denominator typically satisfying

$$C_1\hat{D}_2 - \hat{C}_2D_1 = 0 \quad (12.1)$$

We have observed that the  $k^+$  pole can be tracked through the critical layer branch cut occurring not as a pole of  $\tilde{G}$  but  $\tilde{G}^+$  solving;

$$C_1^-\hat{D}_2 - \hat{C}_2D_1 + 2i\pi AD_1\hat{D}_2 = 0. \quad (12.2)$$

When this occurs it has been seen that the resulting contribution is one that is stable and incorporated with the critical layer. This is of particular interest because it further implies that the pressure perturbation is either stable or neutrally stable in the far-field, depending only if the point mass source is located within the sheared flow. In addition to this in this process the far-field behaviour is no longer dominated by the exponentially growing hydrodynamic instability, and instead may be dominated by either the critical layer branch cut or the model poles. As can be observed by examining the parameter sets of table 3, in comparison to the pole plots given in figures 8 and 9, this stability can be achieved by any combination of: The frequency  $\omega$ , parameter sets  $A$  and  $H$ ; the centreline Mach number  $M$ , parameter sets  $D$  and  $E$ ; or the boundary layer thickness,  $h$ , parameter sets  $C$  and  $G$ .

We note that while the azimuthal wave number  $m$ , may also have an effect on stability, since this parameters can not be deformed continuously, we will not investigate its variation here.

## 12.2 Parameter Studies of the Hydrodynamic ‘Instability’

We aim to examine the location of the  $k^+$  poles in order to identify when it may or may not be an instability. Within applications a system will often be studied for a specific frequency, Mach number, azimuthal wavenumbers, and impedance, with these features being defined by the experimental situation that has been constructed. With the frequency often being prescribed, the Mach number given by the flow speed, the dominant azimuthal wave mode from the number of rotor blades and the impedance fixed for a given lining. The boundary layer thickness however, although likely effected by the flow speed and the wall lining, is left largely unknown, typically assumed to be ‘thin.’ In [Brambley and Gabard, 2016, Khamis and Brambley, 2016] this is  $h = 0.001$ , while in [Rienstra and Darau, 2011], which investigates effects of thin boundary layers,  $h$  is called ‘small enough’ for  $h \simeq 10^{-6}$  or even  $h = 0.2$ , while [Spillere et al., 2020] gives boundary layer thickness experimentally predicted

around 0.2, but ranging, between  $h = 0.4$  and 0 depending on the frequency. For this reasons we will begin our parameter study by observing the effects of varying the boundary layer thickness. In sections 12.2.2-12.2.4 we will then use the results for boundary layer thickness when considering the Mach number  $M$ , frequency,  $\omega$  and impedance,  $Z$ , as a reference frame to make more general statements about the location of the  $k^+$  pole, and what to seek when aiming to capture specific behaviours.

### 12.2.1 Variation of the Boundary Layer Thickness $h$

We seek to understand how the location of the  $k^+$  pole varies as we vary the boundary layer thickness  $h$  which can take values in  $(0, 1)$ . When running numerical code, having found the  $k^+$  poles for a specific parameter set, we can vary the boundary layer thickness and track how the location varies. Tracking the poles in this way gives plots seen in figure 17. In each case it can be observed that as we increase the boundary layer thickness the  $k^+$  modal pole crosses the critical layer branch cut and becomes stable, with the  $k^+$  pole tending towards the end of the branch cut,  $\frac{\omega}{M}$ , as  $h$  becomes large. In addition to this, in the cases where two potential  $k^+$  poles are present, parameter sets *E3* and *F1* it is observed that as the boundary layer is increased the other stable modal pole moves into the usual modal poles reducing the problem to only a single pole.

Observing that in each case that there exists only one value of  $h \in (0, 1)$  such that the  $k^+$  pole is located on the critical layer, we can define  $h_c$  to be this value of boundary layer thickness. It can be noted that the value of  $h_c$  is continuous in each of the other system parameters. Additionally defining  $h_c$  in this way means the study of a specific parameter sets stability can be reduced to finding the value of  $h_c$  and comparing it to the given boundary layer thickness. That is, if  $h < h_c$  the system is at most neutrally stable, and if  $h > h_c$  the system contains a hydrodynamic instability and is unstable.

When  $h = h_c$  and the  $k^+$  pole is located on the critical layer branch cut there are three features that must be considered. Firstly, the  $k^+$  pole would in this case be neutrally stable and will contribute into the far-field. In addition to this, the  $k^+$  pole will interact with the  $k_r$  branch point for a fixed value of  $r$  in the boundary layer with the resulting  $I_r$  decay rate likely varying. Similarly the  $k^+$  pole would be able to interact with the non-modal pole  $k_0$  when the source is located in the shear layer, with the resulting pole no longer being simple. As of yet this case has not been investigated in any further detail.

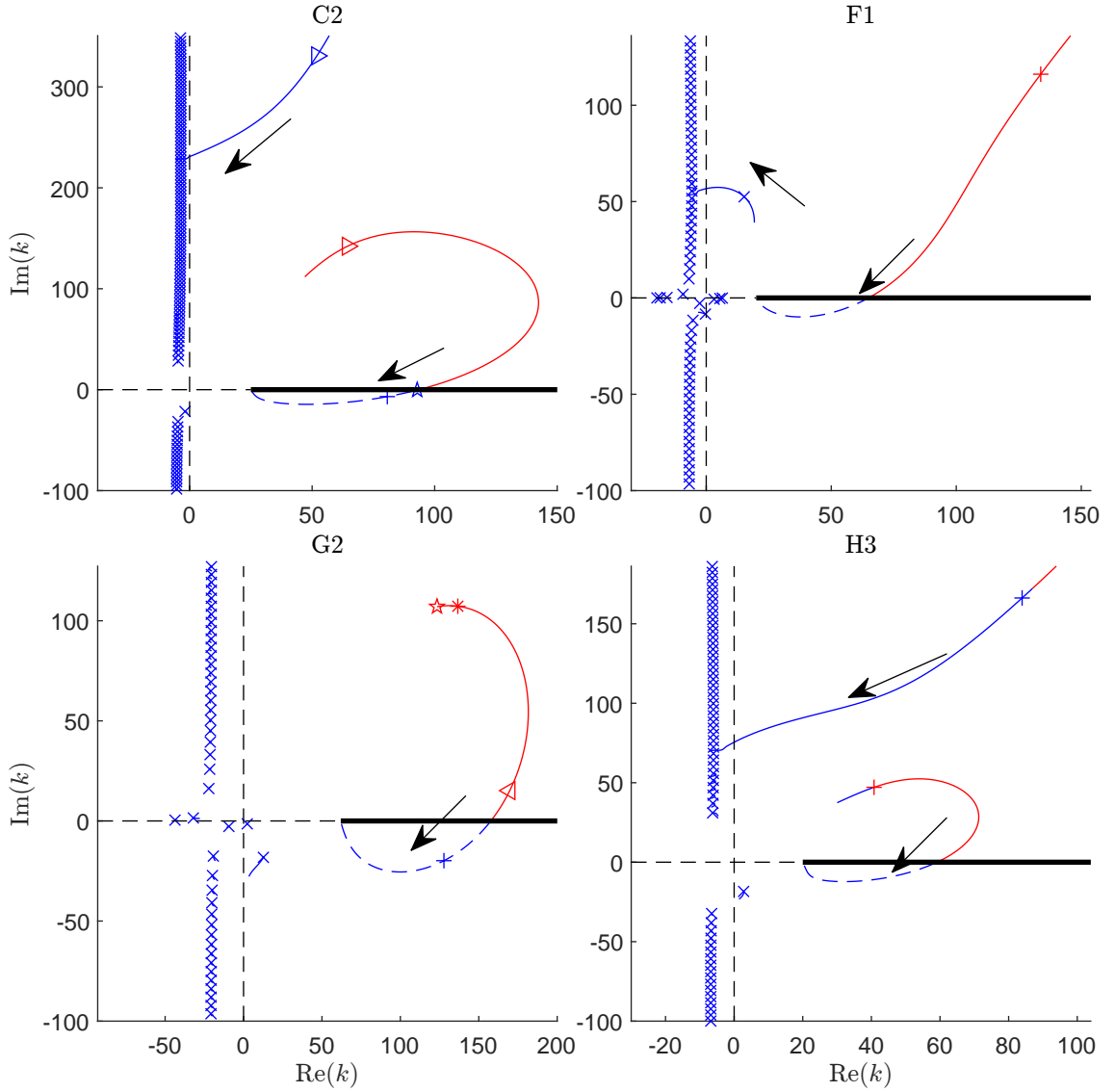


Figure 17: Location of the modal poles as the boundary layer thickness  $h$  is varied between  $0.1$  and  $5 \times 10^{-4}$ . Plotted are parameter sets,  $C2$ ,  $F1$ ,  $G2$  and  $H3$ . Blue lines indicate stable poles, while a red line indicates an instability. Dashed lines (---) indicate a pole is hidden behind the critical layer branch cut. Note that for parameter sets  $C$  and  $G$ , since these only vary in  $h$ , their tracks are uniform between the sub-parameter sets. The  $k^+$  pole associated with each sub-parameter set are indicated as; 1 (+), 2 (\*), 3 ( $\Delta$ ), 4 ( $\star$ ) with the usual acoustic modal poles indicated just for the highlighted given parameter set. Arrows indicate the direction of increasing boundary layer thickness  $h$ .

### 12.2.2 Variation of the Mach Number $M$

When varying the Mach number, as previously discussed we can study the stability of the problem in two ways. By tracking the location of the  $k^+$  poles. And by finding the value of  $h_c$ . In the following section we shall do both as we vary the Mach number.

Looking at the complex  $k$  plane, as in figure 18, it is worth observing that as we vary the Mach number the location of the critical layer branch cut will also vary as the branch point at  $\frac{\omega}{M}$  moves. For this reason we scale the complex  $k$  plane by  $\frac{M}{\omega}$ , such that we have a constant frame of reference as we track the locations of the poles. As would be expected, as we decrease the Mach number, it can be observed that the stable modal poles, tend to the location of their no-flow equivalents, located on the imaginary  $k$  axis, The hydrodynamic instability however is observed to become stable, moving through the critical layer branch cut and towards the branch point located at  $\frac{\omega}{M}$ . As the Mach number is increased however mode of the modal poles are found to become nearly cut-on, with the downstream propagating poles tending towards the origin and the upstream propagating modes tending towards  $-\infty$ , as would be expected. For higher mach numbers the  $k^+$  pole continues to behave as a hydrodynamic instability, though since it remains to the right of the branch point it would be expected that its contribution will become small compared to that modal sum, although no further investigation has been performed on this and it would still dominate the far-field as a result of its unstable behaviour.

When we have two poles present, as for parameter sets  $E$ , we may observe a sudden change in which pole represents the hydrodynamic instability. This is a consequence of our choice of deformation into negative imaginary  $\omega$  under the Briggs-Bers criterion although it is indicative of an absolute instability in the time domain, and although we do not investigate this any further in this thesis. It would be expected, since decreasing the Mach number results in the stable  $k^+$  pole located above the branch cut to move into the usual acoustic modal pole, that as the absolute instabilities can be removed by decreasing the Mach number, and indeed this would be expected of the no-flow case.

If we instead track the value of  $h_c$  as the Mach number is increased, as is done in figure 19, we can again observe the same stabilisation behaviour of the hydrodynamic instability and gain addition insight into the behaviour of the  $k^+$  pole. For lower Mach numbers we once again observe a stabilising effect, with  $h_c$  becoming smaller,

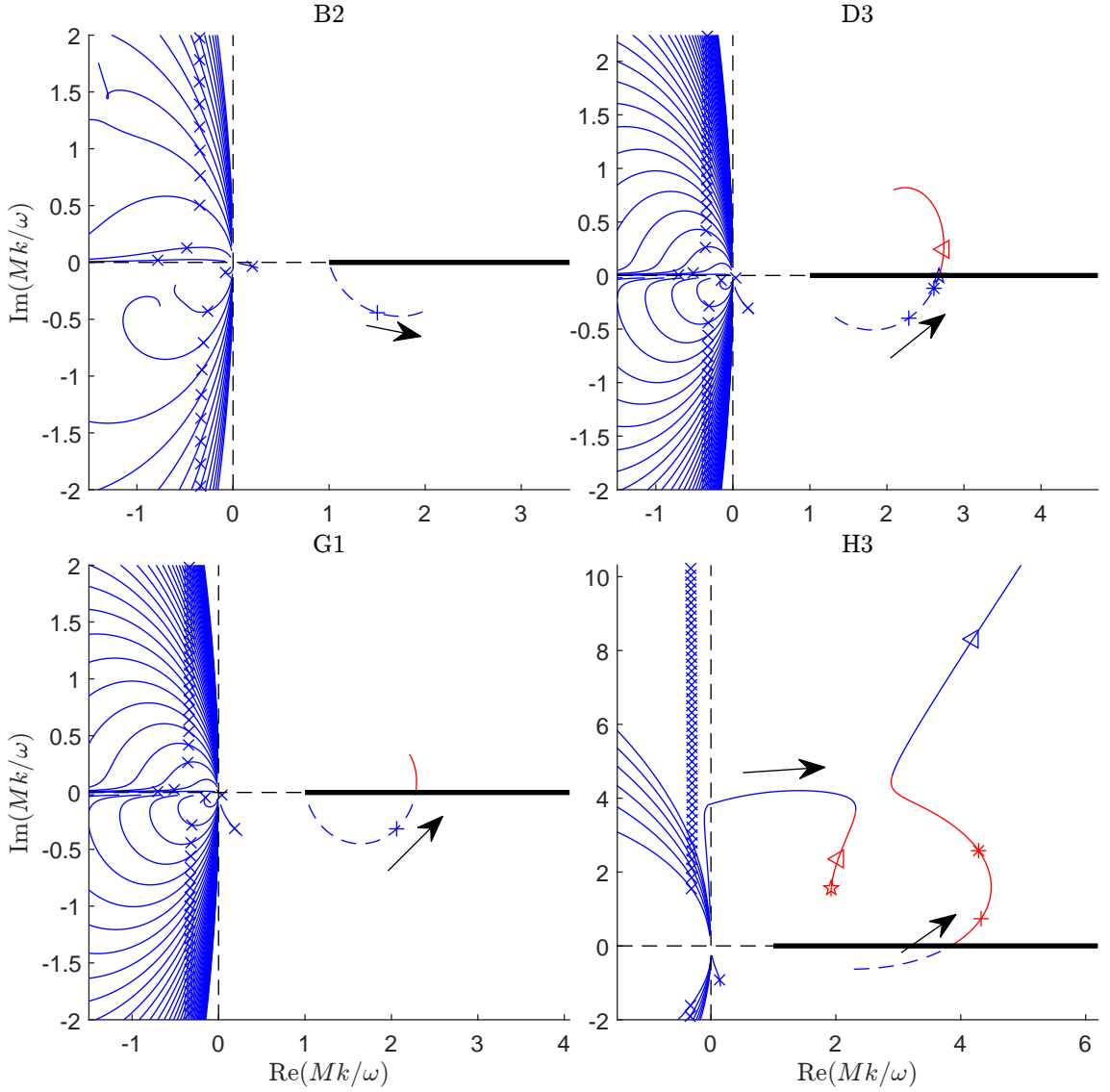


Figure 18: Locations of the modal poles as the Mach number is varied between  $M = 0.1$  and  $M = 0.9$ , scaled by  $\frac{M}{\omega}$ . Blue trajectories indicate stable modal poles, while red trajectories represent instabilities. Dashed lines (---) indicate poles located behind the critical layer branch cut. Plotted are parameter sets  $B2$ ,  $D3$ ,  $G1$  and  $H3$ . Note that the sub-parameter sets of sets  $D$  and  $E$  only vary by Mach number and so their trajectories are consistent. The  $k^+$  pole associated with each sub-parameter set are indicated as; 1 (+), 2 (\*), 3 ( $\Delta$ ), 4 ( $\star$ ) with only the acoustic modal poles indicated for the named sub-parameter set. Only modal poles with Imaginary part  $\text{Im}(k) < \frac{3\omega}{M}$  have been tracked. Arrows indicate the direction of increasing Mach number  $M$ .

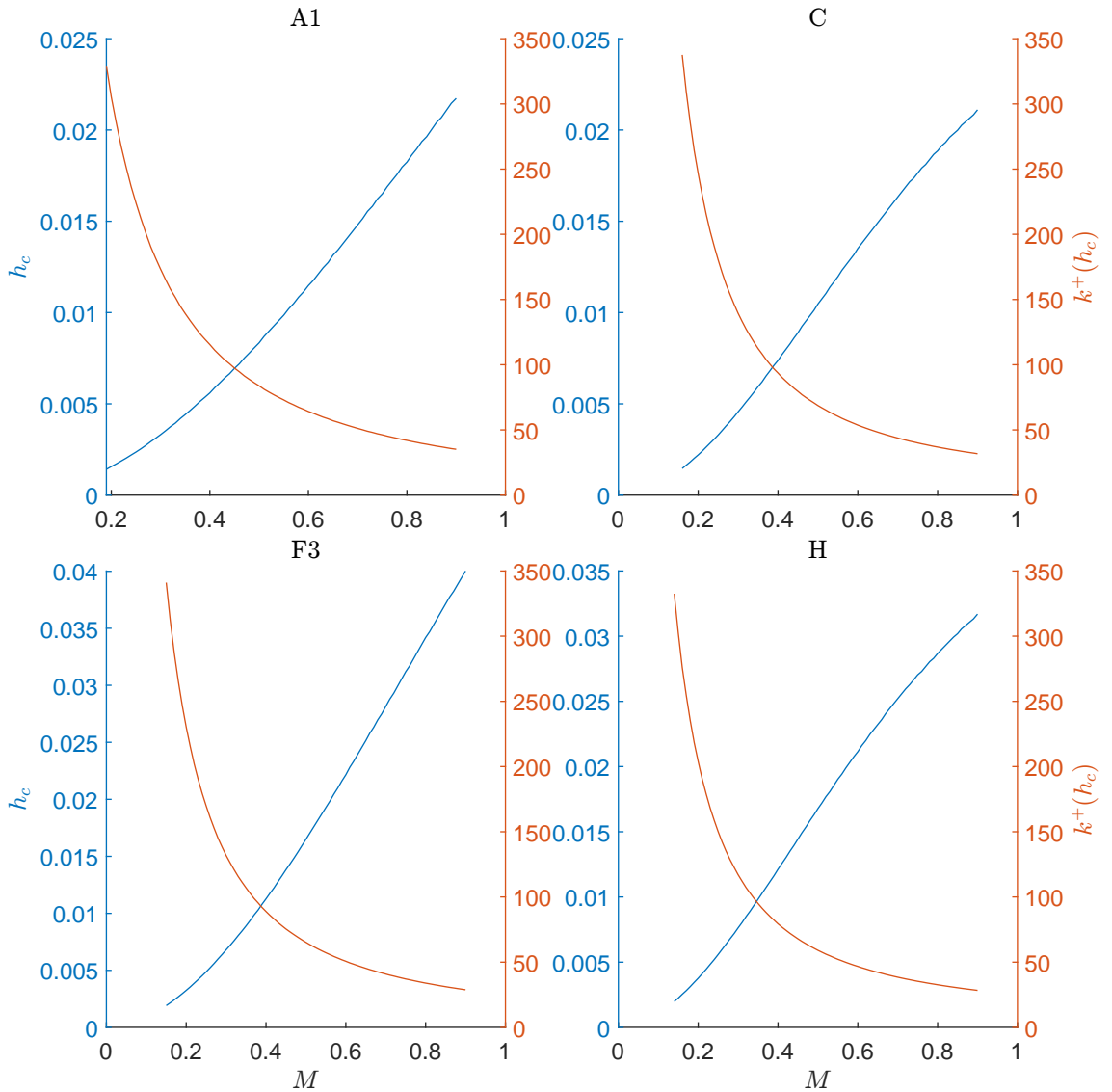


Figure 19: Values of  $h_c$  (blue) (left subplots) and  $k^+(h_c)$  (red) (right subplots) as the Mach number  $M$  is varied. Plotted for parameter sets  $A1$ ,  $C$ ,  $F3$  and  $H$ . Note that parameter set  $C$  only varies in boundary layer thickness  $h$  and parameter set  $H$  in Mach number  $M$  and so these plots are consistent between the sub-parameter sets. Note that unlike figure 18 we have not scaled our values of  $k^+$ .

and thus flow profiles with thinner boundary layer thicknesses would become stable while increasing the Mach number increases the value of  $h_c$ . This appears to follow a near linear relationship between the Mach number and  $h_c$ . In addition as  $M$  is decreased the value of  $k^+(h_c)$  tends towards  $\frac{\omega}{M}$  with the  $k^+$  pole approaching the branch point.

Considering again when two  $k^+$  poles are present, despite observing different poles being the hydrodynamic instability for different values of  $M$ , in figure 18 *E*, we retrieve in figure 19 a continuous value of  $h_c$  in the Mach number. Additionally this same change in pole stability could be observed in figure 17, *E3*, and so it is worth considering the relationship these parameters share for stability. Through tactfully varying the parameters of the system we are able to associate the different  $k^+$  poles with each other. Thus being able to transform one pole onto the other without such a shift in stability, particularly by first increasing the boundary layer thickness to stabilise the unstable  $k^+$  pole behind the critical layer branch cut, then varying the Mach number and reducing the boundary layer thickness once more. In this way, it is suggested that it may be that only one pole can be either a hydrodynamic instability or hidden behind the branch cut for any particular parameter set. However, despite no evidence contrary to this, the statement is yet to be proven. Additionally, the ability to be able to deform the unstable modal poles between each other emphasises an inability to label the hydrodynamic instability without performing the contour deformation under the Briggs-Bers criterion.

### 12.2.3 Variation of the Frequency $\omega$

As the frequency is varied, as seen in figure 20, it can be observed that the  $k^+$  pole is stabilised for both high and low frequencies although there may exist a range of intermediate frequencies for which the pole is unstable. Particularly this can be observed for parameter sets *D4* and *F4*.

As the boundary layer thickness is increased, this range of unstable frequencies is reduced, and there exists a finite thickness  $h$ , depending on the impedance and centre line Mach number, that is stable for all frequencies; that is, the resulting pressure perturbation would remain stable even when considering broadband frequencies as has been achieved for parameter set *H*.

We have previously stated that it is believed that the two pole case will reduce to a one pole  $k^+$  system as the boundary layer thickness is increased. In particular, as either the frequency is increased or decreased, one of the two poles is stable and moves into the cut-off acoustic modes. The other is unstable, becoming stabilised

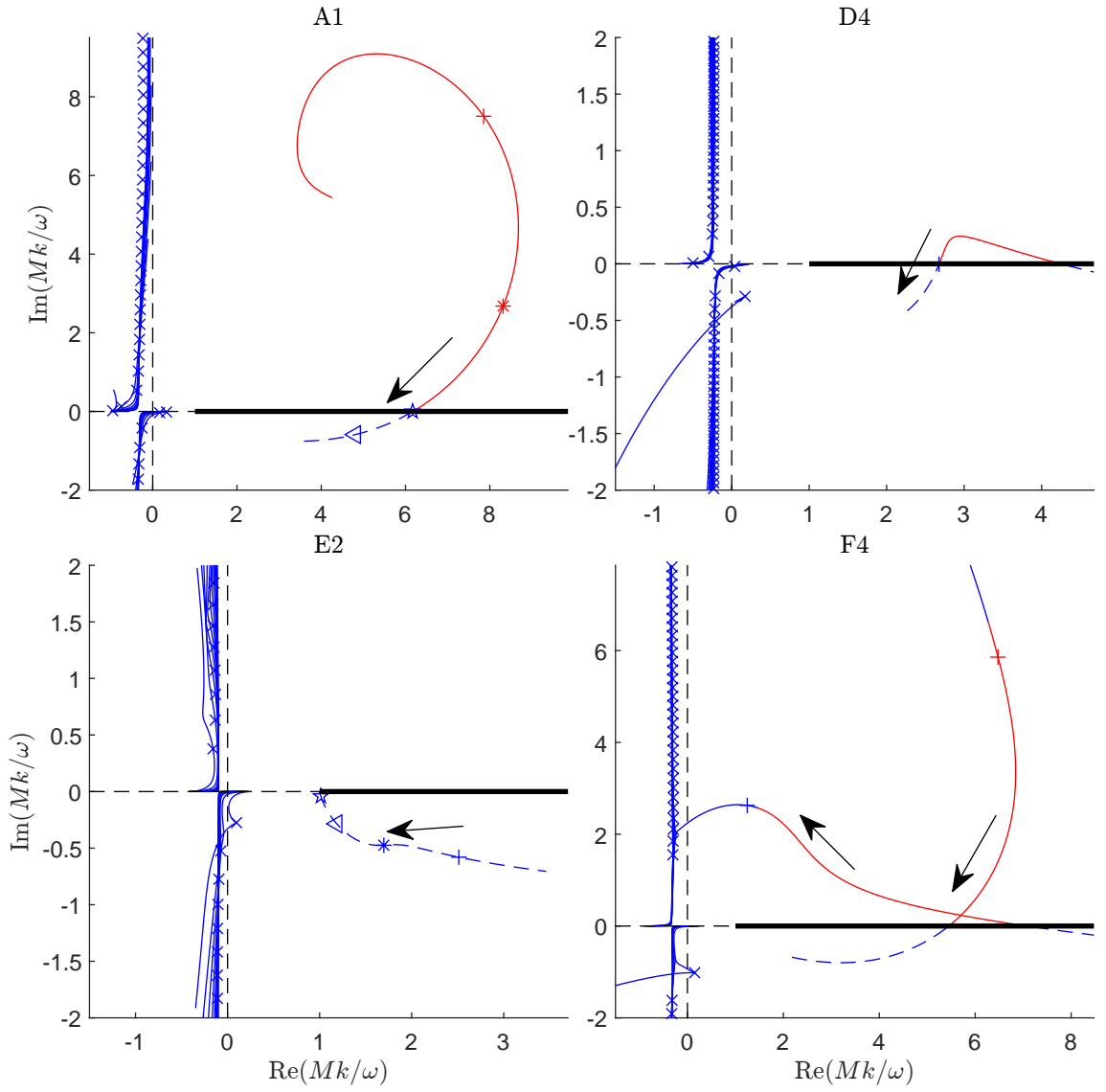


Figure 20: As figure 18, as the frequency  $\omega$  is varied from 1 to 50 for parameter sets A1, D4, E2 and F4. Arrows indicate the direction of increasing frequency  $\omega$ .

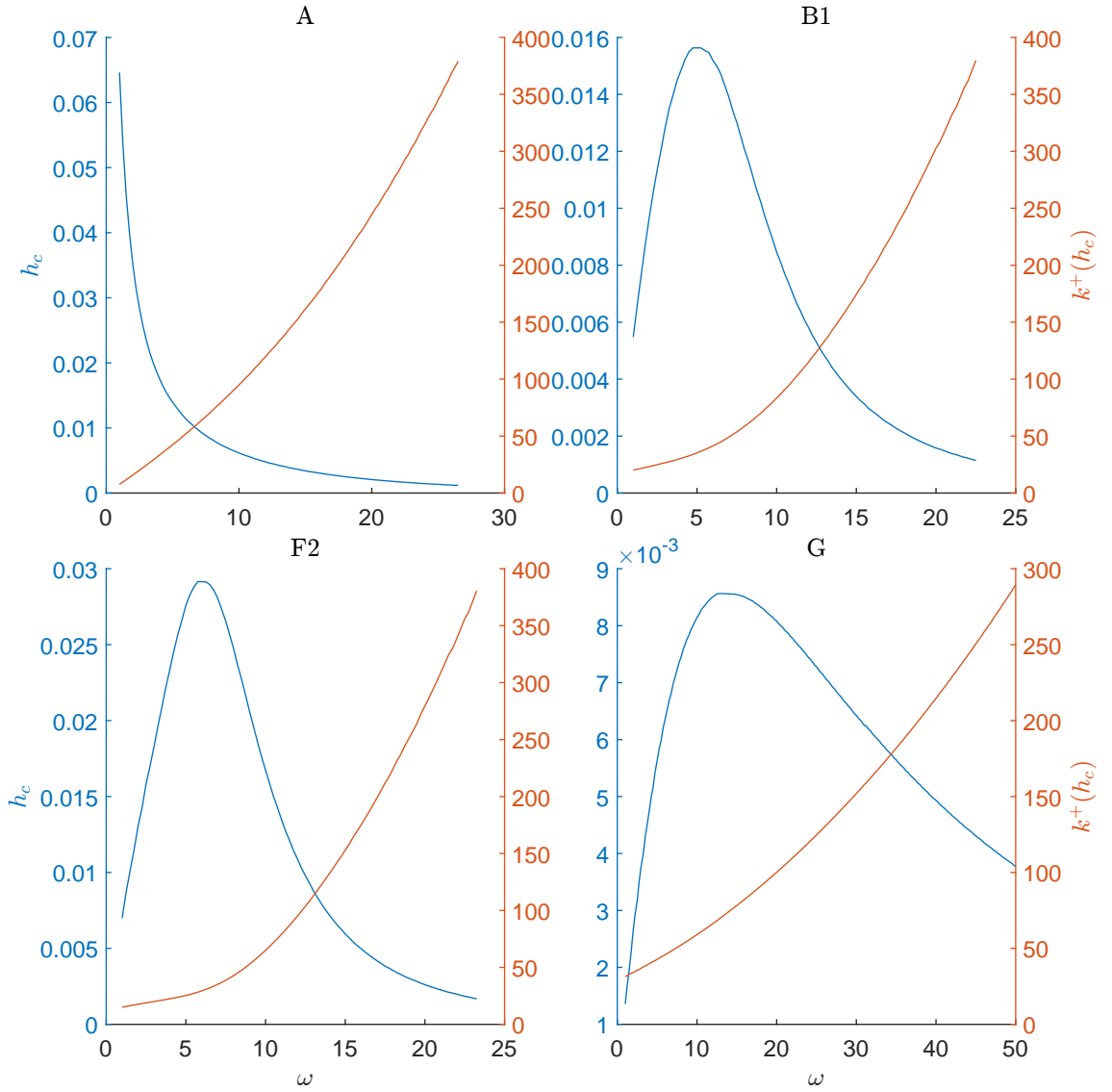


Figure 21: As figure 19, for varying the frequency  $\omega$  for parameter sets  $A$ ,  $B1$ ,  $F2$  and  $G$ . Note that parameter set  $A$  only varies in the frequency  $\omega$  and parameter set  $G$  in boundary layer thickness  $h$  and so these plots are consistent between the sub-parameter sets. Impedance  $Z = Z(\omega)$  is given by the Mass-Spring-Damper model.

by the critical layer branch cut.

Figure 21 indicates the value of  $h_c$  for each of the parameter sets. This is the value of  $h$  such that the  $k^+$  pole is located on the real line for each frequency. Observing the ‘humps’ in figure 21, it becomes more obvious that there exists a single value of  $h_c$  such that all frequencies are stabilised being located at the peak. Although at the high and low ends of frequency range in figure 21 there are values of  $h_c$  that only correspond to a single value of  $\omega$  it is expected that this is once again due to numerical limitations for high and low frequencies.

Observing that the dispersion relation actually depends on  $\omega$  in two ways, both directly, and indirectly, through the impedance  $Z(\omega)$ , it is important to consider

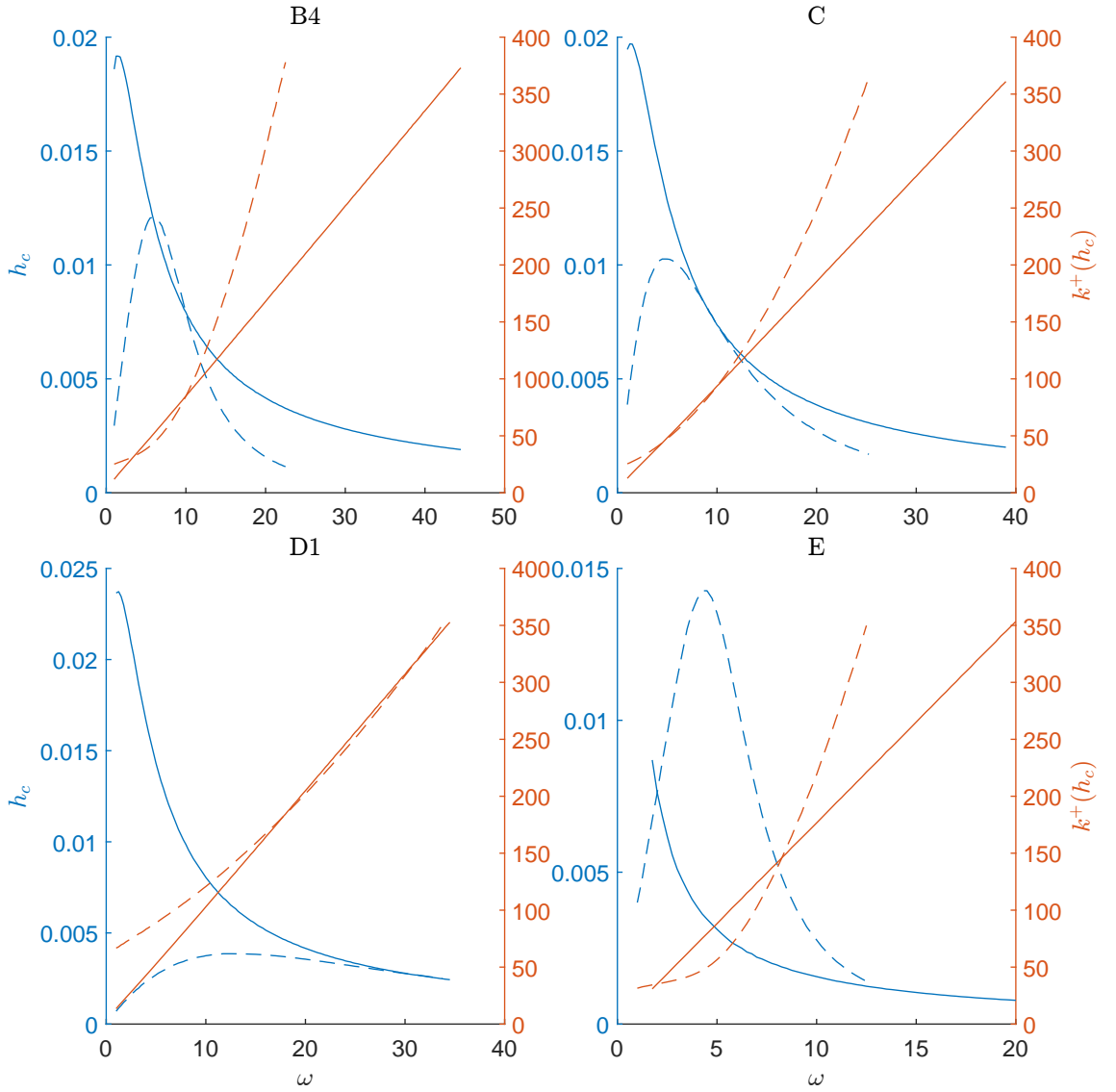


Figure 22: As figure 21, for a fixed impedance as given in table 3 (solid lines), and a varied impedance (dashed lines). Plotted are parameter sets  $B4$ ,  $C$ ,  $D1$  and  $E$ .

how the specific model for the impedance may be having an effect on the resulting trajectories and values of  $h_c$ . To this end, figure 22, finds the values of  $h_c$  for a fixed impedance  $Z$ , under variation of the frequency. The impedance considered for each parameter set is as given in table 3, without considering the Mass-Spring-Damper model. These are further compared to the values under the Mass-Spring-Damper model for the impedance. Firstly we note that the value of  $h_c$  under a fixed impedance is in general thicker than for its variable counterpart in  $\omega$ . That is, when considering a fixed frequency, a smaller number of boundary layer profiles will have a stable  $k^+$  pole, this is particularly true for lower values of  $\omega$ . In addition to this, for the fixed impedance it can be observed that  $k^+$  grows linearly in  $\omega$ .

Finally it may be observed that clearly the stabilisation seen in figure 20 for high frequencies is as a result of the frequency. However, it is likely true that the sta-

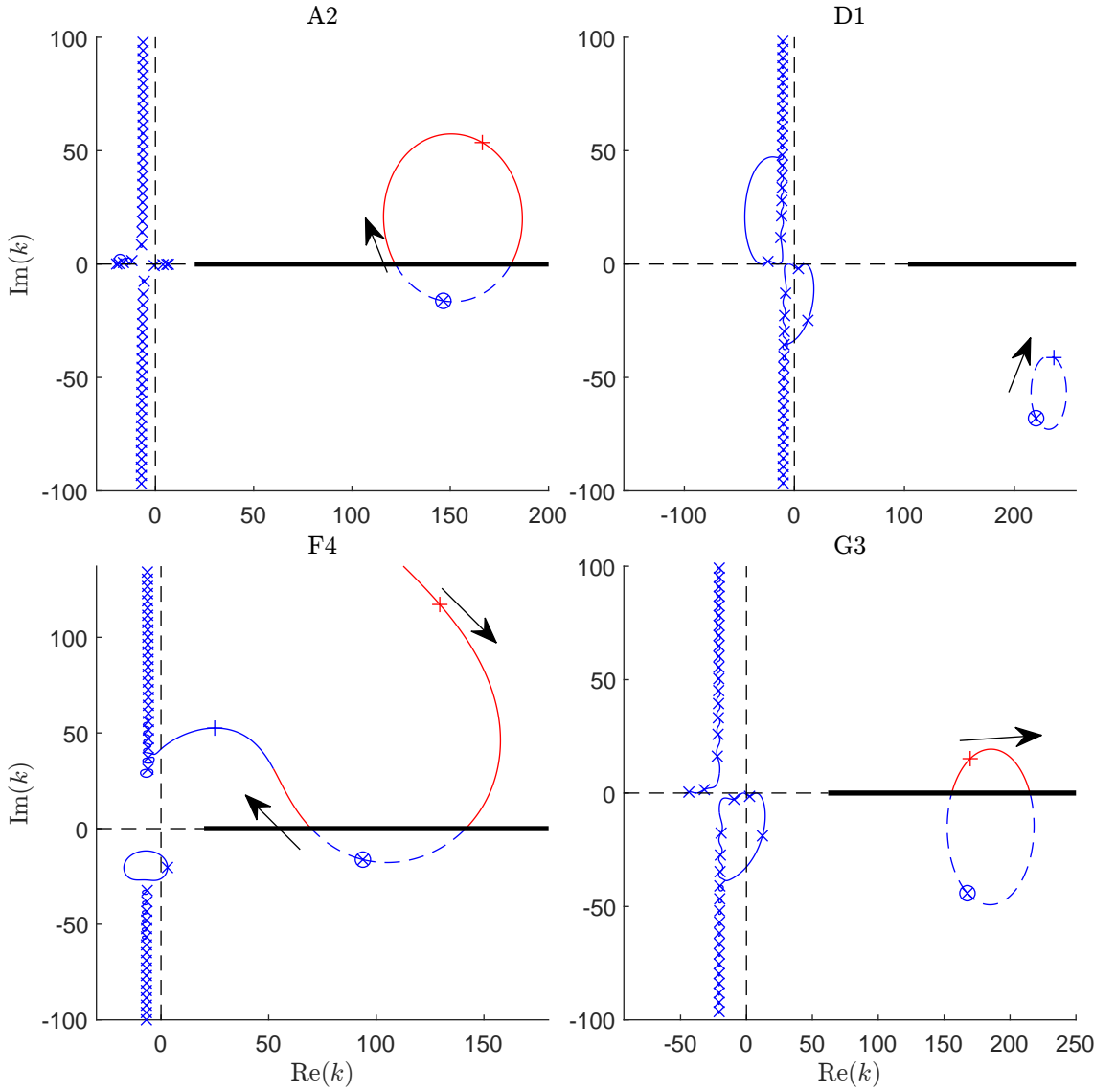


Figure 23: As figure 17, as the reactance  $\text{Im}(Z)$  is varied from  $-\infty$  to  $\infty$  for parameter sets  $A2$ ,  $D1$ ,  $F4$  and  $G3$ . Location of the  $k^+$  mode at  $|Z| = \infty$  is indicated with a circled cross,  $\otimes$ .

bilisation for lower frequencies occurs as a consequence of the resulting Spring-like impedance lining. Although low frequencies may still have a stabilising effect, as can be observed from the ‘humps’ in figure 22 near  $\omega = 1$ , however this is difficult to investigate further due to numerical precision. We can, however, investigate the effect of the acoustic lining on stabilisation, both together with and independently to the frequency  $\omega$ .

#### 12.2.4 Variation of the Impedance $Z$

Figure 23 illustrates the motion of the poles as the reactance  $\text{Im}(Z)$  is varied. In the one pole case, we see the  $k^+$  pole complete a loop, with the location at  $\text{Im}(Z) = -\infty$  the same as that of  $\text{Im}(Z) = +\infty$ . Moreover, as  $|Z| \rightarrow \infty$  the mode is located behind the branch cut. In the two pole case we also observe a pole at the same location

for  $\text{Im}(Z) = \pm\infty$ . This is also located behind the branch cut although approached from the different poles. As this takes place the other  $k^+$  pole is stable and moves into the acoustic modes, which also completes the loop with poles swapping location.

If we were to vary the resistance,  $\text{Re}(Z)$ , taking  $\text{Re}(Z) \rightarrow \infty$  would still retrieve the same hard walled behaviour, located behind the branch cut in each investigated case, suggesting that this behaviour may be intrinsic to the overall behaviour of a hard walled system. Further, the size of  $|Z|$  to have a resulting  $k^+$  pole located behind the branch cut has not been seen to be large.

In order to investigate this further, figure 24 is a contour plot for the values of  $h_c$  against  $\text{Re}(Z)$  and  $\text{Im}(Z)$ . We observe that as  $|Z|$  increases the value of  $h_c$  decreases. However, the figure is not well resolved due to increasing sensitivity to the value of  $h$  and that the value of  $k^+ \in \mathbb{R}$  increases, becoming difficult to locate. Despite this, with the observation that in all cases as  $|Z| \rightarrow \infty$  that have been investigated we find  $k^+$  to be stable, we can infer that as  $|Z| \rightarrow \infty$   $h_c \rightarrow 0$  and  $|k^+| \rightarrow \infty$ .

Noting that the hard walled behaviour may be attained in the used Mass-Spring-Damper impedance figure 25 gives contour plots of  $h_c$  as each of the impedance Mass, impedance Spring and impedance Damper terms are varied alongside the frequency  $\omega$ .

From these graphs two different behaviours may be observed. Firstly, when varying either the impedance mass or spring coefficient, if we choose to maintain a constant impedance, as indicated in figure 25 by the dashed lines, as we increase the frequency we do indeed observe a stabilising effect; that is, as  $\omega$  is increased,  $h_c$  decreases. However, we appear to observe a destabilization as the frequency is decreased at fixed impedance, although as seen in figure 21, this may be stabilising again for suitably small frequencies. A second observation is that, when the damping coefficient is small (as in  $C1$ ), it is found that the impedances with the largest  $h_c$  are those close to the *optimal damping* frequency  $\omega = \sqrt{K/\mu}$ , giving  $\text{Im}(Z) = 0$ . This is shown most clearly in the columns of figure 25 corresponding to parameter sets  $E4$  and  $F3$ , but is also seen in the Damper plots of parameter sets  $A$  and  $C$  of figure 25 near  $R = 0$ , by observing small regions of larger values of  $h_c$ . Moreover, as the damping co-efficient increases the frequency with the largest value of  $h_c$  appears to reduce to zero.

### 12.3 Hard Walled Ducts

Following the observations made in the previous section, it can be worthwhile considering how  $h_c$  behaves in the hard walled limit. It would be expected that as

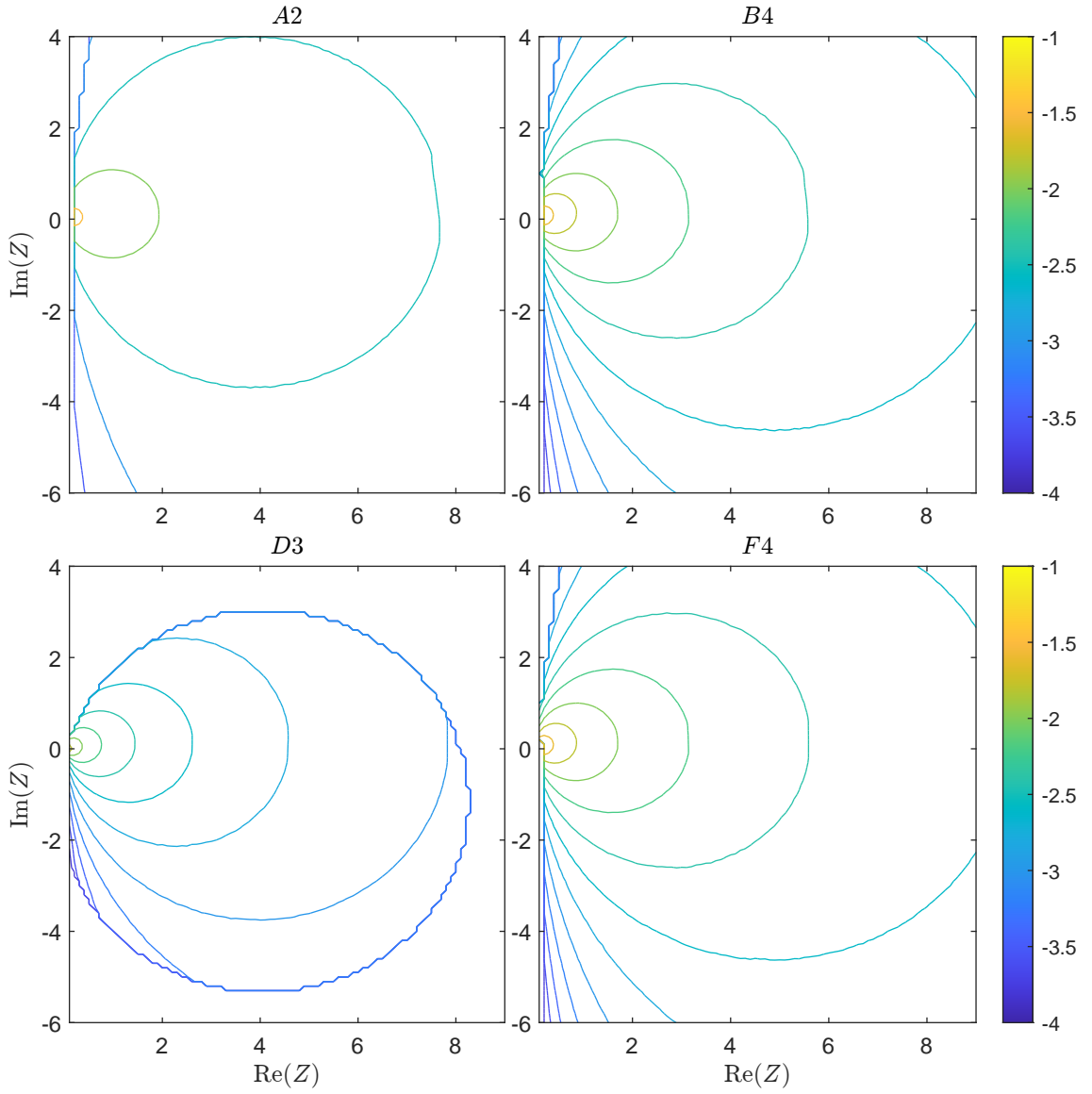


Figure 24: Contour plot of  $h_c$  against  $\text{Re}(Z)$  and  $\text{Im}(Z)$  for parameter sets  $A2$ ,  $B4$ ,  $D3$  and  $F4$ . Values of  $h_c$  as given by the colour bar are indicated on a  $\log_{10}$  scale. The poorly resolved outermost contours are due to a loss of numerical precision resulting from large  $k^+(h_c)$ .

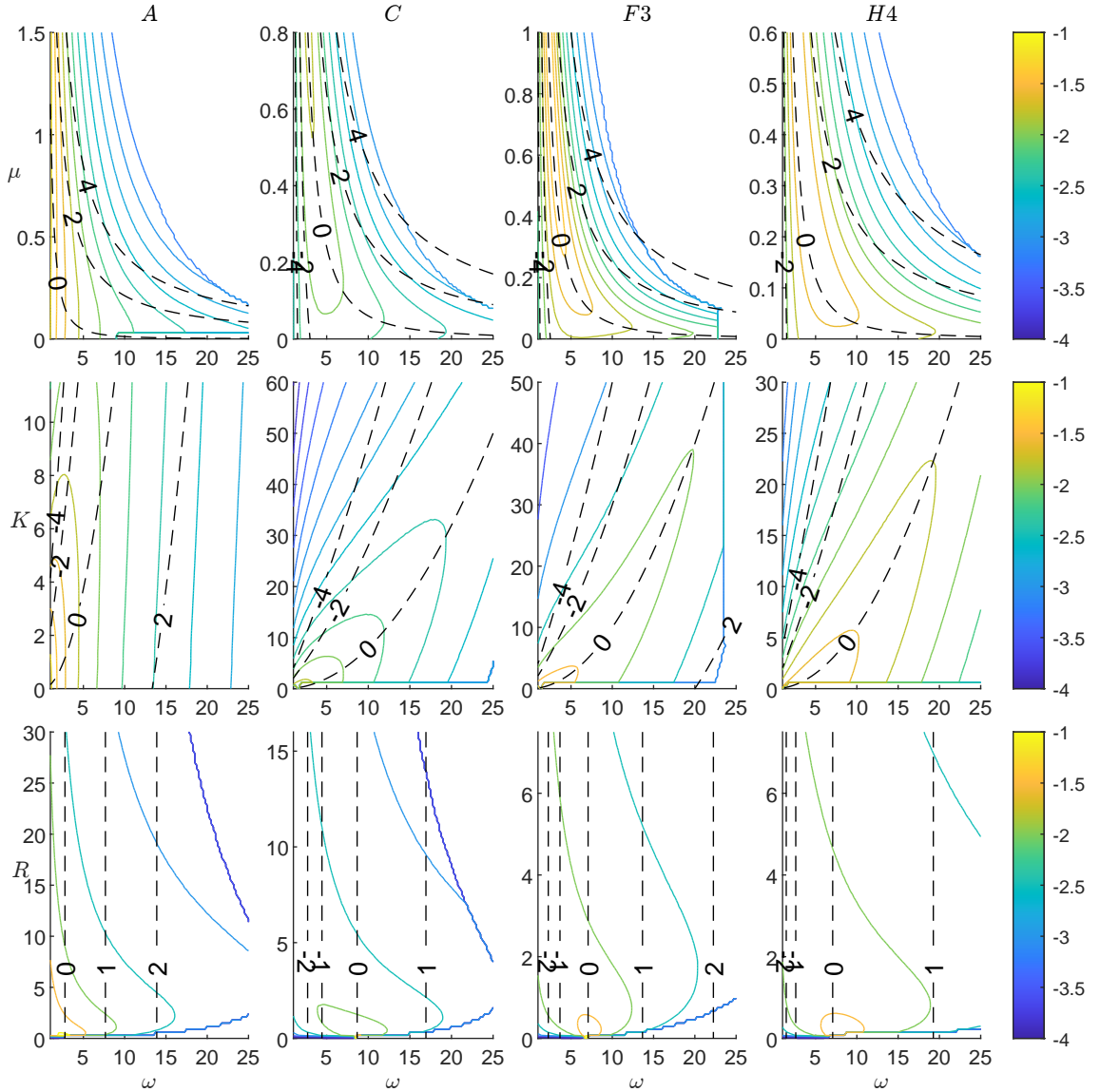


Figure 25: Contour plots of  $h_c$  (on a  $\log_{10}$  scale) as the frequency and impedance are varied, performed for parameter sets *A*, *C*, *F3* and *H4*, with the impedance mass  $\mu$ , spring  $K$  and damper  $R$  terms being varied between 0 and 10 times their original value. Black dashed lines (--) indicate lines of constant impedance  $Z = Z(\omega)$  with the value of  $\text{Im}(Z)$  indicated. Note that parameter set *A* only varies in the frequency  $\omega$  and parameter set *C* in boundary layer thickness  $h$  and so these plots are consistent between the sub-parameter sets.

$|Z| \rightarrow \infty$  then  $h_c \rightarrow 0$ . Unfortunately, this result is yet to be proven. However, we believe the following is true.

For a hard walled duct, under a quadratic shear flow profile, for  $h \in (0, 1)$ , no modal pole can occur on the critical layer branch cut. In particular any  $k^+$  poles will either be stable or unstable for all values of  $h \in (0, 1)$ .

Although the following proof of this statement is incomplete, it is our belief that the direction of query may be completed.

Considering a hard wall duct a modal pole occurs when we have  $\tilde{\psi}_1(r)$  satisfying the boundary condition at  $r = 1$ . That is,

$$\tilde{\psi}'_1(1) = 0. \quad (12.3)$$

Let us assume there exists a  $k^+$  modal pole that occurs exactly on the critical layer branch cut.  $k^+ \in (\frac{\omega}{M}, \infty)$ . This implies that  $Q \in (0, h)$  and  $r_c^+ \in (1 - h, 1)$  are both real valued. Further  $\alpha = i\tilde{\alpha}\omega$  is purely imaginary,  $\tilde{\alpha} \in \mathbb{R}$ . We seek to solve,

$$C_1^+ \tilde{p}'_1(1) + D_1 \tilde{p}'_2(1) = 0 \quad (12.4)$$

Where we have used  $C_1^+$  to indicate that we must account for the discontinuity in  $r$  caused by having  $r_c^+ \in (1 - h, 1)$ . Although details are omitted here, one can deduce the following,

$\tilde{p}_1(r)$  and  $\tilde{p}'(r)$  are both real and have a root when  $r = r_c^+$ .  
 $\tilde{p}_2(r)$  and  $\tilde{p}'(r)$  are also both real, however for  $r < r_c^+$  we are required to make use of  $\tilde{p}_2^+(r)$  and  $\tilde{p}'^+(r)$  which are complex and can be written as

$$\tilde{p}_2^+(r) = \tilde{p}_2(r) - 2\pi i A \tilde{p}_1(r) \quad \tilde{p}'^+(r) = \tilde{p}'(r) - 2\pi i A \tilde{p}'_1(r) \quad (12.5)$$

In addition to this, since  $\alpha$  is purely imaginary it can be deduced that  $D_1$  is also real, making use of the modified Bessel function of the first kind to do so. Finally we can use our understanding of  $\tilde{p}_2(1 - h)$  to conclude that although complex,  $C_1^+$  can be expressed in terms of the real  $C_1$  and  $D_1$ ,

$$C_1^+ = C_1 + 2i\pi A D_1 \quad (12.6)$$

Recall we seek  $\tilde{\psi}'_1(1) = 0$ . This can be written, now specifically considering a  $k^+$  pole as

$$C_1 \tilde{p}'(1) + D_1 \tilde{p}'_2(1) + 2i\pi A D_1 \tilde{p}'_1(1) = 0. \quad (12.7)$$

Equating the imaginary part to zero give that we require either  $D_1 = 0$  or  $\tilde{p}'_1(1) = 0$ . It is believed, although not proven,  $\tilde{p}'_1(1) = 0$  if and only if  $r_c^+ = 1$  which although is approached as  $k^+ \rightarrow \infty$  is not attained. If this is true then it must be that  $D_1 = 0$ . Now equating the real part to zero with this information we must conclude in the same way that  $C_1 = 0$ . That is  $\tilde{\psi}_1(r) = \tilde{\psi}'_1(r) = 0$  for  $r \geq 1 - h$ . This only leads to a continuous  $\tilde{\psi}_1$  if  $m \neq 0$  and  $h = 1$ . Which would not lead to an admissible solution. Thus we conclude that there does not exist a value of  $h = h_c \in (0, 1)$  such that a  $k^+$  pole occurs on the critical layer branch cut. And so any  $k^+$  pole is either always stable or unstable for any boundary layer thickness.

In order to prove this result definitively it is still required to show that for any real fixed  $k > \frac{\omega}{M}$   $\tilde{p}'_1(1) \neq 0$ , likely making use of the knowledge that  $(1 - r_c^+) > 0$ , although additional assumptions may be required.

It is worth noting that in all case we have examined no unstable  $k^+$  pole has been found and as the wall becomes hard we have observed the  $k^+$  pole become or remain stable. The natural extension to this would be to show that for all hard-walled ducts we have a stable pressure perturbation and as a hard wall is approached the system will become stable for some finite  $Z$ .

## 12.4 Comparison to a Linear-Shear flow

Figure 26 compares the wave field generated in a quadratic boundary layer with the wave field in a linear boundary layer profile [as studied by Brambley et al., 2012a]. The process for constructing the Frobenius series solutions and inverting the Fourier transform for the linear shear problem is identical to the construction given here, with the only difference given by the flow profile

$$U(r) = \begin{cases} M & r < 1 - h \\ \frac{M(1-r)}{h} & 1 - h < r \end{cases} \quad (12.8)$$

which simplifies the process of solving the homogeneous Pridmore-Brown equation, as there is only one critical point, and so we have a larger radius of convergence, particularly in the case  $k \rightarrow \frac{\omega}{M}$ . Leading on from this it is found that; the modal poles, hydrodynamic instability and critical layer branch cut contributing in identical forms. The decay rates for the terms of the critical layer branch cut are given for the linear shear flow profile in table 4.

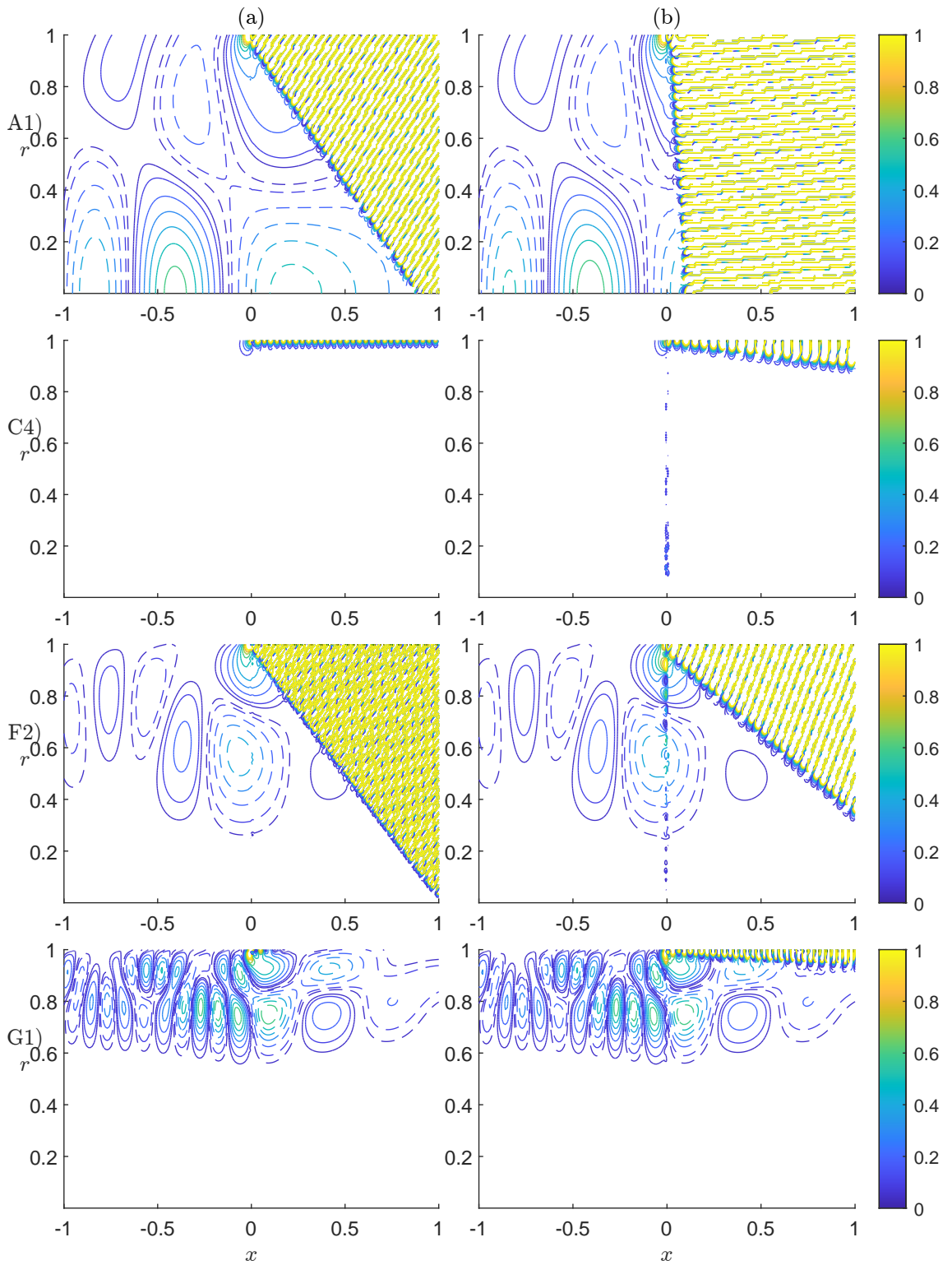


Figure 26: Plotting the real values of the full solution for a quadratic boundary layer flow profile (a) and a linear boundary layer flow profile (b) [from Brambley et al., 2012a]. Plotted for parameter sets  $A1$ ,  $C4$ ,  $F2$  and  $G1$  with  $r_0 = 1 - \frac{4h}{5}$  in each case. Positive values are marked with a solid line (—), while negative real parts are indicated with a dashed line (--).

The wave fields are reasonably similar, particularly in the near field and upstream, however significant differences are seen downstream, especially in the far-field. This is related to whether the  $k^+$  pole is located above or below the branch cut. In the quadratic case, the  $k^+$  pole always contributes, whether it is behind the branch cut or not, while the  $k^-$  is always found above the branch cut and so is not seen to contribute at all. With the linear boundary layer, instead we find a  $k^-$  pole that can be located either above or below the branch cut, while the  $k^+$  pole is instead located above in all cases. The result of this is that the linear boundary layer profile is always found to be a convective instability, while the quadratic boundary layer profile is only found to be unstable if the boundary layer is sufficiently thin. This results in vastly different far-field behaviour, and indeed even in the near field, a noticeable difference is observed near the duct wall. Figure 26 *C4* and *G1*. Even when both flow profiles give rise to a convective instability, we can see in figure 26 (parameter sets *A1* and *F2*) that the growth rate of the instability can be significantly different.

Following a similar method as performed for the quadratic shear flow, we may also repeat the analysis above for a linear shear flow. Tracking the poles in each of the varied parameters. This allows us to compare the quadratic and linear boundary layer profiles, and a significant difference is seen. This is done in figures 27-30 for the boundary layer thickness, Mach number, frequency, and impedance. In each of these it can be observed that indeed the linear flow profile is unstable for all boundary layer thicknesses, and so no equivalent of  $h_c$  exists, and the hydrodynamic instability will always be present. There is some similarity, however, and for cases where stability was found for the quadratic shear, in the linear case we instead have a hydrodynamic instability with a small imaginary part. As a result of this, the growth rate of the mode remains exponential in the linear case, albeit with a small exponent, and thus it will still dominate eventually in the far-field, though it may be comparable in size within the near field. This could be seen in figure 26 within parameter sets *C4* and *G1*.

In addition, for the linear shear flow profile, we also find an additional stable  $k^-$  mode located below the branch cut and not behind the branch cut. Like the  $k^+$  pole for the quadratic shear flow, this  $k^-$  pole may move above and behind the branch cut as the parameters are varied, although this mode would then stop contributing instead of becoming unstable. This mode, when it is located below the branch cut, has a contribution that is exactly cancelled by part of the contribution from the critical layer branch cut, and so in all cases it does not contribute to the final Fourier inversion. For this reason it has not been included in our mode plots for the linear shear flow. However, the presence of this mode further justifies the importance of carefully including the contribution of the critical layer branch cut, else this removal

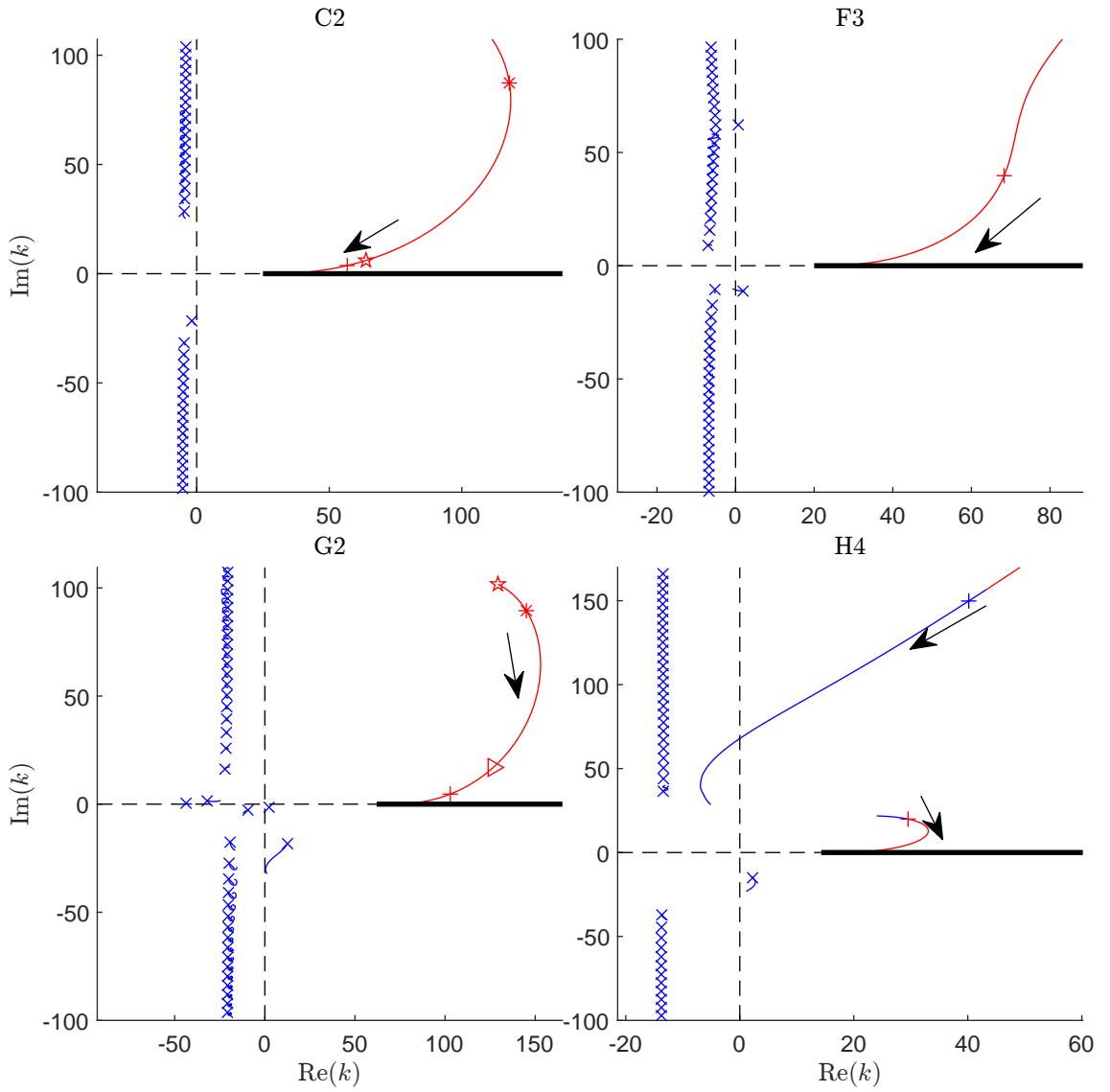


Figure 27: As figure 17 varying boundary layer thickness  $h$ , for a linear shear flow profile.

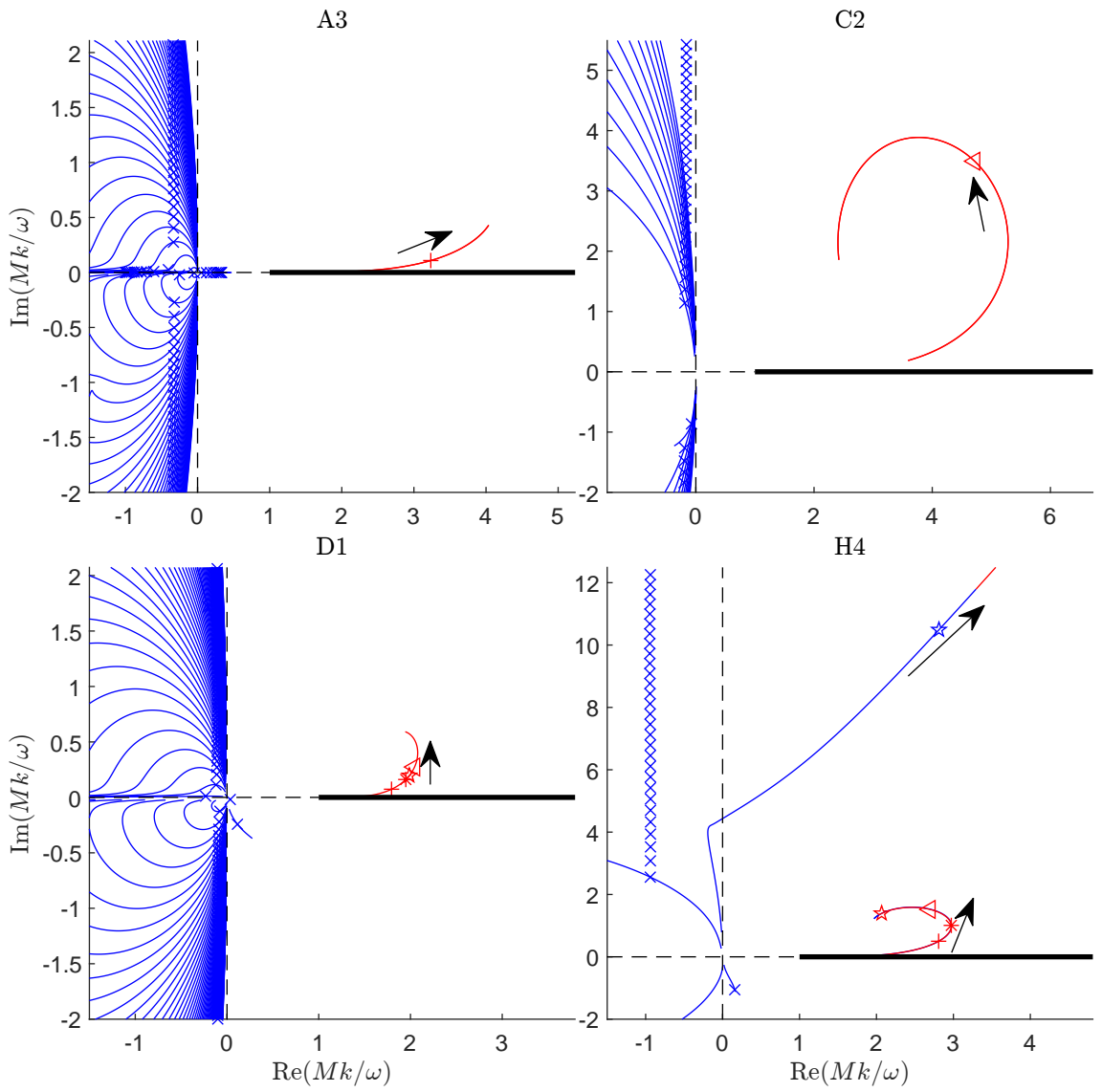


Figure 28: As figure 18 varying the Mach number  $M$ , for a linear shear flow profile.

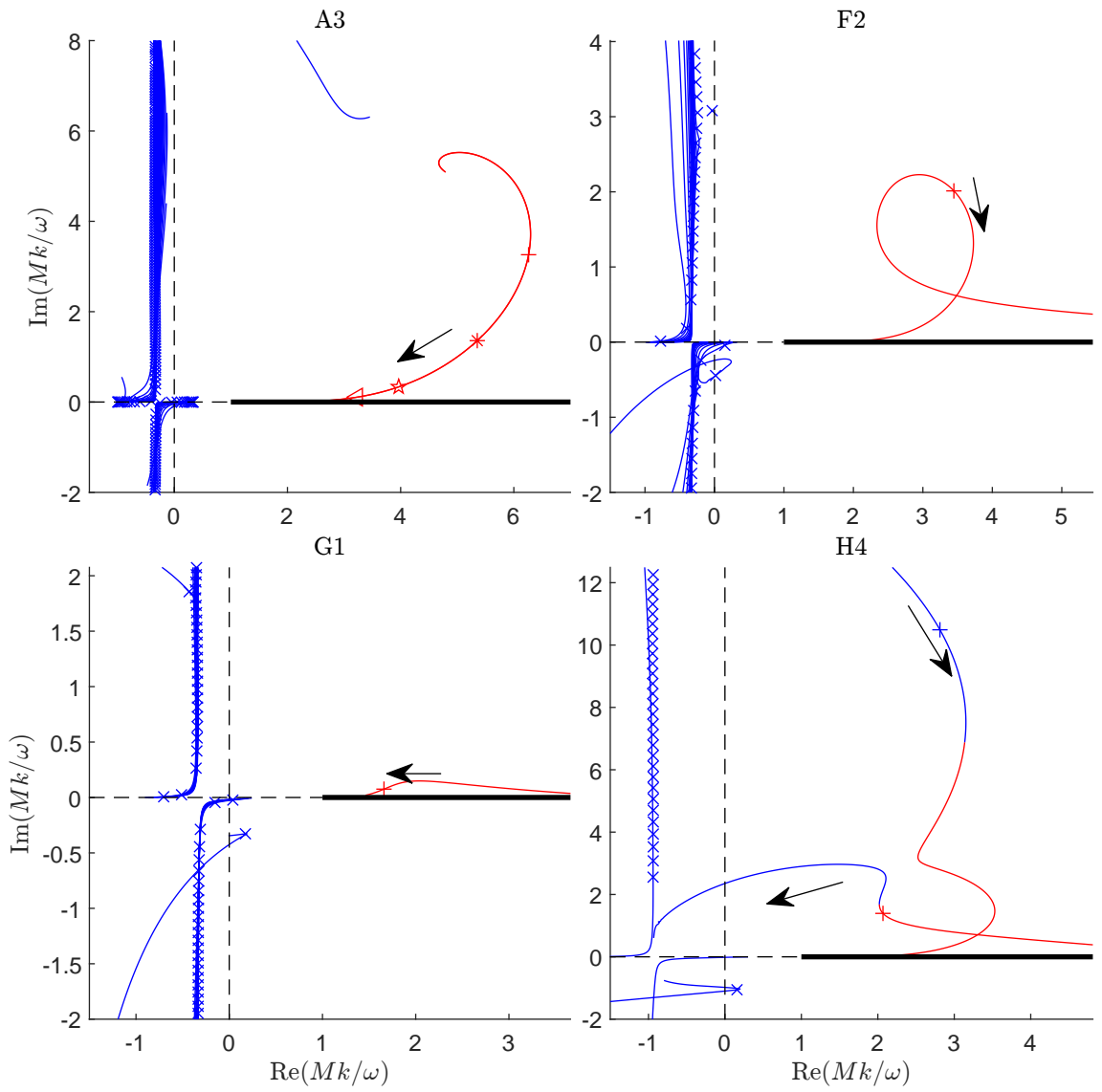


Figure 29: As figure 20, varying the frequency  $\omega$ , for a linear shear flow profile.

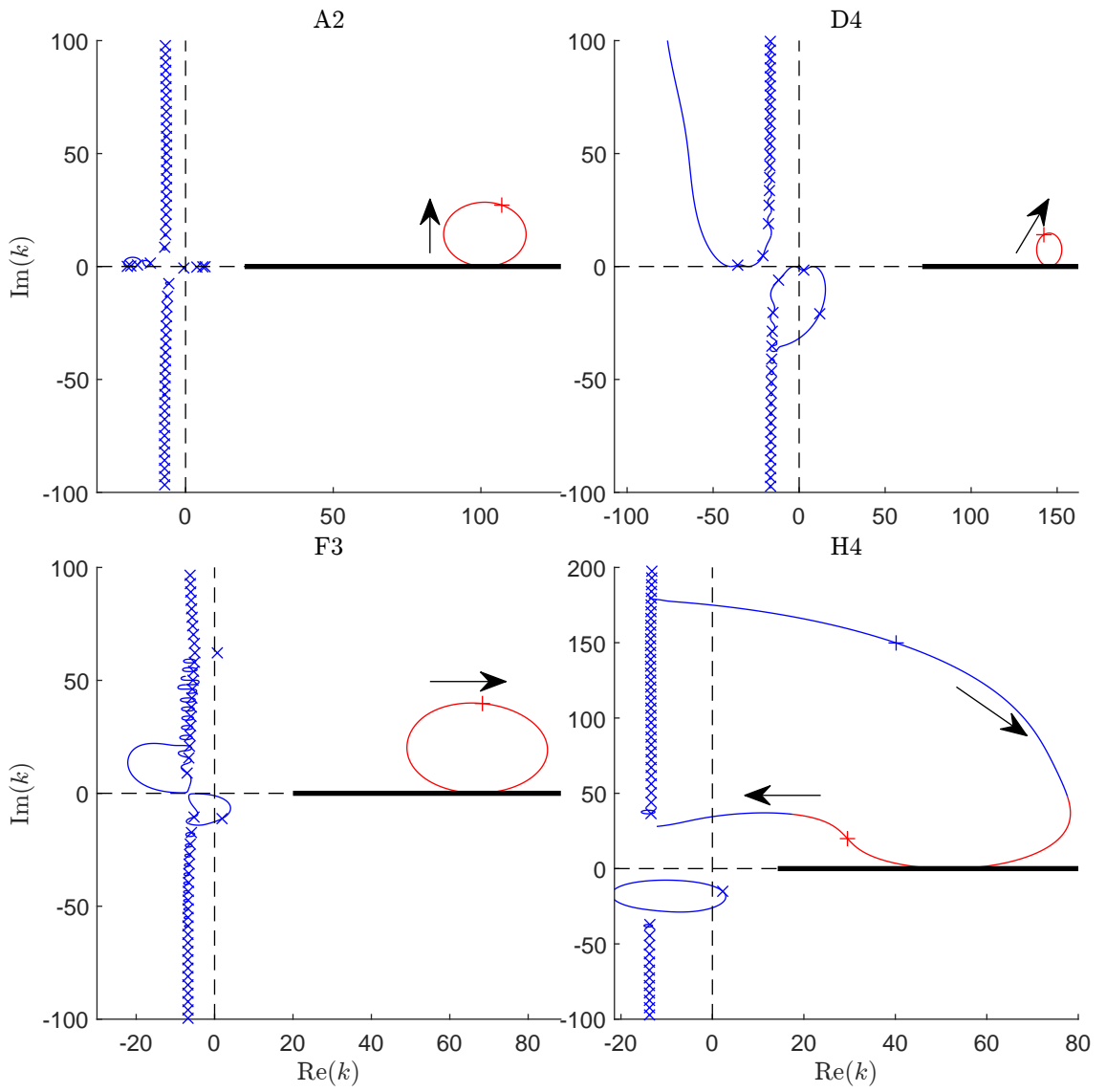


Figure 30: As figure 23, varying the impedance,  $\text{Im}(Z)$ , for a linear shear flow profile.

may be missed.

## Part III

# The Modified Myers Boundary Condition for a Quadratic Shear Flow

## 13 Introduction

In the previous part, we considered a quadratic shear flow profile and solved the Pridmore-Brown equation exactly, this gave rise to the critical layer branch cut, for which each of the solutions experienced a jump over. Despite the boundary condition being applied being simple, due to the the mean flow profile having no slip  $U(1) = 0$ , the solutions are computationally expensive to compute numerically. This is a result of the summation of many terms, and may also introduce errors into these numerical evaluations. Additionally, it was difficult to find closed forms for the far-field behaviour for the critical layer branch cut.

If we were instead to consider a uniform flow profile, which does not retrieve a non-slip boundary condition, the Pridmore-Brown equation reduces to a scaled version of Bessel's equations as already seen in equation (5.18), for which the solutions, are computationally inexpensive, and a far greater wealth of knowledge is held about their behaviour. The disadvantage of considering this problem is the requirement of a more complicated boundary condition at the duct wall. It is however possible to choose the boundary condition in order to account for other features that have otherwise been removed from the mean flow, including boundary layers accounting for an inviscid sheared flow such as the one considered in Part II [e.g. Ingard, 1959, Brambley, 2011b, Rienstra and Darau, 2011, Khamis and Brambley, 2016], or a viscous boundary layer [e.g. Brambley, 2009a, Khamis and Brambley, 2017b]. One feature that may be observed however is, despite the critical layer branch cut being fundamental to the full solution for an inviscid shear flow, it is not present within the inviscid boundary conditions. Within the viscous setting however a branch cut may occur similar to that of the critical layer, with branch point still at  $\frac{\omega}{M}$ , extending along  $\frac{\omega}{M} - iq$ ,  $q \geq 0$ . This aligns with the steepest decent contour for the critical layer branch cut in the full solution to the Pridmore-Brown equation for a shear flow, as seen in figure 7.

The absence of the critical layer branch cut in uniform flow may seem rather inconsequential, particularly where previous work has found that its contribution is small in the majority of cases, and the non-modal pole, which occurs only when a sound source is located in the sheared flow, will no longer be present for uniform flow. However, with the observation in the previous work, contained with part II, and [King et al., 2022, King and Brambley, 2022], that the critical layer branch cut may stabilise the hydrodynamic instability, it is important to observe if this same behaviour can occur for a uniform flow, with a boundary condition chosen in order to capture the effects of a quadratic shear flow.

Two previous boundary conditions we will make comparisons to within this part are; the Ingard-Myers boundary condition [Ingard, 1959, Myers, 1980], which accounts for a vanishing thin sheared boundary layer, although the exact form of this boundary layer profile does not appear; and the Brambley, or Modified-Myers boundary condition [Brambley, 2011b], which considers a thin but finite boundary layer, and is constructed to account for any shear flow profile, although exact forms are only given for a linear shear flow, which the boundary condition has become synonymous with, due to the linear shear solution exactly matching with the predicted asymptotic behaviours for other flow profiles. Since in this work we will be considering the Brambley boundary condition for a quadratic shear flow, we will refer to the Brambley boundary condition for a linear shear flow as the Linear-Brambley boundary condition, and the Brambley boundary condition for a quadratic shear flow as the Quadratic-Brambley boundary condition.

Within the Ingard-Myers boundary condition the hydrodynamic instability is not always present, and in particular, for a hard wall the hydrodynamic instability is never present, akin to the full problem of quadratic shear, and as would have been expected for a hard wall. It should however be noted that the stabilisation of the hydrodynamic instability for the Ingard-Myers boundary condition does not follow the same mechanism as was seen for the full solution to the Pridmore-Brown equation under a the quadratic shear mean flow. In this case the stability occurs due to a change in stability under the Briggs-Bers criterion, and results in the boundary condition being ill-posed in the time domain, since for all  $\Omega > 0$  there exists a real value of  $k$  such that  $k$  is a mode with frequency  $\omega$  and  $\text{Im}(\omega) < -\Omega$ . This remains true even for harder walls, with the hydrodynamic instability only being completely stable when  $|Z| = \infty$ .

The Brambley boundary condition can in some sense be considered the simplest extension to the Ingard-Myers boundary condition, being the next order expansion in boundary layer thickness. Within the work of [Brambley, 2011b] attention is drawn to two quantities labelled  $\delta I_0$  and  $\delta I_1$  (although we will refer to them later  $hI_0$  and  $hI_1$ ) with  $\delta$  used to denote the boundary layer thickness in [Brambley, 2011b]. It was observed that  $\delta I_0$  could be decomposed into a further two quantities, which acted as measures of the mass and momentum of the fluid flow contained within the boundary layer. On the other hand  $\delta I_1$  could not be decomposed in a similar way, and only asymptotic analysis was performed, with the conclusion being that  $\delta I_1$  would contain the effects of the critical layer if they were present. It is not surprising that the Linear-Brambley boundary condition did not observe the effects of the critical layer, with in that case for the full solution being only present due to the cylindrical geometry, a property that the boundary condition does not observe.

In this part we reconstruct the Ingard-Myers and Brambley boundary conditions before applying the latter to a quadratic shear flow profile producing what we refer to as the Quadratic-Brambley boundary condition. We then proceed to study the behaviour of the Quadratic-Brambley boundary condition and the effects of the critical layer branch cut. A second boundary condition is then given to account for modes hidden behind the critical layer branch cut and the effects of this on the Fourier inversion is then studied with comparisons made to the Ingard-Myers and Linear-Brambley boundary conditions throughout.

## 14 Construction of the Brambley Boundary Condition

We once again consider the linearised Euler equations given in equation (5.1), to construct the Pridmore-Brown equation (5.1), which we will consider in homogeneous form. Unlike in part II, here we will specify the relationship between the mean flow density and pressure as

$$c_0^2 = \frac{\gamma p_0}{\rho_0(r)} \quad (14.1)$$

where  $\gamma$  is the ratio of specific heats. The purpose of specifying this relationship may not be immediately obvious, however we later use this to rewrite the Pridmore-Brown equation into an alternative form.

Non-dimensionalising the velocities by the centre-line sound speed, lengths by the duct radius and densities by the centre-line mean density once again, it follows

$p_0 = \frac{1}{\gamma}$ ,  $c_0^2 = \rho_0(r)^{-1}$ , and

$$\tilde{p}'' + \left( \frac{2kU'}{\omega - U(r)k} + \frac{1}{r} - \frac{\rho_0'}{\rho_0} \right) \tilde{p}' + \left( \rho_0(r)(\omega - U(r)k)^2 - k^2 - \frac{m^2}{r^2} \right) \tilde{p} = 0. \quad (14.2)$$

Just as in section 5.1 we require two boundary conditions. These are still given by; equation (5.11) for  $r = 0$  which corresponds to a regular solution. And equation (5.16), for  $r = 1$  and accounts for a non-slip flow profile.

As previously discussed when considering a uniform flow we will require a different boundary condition at the duct wall, because the mean flow will be slipping. The Ingard-Myers boundary condition [Ingard, 1959, Myers, 1980] is constructed by assuming a mean flow profile that is constant except within a boundary layer with non-slip at retrieved at the duct wall. The boundary condition is then given by the leading order terms of the pressure and velocity as the boundary layer thickness is taken to zero. In this way the specific shear flow profile does not effect the resulting boundary condition.

The Brambley boundary condition, also known as the Modified-Myers boundary condition, follows a similar construction, but provides the next order correction to the Ingard-Myers boundary condition in boundary layer thickness, assuming that shear flow region is thin, but finite. And so the Brambley boundary condition also observes effects from the specific mean flow profile being considered.

We proceed by deriving both boundary conditions, for a general flow profile, which follows a uniform flow before retrieving a non-slip condition within a thin boundary layer.

Considering the regular solution to (14.2) which is valid within the region of uniform flow,  $\tilde{p}_u(r) = J_m(\alpha r)$ . In order to achieve an outer expansion we consider  $r = 1 - hy$ , with  $h$  now assumed to be small, and perform a Taylor expansion about the duct wall;

$$\tilde{p}_u(1 - hy) = J_m(\alpha) - hy\alpha J'_m(\alpha) + \frac{h^2 y^2}{2} \alpha^2 J''_m(\alpha) + O(h^3). \quad (14.3)$$

In order to construct the inner solution, which will then be matched against the outer expansion above. We rewrite (14.2) as,

$$\left( \frac{r\tilde{p}'(r)}{(\omega - U(r)k)^2 \rho_0(r)} \right)' + \left( r - \frac{k^2 r + \frac{m^2}{r}}{(\omega - U(r)k)^2 \rho_0(r)} \right) \tilde{p}(r) = 0. \quad (14.4)$$

Making use of the the presence of  $\rho_0(r)$  within the coefficient of  $\tilde{p}(r)$ .

Once again setting  $r = 1 - hy$  with a prime now indicating differentiation with

respect to  $y$ , it follows;

$$\left(\frac{\tilde{p}'}{(\omega - Uk)^2 \rho_0}\right)' - h \left(\frac{y\tilde{p}'}{(\omega - Uk)^2 \rho_0}\right)' + O(h^2) = 0. \quad (14.5)$$

We proceed by making the ansatz for the inner solution of  $\tilde{p} = \tilde{p}_0 + h\tilde{p}_1 + O(h^2)$ , then solving the leading order problem it gives;

$$\left(\frac{\tilde{p}_0'(y)}{(\omega - Uk)^2 \rho_0}\right)' = 0 \quad (14.6a)$$

$$\frac{\tilde{p}_0'(y)}{(\omega - Uk)^2 \rho_0} = B_0 \quad (14.6b)$$

$$\tilde{p}_0'(y) = B_0(\omega - Uk)^2 \rho_0 \quad (14.6c)$$

$$\tilde{p}_0(y) = A_0 + B_0 \int_0^y (\omega - U(1 - h\hat{y})k)^2 \rho_0(1 - h\hat{y}) d\hat{y} \quad (14.6d)$$

Considering the limit  $y \rightarrow \infty$  such that we can match  $\tilde{p}_0(y)$  to our outer solution;

$$\lim_{y \rightarrow \infty} \tilde{p}_0(y) = A_0 + \lim_{y \rightarrow \infty} \int_0^y B_0(\omega - U(1 - h\hat{y})k)^2 \rho_0(1 - h\hat{y}) d\hat{y} \quad (14.7a)$$

$$\lim_{y \rightarrow \infty} \tilde{p}_0(y) = A_0 + \lim_{y \rightarrow \infty} \hat{B}_0 y + C_0(y) \quad B_0 = \frac{\hat{B}_0}{(\omega - Mk)^2} \quad (14.7b)$$

Since,  $U(1 - hy) = M$  and  $\rho_0(1 - hy) = 1$  for  $y > \frac{1}{h}$ , where;

$$c_0(y) = \hat{B}_0 \int_0^y \frac{(\omega - U(1 - h\hat{y})k)^2 \rho_0(1 - h\hat{y})}{(\omega - Mk)^2} d\hat{y} - \hat{B}_0 y \quad (14.7c)$$

Then, when we match the leading order inner and outer solutions. It is found from (14.6d),

$$\tilde{p}_0(y) = A_0 + \hat{B}_0 y - \hat{B}_0 \int_0^y 1 - (\omega - U(1 - h\hat{y})k)^2 \rho_0(1 - h\hat{y}) d\hat{y}, \quad (14.8a)$$

$$\lim_{y \rightarrow \infty} \tilde{p}_0(y) = A_0 + \lim_{y \rightarrow \infty} \hat{B}_0 y, \quad (14.8b)$$

$$= J_m(\alpha) = \lim_{y \rightarrow \infty} \tilde{p}_u(1 - hy) + O(h^2). \quad (14.8c)$$

It therefore follows,  $\hat{B}_0 = 0$  and  $A_0 = J_m(\alpha)$ .

Similarly for the first order terms,  $\tilde{p}_1$ , it is found

$$\left(\frac{\tilde{p}_1'(y)}{(\omega - Uk)^2 \rho_0}\right)' = 0, \quad (14.9)$$

$$\frac{\tilde{p}_1'(y)}{(\omega - Uk)^2 \rho_0} = B_1, \quad (14.10)$$

$$\tilde{p}_1'(y) = B_1(\omega - Uk)^2 \rho_0, \quad (14.11)$$

$$\tilde{p}_1(y) = A_1 + B_1 y - B_1 \int_0^y 1 - \frac{(\omega - U(1 - h\hat{y})k)^2 \rho_0(1 - h\hat{y})}{(\omega - Mk)^2} d\hat{y}. \quad (14.12)$$

Which we match to the order  $h$  term of  $\tilde{p}_u(1 - hy)$  in the large  $y$  limit, giving

$$B_1 = -\alpha J'_m(\alpha) \quad A_1 = B_1 \int_0^\infty 1 - \frac{(\omega - U(1 - h\hat{y})k)^2 \rho_0(1 - h\hat{y})}{(\omega - Mk)^2} d\hat{y}. \quad (14.13)$$

For convenience, this is  $A_1$  is rewritten as

$$A_1 = B_1 I_0 \quad I_0 = \int_0^\infty \frac{(\omega - U(1 - h\hat{y})k)^2 \rho_0(1 - h\hat{y})}{(\omega - Mk)^2} d\hat{y}, \quad (14.14)$$

and at the duct wall,  $y = 0$ , it follows

$$\tilde{p}(1) = J_m(\alpha) - hI_0\alpha J'_m(\alpha) + O(h^2). \quad (14.15)$$

Since the impedance boundary condition is given as  $Z = \frac{\tilde{p}(1)}{\tilde{v}(1)}$ , we next apply the same process to the velocity. Making use of equation (5.6d), we express the outer solution for  $\tilde{v}$  as,

$$\tilde{v}_u(1 - hy) = \frac{\frac{1}{h} \frac{\partial \tilde{p}_u(1 - hy)}{\partial y}}{\omega - Mk} \quad (14.16)$$

which gives,

$$\tilde{v}_u(1 - hy) = -\frac{i\alpha J'_m(\alpha)}{\omega - Mk} - h\gamma i \frac{\alpha J'_m(\alpha) + (\alpha^2 - m^2)J_m(\alpha)}{\omega - Mk} + O(h^2) \quad (14.17)$$

Where we have made use of Bessel's equation to write  $J''_m(\alpha)$  in terms of  $J'_m(\alpha)$  and  $J_m(\alpha)$ ;

$$z^2 J''_m = -z J'_m(z) - (z^2 - m^2)J_m(z). \quad (14.18)$$

In order to construct the inner solution, we start by taking the  $r$  derivative of equation (14.4) and rewriting the result in terms of the normal velocity;

$$\left( \left( \frac{r\tilde{p}'(r)}{(\omega - U(r)k)^2 \rho_0(r)} \right)' \left( r - \frac{k^2 r + \frac{m^2}{r}}{(\omega - U(r)k)^2 \rho_0(r)} \right)^{-1} \right)' + \tilde{p}'(r) = 0, \quad (14.19a)$$

$$\left( \left( \frac{r\tilde{v}(r)}{(\omega - U(r)k)} \right)' \left( r - \frac{k^2 r + \frac{m^2}{r}}{(\omega - U(r)k)^2 \rho_0(r)} \right)^{-1} \right)' + \rho_0(r)(\omega - U(r)k)\tilde{v}(r) = 0, \quad (14.19b)$$

where we have briefly used a prime to once again denote a derivative with respect

to  $r$ . Setting;

$$\bar{\alpha}^2 = \rho_0(r)(\omega - U(r)k)^2 - k^2 - \frac{m^2}{r^2}, \quad (14.20)$$

allows us to rewrite equation (14.4) as

$$\left( \left( \frac{r\tilde{v}(r)}{(\omega - U(r)k)} \right)' \frac{(\omega - U(r)k)^2 \rho_0(r)}{\bar{\alpha}^2 r} \right)' + \rho_0(r)(\omega - U(r)k)\tilde{v}(r) = 0. \quad (14.21)$$

Expanding (14.21) in powers of  $h$  and setting  $r = 1 - hy$  once more and using a prime to denote a derivative with respect to  $y$ , yields;

$$\begin{aligned} \left( \left( \frac{\tilde{v}}{(\omega - Uk)} \right)' \frac{1}{\bar{\alpha}_0^2} \right)' &= h \left( \left( \frac{y\tilde{v}}{\omega - Uk} \right)' \frac{1}{\bar{\alpha}_0^2} \right)' \\ &\quad - h \left( \left( \frac{\tilde{v}}{\omega - Uk} \right)' y \frac{(1 - \frac{k^2 - m^2}{(\omega - Uk)^2 \rho_0})}{\bar{\alpha}_0^4} \right)' \\ &\quad + O(h^2), \end{aligned} \quad (14.22a)$$

where;

$$\bar{\alpha}_0^2 = 1 - \frac{k^2 + m^2}{(\omega - Uk)^2 \rho_0}. \quad (14.22b)$$

Setting,  $\tilde{v}(1 - hy) = \tilde{v}_0(y) + h\tilde{v}_1(y) + O(h^2)$ , to leading order we find

$$\left( \frac{\tilde{v}_0}{\omega - Uk} \right)' = B_0 \left( 1 - \frac{k^2 + m^2}{(\omega - Uk)^2 \rho_0} \right) \quad (14.23a)$$

$$\frac{\tilde{v}_0}{\omega - Uk} = A_0 + B_0 \int_0^y 1 - \frac{k^2 + m^2}{(\omega - U(1 - h\hat{y})k)^2 \rho_0(1 - h\hat{y})} d\hat{y} \quad (14.23b)$$

$$\begin{aligned} \frac{\tilde{v}_0}{\omega - Uk} &= A_0 + \hat{B}_0 y ((\omega - Mk)^2 - (k^2 + m^2)) \\ &\quad - \hat{B}_0 (k^2 + m^2) \int_0^y 1 - \frac{(\omega - Mk)^2}{\alpha^2 (\omega - U(1 - h\hat{y})k)^2 \rho_0(1 - h\hat{y})} d\hat{y} \end{aligned} \quad (14.23c)$$

Which, when matched to the inner solution gives,

$$\lim_{y \rightarrow 0} \frac{\tilde{v}_0}{\omega - U(1 - hy)k} = \frac{\tilde{v}_0}{\omega - Mk} = \frac{\alpha J'_m(\alpha)}{(\omega - Mk)^2} \quad (14.24)$$

and

$$\hat{B}_0 = 0, \quad A_0 = -\frac{i\alpha J'_m(\alpha)}{(\omega - Mk)^2}. \quad (14.25)$$

Solving for the first order correction,

$$\left( \left( \frac{\tilde{v}_1}{(\omega - Uk)} \right)' \frac{1}{\bar{\alpha}_0^2} \right)' = \left( A_0 \frac{1}{\bar{\alpha}_0^2} \right)' \quad (14.26a)$$

$$\left( \frac{\tilde{v}_1}{(\omega - Uk)} \right)' = A_0 + B_1 \left( 1 - \frac{k^2 + m^2}{(\omega - Uk)^2 \rho_0} \right) \quad (14.26b)$$

$$\begin{aligned} \frac{\tilde{v}_1}{(\omega - Uk)} &= A_1 + A_0 y + \hat{B}_1 y ((\omega - Mk)^2 - (k^2 + m^2)) \\ &\quad - \hat{B}_1 (k^2 + m^2) \int_0^y 1 - \frac{(\omega - Mk)^2}{\alpha^2 (\omega - U(1 - h\hat{y})k)^2 \rho_0 (1 - h\hat{y})} d\hat{y}, \end{aligned} \quad (14.26c)$$

noting that,

$$(\omega - Mk)^2 - (k^2 + m^2) = \alpha^2 - m^2, \quad (14.26d)$$

it then follows when matching to the outer solutions,

$$\hat{B}_1 = \left( i \frac{\alpha J'_m(\alpha) + (\alpha^2 - m^2) J_m(\alpha)}{(\omega - Mk)^2} - \frac{\alpha J'_m(\alpha)}{(\omega - Mk)^2} \right) \frac{1}{(\omega - Mk)^2 - (k^2 + m^2)} \quad (14.26e)$$

$$= - \frac{i J_m(\alpha)}{(\omega - Mk)^2} \quad (14.26f)$$

$$A_1 = (k^2 + m^2) \hat{B}_1 \int_0^\infty 1 - \frac{(\omega - Mk)^2}{(\omega - U(1 - h\hat{y})k)^2 \rho_0 (1 - d\hat{y})} d\hat{y} \quad (14.26g)$$

which if we set

$$I_1 = \int_0^\infty 1 - \frac{(\omega - Mk)^2}{(\omega - U(1 - h\hat{y})k)^2 \rho_0 (1 - d\hat{y})} d\hat{y}, \quad (14.27)$$

gives,

$$\tilde{v}(1 - \delta y) = (\alpha J'_m(\alpha) - h J_m(\alpha)(y + (k^2 + m^2) I_1)) \frac{i(\omega - U(1 - \delta y)k)}{(\omega - Mk)^2} + O(h^2). \quad (14.28)$$

Making use of the expression,  $\tilde{p}(1) = Z\tilde{v}(1)$ , we can retrieve both the Ingard-Myers boundary condition, by taking the leading order terms of both, assuming  $U(1) = 0$ ;

$$J_m(\alpha) = Zi\omega \frac{J'_m(\alpha)}{(\omega - Mk)^2} \quad (14.29)$$

and the Brambley boundary condition by additionally considering the first order terms, assuming the pressure is given by the regular solution.

$$(\omega - Mk)^2 (J_m(\alpha) - h I_0 \alpha J'_m(\alpha)) = Zi(\omega - U(1)k) (\alpha J'_m(\alpha) - h I_1 (k^2 + m^2) J_m(\alpha)). \quad (14.30)$$

Which further acts as the dispersion relation for the Brambley Boundary Condition, which is more generally expressed as

$$(\omega - Mk)^2 (\tilde{p}(1) - h I_0 \tilde{p}'(1)) = Zi(\omega - U(1)k) (\tilde{p}'(1) - h I_1 (k^2 + m^2) \tilde{p}(1)). \quad (14.31)$$

where  $\tilde{p}$  is any solution to the Pridmore-Brown equation (14.2) in a slipping mean

flow  $U(1) \neq 0$ , such as uniform flow.

To conclude this section, we re-express  $I_0$  and  $I_1$  as integrals in  $r$ , observing that both are 0 when in the mean flow,

$$hI_0 = \int_{1-h}^1 1 - \frac{(\omega - U(r)k)^2 \rho_0(r)}{(\omega - Mk)^2} dr \quad (14.32)$$

$$hI_1 = \int_{1-h}^1 1 - \frac{(\omega - Mk)^2}{(\omega - U(r)k)^2 \rho_0(r)} dr. \quad (14.33)$$

Solving for  $hI_0$  and  $hI_1$  then becomes the main task for the implementation of the Brambley Boundary condition, with this given for a Linear shear flow profile in Brambley [2011b] as,

$$hI_0 = - \frac{hMk(3\omega - 2Mk)}{3(\omega - Mk)^2}, \quad (14.34)$$

$$hI_1 = \frac{hMk}{\omega}. \quad (14.35)$$

In addition a physical interpretation of  $hI_0$  and asymptotic forms of  $hI_1$  are given for  $\frac{\omega}{k} \gg 1$  and  $\frac{\omega}{k} \ll 1$  which are exact for the linear shear flow. In Brambley [2011b] an alternative approach to deriving the boundary condition involving the second order of  $\tilde{p}(r)$  is given. It is worth noting however, the boundary layer thickness is denoted  $\delta$ , to indicate a thin boundary layer, while here we continue making use of  $h$ .

## 14.1 The Quadratic-Brambley Boundary Condition

Once again assuming a quadratic shear flow profile

$$U(r) = \begin{cases} M & 0 \leq r \leq 1 - h \\ M(1 - (1 - \frac{1-r}{h})^2) & 1 - h \leq r \leq 1 \end{cases} \quad (14.36)$$

and assuming a constant normalised density  $\rho_0(r) = 1$ . Then we can solve for  $hI_0$  and  $hI_1$  exactly,

$$\begin{aligned} hI_0 &= \int_{1-h}^1 1 - \frac{(\omega - Mk + Mk(1 - \frac{1-r}{h})^2)^2}{(\omega - Mk)^2} dr, & (14.37a) \\ &= \int_{1-h}^1 1 - \frac{(\omega - Mk)^2 + 2(\omega - Mk)Mk(1 - \frac{1-r}{h})^2 + M^2k^2(1 - \frac{1-r}{h})^4}{(\omega - Mk)^2} dr, \\ &= - \int_{1-h}^1 \frac{2(\omega - Mk)Mkh^{-2}(h - 1 + r)^2 + M^2k^2h^{-4}(h - 1 + r)^4}{(\omega - Mk)^2} dr, \\ &= - \int_0^h \frac{2Mk\hat{r}^2}{h^2(\omega - Mk)} + \frac{M^2k^2\hat{r}^4}{h^4(\omega - Mk)^2} d\hat{r}, \end{aligned}$$

$$= -\frac{2Mkh}{3(\omega - Mk)} - \frac{M^2k^2h}{5(\omega - Mk)^2} = -h\frac{Mk(10\omega - 7Mk)}{15(\omega - Mk)^2}. \quad (14.37b)$$

and

$$hI_1 = \int_{1-h}^1 1 - \frac{(\omega - Mk)^2}{(\omega - Mk + Mk(1 - \frac{1-r}{h})^2)^2} dr, \quad (14.38a)$$

$$= h - \int_{1-h}^1 \frac{(\omega - Mk)^2}{(\omega - Mk + Mkh^{-2}\hat{r}^2)^2} d\hat{r},$$

$$= h - \int_0^h \frac{1}{(1 + \frac{Mk\hat{r}^2}{h^2(\omega - Mk)})^2} d\hat{r},$$

$$= h - h\sqrt{\frac{\omega - Mk}{Mk}} \int_0^{\sqrt{\frac{Mk}{\omega - Mk}}} \frac{1}{(1 + \tilde{r}^2)^2} d\tilde{r},$$

$$= h - h\sqrt{\frac{\omega - Mk}{Mk}} \int_0^{\sqrt{\frac{Mk}{\omega - Mk}}} \frac{1 - \tilde{r}^2}{2(1 + \tilde{r}^2)^2} + \frac{1}{2(1 + \tilde{r}^2)} d\tilde{r},$$

$$= h - h\sqrt{\frac{\omega - Mk}{Mk}} \frac{\tilde{r}}{2(1 - \tilde{r}^2)} \Big|_0^{\sqrt{\frac{Mk}{\omega - Mk}}} - h\sqrt{\frac{\omega - Mk}{Mk}} \int_0^{\sqrt{\frac{Mk}{\omega - Mk}}} \frac{1}{2(1 + \tilde{r}^2)} d\tilde{r},$$

$$= h - h\frac{(\omega - Mk)}{2\omega} - h\sqrt{\frac{\omega - Mk}{Mk}} \int_0^{\sqrt{\frac{Mk}{\omega - Mk}}} \frac{1}{2(1 + \tilde{r}^2)} d\tilde{r},$$

$$= h - h\frac{(\omega - Mk)}{2\omega} - h\sqrt{\frac{\omega - Mk}{Mk}} \int_0^{\sqrt{\frac{Mk}{\omega - Mk}}} \frac{1}{4i} \left( \frac{i}{1 + i\tilde{r}} - \frac{-i}{1 - i\tilde{r}} \right) d\tilde{r},$$

$$= h - h\frac{(\omega - Mk)}{2\omega} + \frac{ih}{4} \sqrt{\frac{\omega - Mk}{Mk}} \log \left( \frac{1 + i\sqrt{\frac{Mk}{\omega - Mk}}}{1 - i\sqrt{\frac{Mk}{\omega - Mk}}} \right), \quad (14.38b)$$

$$= h - h\frac{(\omega - Mk)}{2\omega} - \frac{h}{2} \sqrt{\frac{\omega - Mk}{Mk}} \tan^{-1} \left( \sqrt{\frac{Mk}{\omega - Mk}} \right). \quad (14.38c)$$

We can then re-write the dispersion relation, (14.31) as

$$\left[ i\omega Z - \frac{hMk(10\omega - 7Mk)}{15} \right] \alpha J'_m(\alpha) - J_m(\alpha) \left[ \frac{ihZ}{2} (k^2 + m^2)(\omega + Mk) + (\omega - Mk)^2 - \frac{i\omega hZ}{2} (k^2 + m^2) \sqrt{\frac{\omega - Mk}{Mk}} \tan^{-1} \left( \sqrt{\frac{Mk}{\omega - Mk}} \right) \right] = 0. \quad (14.39)$$

It is worth noting that this dispersion relation contains a branch cut within the  $\tan^{-1}$  term with a branch point when  $\omega - Mk = 0$ . For conciseness we will denote

$$C = i\omega Z - \frac{hMk(10\omega - 7Mk)}{15} \quad (14.40a)$$

$$D_1 = \frac{ihZ}{2} (k^2 + m^2)(\omega + Mk) + (\omega - Mk)^2 \quad (14.40b)$$

$$D_2 = -\frac{i\omega hZ}{2}(k^2 + m^2)\sqrt{\frac{\omega - Mk}{Mk}} \tan^{-1} \left( \sqrt{\frac{Mk}{\omega - Mk}} \right). \quad (14.40c)$$

Such that the dispersion relation can be rewritten as

$$\mathcal{D}(\omega, k) = \alpha J'_m(\alpha) - \frac{D_1 + D_2}{C} J_m(\alpha) \quad (14.40d)$$

and the Quadratic-Brambley Boundary condition,

$$C\tilde{p}'(1) = (D_1 + D_2)\tilde{p}(1), \quad (14.41)$$

with all of terms that see the branch cut are contained within  $D_2$ . It will be shown in the following section that this  $\tan^{-1}$  branch cut aligns exactly with the critical layer branch cut from the full solutions.

## 14.2 The Critical Layer Branch Cut in the Quadratic-Brambley Boundary Condition

We consider the branch cut of

$$\sqrt{\frac{\omega - Mk}{Mk}} \tan^{-1} \left( \sqrt{\frac{Mk}{\omega - Mk}} \right) = -\sqrt{\frac{\omega - Mk}{Mk}} \frac{i}{2} \log \left( \frac{1 + i\sqrt{\frac{Mk}{\omega - Mk}}}{1 - i\sqrt{\frac{Mk}{\omega - Mk}}} \right) \quad (14.42)$$

Taking the log branch cut along the negative real axis, one can find that  $\log(\frac{1+iZ}{1-iZ})$  has two branch cuts along the positive and negative imaginary  $Z$  axis from  $\pm i$  respectively, these correspond to  $\log(a)$  with  $-1 \geq a \geq -\infty$  and  $-1 \leq a \leq 0$  respectively.

In addition to the log branch cuts, we are also required to consider the square root branch cuts. Writing;

$$z = \sqrt{\frac{Mk}{\omega - Mk}} = z^+ = \frac{i}{\sqrt{1 - \frac{\omega}{Mk}}} \quad (14.43)$$

then we only observe  $z$  being purely imaginary when  $k > \frac{\omega}{M}$ , the positive real half line  $[\frac{\omega}{M}, \infty)$  or when  $k < 0$ . If we instead take the other branch of square root,

$$z = z^- = \frac{-i}{\sqrt{1 - \frac{\omega}{Mk}}}, \quad (14.44)$$

which is only purely imaginary when once again we are on the positive real half line  $[\frac{\omega}{M}, \infty)$  or have  $k < 0$ . Making use of that  $z^+ = -z^-$  then it can be shown that

$$\frac{1}{z^+} \log \left( \frac{1 + iz^+}{1 - iz^+} \right) = -\frac{1}{z^-} \log \left( \frac{1 - iz^-}{1 + iz^-} \right) = \frac{1}{z^-} \log \left( \frac{1 + iz^-}{1 - iz^-} \right) \quad (14.45)$$

and therefore we do not observe a contribution for crossing the square root branch cut irrespective to how it is taken. For clarity we will take the square root branch cut along the negative real axis. In the complex  $k$  plane this is equivalent to being taken along the negative half line  $(-\infty, 0)$  and the positive real half line  $(\frac{\omega}{M}, \infty)$ .

We associate the positive half line  $[\frac{\omega}{M}, \infty)$ , from the log branch cut, as being the critical layer branch cut. We now consider the jump in the dispersion relation for a value of  $k$  that crosses the critical layer branch cut. To this end we set  $k^\pm = \frac{\omega}{M}(\gamma \pm i\epsilon)$ , with  $\gamma \geq 1$ ,  $\epsilon > 0$ , then equation (14.42) becomes;

$$D(k^\pm) = -\sqrt{\frac{\omega - Mk}{Mk}} \frac{i}{2} \log \left( \frac{1 + i\sqrt{\frac{Mk}{\omega - Mk}}}{1 - i\sqrt{\frac{Mk}{\omega - Mk}}} \right) \quad (14.46a)$$

$$= \mp \frac{1}{2} \sqrt{\frac{\gamma - 1}{\gamma}} \pm \frac{i\epsilon}{\gamma^2} \log \left( \frac{1 \mp \frac{1}{\gamma - 1} \sqrt{\gamma(\gamma - 1)} \mp i\epsilon}{1 \pm \frac{1}{\gamma - 1} \sqrt{\gamma(\gamma - 1)} \mp i\epsilon} \right) \quad (14.46b)$$

$$= \mp \frac{1}{2} \sqrt{\frac{\gamma - 1}{\gamma}} \pm \frac{i\epsilon}{\gamma^2} \log \left( 1 \mp \sqrt{\frac{\gamma}{\gamma - 1}} + \frac{i\epsilon}{2\sqrt{\gamma(\gamma - 1)^3}} \right) \\ \pm \frac{1}{2} \sqrt{\frac{\gamma - 1}{\gamma}} \pm \frac{i\epsilon}{\gamma^2} \log \left( 1 \pm \sqrt{\frac{\gamma}{\gamma - 1}} - \frac{i\epsilon}{2\sqrt{\gamma(\gamma - 1)^3}} \right) \quad (14.46c)$$

Taking  $\epsilon \rightarrow 0$ , and continuing to take the log branch cut along the negative real axis gives,

$$D(k^\pm) = \mp \frac{1}{2} \sqrt{\frac{\gamma - 1}{\gamma}} \log \left( \left( \sqrt{\frac{\gamma}{\gamma - 1}} \mp 1 \right) e^{i\pi\mathbb{I}_+} \right) \\ \pm \frac{1}{2} \sqrt{\frac{\gamma - 1}{\gamma}} \log \left( \left( \sqrt{\frac{\gamma}{\gamma - 1}} \pm 1 \right) e^{-i\pi\mathbb{I}_-} \right) \quad (14.46d)$$

Then writing the jump for crossing the branch cut, from above to below, as  $\Delta D(k) = D(k^-) - D(k^+)$ , gives,

$$\Delta D(k) = i\pi \sqrt{\frac{\gamma - 1}{\gamma}} = \pi \sqrt{\frac{\omega - Mk^+}{Mk^+}} = -\pi \sqrt{\frac{\omega - Mk^-}{Mk^-}} \quad (14.47)$$

and as a result,

$$\Delta D_2 = -\frac{i\omega hZ}{2} (k_+^2 + m^2) \pi \sqrt{\frac{\omega - Mk^+}{Mk^+}} = \frac{i\omega hZ}{2} (k_-^2 + m^2) \pi \sqrt{\frac{\omega - Mk^-}{Mk^-}} \quad (14.48)$$

It then further follows that

$$\Delta\mathcal{D}(k) = -\frac{15i\omega hZ(k^2 + m^2)\pi\sqrt{\frac{\omega - Mk^+}{Mk^+}}}{2[15i\omega Z - hMk(10\omega - 7Mk)]} = \frac{15i\omega hZ(k^2 + m^2)\pi\sqrt{\frac{\omega - Mk^-}{Mk^-}}}{2[15i\omega Z - hMk(10\omega - 7Mk)]} \quad (14.49)$$

And our dispersion relation for poles in the  $\text{Im}(k) < 0$  half plane hidden behind the branch cut is,

$$\mathcal{D}^+(\omega, k) = \alpha J'_m(\alpha) - \frac{D_1 + D_2 + \Delta D_2}{C} J_m(\alpha) = 0 \quad (14.50a)$$

Which written in full is;

$$\left[ i\omega Z - \frac{hMk(10\omega - 7Mk)}{15} \right] \alpha J'_m(\alpha) - J_m(\alpha) \left[ \frac{i\omega hZ}{2\omega} (k^2 + m^2)(\omega + Mk) + (\omega - Mk)^2 - \frac{i\omega hZ}{2} (k^2 + m^2) \sqrt{\frac{\omega - Mk}{Mk}} \tan^{-1} \left( \sqrt{\frac{Mk}{\omega - Mk}} \right) + \frac{i\omega h\pi Z}{2} (k^2 + m^2) \sqrt{\frac{\omega - Mk}{Mk}} \right] = 0. \quad (14.50b)$$

or as a boundary condition for uniform mean flow as

$$C\tilde{p}'(1) = (D_1 + D_2 + \Delta D_2)\tilde{p}(1). \quad (14.50c)$$

With the Quadratic-Brambley boundary condition (14.1), and its analytic continuation through the critical layer branch cut, (14.50c) we can once again locate and track the modal poles, including any hydrodynamic instabilities that may be hidden behind the critical layer branch cut just as in the full solutions.

## 15 Mode Locations

In the following section we compare the location of the modal poles of the Brambley boundary condition under a quadratic shear flow profile, the Quadratic-Brambley boundary condition, to that of the Ingard-Myers boundary condition, and the Brambley boundary condition under a linear shear flow profile, the Linear-Brambley boundary condition.

Figures 31 and 32 depict the locations of the modes and critical layer branch cut for the Quadratic-Brambley boundary condition, and  $k^+$  poles located behind and

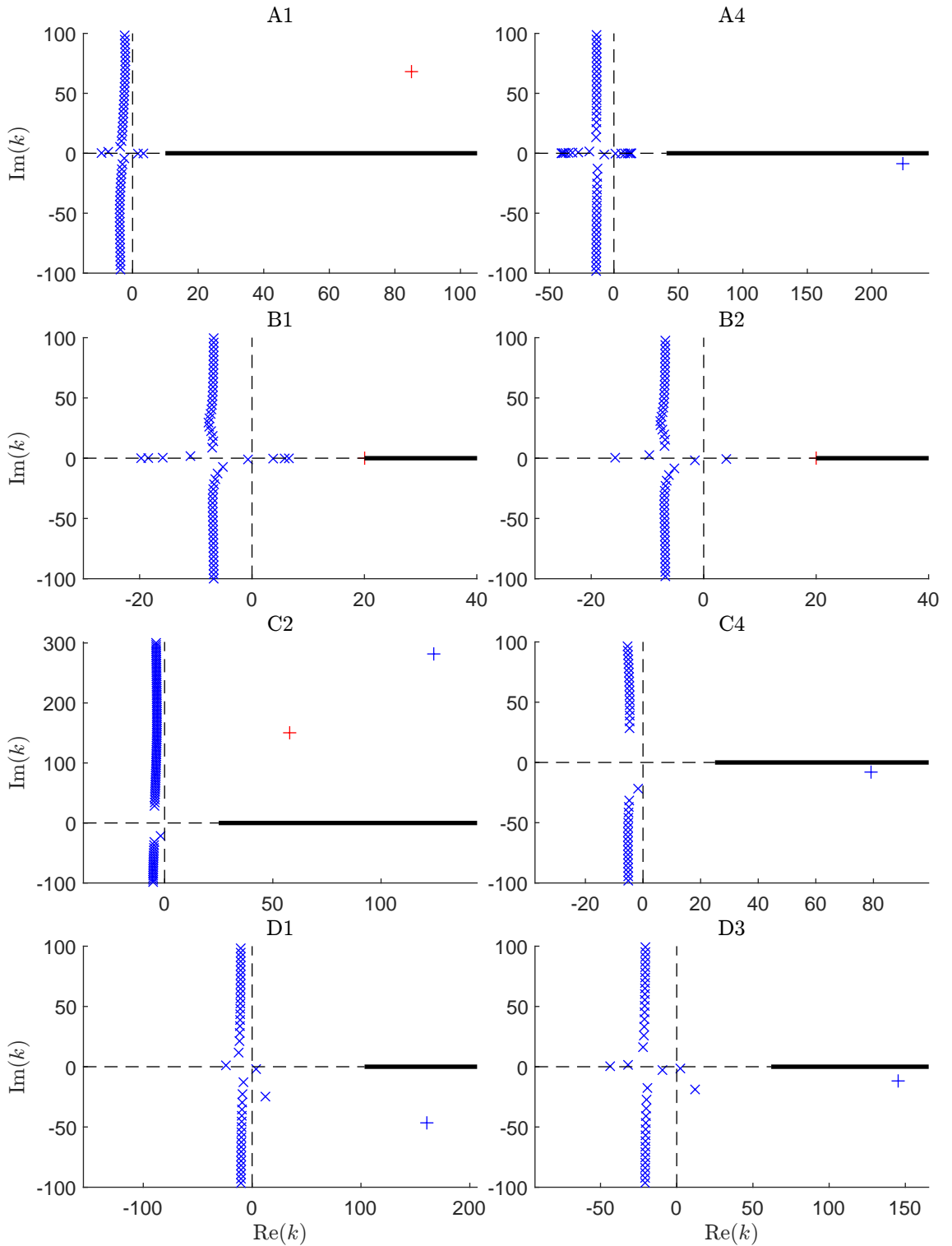


Figure 31: Location of the poles in the complex  $k$  plane for a Uniform flow under the Quadratic-Brambley boundary condition. Plotted for two sub-parameter sets from each of the parameter sets  $A - D$ . The usual acoustic modal poles have been marked with an ( $\times$ ). The critical layer branch cut, ( $-$ ), and any  $k^+$  modal poles ( $+$ ). Modes that are coloured red are unstable under the Briggs-Bers criterion. Stable  $k^+$  modes located in the lower half plane are ‘hidden’ behind the branch cut.

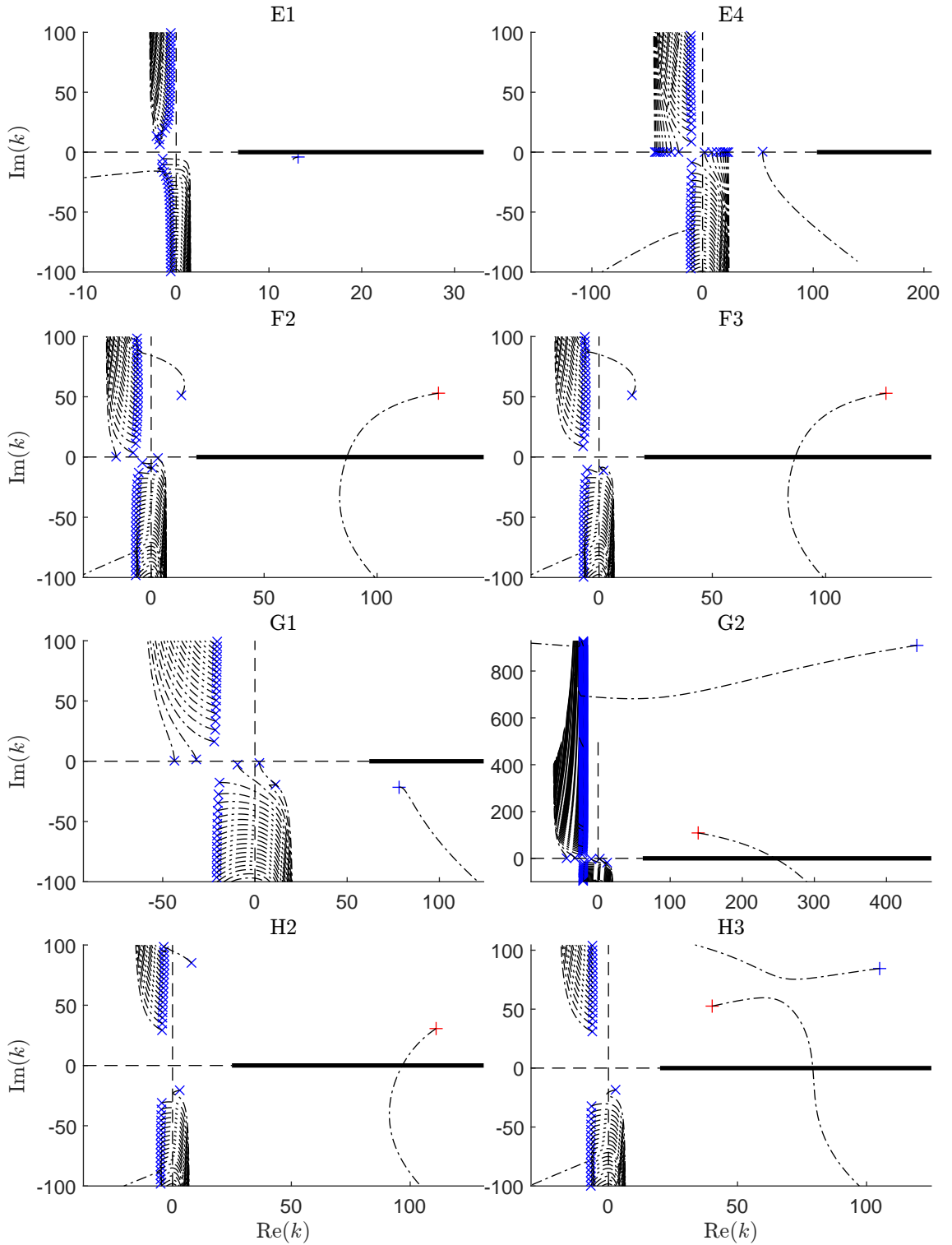


Figure 32: Location of the poles in the complex  $k$  plane for two sub-parameter sets from each of the parameter sets  $E-H$ . As figure 31 with the Briggs-Bers trajectories as  $\text{Im}(\omega)$  is varied from 0 to  $-50$  ( $-\cdot-$ ), with locations at  $\text{Im}(\omega) = 0$  marked as a pole.

below the branch cut using the dispersion relation for these modes. Figure 32 in addition also plots the Briggs-Bers trajectories used to find the stability of the modes. Once again it may be observed that the hydrodynamic instability is present in many cases (*A1, B1, B2, C2, F2, F3, G2, H2* and *H3*.) Although, as was seen for the full solution, it may be stabilised once again by moving through the critical layer branch cut such as for *A4, C4, D1, D4, E1* and *G1*.

This leaves an exception in parameter set *E4*. In this particular case it may at first seem that no  $k^+$  has been located. Rather, for this parameter set, the  $k^+$  is also located below the branch cut, however it has moved to the left of the critical layer branch cut,  $\text{Re}(k^+) < \frac{\omega}{M}$ , and so stops contributing to the Fourier inversion under the deformation onto the steepest descent contours. Similar behaviour will be seen as we vary the different parameter sets and track the movement of the modes.

Figure 33 plots the locations of the modal poles and the critical layer branch cut for each of the Ingard-Myers, Linear-Brambley, and Quadratic-Brambley boundary conditions, although it should be noted that the critical layer branch cut is only present for the Quadratic-Brambley boundary condition.

In this figure it can be observed that while the acoustic modes are all similarly located in each of the boundary conditions, with a small number of outliers, the difference between the  $k^+$  poles, may vary drastically. In particular, the Linear-Brambley boundary condition always has a hydrodynamic instability present, while the Ingard-Myers in some cases (*H1*) presents no such mode. It is additionally observable, as may have been expected from the comparisons of the full solutions in section 12.4, when the  $k^+$  mode is stable for the Quadratic-Brambley boundary condition, the hydrodynamic instability in the Linear-Brambley boundary condition has a small imaginary part. Therefore the mode will have a small growth rate under Fourier inversion. This will be investigated further in section 17.

Just as was done for the full solutions we can once again track the locations of the modes as each of the parameters are varied, this is done in figures 34-37.

It can be observed when varying the boundary layer thickness, figure 34, as may have been expected from the full solutions, the Quadratic-Brambley boundary condition sees a stabilising effect for increasing the boundary layer thickness. However, unlike in the case of the full solution there exists a second thicker boundary layer thickness that cause the stabilised  $k^+$  pole to move back through the critical layer in cases *B2, F1* and *G2*. Although at this time this behaviour has not been investigated further it is expected this is related to the assumptions made on the size of  $h$  as a small parameter in the construction of the Brambley boundary condition. To perform an asymptotic expansion and to construct the boundary condition we have required the

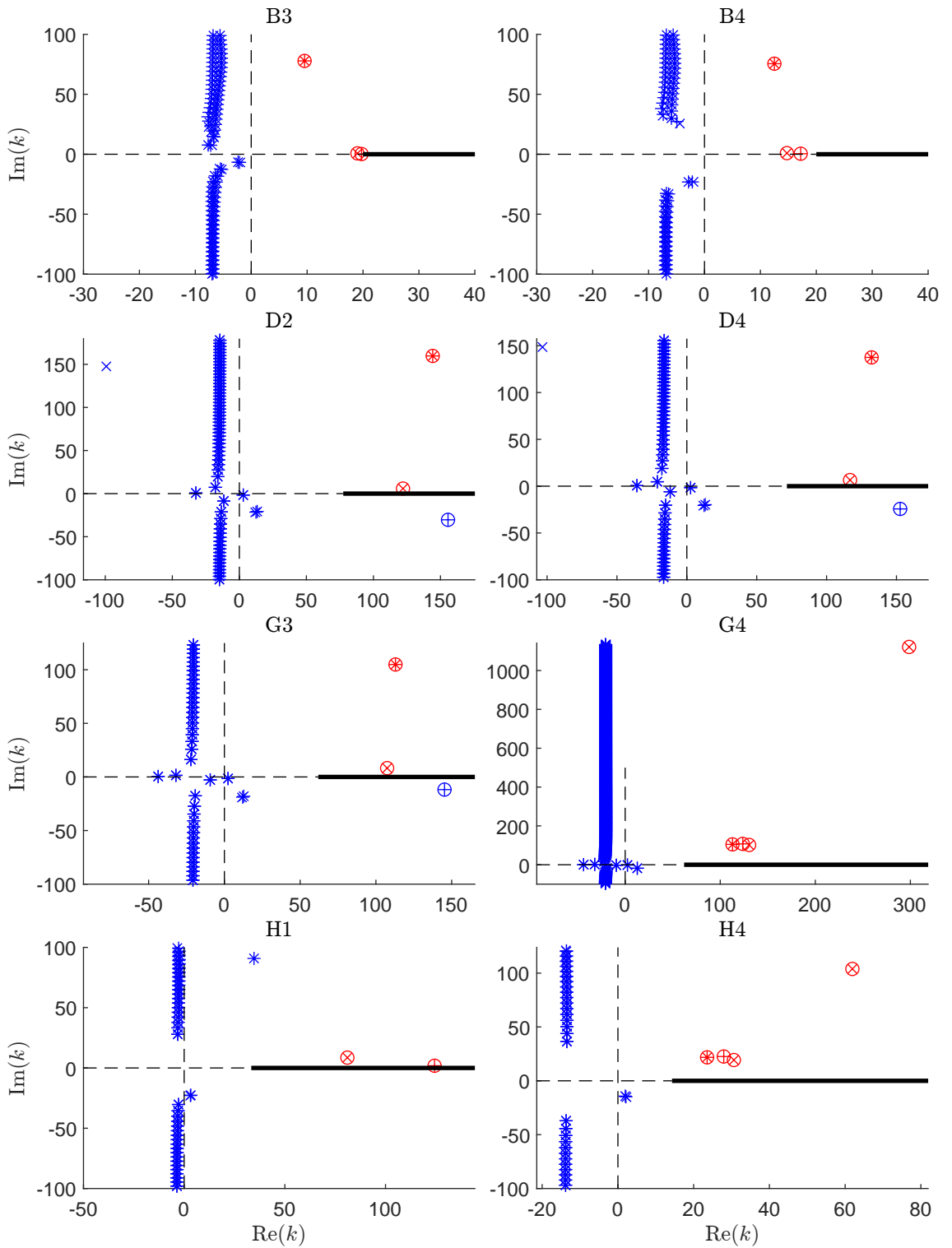


Figure 33: Location of the contributing modes for a uniform flow under each of the Ingard-Myers boundary condition (\*), the Linear-Brambley boundary condition ( $\times$ ), and the Quadratic-Brambley boundary condition ( $+$ ). Stable modes are coloured blue, while unstable modes are red. Any hydrodynamic instabilities, or modes hidden behind the branch cut are circled ( $\otimes$ ,  $\oplus$ ). Plotted for parameter sets  $B3$ ,  $B4$ ,  $D2$ ,  $D4$ ,  $G3$ ,  $G4$ ,  $H1$  and  $H4$

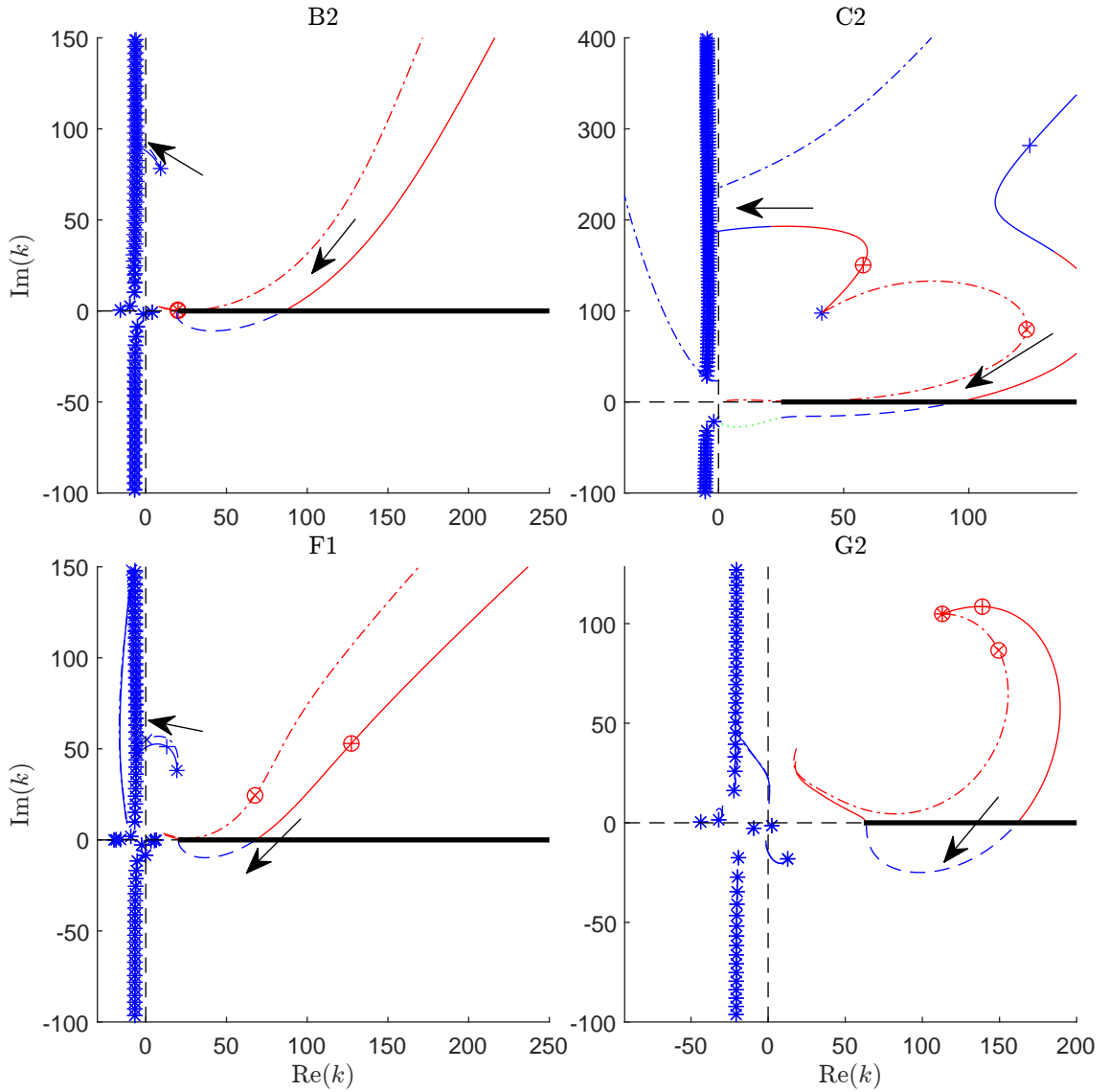


Figure 34: Location of the modes for a uniform flow under the Ingard-Myers boundary condition (\*), the Linear-Brambley boundary condition ( $\times$ ), and the Quadratic-Brambley boundary condition ( $+$ ). Any hydrodynamic instabilities, or modes hidden behind the branch cut are circled ( $\otimes, \oplus$ ). Plotted for parameter sets  $B2$ ,  $C2$ ,  $F1$  and  $G2$  with trajectories as the boundary layer thickness  $h$  is varied from  $h = 0.3$  to  $h = 10^{-6}$ . Tracks for the Linear-Brambley boundary condition are marked  $(-\cdot-)$ , while tracks for the Quadratic-Brambley boundary condition are solid lines  $(--)$ , except when the mode is behind the branch cut, where a dashed line  $(- -)$  is used for a mode below the branch cut, with  $\text{Re}(k) > \frac{\omega}{M}$ , and a green dotted line  $(\dots)$  when  $\text{Re}(k) < \frac{\omega}{M}$ . Arrows indicate the direction of increasing boundary layer thickness  $h$ .

$O(h^2)$  to be negligible. It should be noted that for parameter set *C2* that instead of moving back through the critical layer the  $k^+$  pole moves to the left of the critical layer branch cut and stops contributing to the Fourier Inversion, as was observed for parameter set *E4* in figure 32.

Additionally for parameter set *C2* we observe two potential  $k^+$  poles present, with once again only one appearing as a hydrodynamic instability for any particular parameter set, and as  $h \rightarrow 0$  one of these modes moves out to  $|k^+| = \infty$ , being no longer present in the limit, while the other becomes unstable and moves into the stable modal pole of the Ingard-Myers boundary condition. Thus although the mode locations are retrieved the solutions present different stabilities. It is suspected this is due to the failure of the Ingard-Myers boundary condition in the time domain.

Similar behaviour to the modes of the Quadratic-Brambley is seen within the modes for the Linear-Brambley boundary condition. However, careful consideration of the stability of these modes however is required, and without performing a separate stability analysis one may incorrectly assume the stability of the two potential  $k^+$  poles based off of the Quadratic-Brambley boundary condition. In addition to the Ingard-Myers boundary condition poles being recovered for parameter set *C2* as  $h \rightarrow 0$  in both the Linear and Quadratic-Brambley boundary conditions, it is retrieved for parameter sets *B2* and *F1*, where the Ingard-Myers boundary condition mode was found to be stable. In these cases however it is not the usual hydrodynamic instability mode that converges to this location, but a stable modal pole which has come out of the usual acoustic modes. In these cases no miss-match in stability is observed.

Figure 35 instead varies the Mach number of the flow. Just as in the case of the full solutions figure 35 scales the complex  $k$  plane by  $\frac{M}{\omega}$  such that the critical layer branch cut remains fixed as a frame of reference.

Firstly, we observe that as the Mach number increases, each of the hydrodynamic instabilities converge for the three different boundary conditions while as the no-flow limit is approach a stable system is retrieved, with the unstable modes each being removed with  $|k^+| \rightarrow \infty$ , or joining the usual acoustic modes (figure 35 *F4* and *G4*) noting that the branch point  $\frac{\omega}{M} \rightarrow \infty$  in this limit.

Although not immediately obvious in figure 31 *B2*, in the zoomed plot for *B2* of figure 35, it can be seen that the unstable  $k^+$  modes are actually located to the left of the critical layer branch cut. Despite this, as the Mach number is decreased the mode is still seen to stabilise, moving through the critical layer by first moving right, and then through near  $\frac{\omega}{M}$ , with the stabilised mode not contributing to the steepest descent contours for a range of Mach numbers, before moving back to the right. This behaviour would not have been expected based on observations from the

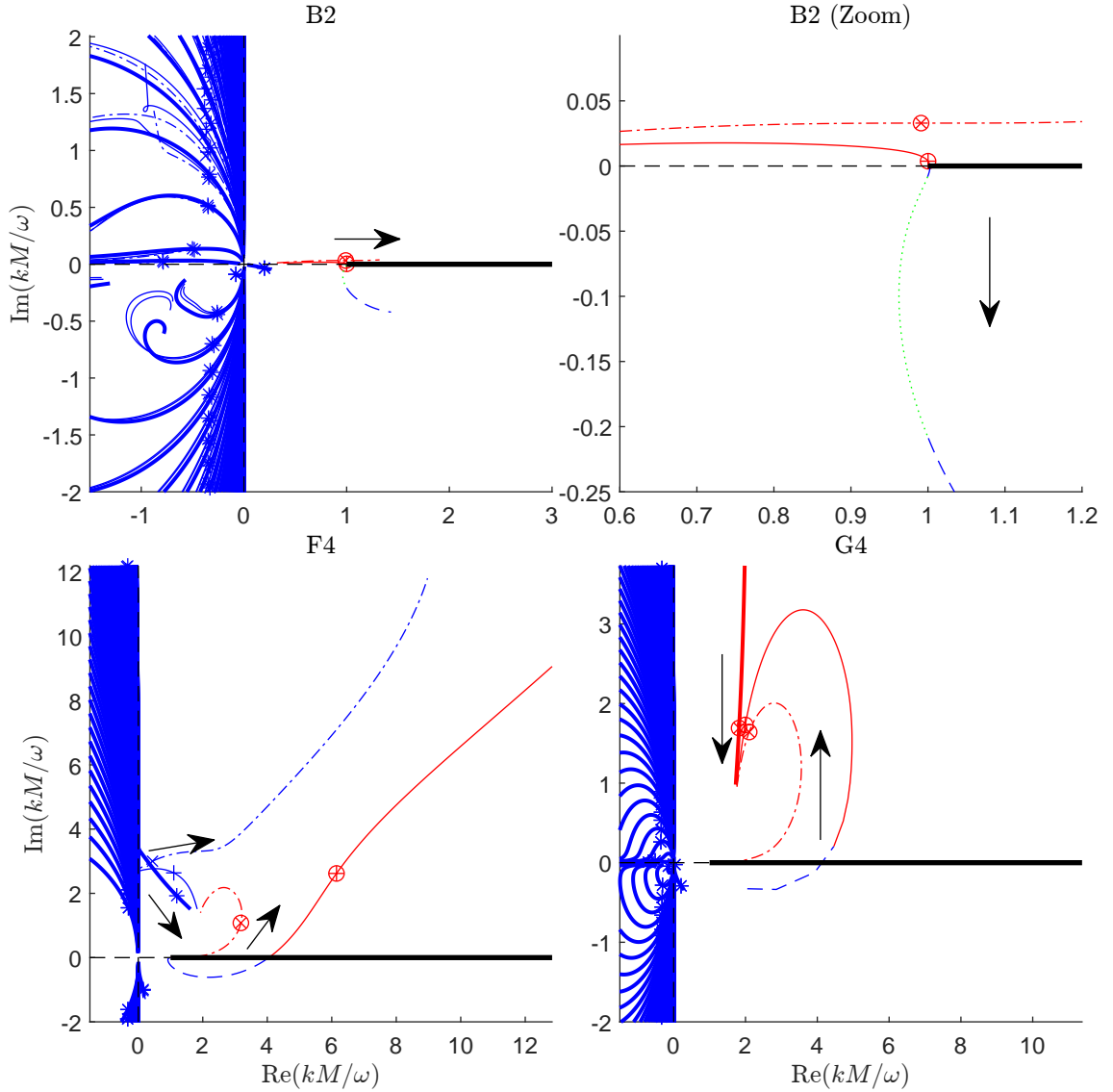


Figure 35: Location of the modes for a uniform flow under the Ingard-Myers boundary condition (\*), the Linear-Brambley boundary condition ( $\times$ ), and the Quadratic-Brambley boundary condition (+) on a scaled complex  $k$  plane. Any hydrodynamic instabilities, or modes hidden behind the branch cut are circled ( $\otimes, \oplus$ ). Plotted for parameter sets  $B2$ ,  $F4$ , and  $G4$  with trajectories as the Mach number  $M$  is varied from  $M = 0.05$  to  $M = 0.95$ . Tracks of the Ingard-Myers boundary condition, using thick solid lines, tracks for the Linear-Brambley boundary condition are marked ( $-\cdot-$ ), while tracks for the Quadratic-Brambley boundary condition are solid lines ( $---$ ), except when the mode is behind the branch cut, where a dashed line ( $---$ ) is used for a mode below the branch cut, with  $\text{Re}(k) > \frac{\omega}{M}$ , and a green dotted line ( $\cdots$ ) when  $\text{Re}(k) < \frac{\omega}{M}$ . Arrows indicate the direction of increasing boundary layer thickness  $M$ .

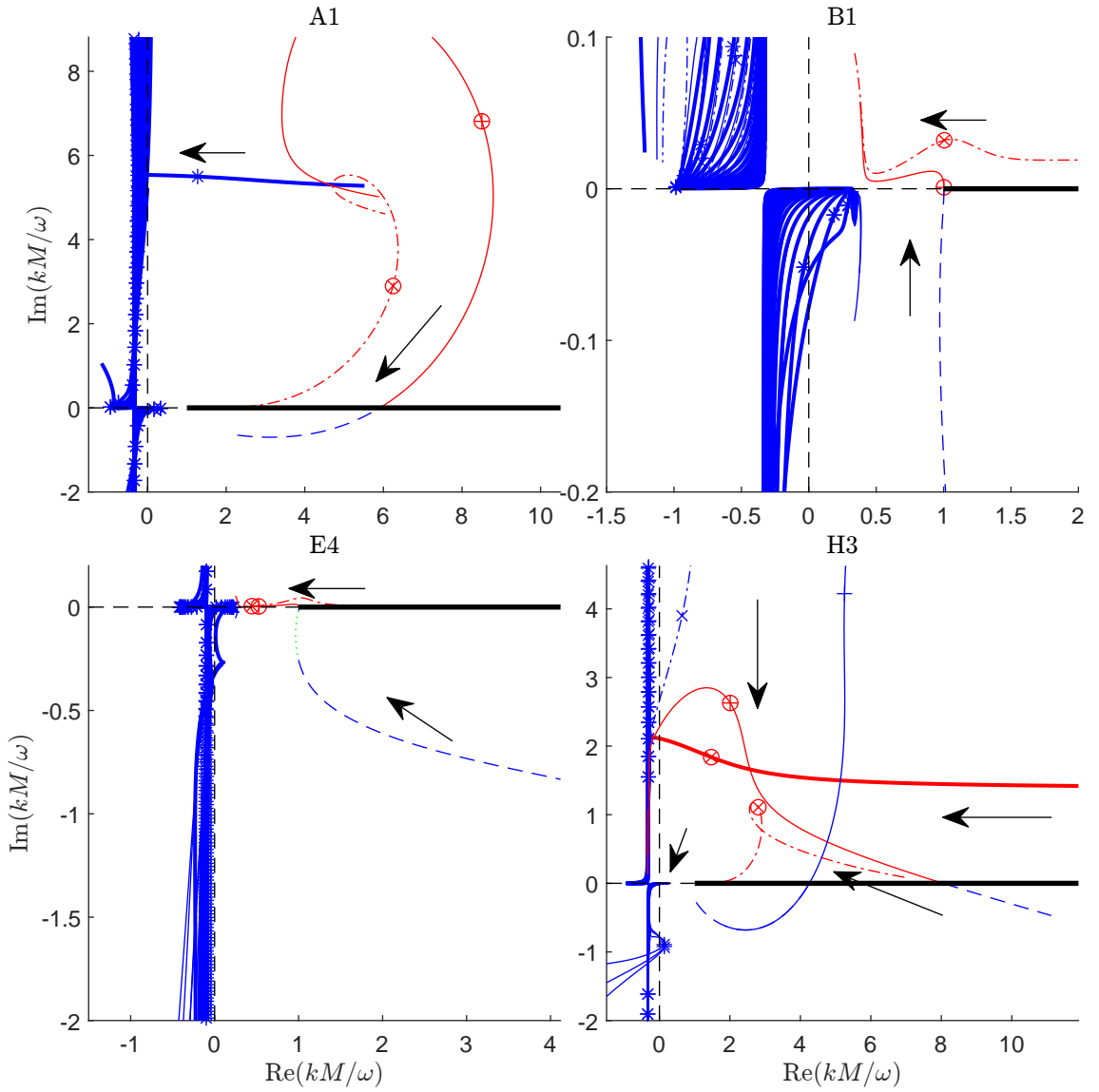


Figure 36: As figure 35, while tracking the frequency number from  $\omega = 0.5$  to  $\omega = 75$ . Arrows indicate the direction of increasing frequency  $\omega$ .

full solutions where in each case the  $k^+$  pole was observed to move into the branch point as the Mach number was decreased, as is still observed for parameter set  $F4$ , and would have otherwise been assumed for  $G4$ .

If we instead vary the frequency  $\omega$ , as is done in figure 36. When  $\omega$  is large, each of the hydrodynamic instabilities, within the Ingard-Myers and the Quadratic-Brambley boundary conditions retrieve stable modes, with the  $k^+$  mode located behind the branch cut in each case for for the Quadratic-Brambley boundary condition. Somewhat similarly, although unstable the Linear-Brambley boundary condition, has small imaginary part, and so a small growth rate, albeit still exponential. It additionally remains true that for small  $\omega$  stability has is observed in some cases. However just as for the linear shear flow when stability has not been observed, the imaginary part is seen to be small, such as for  $B1$ ,  $E4$  and  $H3$ , while for parameter

set  $A1$  we can not make this same conclusion. It is unclear if this lack of stabilisation is a result of the numerics and difficulty resolving the problem for small  $\omega$  or a consequence of the Quadratic-Brambley boundary condition acting as the Linear-Brambley boundary condition within the small  $\frac{\omega}{k}$  limit [Brambley, 2011b]. This is seemingly contrary to the behaviour of the other parameter sets, where in each case the  $k^+$  mode of the Ingard-Myers boundary condition increases as can be observed for parameter set  $H3$ , with imaginary part that tends to some constant under scaling by  $\frac{1}{\omega}$ , suggesting that the true value of this mode decreases in imaginary part linearly with the frequency. This same behaviour is present for parameter sets  $B1$  and  $E4$ , although it is not included here, in favor for observing the stabilised behaviour in greater detail.

Although once again it would be worth while investigating how the poles move as the frequency is varied independently from the impedance this analysis has not been included here due to being unphysical of the applications. We do however vary the impedance  $Z$ , by varying the reactance in figure 37.

As would be expected only the Quadratic-Brambley expresses stabilisation by the poles moving through the critical layer, however this is not seen in every case. In particular, parameter set  $B2$  does not see a stabilisation of the  $k^+$  pole for any impedance, with the mode being located to the left of the critical layer branch cut, and above the real line. Thus despite stability being expected for all hard walled ducts in the case of full solution, we do not see the same behaviour for the Quadratic-Brambley boundary condition. This does however suggest that the only process under which the pressure field can be stabilised is through the crossing of the critical layer branch cut by the hydrodynamic instability. This lack of stabilisation for a hard walled duct is not what would be expected of applications, although case such as  $D3$  and  $H3$  clearly illustrate that cases exist where the hard walled behaviour is stable, and indeed this appears to be more generally true throughout the various investigated parameter sets.

For the Ingard-Myers boundary condition this stability for a hard walled duct is attained, although the specific behaviour varies depending on how the hard walled limit is taken. Particularly, for  $\text{Im}(Z) \rightarrow -\infty$ , the  $k^+$  pole is seen to join the usual modal sum, becoming stable based on how the imaginary part of the frequency  $\text{Im}(\omega) \rightarrow 0$  from below, once again suggesting an ill-posed time domain problem. As  $\text{Im}(Z) \rightarrow \infty$ , as can be observed in figure 37, the  $k^+$  pole has increasing real part, and is not present in the limit, although for any fixed impedance  $|Z| \neq \infty$ , it remains unstable, and will dominate the far-field.

An advantage of the Quadratic-Brambley over these other two Brambley condition

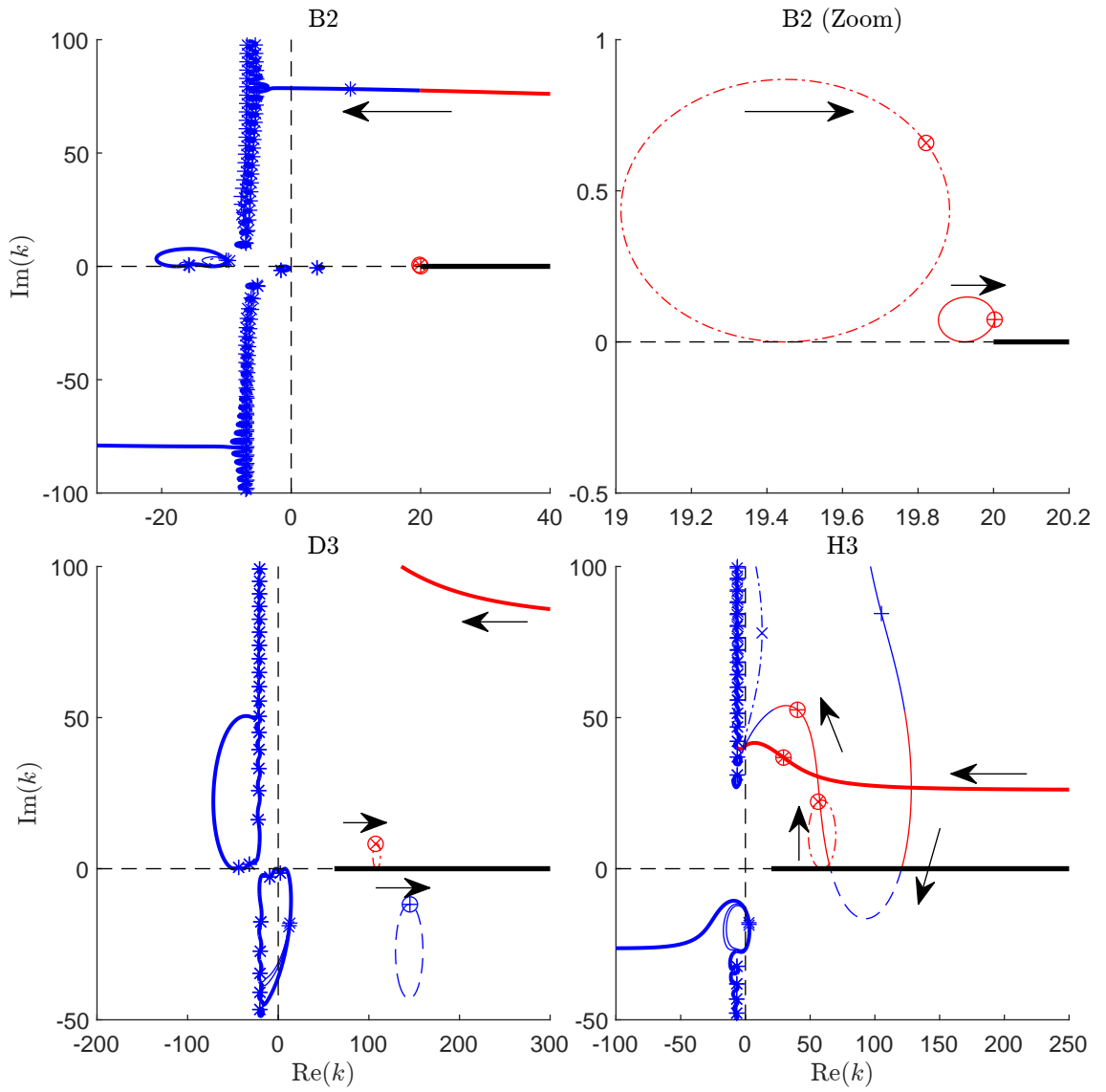


Figure 37: As figure 34, tracking the Reactance  $\text{Im}(Z)$  for  $\text{Im}(Z) = -\infty$  to  $\text{Im}(Z) = \infty$ . Including tracks of the Ingard-Myers boundary condition with thick solid lines. Arrows indicate the direction of increasing  $\text{Im}(Z)$ .

is that when stability is achieved, the stability does not lead to an ill-posed problem, but also there exist a range of impedance's such that as long as the wall is 'hard enough' and the resulting flow is stable, or in the case of  $D3$ , the flow may be stable for any wall impedance. This would be more expected of applications over a system that is always unstable such as the Linear-Brambley boundary condition, or sudden jumps between stability, with only 'perfectly' hard walls being stable.

To further support the claims given above, figures 38 to 41, compare the mode locations between the full problem, making use of the Frobenius series solutions given in part II. In the first of these, figure 38, It can be observed that not only do the modes stabilise following a similar process but additionally, they have a very similar value of  $k^+(h_c)$ . For small  $h$ , where the  $k^+$  poles are hydrodynamic instabilities, although both poles experience growth in their imaginary part, increasing the growth rate of their contribution to the pressure perturbation, this occurs a different rates with the modes diverging for sufficiently small  $h$ .

If we instead examine the large  $h$  behaviour, where the  $k^+$  pole is behind the branch cut for the full shear flow solution, then a region immediately following stabilisation can be observed where the modes follow very similar trajectories as  $h$  increases. Although as  $h$  become sufficiently large the two diverge once more, with the Quadratic-Brambley modes either becoming unstable again, or stop contributing by moving to the left of the critical layer branch cut.

If we instead consider figure 39, which compares the variation of Mach number  $M$ , we can once again observe regions of agreement between the solutions. This is particularly true for low Mach numbers where the poles are hidden behind the branch cut, an exception to this in parameter set  $B3$ . It is suspected in these cases that the boundary layer thickness  $h = 0.05$  is too large in comparison to the other parameters, such that the higher order corrections to the Quadratic-Brambley boundary condition,  $O(h^2)$  can no longer be ignored in order to produce an accurate solution. Additionally, for parameter set  $C5$ , where in each case we have two potential  $k^+$  modes, Despite both retrieving similar mode locations in the limit as  $M \rightarrow 1$ , the stability of these modes is different. This is likely a result of the how we choose to deform  $\text{Im}(\omega) \rightarrow \infty$  under the Briggs-Bers criterion as a result of a potential absolute instability, however further investigation has not been provided for this.

Figure 40 tracks the locations of the modes both for the full solution and for the Quadratic-Brambley boundary condition as the frequency  $\omega$  is varied. In each case the resulting behaviour can be observed to be very similar, with the Quadratic-

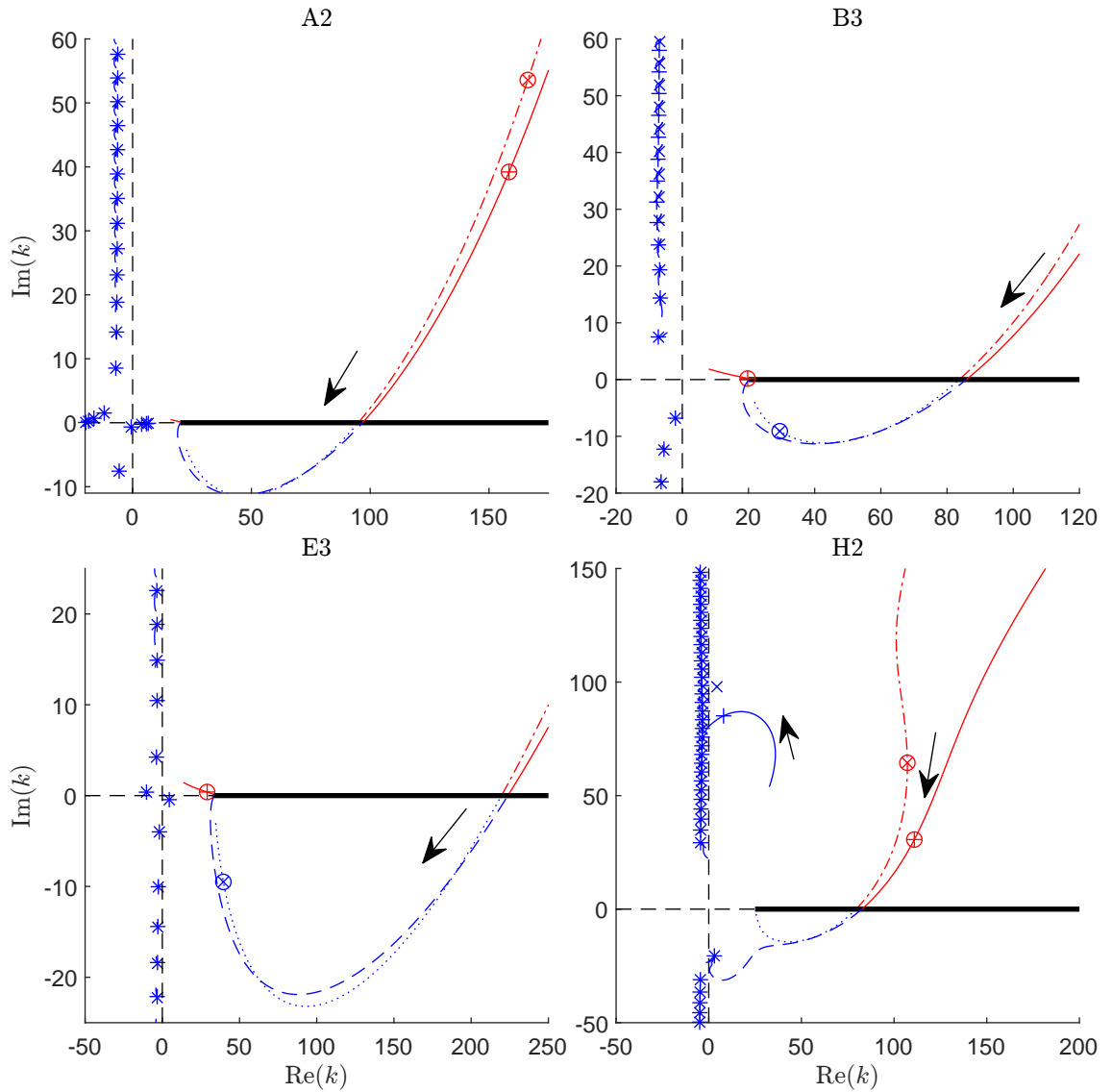


Figure 38: Tracks of the modal locations of the full Frobenius series solution against the Quadratic-Brambley boundary condition as the boundary layer thickness  $h$  is varied from  $10^{-5}$  to  $0.1$ . Modes of the full solution are marked with a cross ( $\times$ ), and tracked on dot-dash lines ( $-\cdot-$ ), except when behind the critical layer branch cut where they are tracked on dotted line ( $\cdots$ ). Modes of the Quadratic-Brambley boundary condition are marked with a plus ( $+$ ) and are tracked on solid lines ( $-$ ), or on dashed lines ( $--$ ) when behind the branch cut, irrespective is to the left or right. Stable modes are coloured blue, unstable modes are red, any  $k^+$  modes are circled  $\circ$ . Arrows indicate the direction of increasing boundary layer thickness  $h$ .

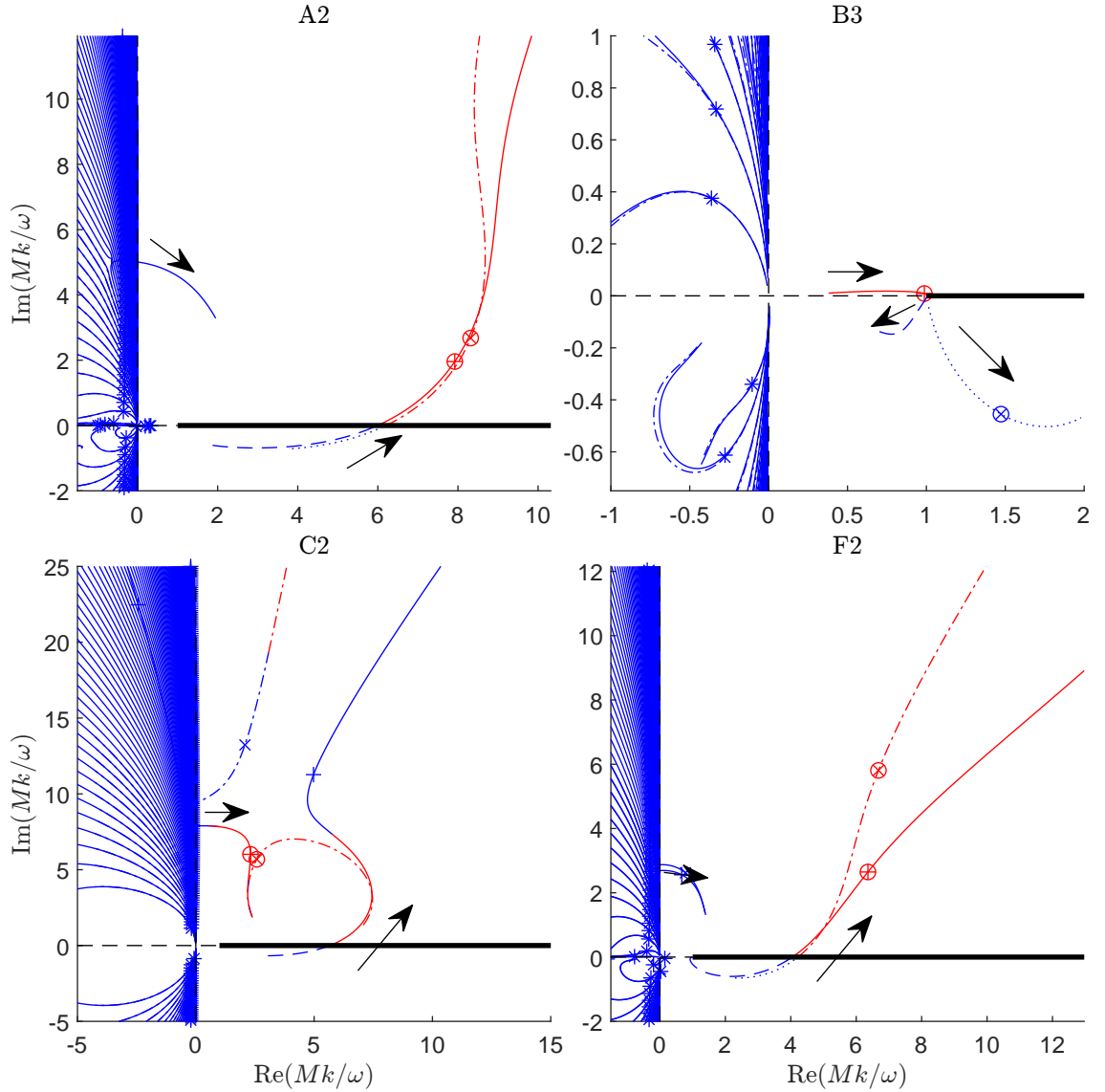


Figure 39: Tracks of the modal locations on a scaled complex  $k$  plane of the full Frobenius series solution against the Quadratic-Brambley boundary condition as the Mach number  $M$  is varied from 0.1 to 0.9. Modes of the Full solution are marked with a cross ( $\times$ ) and tracked on dot-dash lines ( $-\cdot-$ ), except when behind the critical layer branch cut where they are tracked on dotted lone ( $\cdots$ ). Modes of the Quadratic-Brambley boundary condition are marked with a plus ( $+$ ) and are tracked on solid lines ( $-$ ), or on dashed lines ( $--$ ) when behind the branch cut, irrespective is to the left or right. Stable modes are coloured blue, unstable modes are red, any  $k^+$  modes are circled  $\circ$ . Arrows indicate the direction of increasing Mach number  $M$ .

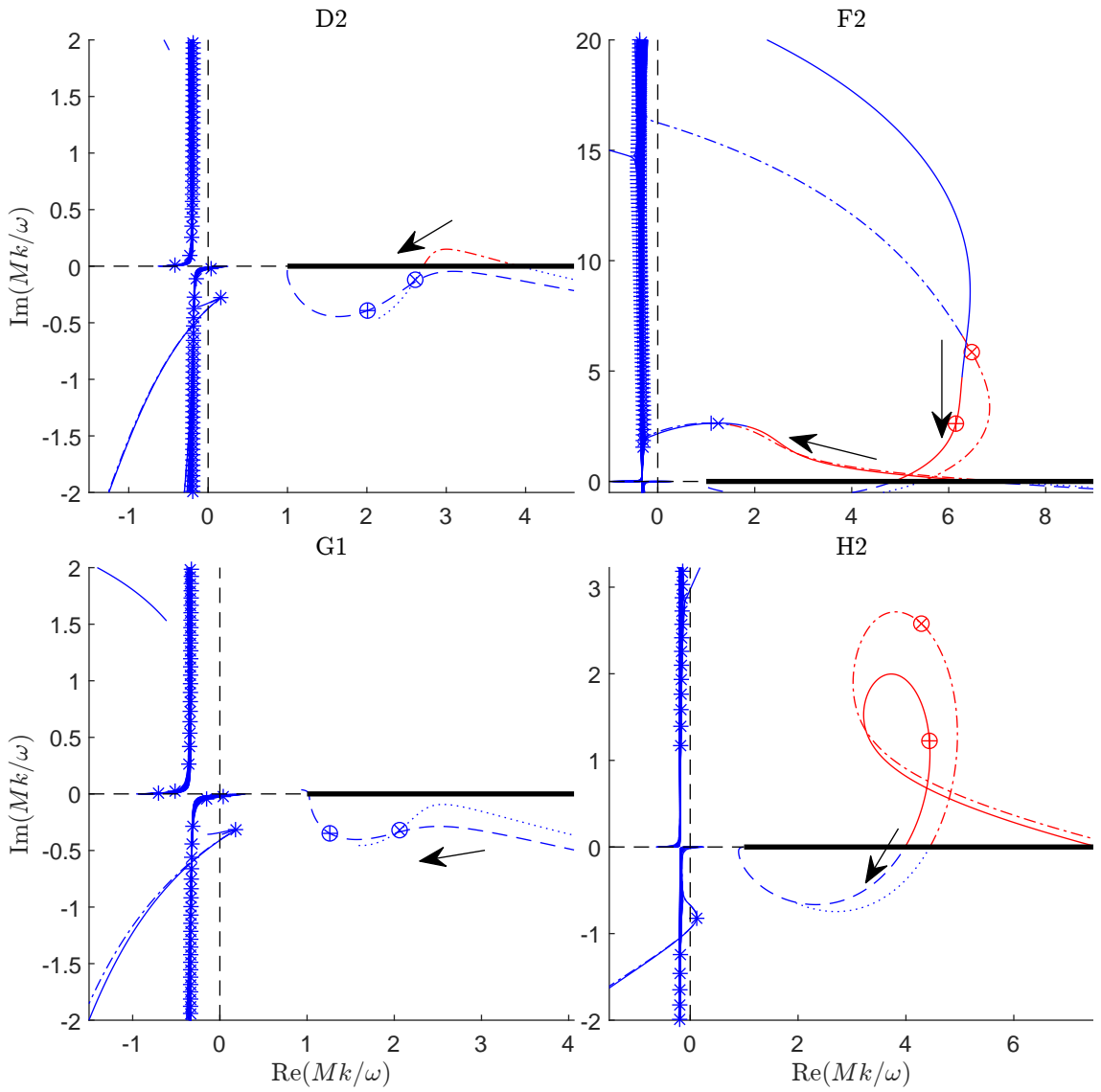


Figure 40: As figure 39, but for varying the frequency  $\omega$  from 1 to 50.

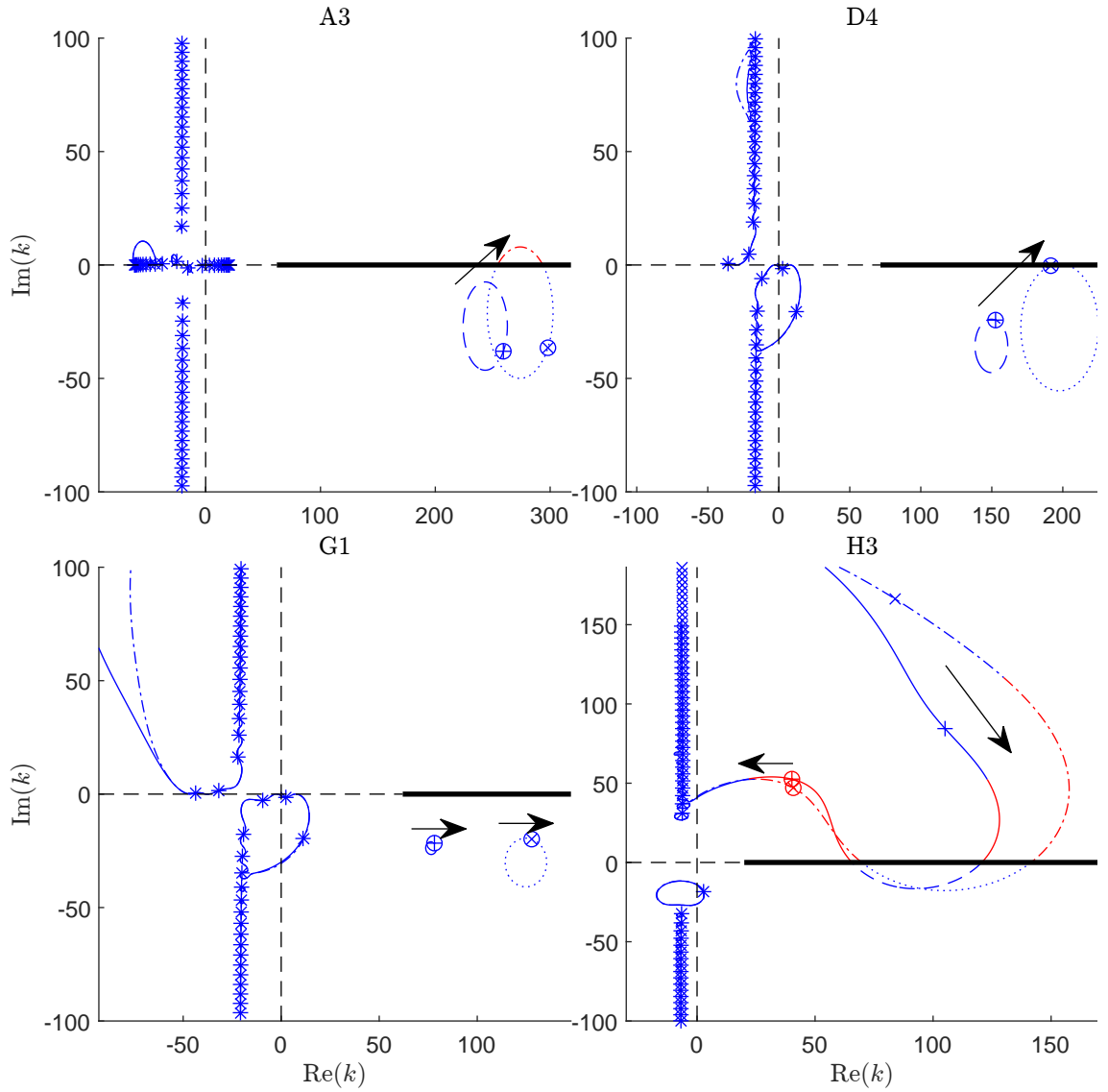


Figure 41: As figure 38 but for varying the Reactance from  $\text{Im}(Z) = -\infty$  to  $\text{Im}(Z) = \infty$  in the complex  $k$  plane.

Brambley boundary condition being ‘more’ stable than the full solution, with a smaller imaginary part. In each case investigated the same number of potential  $k^+$  poles have been located, with comparable stabilities unlike in the case of the Mach number. Once again we observe that the modes are stable for both small and large values of  $\omega$ , and may be unstable only for a finite intermediate range. Although alongside previous observations, this may be related to the impedance  $Z(\omega)$  and the resulting Mass and Spring-like wall impedance’s.

Finally, we vary the reactance of the wall impedance in figure 41. Once again similar overall behaviour is observed between the two problems, with similar stabilities and number of  $k^+$  modes. Although in this case greater discrepancies between the real part of  $k^+$  may be observed between when comparing the mode locations.

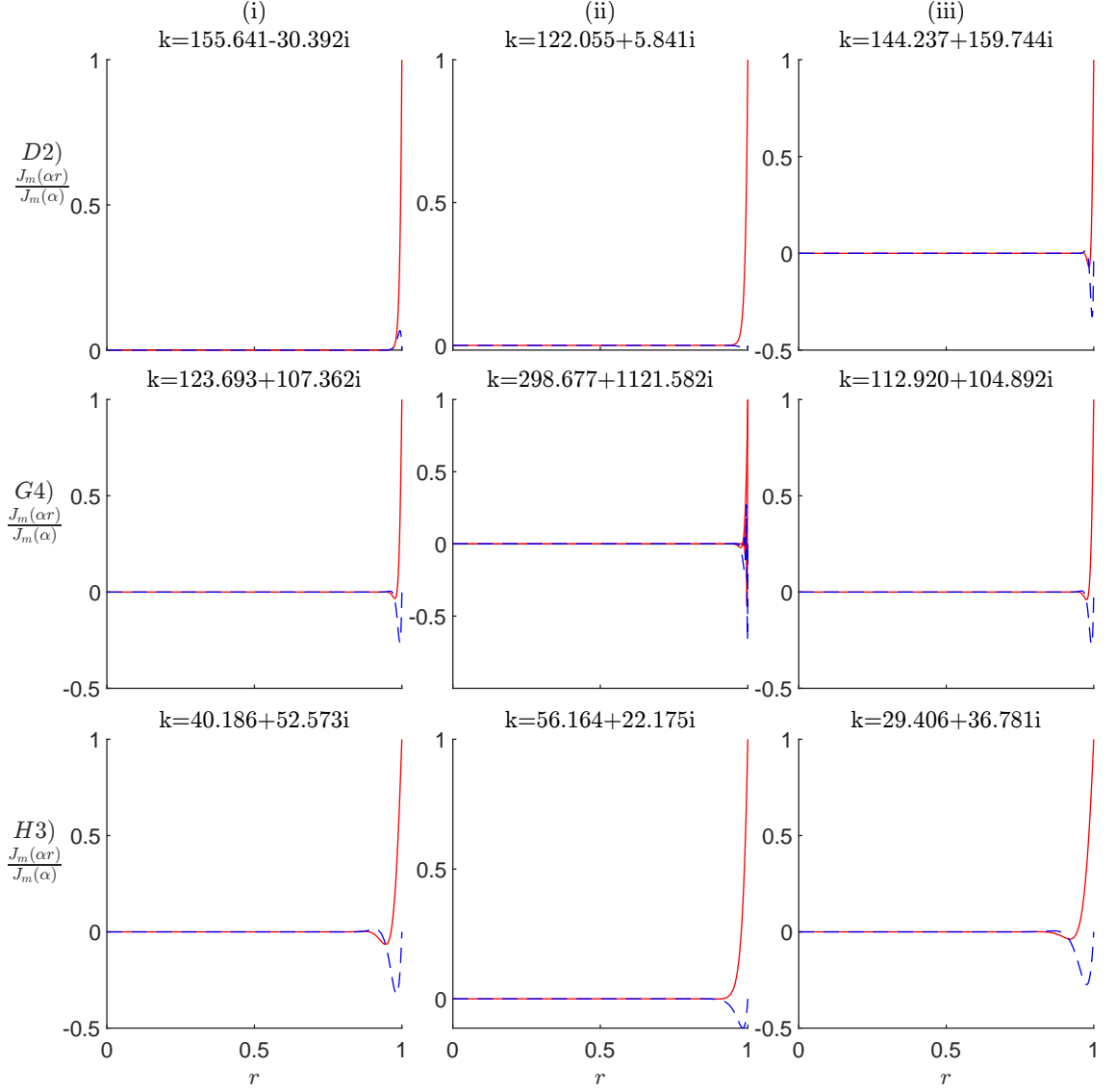


Figure 42: Mode shapes,  $\frac{J_m(ar)}{J_m(a)}$  against the radial location  $r$ , of the  $k^+$  modes for the; Quadratic-Brambley boundary condition (i). Linear-Brambley boundary condition (ii) and the Ingard-Myers boundary condition (iii). Real parts are solid lines coloured red, imaginary parts are dashed lines coloured blue.

In all cases plotted, stability is seen as the hard wall setting is approached for either increasing or decreasing  $\text{Im}(Z)$ , although we once again draw attention to figure 37, where the  $k^+$  mode was found to be unstable for all impedance values.

In figure 42 the mode shapes corresponding to the hydrodynamic instability, or stabilised  $k^+$  pole ( $D2,i$ ) are plotted for the Quadratic-Brambley (i), Linear-Brambley (ii) and the Ingard-Myers (iii) boundary conditions. From these it can be observed that the mode shapes are very similar between the different boundary conditions, with a contribution contained near the duct wall. While a significantly higher difference may be observed between the stabilised  $k^+$  of the Quadratic-Brambley boundary condition (i) and the hydrodynamic instability of the Ingard-Myers bound-

ary condition (iii), the behaviour between the Quadratic-Brambley and Linear-Brambley (ii) boundary conditions remains close.

## 16 Fourier Inversion for a Point Mass Source

### 16.1 Construction of the Green's Function

To consider the effect of the critical layer branch cut on the Fourier inversion contour we will once again consider the Green's function solution, introducing a point mass source into the Euler equations (5.4). Since we are now considering a uniform mean flow we retrieve Bessel's equation,

$$\tilde{p}''(r) + \frac{1}{r}\tilde{p}'(r) + \left( (\omega - Mk)^2 - k^2 + \frac{m^2}{r^2} \right) \tilde{p}(r) = \frac{\omega - Mk}{2i\pi r_0} \delta(r - r_0) \quad (16.1)$$

With the Green's function solution given by

$$\tilde{G}(r; k, m, \omega) = \frac{\omega - Mk}{2i\pi r_0} \frac{\tilde{\psi}_1(r_{<})\tilde{\psi}_2(r_{>})}{\mathcal{W}(\tilde{\psi}_1(r), \tilde{\psi}_2(r); r_0)} \quad (16.2)$$

Where  $\tilde{\psi}_1$  solves homogeneous form of Bessel's equation (16.1) and satisfies the boundary condition at  $r = 0$ , (5.11) resulting in Bessel's function of the first kind

$$\tilde{\psi}_1(r) = J_m(\alpha r). \quad (16.3)$$

For  $\tilde{\psi}_2(r)$  we instead make use of the Hankel functions once more, and set coefficients such that they satisfy the Brambley boundary condition for a quadratic shear flow (14.39), which is done by setting  $\tilde{\psi}_2(1) = 1$  and  $\tilde{\psi}_2'(1) = \frac{D_1 + D_2}{C}$ , with  $D_1, D_2$  and  $C$  given by (14.40)

$$\tilde{\psi}_2(r) = AH_m^{(1)}(\alpha r) + BH_m^{(2)}(\alpha r) \quad (16.4a)$$

$$A = \frac{\pi i}{4} \left( \alpha H_m^{(2)'}(\alpha) - \frac{D_1 + D_2}{C} H_m^{(2)}(\alpha) \right) \quad (16.4b)$$

$$B = -\frac{\pi i}{4} \left( \alpha H_m^{(1)'}(\alpha) - \frac{D_1 + D_2}{C} H_m^{(1)}(\alpha) \right) \quad (16.4c)$$

Once again making use of the Wronskian between  $H_m^{(1)}$  and  $H_m^{(2)}$  as given in [Abramowitz and Stegun, 1964].

From this we can find  $\mathcal{W}(\tilde{\psi}_1, \tilde{\psi}_2; r)$  to be,

$$\begin{aligned} \mathcal{W}(\tilde{\psi}_1, \tilde{\psi}_2; r_0) &= \mathcal{W}(J_m(\alpha r), AH_m^{(1)}(\alpha r) + BH_m^{(2)}(\alpha r); r_0) \\ &= A\mathcal{W}(J_m(\alpha r), H_m^{(1)}(\alpha r); r_0) + B\mathcal{W}(J_m(\alpha r), H_m^{(2)}(\alpha r); r_0) \end{aligned} \quad (16.5)$$

$$\begin{aligned}
&= -A \frac{2}{\pi i r_0} + B \frac{2}{\pi i r_0} \\
&= -\frac{1}{2r_0} \left( \alpha (H_m^{(1)'}(\alpha) + H_m^{(2)'}(\alpha)) - \frac{D_1 + D_2}{C} (H_m^{(1)}(\alpha) + H_m^{(2)}(\alpha)) \right) \\
&= -\frac{1}{r_0} \left( \alpha J_m'(\alpha) - \frac{D_1 + D_2}{C} J_m(\alpha) \right) \tag{16.6}
\end{aligned}$$

and the Green's function solution can be re-expressed as

$$\tilde{G}(r; k, m, \omega) = -\frac{\omega - Mk}{2i\pi} \frac{\tilde{\psi}_1(r_<) \tilde{\psi}_2(r_>)}{\mathcal{D}(\omega, k)} \tag{16.7}$$

confirming once again that the roots of the dispersion relation act as poles of the Green's function. Additionally, we can find the Green's function for having crossed the branch cut by making use of the boundary condition and dispersion relation (14.50) for having crossed the branch cut,

$$\tilde{G}^+(r; k, m, \omega) = -\frac{\omega - Mk}{2i\pi} \frac{\tilde{\psi}_1(r_<) \tilde{\psi}_2^+(r_>)}{\mathcal{D}^+(\omega, k)} \tag{16.8}$$

$$\tilde{\psi}_2^+(r) = A^+ H_m^{(1)}(\alpha r) + B^+ H_m^{(2)}(\alpha r) \tag{16.9a}$$

$$A^+ = \frac{\pi i}{4} \left( \alpha H_m^{(2)'}(\alpha) - \frac{D_1 + D_2 + \Delta D_2}{C} H_m^{(2)}(\alpha) \right) \tag{16.9b}$$

$$B^+ = -\frac{\pi i}{4} \left( \alpha H_m^{(1)'}(\alpha) - \frac{D_1 + D_2 + \Delta D_2}{C} H_m^{(1)}(\alpha) \right) \tag{16.9c}$$

$$\tilde{\psi}_2^+(r) = \tilde{\psi}_2(r) - \frac{\pi i}{4} \frac{\Delta D_2}{C} (H_m^{(2)}(\alpha) H_m^{(1)}(\alpha r) - H_m^{(1)}(\alpha) H_m^{(2)}(\alpha r)) \tag{16.9d}$$

## 16.2 Contribution of the Modal Poles

We wish to examine the contributions of the modal poles, to the Fourier inversion of the Green's function solution. We do so by once again appealing to the Briggs-Bers criterion to invoke causality and perform stability analysis. This proceeds exactly as described in part II section 8.1

We wish to compute

$$G(x, r; m) = \frac{1}{2\pi} \int_{\mathcal{C}} \tilde{G}(r; k, m) e^{-ikx} dk. \tag{16.10}$$

Example pole locations given in section 15, figures 31 and 32, and an example inversion contour given by the schematic in figure 43, with  $\mathcal{C}_b$  required for closure in the lower half plane. It can be observed that we once again have acoustic modes, in the upper and lower half plane that contribute to  $x < 0$  and  $x > 0$  respectively.

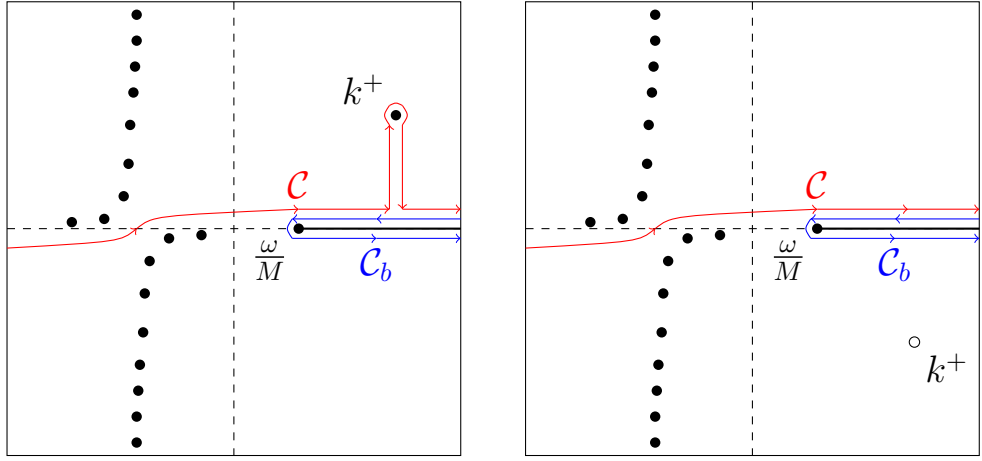


Figure 43: Illustration of the integration contour used for inverting the Fourier transform for a uniform flow under the Quadratic-Brambley boundary condition, both when a hydrodynamic instability is present (Left), and when it has been stabilised by the critical layer (Right). The  $k^+$  modal pole is hollow when behind the critical layer branch cut to indicate that it would not contribute as a usual modal pole. Note that these are the same contours as given in figure 6, and the integration around the critical layer Branch cut  $\mathcal{C}_b$  is only present when closing the contour in the lower half plane.

For  $x > 0$  we additionally consider; the critical layer branch cut, along the half line  $[\frac{\omega}{M}, \infty)$ . The surface modes  $k^+$  which may be located in the upper plane, and may or may not relate to the hydrodynamic instability, based on the Briggs-Bers criterion. Or a  $k^+$  pole located behind the branch cut.

Of these contributions, the modal poles, which would include the hydrodynamic instability if it is present will have a contribution similar to that given in equation (8.3), in this case giving,

$$R(k_j) = -\text{sgn}(x) \frac{\omega - Mk}{2\pi i} \frac{\frac{\partial}{\partial k} [\alpha J'_m(\alpha) - \frac{D_1 + D_2}{C} J_m(\alpha)]_{k=k_j}}{\tilde{\psi}_1(r) \tilde{\psi}_2(r_>)} e^{-ik_j x} \quad (16.11)$$

for a modal pole located at  $k = k_j$ .

Note that for a mode,  $A = B$  and so,  $\tilde{\psi}_2(r) = 2A\tilde{\psi}_1(r)$  It is possible to give an exact expression for the  $k$  derivative of the dispersion relation, although we leave it in this form here for conciseness, noting that  $\alpha = \alpha(k)$ .

### 16.3 Branch Points of the Critical Layer Branch Cut

Noting that in the case of the shear mean flow it could be observed that we had branch points at  $k = \frac{\omega}{M}$ ,  $k = k_r$  and a non-modal pole at  $k = k_0$ , for  $r, r_0 > 1 - h$  respectively, we once again examine the jump across the branch cut, observing where any branch points may occur.

Firstly, we express the jump across the branch cut,  $\Delta\tilde{G}(k)$  as,

$$\Delta\tilde{G}(k) = \tilde{G}^+(k) - \tilde{G}^-(k) \quad (16.12a)$$

$$\begin{aligned} &= -\frac{\omega - Mk}{2i\pi} \frac{\tilde{\psi}_1(r_{<})\tilde{\psi}_2^+(r_{>})}{\mathcal{D}^+(\omega, k)} + \frac{\omega - Mk}{2i\pi} \frac{\tilde{\psi}_1(r_{<})\tilde{\psi}_2(r_{>})}{\mathcal{D}(\omega, k)} \\ &= -\frac{(\omega - Mk)\tilde{\psi}_1(r_{<})}{2i\pi} \left( \frac{\tilde{\psi}_2^+(r_{>})}{\mathcal{D}^+(\omega, k)} - \frac{\tilde{\psi}_2(r_{>})}{\mathcal{D}(\omega, k)} \right) \\ &= -\frac{(\omega - Mk)\tilde{\psi}_1(r_{<})}{2i\pi\mathcal{D}(\omega, k)\mathcal{D}^+(\omega, k)} \left( \tilde{\psi}_2^+(r_{>})\mathcal{D}(\omega, k) - \tilde{\psi}_2(r_{>})\mathcal{D}^+(\omega, k) \right) \end{aligned} \quad (16.12b)$$

Making use of the expressions for  $\tilde{\psi}_2^+$  and  $\mathcal{D}^+$  in terms of  $\tilde{\psi}_2$  and  $\mathcal{D}$  it can be found that

$$\begin{aligned} \tilde{\psi}_2^+(r_{>})\mathcal{D} - \tilde{\psi}_2(r_{>})\mathcal{D}^+ &= \tilde{\psi}_2^+(r_{>})\mathcal{D} - \tilde{\psi}_2(r_{>}) \left( \mathcal{D} - \frac{\Delta D_2}{C} J_m(\alpha) \right) \\ &= \frac{\Delta D_2}{C} \left( \frac{\pi i}{4} (H_m^{(2)}(\alpha)H_m^{(1)}(\alpha r_{>}) - H_m^{(1)}(\alpha)H_m^{(2)}(\alpha r_{>})) \mathcal{D} \right. \\ &\quad \left. - \tilde{\psi}_2(r_{>})J_m(\alpha) \right) \end{aligned} \quad (16.13a)$$

$$\begin{aligned} &= \frac{\Delta D_2}{C} \left( \left( \frac{\pi i}{4} H_m^{(2)}(\alpha)\mathcal{D} - AJ_m(\alpha) \right) H_m^{(1)}(\alpha r_{>}) \right. \\ &\quad \left. - \left( \frac{\pi i}{4} H_m^{(1)}(\alpha)\mathcal{D} + BJ_m(\alpha) \right) H_m^{(2)}(\alpha r_{>}) \right) \\ \frac{\pi i}{4} H_m^{(2)}(\alpha)\mathcal{D} - AJ_m(\alpha) &= \frac{\pi i}{4} \left( \alpha J_m' H_m^{(2)} - \frac{D_1 + D_2}{C} J_m H_m^{(2)} \right. \\ &\quad \left. - \alpha H_m^{(2)'} J_m + \frac{D_1 + D_2}{C} H_m^{(2)} J_m \right) \\ &= \frac{\pi i}{4} \alpha \mathcal{W}(J_m, H_m^{(2)}; \alpha) \\ &= -\frac{\pi i}{4} \alpha \mathcal{W}(J_m, H_m^{(1)}; \alpha) \end{aligned} \quad (16.13b)$$

$$= \frac{1}{2} \quad (16.13c)$$

$$\begin{aligned} \tilde{\psi}_2^+(r_{>})\mathcal{D} - \tilde{\psi}_2(r_{>})\mathcal{D}^+ &= \frac{\Delta D_2}{C} \left( \frac{1}{2} H_m^{(1)}(\alpha r_{>}) + \frac{1}{2} H_m^{(2)}(\alpha r_{>}) \right) \\ &= \frac{\Delta D_2}{C} J_m(\alpha r_{>}) \end{aligned} \quad (16.13d)$$

which results in the expression for  $\Delta\tilde{G}$ ,

$$\Delta\tilde{G}(k) = -\frac{(\omega - Mk)J_m(\alpha r_{<})J_m(\alpha r_{>})\Delta D_2}{2i\pi C \mathcal{D}(\omega, k)\mathcal{D}^+(\omega, k)} \quad (16.14)$$

Just as before, there are at most three possible branch points, the first at  $k = \frac{\omega}{M}$ , and two more which would occur when we lose independence between  $\tilde{\psi}_1$  and  $\tilde{\psi}_2$

at either  $r$  or  $r_0$ , which would give rise to  $k_r$  and  $k_0$  respectively. Checking the Wronskian between  $\tilde{\psi}_1$  and  $\tilde{\psi}_2$  (16.6) which will be zero exactly where we experience this loss of independence, it can be observed that no zeros are found for any real  $r$ , thus we will only have one branch point for any value of  $r$  and  $r_0$ . This would be expected as these branch points were only present for  $r$  and  $r_0$  contained within the sheared flow region of the mean flow, while the mean flow taken in this case is uniform. All that remains therefore is to check if we observe a non-modal pole or a branch point at  $k = \frac{\omega}{M}$ .

Considering  $k = \frac{\omega}{M} + \xi$ , it can be found that

$$\alpha = \frac{\omega}{M} + O(\xi) \quad (16.15a)$$

$$C = i\omega Z - \frac{h\omega^2}{5} + O(\xi) \quad (16.15b)$$

$$D_1 = \frac{ihZ\omega^3}{M^2} + O(\xi) \quad (16.15c)$$

$$D_2 = -\frac{\omega Zh\pi}{4} \left( \frac{\omega^2}{M^2} + m^2 \right) \sqrt{\frac{M}{\omega}} \xi^{\frac{1}{2}} + O(\xi^{\frac{3}{2}}) \quad (16.15d)$$

$$\Delta D_2 = -\frac{\omega hZ\pi}{2} \left( \frac{\omega^2}{M^2} + m^2 \right) \sqrt{\frac{M}{\omega}} \xi^{\frac{1}{2}} + O(\xi^{\frac{3}{2}}) \quad (16.15e)$$

$$\mathcal{D} = \frac{\omega}{M} J'_m \left( \frac{\omega}{M} \right) - \frac{\frac{ihZ\omega^3}{M^2}}{i\omega Z - \frac{h\omega^2}{5}} J_m \left( \frac{\omega}{M} \right) + O(\xi^{\frac{1}{2}}) \quad (16.15f)$$

$$\mathcal{D}^+ = \mathcal{D} + O(\xi^{\frac{1}{2}}) \quad (16.15g)$$

$$A = \frac{i\pi}{4} \left( \frac{\omega}{M} H_m^{(2)'} \left( \frac{\omega}{M} \right) - \frac{\frac{ihZ\omega^3}{M^2}}{i\omega Z - \frac{h\omega^2}{5}} H_m^{(2)} \left( \frac{\omega}{M} \right) \right) + O(\xi^{\frac{1}{2}}) \quad (16.15h)$$

$$B = -\frac{i\pi}{4} \left( \frac{\omega}{M} H_m^{(1)'} \left( \frac{\omega}{M} \right) - \frac{\frac{ihZ\omega^3}{M^2}}{i\omega Z - \frac{h\omega^2}{5}} H_m^{(1)} \left( \frac{\omega}{M} \right) \right) + O(\xi^{\frac{1}{2}}) \quad (16.15i)$$

Which results in

$$\tilde{G}(k) = \frac{M\xi}{2i\pi} \frac{J_m\left(\frac{\omega}{M}r_<\right)\tilde{\psi}_2(r_>)}{\frac{\omega}{M}J'_m\left(\frac{\omega}{M}\right) - \frac{\frac{ihZ\omega^3}{M^2}}{i\omega Z - \frac{h\omega^2}{5}}J_m\left(\frac{\omega}{M}\right)} \quad (16.15j)$$

$$\Delta\tilde{G}(k) = \frac{i\sqrt{\omega}hZM^{\frac{3}{2}} \left( \frac{\omega^2}{M^2} + m^2 \right) J_m\left(\frac{\omega}{M}r_<\right)J_m\left(\frac{\omega}{M}r_>\right)\xi^{\frac{3}{2}}}{4 \left( i\omega Z - \frac{h\omega^2}{5} \right) \left( \frac{\omega}{M}J'_m\left(\frac{\omega}{M}\right) - \frac{\frac{ihZ\omega^3}{M^2}}{i\omega Z - \frac{h\omega^2}{5}}J_m\left(\frac{\omega}{M}\right) \right)^2} + O(\xi^2) \quad (16.15k)$$

From equation (16.15j) it can be observed that  $\tilde{G}$  does not experience a non-modal pole at  $k = \frac{\omega}{M}$ . Moreover we will make use of equation (16.15k) within Watson's lemma in order to find the contribution of the critical layer branch cut in the far-field

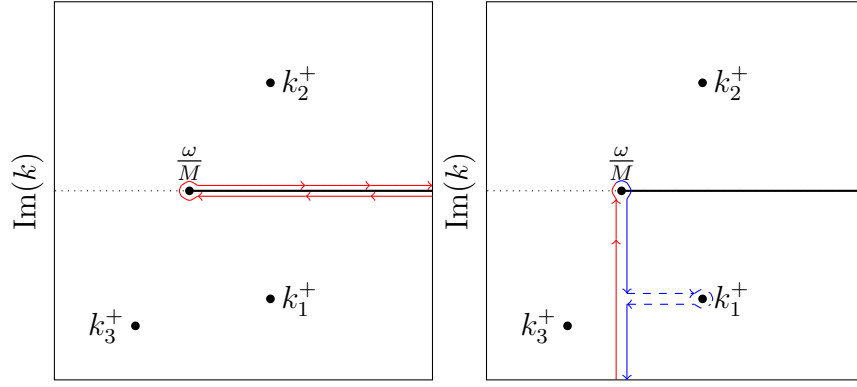


Figure 44: As figure 7, for the Quadratic-Brambley boundary condition; (Left) The integration contour  $\mathcal{C}_b$  around the critical layer branch cut. (Right) The integration contour transformed onto the steepest descent contour. Note we have illustrated three differently located  $k^+$  poles,  $k_1^+$  is located directly below the branch cut and contributes as part of the steepest descent contour, while the hydrodynamic instability mode  $k_2^+$ , or hidden mode to the left of the steepest descent contour do not contribute to the critical layer branch cut. Note that the hydrodynamic instability mode  $k_2^+$  would contribute as part of the modal sum.

under the method of steepest descent.

## 16.4 Contribution of the Critical Layer Branch Cut and the Stabilised $k^+$ Mode

In order to evaluate the contribution of the critical layer branch cut to the Fourier inversion of  $\tilde{G}$  we are required to evaluate the integral,

$$I(x, r) = \frac{1}{2\pi} \int_{\mathcal{C}_b} \tilde{G}(k, r) e^{-ikx} dk = -\frac{1}{2\pi} \int_{\frac{\omega}{M}}^{\infty} \Delta\tilde{G}(k, r) e^{-ikx} dk. \quad (16.16)$$

In order to avoid having to perform this highly oscillatory integral, due to the exponential term, we instead transform the integral onto its steepest descent contour, as illustrated in figure 44. Unlike in the case of the full solution, since we do not have any additional branch points there is no distinction or discontinuities in the evaluation of any  $k^+$  poles hidden behind the branch cut, and we are always computing its residue as if above the critical layer,

$$R^+(k^+, r) = -\text{sgn}(x) \frac{\omega - Mk}{2\pi i} \frac{\tilde{\psi}_1(r) \tilde{\psi}_2^+(r_>)}{\frac{\partial}{\partial k} \left[ J'_m(\alpha) - \frac{D_1 + D_2 + \Delta D_2}{C} J_m(\alpha) \right]_{k=k^+}} e^{-ik^+ x} \quad (16.17)$$

Having deformed the integral onto the steepest descent contour, it can then be found in the far-field, that,

$$I(x, r) = \sum_{\substack{\text{Im}(k^+) < 0 \\ \text{Re}(k^+) \geq \frac{\omega}{M}}} R^+(k^+) + \frac{i}{2\pi} \int_0^\infty \Delta \tilde{G} e^{-i(\frac{\omega}{M} - i\xi)x} d\xi \quad (16.18)$$

which results in a wave with phase velocity equal to the mean flow, decaying like  $x^{-\frac{5}{2}}$  by equation (16.15k) and Watson's lemma as given in section 9.4. This can be considered as the equivalent to the same contribution from the critical layer branch cut of the full problem for a sound source and observer located within the uniform flow, as may be expected apriori.

Not covered in  $I(x, r)$  is the case where a  $k^-$  pole may be present below the critical layer branch cut. This would follow exactly as in section 8.3, with the contribution for the mode in the acoustic modes and for the critical layer branch cut cancelling each other exactly.

## 16.5 Fourier Inversion under the Quadratic-Brambley Boundary Condition

To summarise the previous sections; under the Briggs-Bers criterion, the Green's function for a single azimuthal wave number from a point mass source applied to a uniform flow within a duct under the Quadratic-Brambley boundary condition is given by;

$$G(x, r; m) = \sum_{\text{Im}(k_j) > \mathcal{C}} R(k_j, r) \quad x < 0 \quad (16.19a)$$

$$\begin{aligned} &= \sum_{\text{Im}(k_j) < \mathcal{C}} R(k_j, r) + \sum_{\substack{\text{Im}(k^+) < 0 \\ \text{Re}(k^+) \geq \frac{\omega}{M}}} R^+(k^+, r) \\ &\quad - \sum_{\substack{\text{Im}(k^-) < 0 \\ \text{Re}(k^-) \geq \frac{\omega}{M}}} R(k^-, r) + I_{\frac{\omega}{M}}(x, r) \quad x > 0 \quad (16.19b) \end{aligned}$$

Where; the  $k_j, k^-$  are roots of the Quadratic-Brambley dispersion relation (14.40d).  $k^+$  are roots of the Quadratic-Brambley dispersion relation behind the critical layer branch cut, (14.50c).  $R(k, r)$  is given by equation (16.11).  $R^+(k, r)$  is given by equation (16.17). Finally,

$$I_{\frac{\omega}{M}}(x, r) = \frac{i}{2\pi} e^{-\frac{i\omega x}{M}} \int_0^{-\infty} \Delta \tilde{G}(\frac{\omega}{M} + i\xi, r) e^{\xi x} d\xi \quad (16.19c)$$

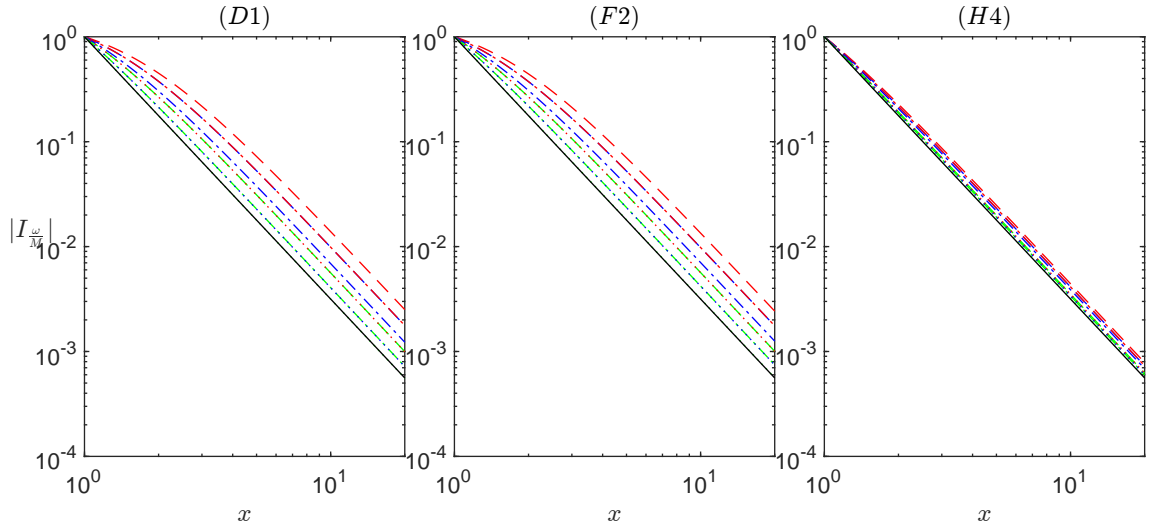


Figure 45: Contribution of  $|I_{\bar{M}}^{\omega}(x, r; r_0)|$  for parameter sets  $D1$ ,  $F2$  and  $H4$  normalised by the value at  $x = 1$ . Plotted are  $r = 0.1$  (red)  $r = 0.5$  (blue) and  $r = 0.995$  (green), and  $r_0 = 0.1$  (–)  $r_0 = 0.5$  (– · –) and  $r_0 = 0.995$  (···). Also indicated with a solid black line is the predicted decay rate  $x^{-\frac{5}{2}}$ .

## 17 Numerical Comparisons of the Fourier Inversion

In the following section we will illustrate, through numerical evaluation of the Fourier inversion, the comparison between the modal poles and the critical layer branch cut in both near and far-field effects; confirm the rate of decay for the critical layer branch cut and predicted effect of the location on the sound source; and compare to the other boundary conditions discussed. We once again make use of the parameter sets given in table 3.

### 17.1 Contribution of the Critical Layer Branch Cut

Firstly we examine the contribution and predicted decay rate of the steepest descent contour from the critical layer branch cut. This is done in figure 45 for three different parameter sets;  $D1$ ,  $F2$  and  $H4$ . In each case very good agreement is observed, particularly for larger values of  $x$ . These decay rates have been plotted for five pairs of  $r, r_0$ , noting that  $I_{\bar{M}}^{\omega}(x, r; r_0) = I_{\bar{M}}^{\omega}(x, r_0; r)$ , however this same behaviour has been observed for a much larger range of  $r$  and  $r_0$  values, with the agreement in all cases investigated easily observable after at most three radial distances downstream of the source.

## 17.2 Full Fourier Inversion

As was done in section 11.2, we can once again generate contour plots of the Fourier inversion for a point mass source. This is done for Parameter sets  $B1$ ,  $C3$ ,  $F4$ ,  $E1$  and  $G1$  in figures 46 and 47, where we plot separately the stable modal sum (*i*) and the steepest descent contours (*ii*), as well as the full Fourier inversion (*iii*), including both the stable modal poles, the steepest descent contour, and any  $k^+$  surface modes, which may or may not be stable. For each of the parameter sets plotted in figure 46 a hydrodynamic instability is observed. In each of the cases observed the effect of the hydrodynamic instability is not just dominant in the far-field, but also is significantly larger than both the modal sum and the critical layer branch cut in the near field. This is particularly true near the duct wall. And in many cases such as for parameter sets  $C3$  and  $F4$ , it is the only visible downstream contribution. Irrespective of this it can additionally be observed that near the duct wall, it may be that the modal sum and the critical layer are similar in magnitude to each other, as is the case for parameter sets  $B1$  and  $C3$ , while paying careful attention to the colour bars given. This suggests that when the hydrodynamic instability has been removed, by stabilisation by the critical layer branch cut, it may be that we continue to be unable to justify ignoring the contribution from the steepest descent contour, as was seen for the full solutions. This is reinforced in figure 47.

As already highlighted, figure 47 also plots the modal sum; the steepest descent contour of the critical layer branch cut; and the full Fourier inversion. In these cases the hydrodynamic instability has been stabilised and only contributes as part of the critical layer branch cut, although it is only plotted in (*iii*). Although we do not observe the unstable behaviour of the hydrodynamic instability, this stabilised mode continues in each observed case to dominate the near field with a contribution larger than that of the modal sum or the steepest descent contour. We continue to be able to observe for set  $E1$  that the modal sum and the steepest descent contour have comparable contributions near the wall, although for this particular case they remain comparable within much of the duct. In addition we can plot the far-field effects of the Fourier inversion, as is done in figure 48.

Figure 48 is plotted exactly as figures 46 and 47 on larger  $x$  scale, while only considering stabilised  $k^+$  modes. Unlike the case of the full solutions to the sheared flow we do not observe the non-modal pole, with its neutrally stable contribution, however in each case the critical layer can be seen as the dominant downstream contribution. For parameter set  $A4$ , this is due to the very large but exponentially decaying contribution of the stabilised  $k^+$  mode, while in the case of parameter set  $C1$ , the modal sum is considerable as negligible, but in addition, the  $k^+$  modes

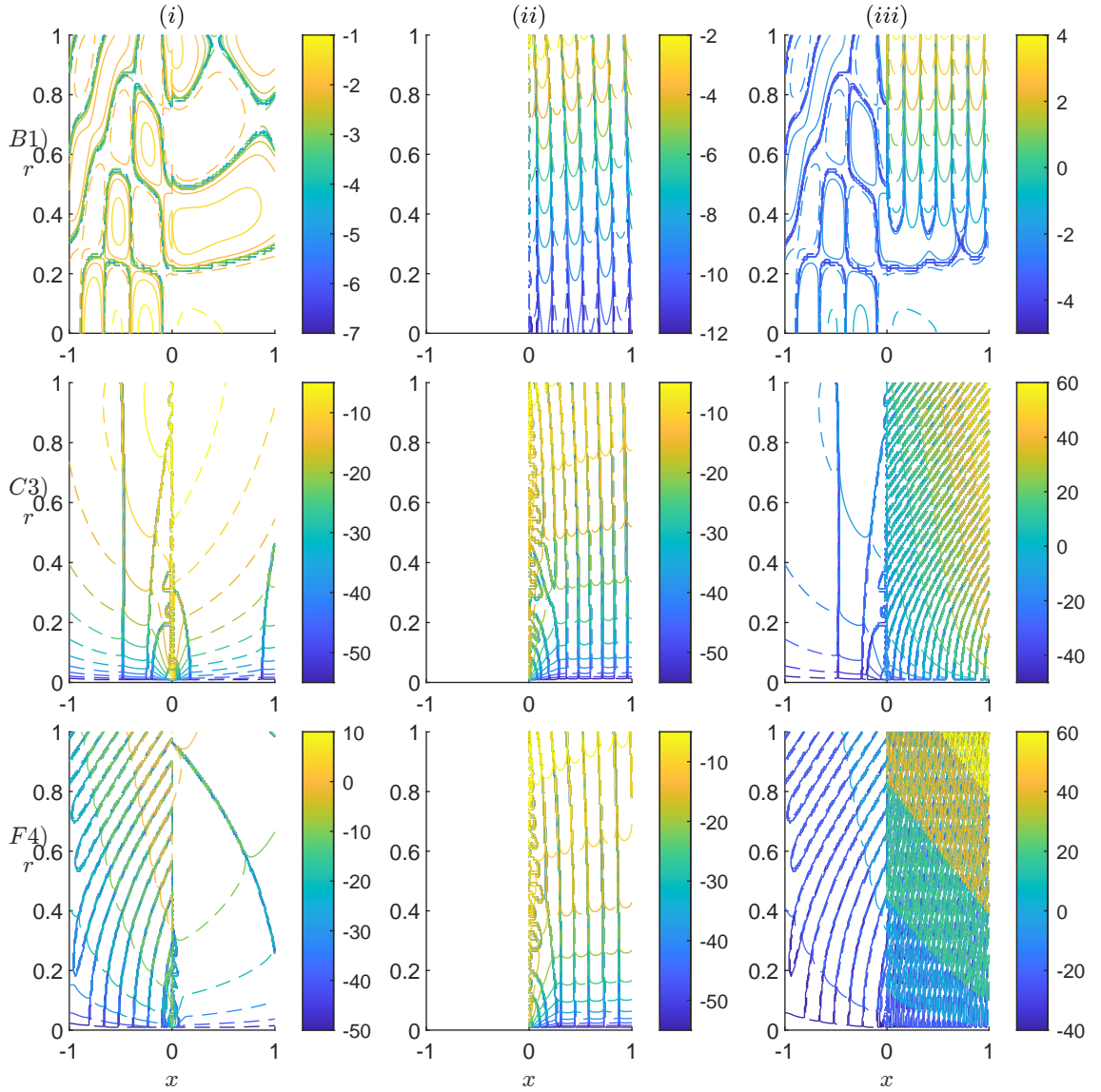


Figure 46: Plotting the real values of the different contributions.  $(i)$  just the contribution for the stable modal poles.  $(ii)$  the contribution of the critical layer branch cut.  $(iii)$  the Full Fourier Inversion, which also includes an unstable  $k^+$  pole. The parameter sets used from top to bottom are  $B1$ ,  $C3$  and  $F4$ , with  $r_0 = 1 - 4h/5$  in each case. Solid lines indicate positive real parts while dashed lines are negative. Colour bars are given on a  $\log_{10}$  scale.

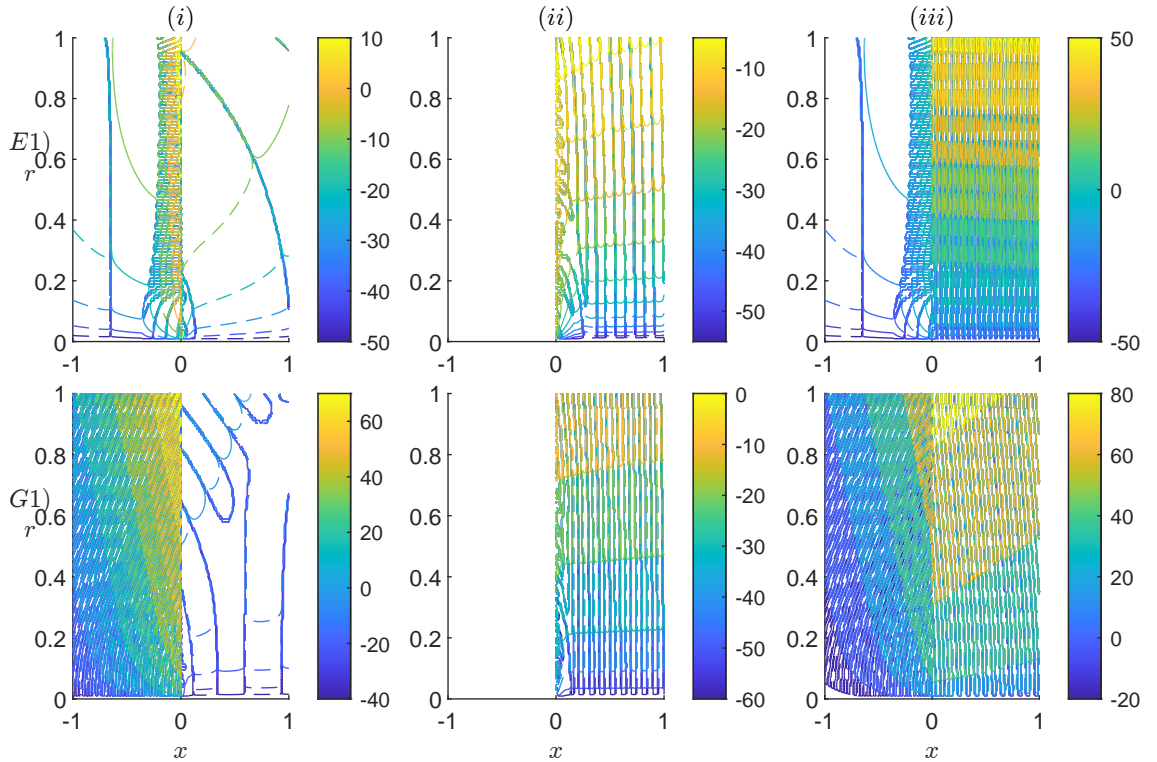


Figure 47: Plotting the real values of the different contributions. (i) just the contribution for the stable modal poles. (ii) the contribution of the steepest descent contour of the critical layer branch cut. (iii) the Full Fourier Inversion, which also includes a stable  $k^+$  pole hidden behind and contributing as part of the critical layer branch cut. Plotted for parameter sets  $E1$  and  $G1$  with  $r_0 = 1 - 4h/5$  in each case. Solid lines indicate positive real parts, while dashed lines are negative. Colour bars are given on a  $\log_{10}$  scale.

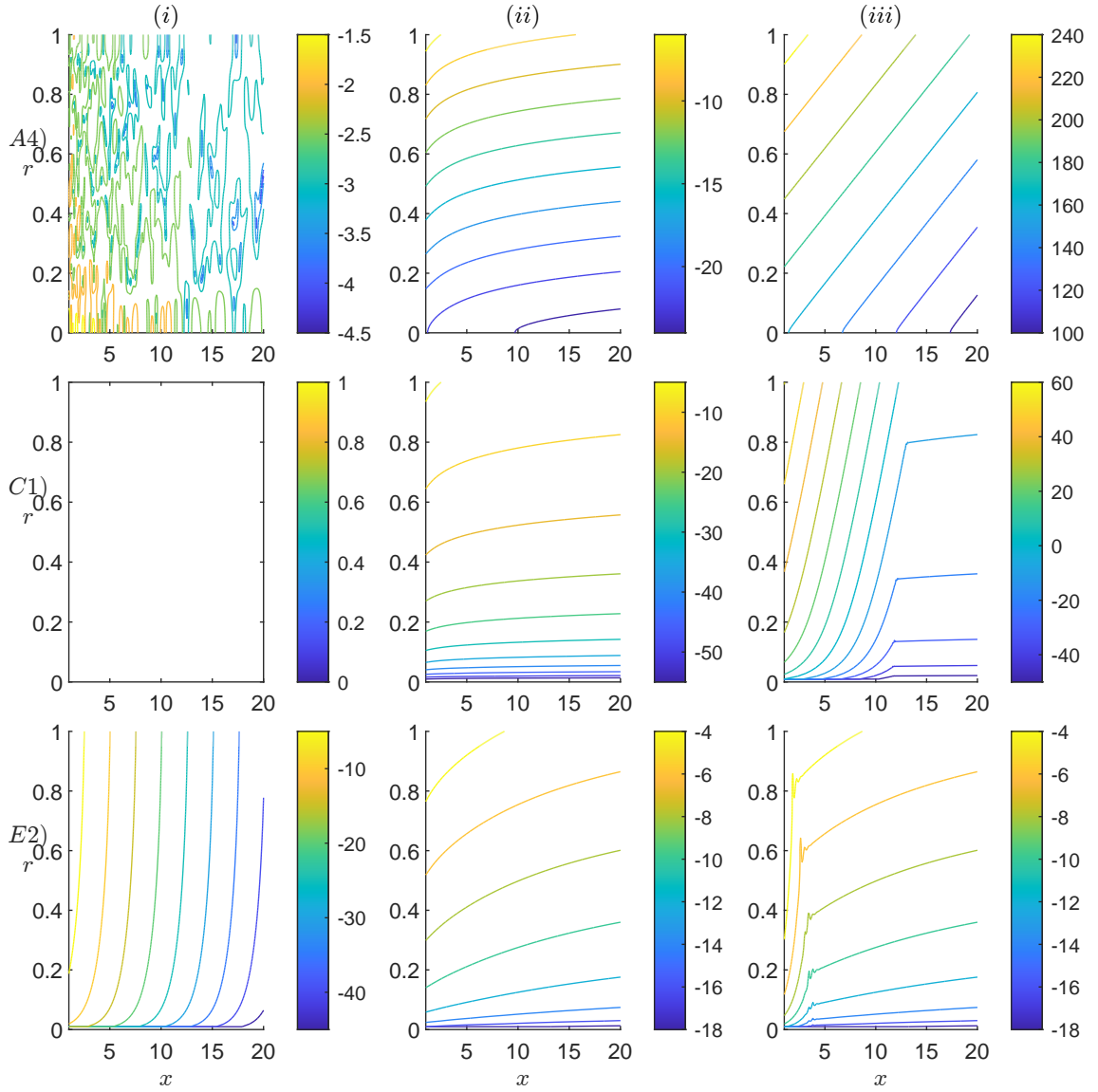


Figure 48: Plotting the absolute values of the different contributions for large values of  $x > 0$ .  $(i)$  just the contribution for the stable modal poles.  $(ii)$  the contribution of the steepest descent contour of the critical layer branch cut.  $(iii)$  the Full Fourier Inversion, which also includes a stable  $k^+$  pole hidden behind and contributing as part of the critical layer branch cut. Plotted for parameter sets  $A4$ ,  $C1$  and  $E2$  with  $r_0 = 1 - 4h/5$  in each case. Solid lines indicate positive real parts, while dashed lines are negative. Colour bars are given in a  $\log_{10}(|p|)$ .  $C1(i)$  is left blank due to the modal sum having magnitude  $\log_{10}(|p|) < -78$ .

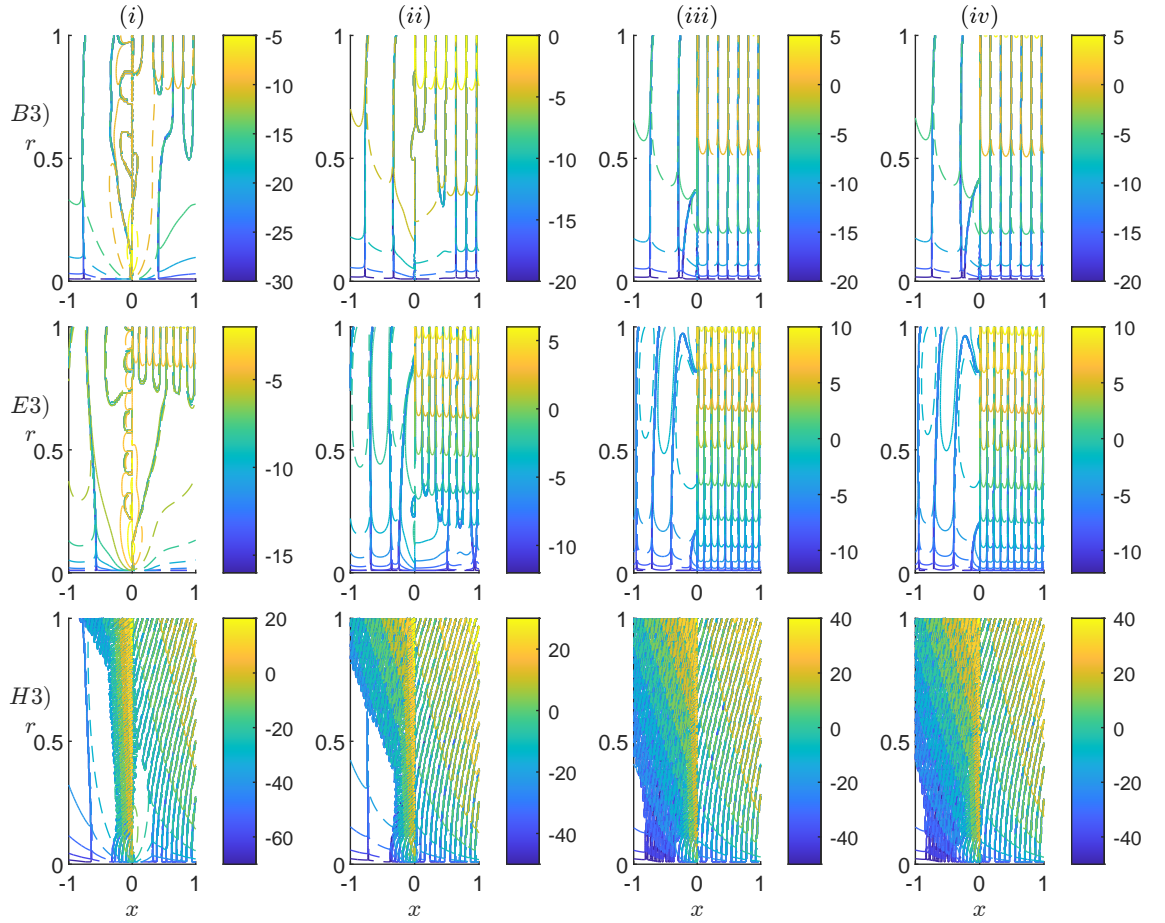


Figure 49: Plots of the real part of the Fourier inversion for parameter sets  $B3$ ,  $E3$  and  $H3$ . Solid lines indicate positive values, dashed lines indicate negative values with the colour bars given on a  $\log_{10}(|\text{Re}(p)|)$  scale. i):  $r_0 = 0.1$ ; ii):  $r_0 = 0.7$ ; iii):  $r_0 = 0.99$ ; iv):  $r_0 = 0.9995$ .

contribution decays faster than that of the steepest descent contour, resulting in a far-field that is actually dominated by the algebraically decaying behaviour. Finally for parameter set  $E2$ , no  $k^+$  mode contributes to the Fourier inversion, however it can clearly be seen that while the modal sum dominates the near field, the far-field is dictated once more by the steepest descent contour.

All three of these plots highlight the importance of including the critical layer within the overall Fourier inversion and why it is paramount when considering the Quadratic-Brambley boundary condition its contribution is carefully considered, and not just neglected in favour of either a fully modal description with or without the potentially stable  $k^+$  mode.

Finally, we conclude this section by observing how the location of the sound source may effect the overall sound field. This is done in figure 49. It can be observed that as the sound source approaches the duct wall the resulting pressure field increases both upstream and downstream, with the greatest increase felt by the surface modes and the steepest descent contours resulting in pressure field growing most significantly near the duct wall. In addition to this, despite considering a fixed finite

thickness boundary layer there is no change in behaviour for  $r_0$  being contained within what would be the shear flow. This is contrary to the full solutions, where not only was the non-modal pole observed but in addition the decay rate of the steepest descent contours would also vary.

### 17.3 Comparison to other Boundary conditions and the Full Solution

In figure 50 we compare the full Fourier inversion for each of the the Quadratic-Brambley boundary condition (*i*), the Linear-Brambley (*ii*) boundary condition, the Ingard-Myers boundary condition (*iii*), and the full solution to the Pridmore-Brown equation under a quadratic shear boundary layer (*iv*). Firstly note that each of the solutions produce similar modal behaviours. As a result, if the Fourier inversion was taken by just considering the modal sums in many cases it would be suitable to just make use of the Ingard-Myers boundary condition. However, the behaviours vary drastically once you consider the unstable behaviour. It should however be observed that only the full solution to the Pridmore-Brown equation for a sheared flow appears to produce a continuous solution. This may be indicative of missing poles or errors within the code evaluating the residues of the hydrodynamic instability or stabilised  $k^+$  modal pole.

With this acknowledged we are still able to compare the remaining three flow profile and observe the differences in stability, and therefore far-field behaviour of each of the boundary conditions, and the differing growth rates. Further, the stability of the Quadratic-Brambley boundary condition is not the same as the full solution despite that both can be stabilised by the same mechanisms.

In addition to the comparisons made in figure 50 it is clear that the errors suggested above are also present in figures 46-49. Despite this the results and conclusions discussed are expected to hold true.

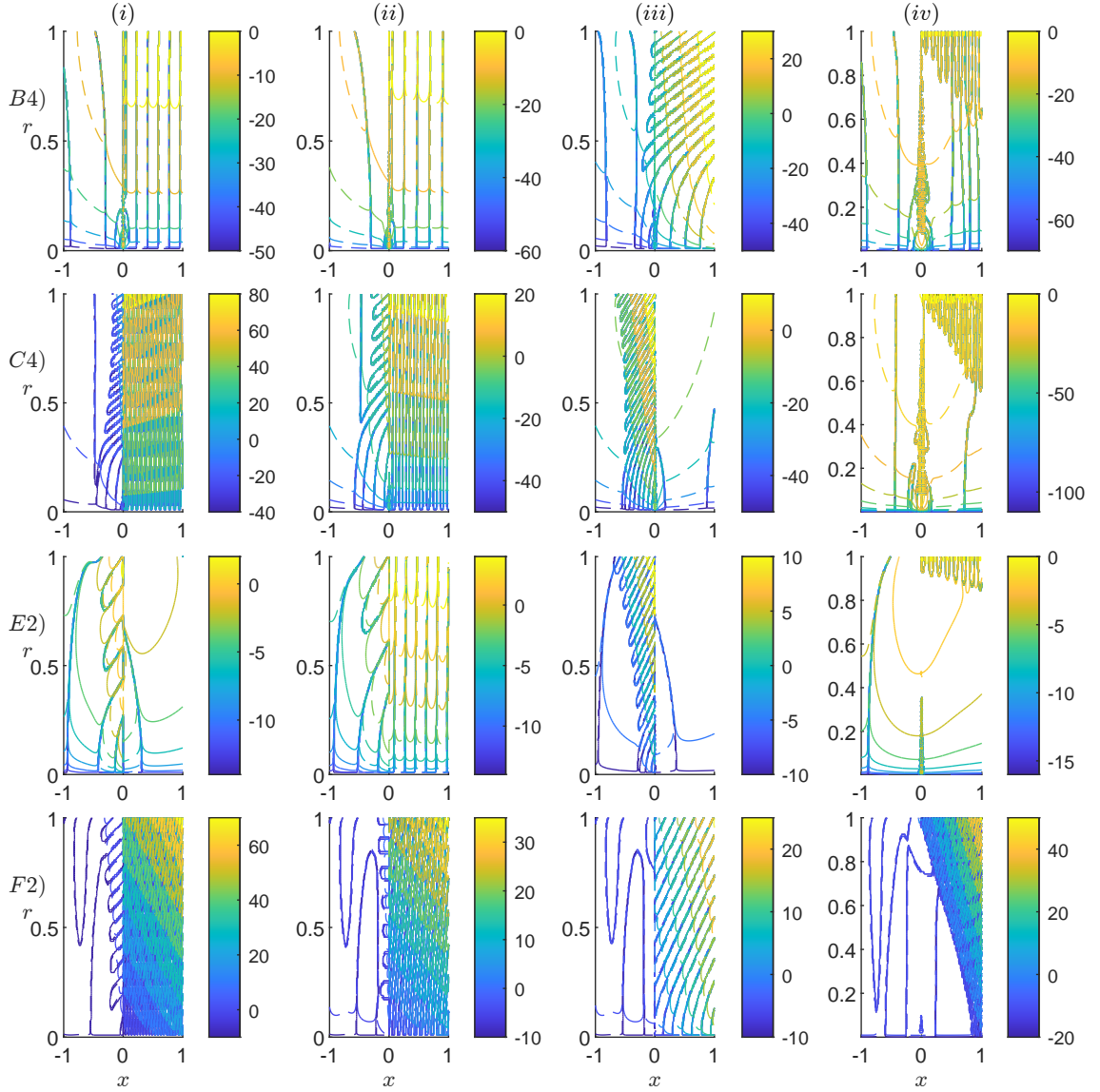


Figure 50: Comparisons of the real part of the Fourier inversion for parameter sets  $B4, C4, E2$  and  $F2$ . For a uniform flow under the Quadratic-Brambley (i), Linear-Brambley (ii) and Ingard-Myers (iii) boundary conditions, and the full quadratic sheared flow solution (iv). Solid lines indicate positive values, while dashed lines indicate negative values with the colour bars given in  $\log_{10}(|Re(p)|)$ .

## Part IV

# Wave Scattering due to a Change in Boundary Conditions

## 18 Introduction

Despite modelling aircraft engines, in the previous two parts we have a duct that is infinite and lined. In reality however, we would instead be considering have a finite length cylindrical duct with lined sections along with other complications, such as regions that are annulus, with a second wall near the duct centre line, or with a variable total radius along the length of the duct.

On the other hand, if we wish to model impedance education techniques, a rectangular duct is considered, with long hard walled sections either side of a finite lined section that contains a single lined wall.

Mathematically, the latter of these is significantly easier to model. However, with the aim of being able to closer approximate the behaviour within an actual aero-engine, we will consider an intermediate setting. Firstly, we will consider the same flow profile as in part II within an infinitely long duct that contains both hard walled and lined regions. Specifically, we will consider a hard walled section to be upstream of the lined walled section.

Similar settings as this have been considered in [Yang et al., 2018] where a rectangular duct with one lined wall is considered against the convective wave equation with comparisons being made between experiments and the numerical model used. Or in [Gabard and Astley, 2008] where a duct of general cross section is considered under a uniform flow with the Ingard-Myers boundary condition. These both make use of mode-matching techniques in order to construct a scattered field by assuming a fully modal decomposition both upstream and downstream of the change in boundary condition. As the name suggests, mode-matching would not be appropriate here without ignoring the contribution of the critical layer branch cut which, as was discussed in part II, is non-modal.

One alternative is the Wiener-Hopf technique. Unlike for mode-matching, the Wiener-Hopf technique does not require the assumption that the solutions are fully modal, instead making use of the analytic solutions, to construct the scattered wave field. This technique has been used in multiple instances for studying similar prob-

lems to the one we consider here; with Koch and Mohring [1983] considering a rectilinear duct with two opposite lined walls taking a uniform flow profile and solving the Helmholtz equation; in [Rienstra and Peake, 2005] for which a cylindrical duct containing uniform flow under the Ingard-Myers boundary condition is considered and the effects of a Kutta condition on the hydrodynamic instability when it is present by choosing the smoothness of the streamline at the scattering point; or within [Sobolev and Yakovets, 2017], where the scattering caused by a change between two lined walls for a uniform mean flow under the Ingard-Myers boundary condition. Of these only the work of Rienstra and Peake consider the effects of the hydrodynamic instability, observing the effects of a Kutta condition on the hydrodynamic instability; with Koch and Mohring acknowledging the instability mode but opting to ignore it as unphysical; and Sobolev and Yakovets deliberately removing the hydrodynamic instability mode without further justification. More detail on how to correctly account for the hydrodynamic instability within these settings is investigated in [Rienstra, 2007], noting that it is the dominant contribution. This is performed by tactfully incorrectly choosing the integration contour, and accounting for this choice accordingly through pole removal. The Wiener-Hopf technique involves constructing a Wiener-Hopf equation. This involves special half plane analytic functions, detailed in section 18.1, that overlap within some strip  $D$  across the real part of the complex plane. These half plane analytic functions may be constructed making use of a decomposition akin to that of Riemann-Hilbert problems, through the use of Cauchy-type integrals, and are only separated from these problems by the requirement of the strip  $D$  to have a finite width, as opposed to only being required along a line.

Relating this back to our previous work, when performing the Briggs-Bers deformation to produce the Fourier Inversion contour, if we were instead to choose the highest and lowest lines parallel to the real line for large  $-\text{Im}(\omega)$ , such that all of the modes are correctly located in the upper and lower half planes, and deformed under  $\text{Im}(\omega) \rightarrow 0$ . The strip contained and deformed between these lines would result in our strip  $D$ , and still contain the Briggs-Bers contour used. This is depicted in figure 51

In addition the Wiener-Hopf technique also allows us to more easily isolate the contribution from each of the modes of the pressure perturbation while mode-matching is a numerical technique and requires careful consideration of all of the incoming and outgoing modes. As a result when including additional modes, in order to increase accuracy, the mode-matching method needs to be repeated.

As previously mentioned we will once again consider the full sheared flow problem,

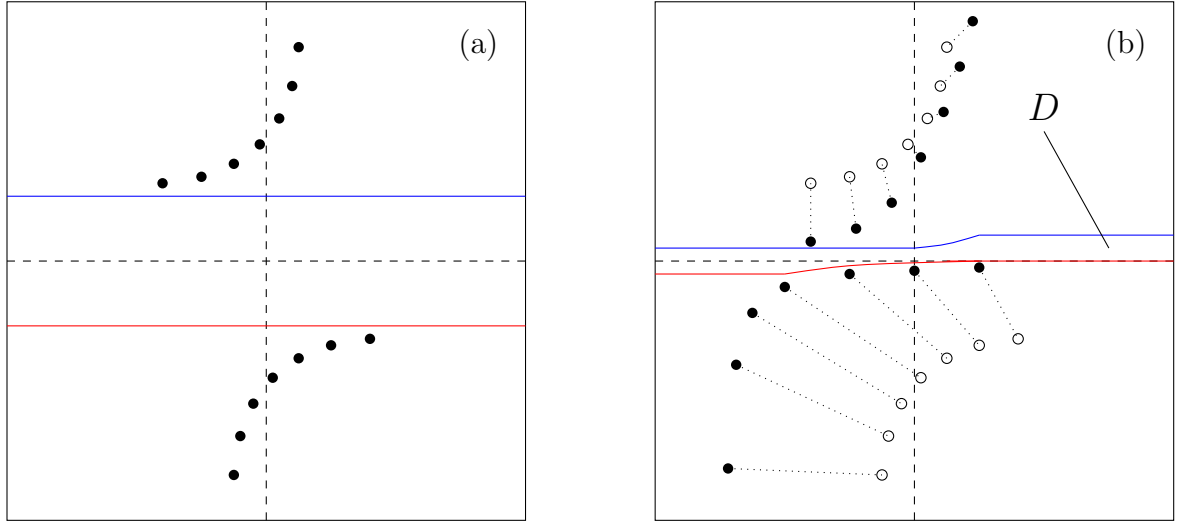


Figure 51: Illustration of the complex  $k$  plane illustrating how the strip  $D$  may be constructed through considering the Briggs-Bers criterion. (a) shows the pole locations and the upper and lower bound of the strip for large  $-\text{Im}(\omega)$ , while (b) shows the pole locations and the strip  $D$  for real  $\omega$ , having been deformed in order to maintain the poles in the correct half planes. This illustration is not representative of any particular parameter set and does not include effects of a branch cut singularity. Later we refer to the blue lines as  $\Gamma_-$  and the red line as  $\Gamma_+$

not the uniform flow under a Quadratic-Brambley boundary condition.

Having constructed a solution for the pressure perturbation, under Fourier series, for a point mass-source in an infinite lined duct. We will reapply these solutions as we consider either the behaviour for either a semi-infinite or a finite lined section of duct. These are depicted in figures 52 and 53 respectively.

We first consider a semi-infinite lined duct, with a point mass source located far downstream within a hard walled section. That is, a cylindrical duct that is hard walled for  $x < 0$  and lined for  $x > 0$ . The mass source, located at some  $x < 0$ , is further broken down into constituent parts. Namely, we consider an incoming wave  $p_{in}(x, r)$  of either; a single wave mode from one of a stable modal poles, a neutrally stable wave for from the non-modal pole with a sound source located within the sheared flow region, and from a hidden stabilised hydrodynamic instability.

When the incoming wave reaches  $x = 0$  the boundary condition changes and this causes the incoming wave to scatter into a scattered wave  $p_0(x, r)$ . We will then consider the total pressure perturbation to be the sum of the incoming wave and the scattered waves. As depicted in figure 52.

We may in addition assume that  $p_{in}(x, r)$  takes the form of any of the branch cut

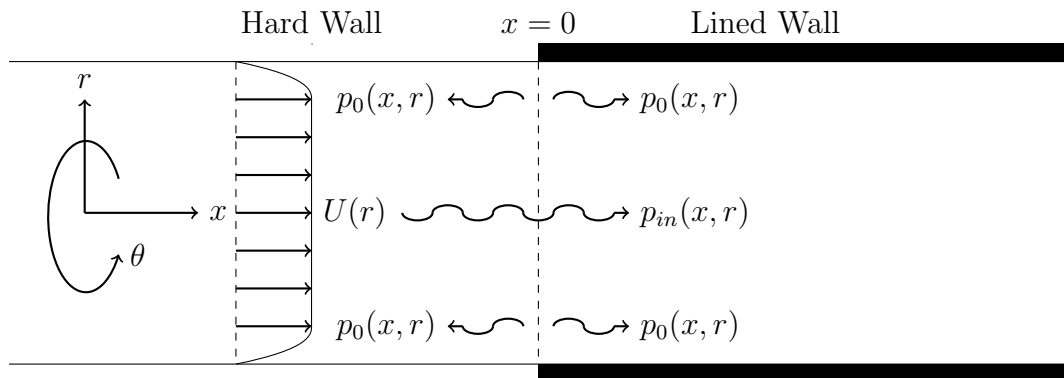


Figure 52: A cross sectional view of a cylindrical duct with lined walls containing sheared axial flow.  $\rho_0(r)$  is the mean flow density (here taken constant), and  $U(r)$  is the mean flow velocity, here taken to be uniform outside a boundary layer of width  $h$ .  $Z$  is the boundary impedance and defines the boundary condition at the wall of the duct.

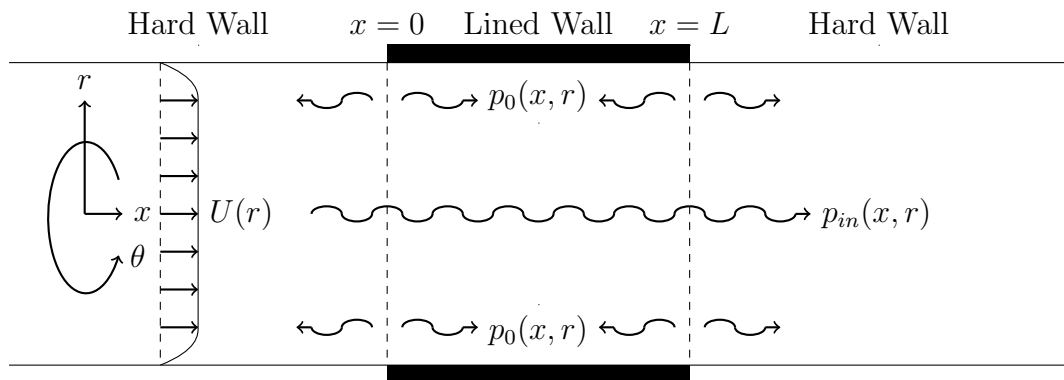


Figure 53: A cross sectional view of a cylindrical duct with lined walls containing sheared axial flow.  $\rho_0(r)$  is the mean flow density (here taken constant), and  $U(r)$  is the mean flow velocity, here taken to be uniform outside a boundary layer of width  $h$ .  $Z$  is the boundary impedance and defines the boundary condition at the wall of the duct.

terms given in section 9.4, however due to its complexity and the knowledge that these contributions will decay algebraically, alongside our assumption that the source is located far-downstream, we will not consider this case here.

In addition to this we have further assumed that  $p_{in(x,r)}$  will always be at most neutrally stable, removing the case of the hydrodynamic instability. This is as a result of our conjecture in section 12.3 where we indicated our belief that no hard wall ducts can have a  $k^+$  pole occur on the critical layer branch cut, resulting in all hard walled ducts being at most neutrally stable, and our observations support this conjecture.

In the final section of this part we will focus on the case of a finite length duct as depicted in figure 53. This work has yet to be completed in full and the results are at this time inconclusive. Although the problem is formulated, and discussion is given regarding the solution presented and how further progress may be made.

## 18.1 Half Range Transforms

In the following section we will define some of the notation we will be using throughout the remainder of this part.

We first define the two half range transforms,

$$\int_{-\infty}^{\infty} f(x)e^{ikx} dx = \tilde{f}(k) = \int_{-\infty}^0 f(x)e^{ikx} dx + \int_0^{\infty} f(x)e^{ikx} dx \quad (18.1a)$$

$$\tilde{f}_+(k) + \tilde{f}_-(k). \quad (18.1b)$$

Here  $f_{\pm}$  are functions that are analytic above/below some continuous lines  $\Gamma_{\pm}$ . We define  $\Gamma_{\pm}$  to be able to be parameterised as follows, Let  $s \in \mathbb{R}$ , then  $\Gamma_{\pm}(s) = s + i\gamma_{\pm}(s)$  for some real continuous function  $\gamma$  with  $\gamma_+(s) < \gamma_-(s) - \delta$ , for some  $\delta > 0$ . In this way there exists a strip  $D$ , between  $\Gamma_{\pm}$  where both functions are analytic, see figure 54. We can then define the Fourier inversion to be

$$f(x) = \frac{1}{2\pi} \int_{\Gamma} (f_+(\tilde{k}) + f_-(\tilde{k}))e^{-ikx} d\tilde{k} \quad \Gamma = \Gamma(s) \in (\Gamma_+(s), \Gamma_-(s)). \quad (18.2)$$

We additionally define the additive decomposition of a function, Let  $\tilde{f}(k)$  be analytic within a strip  $D$  between some  $\Gamma_+$  and  $\Gamma_-$ , as described above, such that as  $|k| \rightarrow \infty$  in  $D$ , we have  $\tilde{f}(k) \rightarrow 0$ . Then,

$$\tilde{f}_{\pm}(k) = \frac{\pm 1}{2\pi i} \int_{\Gamma_{\pm}} \frac{\tilde{f}(\tilde{k})}{\tilde{k} - k} d\tilde{k}. \quad (18.3)$$

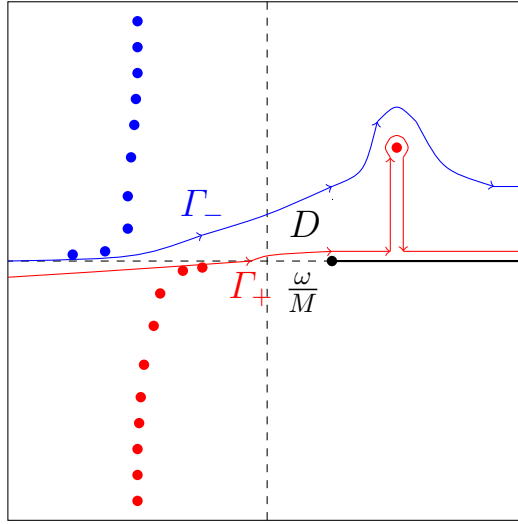


Figure 54: Illustration of  $\Gamma_{\pm}$  and the strip  $D$ . Blue poles, located in the upper half plane, would correspond to a hard walled duct. While the red mode poles including a hydrodynamic instability are associated with the lined wall. Note that  $\Gamma_{+}$  has been taken above the critical layer branch cut.

And  $\tilde{f}_{\pm}(k)$  is analytic above/below  $\Gamma_{\pm}$ , with

$$\tilde{f}_{+}(k) + \tilde{f}_{-}(k) = \tilde{f}(k). \quad (18.4)$$

Additionally we can define the multiplicative decomposition of  $\tilde{f}$ . Once again, let  $\tilde{f}(k)$  be analytic within a strip  $D$  between some  $\Gamma_{+}$  and  $\Gamma_{-}$ , as described above. In addition we require  $\tilde{f}(k)$  to be non-zero within  $D$ . And we require  $\tilde{f}(k) \rightarrow 1$  as  $|k| \rightarrow \infty$  in  $D$ . Then

$$\tilde{f}_{\pm}(k) = \exp \left( \frac{\pm 1}{2\pi i} \int_{\Gamma_{\pm}} \frac{\log(\tilde{f}(\tilde{k}))}{\tilde{k} - k} d\tilde{k} \right). \quad (18.5)$$

And  $\tilde{f}_{\pm}(k)$  is analytic and non-zero above/below  $\Gamma_{\pm}$ , with

$$\tilde{f}_{+}(k)\tilde{f}_{-}(k) = \tilde{f}(k). \quad (18.6)$$

Throughout the remainder of this part we will use subscript  $\pm$  to indicate these half-plane analytic functions, with bold case  $\pm$  to indicate where a multiplicative decomposition has taken place.

## 19 Problem Formulation and Solutions

Firstly we highlight that we will be once again consider the solutions presented in part *II*. We once again are considering the linearised Euler equations under a Fourier series, and will be considering a single wave mode  $m$ . Further our mean

flow is that of a uniform quadratic shear flow (5.14). We are taking the same non-dimensionalisations such that the duct wall is located at  $r = 1$  and are considering the boundary conditions to be impedance boundary conditions given by  $p = Zv$ . In this way, under a Fourier transform we will once again retrieve the homogeneous Pridmore-Brown equation, given by (5.17).

Consider the pressure perturbation to have the following form;

$$p(x, r) = p_{in}(x, r) + p_0(x, r). \quad (19.1)$$

That is,  $p$  has two component parts, an incoming wave  $p_{in}$ , and a scattered wave  $p_0$ . As previously described we split the duct into two sections with different boundary conditions at the wall as illustrated in figure 52 with a hard wall for  $x < 0$  and a lined wall for  $x > 0$ .

$$p'(x, 1) = 0 \quad x < 0. \quad (19.2a)$$

$$p'(x, 1) = -\frac{i\omega}{Z}p(x, 1) \quad x > 0. \quad (19.2b)$$

These are exactly the boundary conditions (5.16) but for the hard and lined wall sections respectively. For now we will assume that the incoming wave is modal in nature. We take

$$p_{in}(x, r) = A_{in}\tilde{\psi}_1(k_{in}, r)e^{-ik_{in}x} \quad (19.3)$$

where  $k_{in}$  is a axial wave mode of the hard wall duct and  $\tilde{\psi}_1$  given by (6.16). This gives us by the definition of a mode that that  $p_{in}(x, r)$  satisfies the boundary conditions at the centre of the duct, (5.11), and within the hard walled region

$$p'_{in}(x, 1) = 0. \quad (19.4)$$

We can then define the boundary conditions for the scattered waves  $p_0(x, r)$  at  $r = 1$  to be;

$$p'_0(x, 1) = 0 \quad x < 0. \quad (19.5a)$$

$$p'_0(x, 1) = -\frac{i\omega}{Z}(p_0(x, 1) + p_{in}(x, 1)) \quad x > 0. \quad (19.5b)$$

As before we Fourier transform  $p_0(x, r)$  into  $\tilde{p}_0(k, r)$  in  $x$  to the axial wave number  $k$ .

$$\tilde{p}_0(k, r) = \int_{-\infty}^{\infty} p_0(x, r)e^{ikx} dx. \quad (19.6)$$

We note that  $\tilde{p}_0(k, r)$  will satisfy the homogeneous Pridmore-Brown equation (5.17). We further enforce that  $\tilde{p}$ , and as a consequence  $\tilde{p}_0$ , will satisfy the boundary condition at  $r = 0$  (5.11). Note that this boundary condition is already satisfied by  $p_{in}(x, r)$  since it is formulated with  $r$  dependence in  $\tilde{\psi}_1(k_{in}, r)$ . In the same way we

can therefore describe  $\tilde{p}_0(k, r)$  as,

$$\tilde{p}_0(k, r) = A(k)\tilde{\psi}_1(k, r). \quad (19.7)$$

Note that we have no reference to the boundary conditions at  $r = 1$  in  $\tilde{p}_0(k, r)$  since we have integrated over all values of  $x$ . To retrieve the boundary conditions we make use of the half range transforms (18.1)

$$\tilde{p}_0(k, r) = \tilde{p}_{0-}(k, r) + \tilde{p}_{0+}(k, r). \quad (19.8a)$$

It follows;

$$\tilde{p}'_{0+}(k, 1) = -\frac{i\omega}{Z}(\tilde{p}_{0+}(k, 1) + \tilde{p}_{in+}(k, 1)), \quad (19.9a)$$

$$\tilde{p}'_{0-}(k, 1) = 0. \quad (19.9b)$$

by taking the  $-$  half range transform (18.1) of the boundary conditions.

We can explicitly formulate  $\tilde{p}_{in+}(k, r)$ , for  $\text{Im}(k) > \text{Im}(k_{in})$  to be

$$\tilde{p}_{in+}(k, r) = \int_0^\infty p_{in}(x, r)e^{ikx} dx = \frac{iA_{in}\tilde{\psi}_1(k_{in}, r)}{k - k_{in}}. \quad (19.10)$$

We can additionally apply the half range transforms to the derivative of  $\tilde{p}_0(x, r)$  with the resulting two equations,

$$A(k)\tilde{\psi}_1(k, r) = \tilde{p}_{0-}(k, r) + \tilde{p}_{0+}(k, r), \quad (19.11a)$$

$$A(k)\tilde{\psi}'_1(k, r) = \tilde{p}'_{0-}(k, r) + \tilde{p}'_{0+}(k, r). \quad (19.11b)$$

Considering the behaviour at the duct wall  $r = 1$  and applying the boundary conditions (19.9) results in,

$$A(k)\tilde{\psi}_1(k, 1) = \tilde{p}_{0-}(k, 1) + \tilde{p}_{0+}(k, 1), \quad (19.12a)$$

$$A(k)\tilde{\psi}'_1(k, 1) = -\frac{i\omega}{Z}(\tilde{p}_{0+}(k, 1) + \tilde{p}_{in+}(k, 1)). \quad (19.12b)$$

Multiplying these equation by  $\tilde{\psi}'_1(k, 1)$  and  $\tilde{\psi}_1(k, 1)$  respectively, it then follows

$$(\tilde{p}_{0-}(k, 1) + \tilde{p}_{0+}(k, 1))\tilde{\psi}'_1(k, 1) = -\frac{i\omega}{Z}(\tilde{p}_{0+}(k, 1) + \tilde{p}_{in+}(k, 1))\tilde{\psi}_1(k, 1) \quad (19.13)$$

which may be rewritten as

$$(\tilde{p}_{0+}(k, 1) + \tilde{p}_{in+}(k, 1)) \left( 1 + \frac{i\omega}{Z} \frac{\tilde{\psi}(k, 1)}{\tilde{\psi}'_1(k, 1)} \right) + \tilde{p}_{0-}(k, 1) = \tilde{p}_{in+}(k, 1). \quad (19.14)$$

(19.14) is a Wiener-Hopf equation with kernel,

$$K(k) = 1 + \frac{i\omega}{Z} \frac{\tilde{\psi}(k, 1)}{\tilde{\psi}'_1(k, 1)} = \frac{\tilde{\psi}'_1(k, 1) + \frac{i\omega}{Z}\tilde{\psi}(k, 1)}{\tilde{\psi}'_1(k, 1)} \quad (19.15)$$

The Wiener-Hopf kernel  $K(k)$  can be seen to be exactly the ratio between the dispersion relations of the lined and hard wall regions. In addition we will show that as  $|k| \rightarrow \infty$  we have  $K(k) \rightarrow 1$ . This is done in section 19.1. Further we have a strip  $D$  such that  $K(k)$  has no poles or zeros, this is done by taking  $\Gamma_-$  under all of the poles associated with  $x < 0$  for both the hard and lined walled sections under the Briggs-Bers criterion, see section 8.3, and  $\Gamma_+$  to be above all the poles associated with  $x > 0$ , including the critical layer branch cut and unstable  $k^+$  poles. As previously illustrated in figure 54. This allows us to perform a multiplicative decomposition of  $K(k)$  as given by (18.5).

$$K(k) = K_-(k)K_+(k) \quad (19.16)$$

Note that although no explicit form of  $K_{\pm}(k)$  is given, these functions can be computed numerically. With code present within both the Mathematica and Julia coding languages. This code is described in [Olver, 2011]. Additionally, despite the lack of analytic solutions for  $K_{\pm}(k)$ , we know that  $K_{\pm}(k)$  are bounded, non-zero and analytic above/below  $\Gamma_{\pm}$  respectively.

We divide our Wiener-Hopf equation by  $K_-(k)$  such that the left hand side is the sum between a (+) function and a (-) function only, while the right hand side is neither.

$$(\tilde{p}_{0+}(k, 1) + \tilde{p}_{in+}(k, 1))K_+(k) + \frac{\tilde{p}_{0-}(k, 1)}{K_-(k)} = \frac{\tilde{p}_{in+}(k, 1)}{K_-(k)}. \quad (19.17)$$

We shall now perform an additive decomposition (18.3) on the right hand side of 19.17;

$$\frac{\tilde{p}_{in+}(k, 1)}{K_-(k)} = S(k) = S_+(k) + S_-(k) \quad (19.18)$$

Using the explicit form of  $\tilde{p}_{in+}(k, 1)$  as given in equation (19.10) it follows

$$S_+(k) = \frac{1}{2\pi i} \int_{\Gamma_+} \frac{iA_{in}\tilde{\psi}_1(k_{in}, 1)}{(\tilde{k} - k)(\tilde{k} - k_{in})K_-(\tilde{k})} d\tilde{k} \quad (19.19)$$

and we can find  $S_+(k)$  by closing in the lower half plane, since we know that  $K_-(k)$  is analytic, non-zero and bounded. In the lower half plane we must be aware that we are also required to consider the critical layer branch cut  $[\frac{\omega}{M}, \infty)$ , although in this case its contribution is 0. This is due to  $K_-$  being analytic in below  $\Gamma_-$ , and

hence does not see the branch cut. It is trivial to show that  $\frac{1}{k-k}$  also does not see the branch cut along the critical layer. This results in,

$$S_+(k) = \frac{\tilde{p}_{in+}(k, 1)}{K_-(k_{in})}, \quad (19.20)$$

and it follow by being an additive decomposition of  $S(k)$  that

$$S_-(k) = \tilde{p}_{in+}(k) \left( \frac{1}{K_-(k)} - \frac{1}{K_-(k_{in})} \right). \quad (19.21)$$

We can therefore write (19.17)

$$(\tilde{p}_{0+}(k, 1) + \tilde{p}_{in+}(k, 1))K_+(k) - \frac{\tilde{p}_{in+}(k, 1)}{K_-(k_{in})} = \tilde{p}_{in+}(k) \left( \frac{1}{K_-(k)} - \frac{1}{K_-(k_{in})} \right) - \frac{\tilde{p}_{0-}(k, 1)}{K_-(k)}. \quad (19.22)$$

Since we have a (+) function being equal to a (-) function it must be that we can write both sides to be equal to a single entire function. To do this we observe the large  $k$  behaviour in the strip  $D$ ,  $|k| \rightarrow \infty$ . We will denote this entire function  $E(k)$ .

$$E(k) = (\tilde{p}_{0+}(k, 1) + \tilde{p}_{in+}(k, 1))K_+(k) - \frac{\tilde{p}_{in+}(k, 1)}{K_-(k_{in})} \quad (19.23a)$$

$$E(k) = \tilde{p}_{in+}(k) \left( \frac{1}{K_-(k)} - \frac{1}{K_-(k_{in})} \right) - \frac{\tilde{p}_{0-}(k, 1)}{K_-(k)}. \quad (19.23b)$$

## 19.1 Asymptotic Behaviour in the Strip $D$

We will begin this section by first showing that as  $|k| \rightarrow \infty$ ,  $K(k) \rightarrow 1$ . First note that by (19.15) this is equivalent to

$$\frac{\psi_1(k, 1)}{\psi_1'(k, 1)} = \frac{C_1 \tilde{p}_1(k, 1) + D_1 \tilde{p}_2(k, 1)}{C_1 \tilde{p}_1'(k, 1) + D_1 \tilde{p}_2'(k, 1)} \rightarrow 0. \quad (19.24)$$

Recalling (6.3) and (6.12) for the expressions of  $\tilde{p}_1(k, r)$  and  $\tilde{p}_2(k, r)$ , which are additionally used in the definitions of  $C_1$  and  $D_1$  (6.17) we may show this limit holds as follows;

First, we make the observations that as  $|k| \rightarrow \infty$ ,

$$Q = h - \frac{\omega h}{2Mk} + O(k^{-2}), \quad (19.25)$$

$$r_c^+ = 1 - \frac{\omega h}{2Mk} + O(k^{-2}). \quad (19.26)$$

with  $Q$  and  $r_c^+$  as given in (5.20). Recalling the formula for the  $a_n$  (6.4b) in order to evaluate  $\tilde{p}_1(k, r)$  it can be found, to leading order in  $k$ ,

$$a_0 = 1, \quad (19.27)$$

$$a_1 = \frac{3}{4}\left(1 - \frac{1}{h}\right) + O(k^{-1}), \quad (19.28)$$

$$a_2 = \frac{1}{10}k^2 + O(1), \quad (19.29)$$

$$\begin{aligned} a_{2n} &= k^2 \frac{a_{2(n-1)}}{2n(2n+3)} + O(k^{2n-2}) \\ &= \frac{3}{(2n+3)(2n+1)!} k^{2n} + O(k^{2n-2}), \end{aligned} \quad (19.30)$$

$$\begin{aligned} a_{2n+1} &= \frac{k^2 a_{2n-1} - (2n+3)\left(\frac{1}{h} - 1\right)a_{2n}}{(2n+1)(2n+4)} + O(k^{2n-1}) \\ &= \frac{3(2n+3)\left(\frac{1-h}{h}\right)k^{2n}}{(2n+4)!} \left(2+n + \sum_{j=1}^n \frac{1}{2j+1}\right) + O(k^{2n-1}). \end{aligned} \quad (19.31)$$

Using this, it follows,

$$\tilde{p}_1(k, 1) = \sum_{n=0}^{\infty} a_n (1 - r_c^+)^{n+3}, \quad (19.32a)$$

$$= - \left(\frac{\omega h}{2Mk}\right)^3 \sum_{n=0}^{\infty} a_{2n} \left(\frac{\omega h}{2M}\right)^{2n} + O(k^{-4}). \quad (19.32b)$$

$$\tilde{p}'_1(k, 1) = \left(\frac{\omega h}{2Mk}\right)^2 \sum_{n=0}^{\infty} a_{2n} (2n+3) \left(\frac{\omega h}{2M}\right)^{2n} + O(k^{-3}). \quad (19.32c)$$

Doing the same for the  $b_n$ , (6.4f), required for  $\tilde{p}_2(k, 1)$  reveals;

$$A = - \frac{k^2}{3} \left(\frac{1-h}{h}\right) \quad (19.33a)$$

$$b_0 = 1, \quad (19.33b)$$

$$b_1 = 0, \quad (19.33c)$$

$$b_2 = - \frac{k^2}{2}, \quad (19.33d)$$

$$b_3 = 0, \quad (19.33e)$$

$$\begin{aligned} b_{2n} &= k^2 \frac{b_{2(n-1)}}{2n(2n-3)} + O(k^{2n-2}), \\ &= \frac{-(2n-1)}{(2n)!} k^{2n} + O(k^{2n-2}), \end{aligned} \quad (19.33f)$$

$$\begin{aligned} b_{2n+1} &= - \frac{A(4n-1)a_{2n-2} - k^2 b_{2n-1} - 2n\left(\frac{1-h}{h}\right)b_{2n}}{(2n+1)(2n-2)} + O(k^{2n-1}), \\ &= \frac{4\left(\frac{1-h}{h}\right)k^{2n}}{(2n+1)!} \sum_{j=1}^n \frac{j+2}{2j+5} + O(k^{2n-1}). \end{aligned} \quad (19.33g)$$

It then follows,

$$\tilde{p}_2(k, 1) = A \log(1 - r_c^+) \tilde{p}_1(k, 1) + \sum_{n=0}^{\infty} b_n (1 - r_c^+)^n \quad (19.34a)$$

$$= \sum_{n=0}^{\infty} b_{2n} \left( \frac{\omega h}{2M} \right)^{2n} + O(k^{-1}) \quad (19.34b)$$

$$\tilde{p}'_2(k, 1) = - \frac{Mk}{\omega h} \sum_{n=1}^{\infty} 2nb_{2n} \left( \frac{\omega h}{Mk} \right)^{2n} + O(\log(k^{-1})) \quad (19.34c)$$

Rewriting (19.24) as

$$\frac{\tilde{\psi}_1(k, 1)}{\tilde{\psi}'_1(k, 1)} = \frac{\tilde{p}_1(k, 1) + \frac{D_1}{C_1} \tilde{p}_2(k, 1)}{\tilde{p}'_1(k, 1) + \frac{D_1}{C_1} \tilde{p}'_2(k, 1)} \quad (19.35)$$

by making the assumption that  $\frac{D_1}{C_1} \geq O(k^{-3})$  it follows as  $|k| \rightarrow \infty$

$$\frac{\tilde{\psi}_1(k, 1)}{\tilde{\psi}'_1(k, 1)} = \frac{\tilde{p}_1(k, 1) + \frac{D_1}{C_1} \tilde{p}_2(k, 1)}{\tilde{p}'_1(k, 1) + \frac{D_1}{C_1} \tilde{p}'_2(k, 1)} \approx \frac{\tilde{p}_2(k, 1)}{\tilde{p}'_2(k, 1)} + O\left(\frac{C_1}{D_1} k^{-4}\right), \quad (19.36)$$

It turns out that  $\frac{D_1}{C_1} \geq O(k^{-3}) \sim O(k^{-3})$ . In order to show this first note that as  $|k| \rightarrow \infty$  in  $D$ , we have  $|\operatorname{Re}(k)| \rightarrow \infty$  and  $\alpha \approx ik\sqrt{1 - M^2}$ , and for large arguments. Since,

$$J_m(\alpha(1 - h)) \sim J'_m(\alpha(1 - h)) \sim \frac{e^{(|\operatorname{Re}(k)|\sqrt{1 - M^2})}}{ik\sqrt{1 - M^2}}. \quad (19.37)$$

it follows

$$\frac{D_1}{C_1} = - \frac{\alpha J'_m(\alpha(1 - h)) \tilde{p}_1(k, 1 - h) - J_m(\alpha(1 - h)) \tilde{p}'_1(k, 1 - h)}{\alpha J'_m(\alpha(1 - h)) \tilde{p}_2(k, 1 - h) - J_m(\alpha(1 - h)) \tilde{p}'_2(k, 1 - h)} = \frac{\tilde{p}_1(k, 1 - h)}{\tilde{p}_2(k, 1 - h)} \quad (19.38)$$

with only the  $\alpha J'_m(\alpha(1 - h))$  contributing to the leading order expansion. Writing both  $\tilde{p}_1(k, 1 - h)$  and  $\tilde{p}_2(k, 1 - h)$  as power series in  $k$  making use of the leading orders of  $a_n$  and  $b_n$

$$\frac{\tilde{p}_1(k, 1 - h)}{\tilde{p}_2(k, 1 - h)} = - h^3 \frac{3 \sum_{n=0}^{\infty} (kh)^{2n} \left( \frac{1}{(2n+3)(2n+1)!} - \frac{(1-h)(2n+3)(2+n+\sum_{j=1}^n \frac{1}{2j+1})}{(2n+4)!} \right)}{\sum_{n=0}^{\infty} (kh)^{2n} \left( \frac{2n-1}{(2n)!} + \frac{4(1-h) \sum_{j=1}^n \frac{j+2}{2j+5}}{(2n+1)!} \right)} \quad (19.39a)$$

$$= - 3h^3 \frac{\sum_{n=0}^{\infty} \frac{(kh)^{2n}}{(2n)!} A_n}{\sum_{n=0}^{\infty} \frac{(kh)^{2n}}{(2n)!} B_n} \quad (19.39b)$$

$$A_n = \frac{1}{2n+1} \left( \frac{1}{(2n+3)} - \frac{(1-h)}{(2n+2)(2n+4)} (2+n + \sum_{j=1}^n \frac{1}{2j+1}) \right) \quad (19.39c)$$

$$B_n = 2n - 1 + \frac{4(1-h)}{(2n+1)} \sum_{n=1}^n \frac{j+2}{2j+5}. \quad (19.39d)$$

For any fixed  $k$ , both of these sums will converge, however as  $|k| \rightarrow \infty$  both will diverge to infinity. Appealing to L'Hôpital's rule for the large  $k$  limit, we can examine the ratio of  $\tilde{p}_1(k, 1-h)$  and  $\tilde{p}_2(k, 1-h)$  by taking the derivatives of the numerator and denominator of (19.39a) with respect to  $k$ , and consider the same limit,  $|k| \rightarrow \infty$  in  $D$ . We proceed by bounding the two sums from above and below for general  $k$  in order to resolve their behaviour in the limit.

$$\frac{\frac{\partial \tilde{p}_1(k, 1-h)}{\partial k}}{\frac{\partial \tilde{p}_2(k, 1-h)}{\partial k}} = -3h^3 \frac{\sum_{n=0}^{\infty} \frac{(kh)^{2n+1}}{(2n+1)!} A_{n+1}}{\sum_{n=0}^{\infty} \frac{(kh)^{2n+1}}{(2n+1)!} B_{n+1}}. \quad (19.40a)$$

$$\begin{aligned} \frac{A_{n+1}}{(2n+1)!} &= \frac{1}{(2n+3)!} \left( \frac{(2n+2)(2n+3)}{(2n+1)(2n+5)} - \frac{(1-h)}{2} \frac{(2n+2)(2n+3)}{(2n+4)(2n+1)} \right. \\ &\quad \left. - (1-h) \frac{(2n+2)(2n+3)}{(2n+4)(2n+1)} \sum_{j=1}^{n+1} \frac{1}{(2j+1)(2n+6)} \right) \end{aligned} \quad (19.40b)$$

$$\begin{aligned} &< \frac{1}{(2n+3)!} \left( \frac{6}{5} - \frac{1-h}{2} \right) \\ &= \frac{1}{(2n+3)!} \left( \frac{7}{10} + \frac{h}{2} \right) \end{aligned} \quad (19.40c)$$

$$\begin{aligned} &> \frac{1}{(2n+3)!} \left( \frac{42}{45} - (1-h) \frac{3}{4} - (1-h) \frac{1}{12} \right) \\ &= \frac{1}{(2n+3)!} \left( \frac{1}{10} + \frac{5h}{6} \right) \end{aligned} \quad (19.40d)$$

$$\frac{B_{n+1}}{(2n+1)!} = \frac{1}{(2n)!} \left( 1 + \frac{4(1-h)}{(2n+3)(2n+1)} \sum_{j=1}^{n+1} \frac{j+2}{2j+5} \right) \quad (19.40e)$$

$$> \frac{1}{(2n)!} \quad (19.40f)$$

$$< \frac{1}{(2n)!} \left( 1 + (1-h) \frac{3}{7} \right) \quad (19.40g)$$

$$= \frac{1}{(2n)!} \frac{10-3h}{7} \quad (19.40h)$$

In this was we can then write,

$$\sum_{n=0}^{\infty} \frac{(kh)^{2n+1}}{(2n+1)!} A_{n+1} < \frac{7+5h}{10(kh)^2} \sum_{n=0}^{\infty} \frac{(kh)^{2n+3}}{(2n+3)!} = \frac{7+5h}{10(kh)^2} \sinh(kh) \quad (19.41a)$$

$$> \frac{3 + 25h}{30(kh)^2} \sum_{n=0}^{\infty} \frac{(kh)^{2n+3}}{(2n+3)!} = \frac{3 + 25h}{30(hk)^2} \sinh(kh) \quad (19.41b)$$

$$\sum_{n=0}^{\infty} \frac{(kh)^{2n+1}}{(2n+1)!} B_{n+1} < (kh) \sum_{n=0}^{\infty} \frac{(kh)^{2n}}{(2n)!} = kh \cosh(kh) \quad (19.41c)$$

$$> \frac{3 + 25h}{30(kh)^2} \sum_{n=0}^{\infty} \frac{(kh)^{2n}}{(2n)!} = \frac{10 - 3h}{7} kh \cosh(kh) \quad (19.41d)$$

$$\frac{\frac{\partial \tilde{p}_1(k, 1-h)}{\partial k}}{\frac{\partial \tilde{p}_2(k, 1-h)}{\partial k}} < \frac{\frac{7+5h}{10k^2 h^2} \sinh(kh)}{\frac{10-3h}{7} kh \cosh(kh)} \quad (19.41e)$$

$$> \frac{\frac{3+25h}{30k^2 h^2} \sinh(kh)}{kh \cosh(kh)} \quad (19.41f)$$

Finally we may conclude that in the limit of  $|k| \rightarrow \infty$  in D we have

$$\frac{D_1}{C_1} \approx \frac{\tilde{p}_1(k, 1-h)}{\tilde{p}_2(k, 1-h)} \approx \frac{\frac{\partial \tilde{p}_1(k, 1-h)}{\partial k}}{\frac{\partial \tilde{p}_2(k, 1-h)}{\partial k}} = O\left(k^{-3} \frac{\sinh(hk)}{\cosh(hk)}\right) \quad (19.42)$$

as was previous sought.

In order to then conclude the behaviour of  $K(k)$  we need only investigate the limit of  $\frac{\tilde{p}_2(k, 1)}{\tilde{p}'_2(k, 1)}$ , which follows from (19.34) and gives us

$$K(k) = \frac{\psi'_1(k, 1) + \frac{i\omega}{Z} \psi_1(k, 1)}{\psi'_1(k, 1)} = 1 + O(k^{-1}) \quad (19.43)$$

And we can proceed with multiplicative decomposition of the kernel as given in (18.5) and was used in the formulation of (19.17). Further note that wlog we also have  $K_{\pm}(k) \rightarrow 1$ .

## 19.2 Asymptotic Behaviour of the Entire Function

In addition, it follows from (19.10)  $\tilde{p}_{in+}(k, 1) \rightarrow 0$ . Therefore, when we wish to examine the asymptotic behaviour of our entire function, given in (19.23), we need only consider  $\tilde{p}_{0\pm}(k, 1)$ . Considering  $\tilde{p}_0(x, r)$  near the wall, we expect continuity irrespective of if we approach  $x = 0$  from above or below, which is equivalent to considering  $|k| \rightarrow \infty$  in  $D$ . Considering the Pridmore-Brown equation in the sheared flow for large  $k$  we have that

$$\begin{aligned} \tilde{p}''(r) + \left( \frac{1}{r} - \frac{2}{r-1} - \frac{2}{r-1+2h} \right) \tilde{p}'(r) \\ + k^2 \left( \frac{M^2(r-1)^2(r-1+2h)^2}{h^4} - 1 \right) \tilde{p}(r) = 0 \end{aligned} \quad (19.44a)$$

If we then consider  $r = 1 - \epsilon$ , i.e. we are near the duct wall,

$$\tilde{p}''(\epsilon) - \frac{2}{\epsilon} \tilde{p}'(\epsilon) - k^2 \tilde{p}(\epsilon) = 0 \quad (19.44b)$$

where  $'$  temporarily indicates derivative with respect to  $\epsilon$ . If we assume we have taken the limit  $x \rightarrow 0^-$ , then it follows in this  $k$  limit,

$$\tilde{p}''_-(\epsilon) = k^2 \tilde{p}_-(\epsilon) \quad \tilde{p}_-(\epsilon) = Ae^{k\epsilon} + Be^{-k\epsilon} \quad (19.44c)$$

And so, either our entire function decays to zero, or is unbounded. Now assuming  $x \rightarrow 0^+$ ,

$$\tilde{p}''_+(\epsilon) = \left(\frac{2i\omega}{\epsilon Z} + k^2\right) \tilde{p}_+(\epsilon) \quad (19.44d)$$

Which making use of continuity at  $x = 0$  gives that for  $|k| \rightarrow \infty$  in  $D$

$$\frac{2i\omega}{\epsilon Z} (Ae^{k\epsilon} + Be^{-k\epsilon}) = 0 \quad (19.44e)$$

And so it must be that  $A = 0$ . Hence,  $\tilde{\psi}_-(k, 1), \tilde{\psi}_+(k, 1) \rightarrow 0$  as  $|k| \rightarrow \infty$  in  $D$ . From this it is both possible to conclude that the resulting entire function is bounded in  $D$  and so by *Louville's Theorem* which states every bounded Entire function must be a constant. Thus  $E(k)$  must be a constant, and further this constant is zero by examining the large  $|k|$  limits. That is,

$$\tilde{p}_{0+}(k, 1) = -\tilde{p}_{in+}(k, 1) + \frac{\tilde{p}_{in+}(k, 1)}{K_-(k_{in})K_+(k)}, \quad (19.45a)$$

$$\tilde{p}_{0-}(k, 1) = \tilde{p}_{in+}(k, 1) - \frac{\tilde{p}_{in+}(k, 1)K_-(k)}{K_-(k_{in})}. \quad (19.45b)$$

## 20 Scattering due to Change in Boundary Condition for a Modal Source

We now seek to retrieve  $p_0(x, r)$

$$p_0(x, r) = \frac{1}{2\pi} \int_{\Gamma} A(k) \tilde{\psi}_1(k, r) e^{-ikx} dk \quad (20.1a)$$

$$p_0(x, r) = \frac{1}{2\pi} \int_{\Gamma} (\tilde{p}_0^+(k, 1) + \tilde{p}_0^-(k, 1)) \frac{\tilde{\psi}_1(k, r)}{\tilde{\psi}_1(k, 1)} e^{-ikx} dk \quad (20.1b)$$

Where  $\Gamma$  is some suitable Fourier inversion contour contained within  $D$ . As was done in section 8.1 we compute the Fourier inversion by closing in the upper half plane for  $x < 0$  and in the lower half plane for  $x > 0$ .

Note that we already know that only  $\tilde{p}_0^-(k, 1)$  has no poles in the lower half plane,

while  $\tilde{p}_0^+(k, 1)$  has no poles in the upper half plane. It may be tempting to think that we also have poles where  $\tilde{\psi}_1(k, 1) = 0$ , however due to our formulations of  $\tilde{p}_{0+}(k, 1)$  and  $\tilde{p}_{0-}(k, 1)$  we would also have a zero of the numerator and so no pole occurs. In the same way, when considering the critical layer branch cut we must consider both  $\tilde{p}_{0+}(k, 1)$  and  $\tilde{p}_{0-}(k, r)$ , not just  $\tilde{p}_{0+}(k, 1)$ , since we would experience a contribution from the  $\tilde{p}_{0-}(k, 1)$  terms through the jump in  $\frac{\tilde{\psi}_1(k, r)}{\tilde{\psi}_1(k, 1)}$ .

## 20.1 Modal Scattering for $x < 0$

When we close in the upper half plane,  $x < 0$ , we first rewrite  $\tilde{p}_{0-}(k, 1)$  as

$$\tilde{p}_{0-}(k, 1) = \tilde{p}_{in+}(k, 1) - \frac{\tilde{p}_{in}(k, 1) \left( \tilde{\psi}'_1(k, 1) + \frac{i\omega}{Z} \tilde{\psi}_1(k, 1) \right)}{\tilde{\psi}'_1(k, 1) K_+(k) K_-(k_{in})} \quad (20.2)$$

Doing so results in an expression that has poles in the upper half plane only when  $\tilde{\psi}'_1(k, 1) = 0$ . We denote these modes as  $k_{1,n}$ . Since it is known, by construction,  $K_+$  is analytic and non-zero in the upper half plane. It then follows easily from the residue theorem that;

$$\tilde{p}_0(x, r) = \frac{i\omega}{Z} \frac{A_{in} \tilde{\psi}_1(k_{in}, 1)}{K_-(k_{in})} \sum_{k_{1,n}} \frac{\tilde{\psi}_1(k_{1,n}, r) e^{-ik_{1,n}x}}{(k_{1,n} - k_{in}) \frac{\partial \tilde{\psi}'_1}{\partial k}(k_{1,n}, 1) K_+(k_{1,n})} \quad (20.3)$$

where  $k_{1,n}$  are modal poles of the hard walled region located above  $\Gamma$ .

That is,  $\tilde{p}_0(x, r)$  is expressed as the sum of hard walled upstream propagating modal solutions, each with an associated amplitude  $A_{1,n}$ , which scales linearly with the amplitude of the incoming wave  $A_{in}$ .

$$\tilde{p}_0(x, r) = \sum_{k_{1,n}} A_{1,n} \tilde{\psi}_1(k_{1,n}, r) e^{-ik_{1,n}x} \quad (20.4a)$$

$$A_{1,n} = \frac{i\omega}{Z} \frac{A_{in} \tilde{\psi}_1(k_{in}, 1)}{K_-(k_{in}) K_+(k_{1,n}) (k_{1,n} - k_{in}) \frac{\partial \tilde{\psi}'_1}{\partial k}(k_{1,n}, 1)} \quad (20.4b)$$

## 20.2 Scattering for $x > 0$

### 20.2.1 Modal Scattering for $x > 0$

When considering  $x > 0$ , as previously mentioned we must consider both the poles and the critical layer branch cut. In order to consider the poles we first rewrite

$\tilde{p}_0^+(k, 1)$  as

$$\tilde{p}_{0+}(k, 1) = -\tilde{p}_{in+}(k, 1) - \frac{\tilde{p}_{in+}(k, 1)\tilde{\psi}'_1(k, 1)K_-(k)}{K_-(k_{in})\left(\tilde{\psi}'_1(k, 1) + \frac{i\omega}{Z}\tilde{\psi}_1(k, 1)\right)} \quad (20.5)$$

Which has poles occur in two place. The first occurs as a zero of  $(k - k_{in})$  within  $\tilde{p}_{in+}(k, 1)$ , since  $k_{in}$  is contained below  $\Gamma$ . All of the other poles occur instead as modal solutions to the lined wall dispersion relation, which we denote  $k_{2,n}$ . This would include any unstable hydrodynamic instabilities.

It can trivially be shown that the residue of the first pole exactly retrieves  $-\tilde{p}_{in}(k, r)$ . It then follows

$$p_0(x, r) = -p_{in}(x, r) + \Sigma(x, r) + I(x, r) \quad (20.6)$$

$$\Sigma(x, r) = -\frac{i\omega}{Z} \frac{A_{in}\tilde{\psi}_1(k_{in}, 1)}{K_-(k_{in})} \sum_{k_{2,n}} \frac{K_-(k_{2,n})\tilde{\psi}_1(k_{2,n}, r)e^{ik_{2,n}x}}{(k_{2,n} - k_{in})\left(\frac{\partial\tilde{\psi}'_1}{\partial k}(k_{2,n}, 1) + \frac{i\omega}{Z}\frac{\partial\tilde{\psi}_1}{\partial k}(k_{2,n}, 1)\right)} \quad (20.7)$$

Where  $I(x)$  will be the contribution due to integrating around the critical layer branch cut.

### 20.2.2 Non-modal Scattering for $x > 0$

$$I(x, r) = -\int_{\frac{\omega}{M}}^{\infty} \frac{1}{2\pi} \Delta \left( \tilde{p}_{0+}(k, 1) + \tilde{p}_{0-}(k, 1) \frac{\tilde{\psi}_1(k, r)}{\tilde{\psi}_1(k, 1)} e^{-ikx} \right) dk \quad (20.8a)$$

$$= -\int_{\frac{\omega}{M}}^{\infty} \frac{e^{-ikx}}{2\pi} \Delta \left( \frac{\tilde{p}_{in+}(k, 1)}{K_-(k_{in})} \left( \frac{1}{K_+(k)} - K_-(k) \right) \frac{\tilde{\psi}_1(k, r)}{\tilde{\psi}_1(k, 1)} \right) dk \quad (20.8b)$$

$$= -\int_{\frac{\omega}{M}}^{\infty} \frac{e^{-ikx}}{2\pi} \frac{\tilde{p}_{in+}(k, 1)K_-(k)}{K_-(k_{in})} \Delta \left( \left( \frac{\tilde{\psi}'_1(k, 1)}{\tilde{\psi}'_1(k, 1) + \frac{i\omega}{Z}\tilde{\psi}_1(k, 1)} - 1 \right) \frac{\tilde{\psi}_1(k, r)}{\tilde{\psi}_1(k, 1)} \right) dk \quad (20.8c)$$

$$= -\int_{\frac{\omega}{M}}^{\infty} \frac{e^{-ikx}}{2\pi} \frac{\tilde{p}_{in+}(k, 1)K_-(k)}{K_-(k_{in})} \Delta \left( \frac{-\frac{i\omega}{Z}\tilde{\psi}_1(k, r)}{\tilde{\psi}'_1(k, 1) + \frac{i\omega}{Z}\tilde{\psi}_1(k, 1)} \right) dk \quad (20.8d)$$

$$= -\frac{\omega}{Z} \frac{A_{in}\tilde{\psi}_1(k_{in}, 1)}{K_-(k_{in})} \int_{\frac{\omega}{M}}^{\infty} \frac{K_-(k)e^{-ikx}}{2\pi(k - k_{in})} \Delta \left( \frac{\tilde{\psi}_1(k, r)}{\tilde{\psi}'_1(k, 1) + \frac{i\omega}{Z}\tilde{\psi}_1(k, 1)} \right) dk \quad (20.8e)$$

$$= -\frac{\omega}{Z} \frac{A_{in}\tilde{\psi}_1(k_{in}, 1)}{K_-(k_{in})} (I_{\frac{\omega}{M}}(x, r) + I_r(x, r)H(r - (1 - h))). \quad (20.8f)$$

In this way  $I_{\frac{\omega}{M}}(x, r)$  is the jump due to the crossing the branch cut observed at  $1 - h$ , and  $I_r(x, r)$  is the jump for crossing the branch cut at  $r$ . We therefore have

two cases, when  $r < 1 - h$ , and  $r > 1 - h$ .

$$I_{\frac{\omega}{M}} = \int_{\frac{\omega}{M}}^{\infty} \frac{-J_m(\alpha r)(\tilde{p}'_1(1) + \frac{i\omega}{Z}\tilde{p}_1(1))}{(\tilde{\psi}'_1(k, 1) + \frac{i\omega}{Z}\tilde{\psi}_1(k, 1) + 2\pi i AD_1(\tilde{p}'_1(1) + \frac{i\omega}{Z}\tilde{p}_1(1)))} \times \frac{iAD_1 K_-(k)e^{-ikx}}{(k - k_{in})(\tilde{\psi}'_1(1) + \frac{i\omega}{Z}\tilde{\psi}_1(1))} dk \quad r \leq 1 - h \quad (20.8g)$$

$$I_{\frac{\omega}{M}} = \int_{\frac{\omega}{M}}^{\infty} \frac{(\tilde{p}_1(r)(\tilde{p}'_2(1) + \frac{i\omega}{Z}\tilde{p}_2(1)) - \tilde{p}_2(r)(\tilde{p}'_1(1) + \frac{i\omega}{Z}\tilde{p}_1(1)))}{(\tilde{\psi}'_1(k, 1) + \frac{i\omega}{Z}\tilde{\psi}_1(k, 1) + 2\pi i AD_1(\tilde{p}'_1(1) + \frac{i\omega}{Z}\tilde{p}_1(1)))} \times \frac{iAD_1^2 K_-(k)e^{-ikx}}{(k - k_{in})(\tilde{\psi}'_1(k, 1) + \frac{i\omega}{Z}\tilde{\psi}_1(k, 1))} dk \quad r > 1 - h \quad (20.8h)$$

$$I_r = \int_{k_r}^{\infty} \frac{-\tilde{p}_1(r)(\tilde{\psi}'_1(k, 1) + \frac{i\omega}{Z}\tilde{\psi}_1(k, 1))}{(\tilde{\psi}'_1(k, 1) + \frac{i\omega}{Z}\tilde{\psi}_1(k, 1) + 2\pi i AD_1(\tilde{p}'_1(1) + \frac{i\omega}{Z}\tilde{p}_1(1)))} \times \frac{iAD_1 K_-(k)e^{-ikx}}{(k - k_{in})(\tilde{\psi}'_1(1) + \frac{i\omega}{Z}\tilde{\psi}_1(1))} dk \quad r > 1 - h \quad (20.8i)$$

with  $k_r$  once again given by,

$$\omega - U(r)k_r = 0, \quad k_r = \frac{\omega}{M} \left( 1 - \left( 1 - \frac{1-r}{h} \right)^2 \right)^{-1} \quad (20.9)$$

exactly as in equation (7.5). Additionally as in section 9.4 we can transform both of these integrals onto the steepest descent contour, which may once again reveal a  $k^+$  and  $k^-$  pole located below the branch cut.

If a  $k^-$  pole is revealed then it would have already been included in the modal sum and so deforming around the branch cut would subtract the pole from the modal sum.

If a  $k^+$  pole is revealed then it would not normally be included in the modal sum. It contributes to the Fourier inversion as

$$R^+(k^+) = -\frac{i\omega}{Z} \frac{A_{in} K_-(k^+) \tilde{\psi}_1(k_{in}, 1) \tilde{\psi}_1^+(k^+, r) e^{-ik^+ x}}{K_-(k_{in})(k^+ - k_{in}) \left( \frac{\partial \tilde{\psi}_1^+(k^+, 1)}{\partial k} + \frac{i\omega}{Z} \frac{\partial \tilde{\psi}_1^+(k^+, 1)}{\partial k} \right)} \quad (20.10)$$

$$\tilde{\psi}_1^+(k, r) = \tilde{\psi}_1(k, r) + 2\pi i D_1 \tilde{p}_1(k, r) \quad (20.11)$$

where  $\tilde{\psi}_1(k, r)$  is evaluated as if below the branch cut. Using the method of steepest descent we can rewrite the integral around the branch cut as

$$I(x, r) = -\frac{\omega}{Z} \frac{A_{in} \tilde{\psi}_1(k_{in}, 1)}{K_-(k_{in})} (\bar{I}_{\frac{\omega}{M}}(x, r) + \bar{I}_r(x, r) H(r - 1 + h)) + \sum_{k^+ : \text{Im}(k^+) < 0} R^+(k^+) - \sum_{k^- : \text{Im}(k^-) < 0} R(k^-). \quad (20.12a)$$

$$\bar{I}_{\frac{\omega}{M}} = \int_0^\infty \frac{-J_m(\alpha r)(\tilde{p}'_1(1) + \frac{i\omega}{Z}\tilde{p}_1(1))}{(\tilde{\psi}'_1(k, 1) + \frac{i\omega}{Z}\tilde{\psi}_1(k, 1) + 2\pi i AD_1(\tilde{p}'_1(1) + \frac{i\omega}{Z}\tilde{p}_1(1)))} \times \frac{AD_1 K_-(k)e^{-\xi x} e^{-i\frac{\omega}{M}x}}{(k - k_{in})(\tilde{\psi}'_1(1) + \frac{i\omega}{Z}\tilde{\psi}_1(1))} \Big|_{k=\frac{\omega}{M}-i\xi} d\xi \quad r \leq 1 - h \quad (20.12b)$$

$$\bar{I}_{\frac{\omega}{M}} = \int_0^\infty \frac{(\tilde{p}_1(r)(\tilde{p}'_2(1) + \frac{i\omega}{Z}\tilde{p}_2(1)) - \tilde{p}_2(r)(\tilde{p}'_1(1) + \frac{i\omega}{Z}\tilde{p}_1(1)))}{(\tilde{\psi}'_1(k, 1) + \frac{i\omega}{Z}\tilde{\psi}_1(k, 1) + 2\pi i AD_1(\tilde{p}'_1(1) + \frac{i\omega}{Z}\tilde{p}_1(1)))} \times \frac{AD_1^2 K_-(k)e^{-\xi x} e^{-i\frac{\omega}{M}x}}{(k - k_{in})(\tilde{\psi}'_1(k, 1) + \frac{i\omega}{Z}\tilde{\psi}_1(k, 1))} \Big|_{k=\frac{\omega}{M}-i\xi} d\xi \quad r > 1 - h \quad (20.12c)$$

$$\bar{I}_r = \int_0^\infty \frac{-\tilde{p}_1(r)}{(\tilde{\psi}'_1(k, 1) + \frac{i\omega}{Z}\tilde{\psi}_1(k, 1) + 2\pi i AD_1(\tilde{p}'_1(1) + \frac{i\omega}{Z}\tilde{p}_1(1)))} \times \frac{AD_1 K_-(k)e^{-\xi x} e^{-ik_r x}}{(k - k_{in})} \Big|_{k=k_r-i\xi} d\xi \quad r > 1 - h \quad (20.12d)$$

When evaluating these integrals in the far field we can appeal to Watson's lemma once more. Where we make use of the scalings given in section 9. This gives us an output of at most two waves. The first is derived from  $\bar{I}_{\frac{\omega}{M}}$  and is convected with the mean flow  $M$ . The second is only present when the observer is in the sheared flow region, corresponding to  $\bar{I}_r$ , and is a wave convected at the flow speed  $U(r)$  at the observer. For the first of these waves we find the integrand behaves, excluding the exponents as  $k \rightarrow \frac{\omega}{M}$ , like,

$$\frac{-J_m(\alpha r)(\tilde{p}'_1(1) + \frac{i\omega}{Z}\tilde{p}_1(1))}{(\tilde{\psi}'_1(k, 1) + \frac{i\omega}{Z}\tilde{\psi}_1(k, 1) + 2\pi i AD_1(\tilde{p}'_1(1) + \frac{i\omega}{Z}\tilde{p}_1(1)))} \frac{AD_1 K_-(k)}{(k - k_{in})(\tilde{\psi}'_1(1) + \frac{i\omega}{Z}\tilde{\psi}_1(1))} \approx \frac{J_m(\alpha r)(A_1 + \frac{i\omega}{M}B_1) \frac{1}{3Q^2} (\frac{\omega^2}{M^2} + \frac{m^2}{(1-h)^2}) J_m(\alpha(1-h)) K_-(\frac{\omega}{M})}{(\frac{\omega}{M} - k_{in}) (\frac{4\alpha J'_m(\alpha(1-h))}{3Q^2})^2 (A_1 + \frac{i\omega}{M}B_1)^2} \approx \frac{3Q^3 J_m(\alpha r) J_m(\alpha(1-h)) K_-(\frac{\omega}{M})}{16(\frac{\omega}{M} - k_{in}) \alpha^2 J'_m(\alpha(1-h))^2 (A_1 + \frac{i\omega}{M}B_1)} \quad r < 1 - h \quad (20.13a)$$

$$\frac{\tilde{p}_1(r)(\tilde{p}'_2(1) + \frac{i\omega}{M}\tilde{p}_2(1)) - \tilde{p}_2(r)(\tilde{p}'_1(1) + \frac{i\omega}{M}\tilde{p}_1(1))}{(\tilde{\psi}'_1(k, 1) + \frac{i\omega}{Z}\tilde{\psi}_1(k, 1) + 2\pi i AD_1(\tilde{p}'_1(1) + \frac{i\omega}{Z}\tilde{p}_1(1)))} \frac{AD_1^2 K_-(k)}{(k - k_{in})(\tilde{\psi}'_1(1) + \frac{i\omega}{Z}\tilde{\psi}_1(1))} \approx - \frac{3Q^3 (A_1 B_2 - B_1 A_2) (\tilde{p}_{12}(r) + \frac{i\omega}{Z}\tilde{p}_{11}(r)) (\frac{\omega^2}{M^2} + \frac{m^2}{(1-h)^2}) J_m(\alpha(1-h))^2 K_-(\frac{\omega}{M})}{16(\frac{\omega}{M} - k_{in}) \alpha^2 J'_m(\alpha(1-h))^2 (A_1 + \frac{i\omega}{Z}B_1)^2} \quad (20.13b)$$

leading to an integrand, including the pre-factor in (20.12a) and exponent terms, within Watson's Lemma, behaving like

$$\sim - \frac{\omega}{Z} \frac{A_{in} \tilde{\psi}_1(k_{in}, 1) K_-(\frac{\omega}{M})}{K_-(k_{in}) (\frac{\omega}{M} - k_{in})} \frac{J_m(\alpha(1-h))^2}{\alpha^2 J'_m(\alpha(1-h))^2} j(x) f(r) \quad (20.14a)$$

$$j(x) = \frac{3(\frac{\omega^2}{M^2} + \frac{m^2}{(1-h)^2}) h^3 \frac{\omega}{M} \frac{3}{2} \frac{i-1}{\sqrt{2}} \xi^{\frac{3}{2}} e^{i\frac{\omega}{M}x}}{16(A_1 + \frac{i\omega}{Z}B_1)} \sim \xi^{\frac{5}{2}} \quad (20.14b)$$

$$f(r) = \begin{cases} \frac{\psi_1(r)}{D_1} & r \leq 1 - h \\ \frac{\psi_2(r)}{D_2} & r > 1 - h \end{cases} \quad (20.14c)$$

which leads to a wave that decays like  $x^{-\frac{7}{2}}$ . The equivalent of  $I_{\frac{\omega}{M}}$  for a sound source in the sheared flow in the infinite lined duct under a point mass source case. While, for the second we have a wave that decays like  $x^{-4}$ , as was also seen for  $r > 1 - h$  in the the case of a point mass source within a infinite lined duct under the same shear mean flow profile. See table 4. With integrand, as  $k \rightarrow k_r$ , like

$$\sim \frac{-AD_1 K_-(k_r) e^{-ik_r x} (k - k_r)^3}{(\tilde{\psi}'_1(k_r, 1) + \frac{i\omega}{Z} \tilde{\psi}_1(k_r, 1) + 2\pi i AD_1 (\tilde{p}'_1(1) + \frac{i\omega}{Z} \tilde{p}_1(1)))(k_r - k_{in})} \sim \xi^3 \quad (20.15a)$$

noting that  $k_r = k_r(r)$ . Within each of these  $A_1$  and  $B_1$  are given as in (6.13).

### 20.2.3 Total Scattering for $x > 0$

In Summary, for  $x > 0$  our scattered field can be described as; the removal of the incoming field, which would not satisfy the boundary condition for  $x > 0$ . The sum over the downstream propagating lined duct modes with associated amplitudes, that once again scale linearly with the incoming waves amplitude  $A_{in}$ , this includes any hydrodynamic instabilities. The removal of any modal poles located below the critical layer branch cut, and inclusion of modal poles located behind the branch cut, as in figure 7. Finally, there are up to two non-modal waves with algebraically decaying amplitudes from the critical layer branch cut, the first with phase velocity equal to the mean flow speed at the centre line of the duct, decaying like  $x^{-\frac{7}{2}}$ , and the second with phase velocity equal to that of the flow speed at the observer, when they are located in the sheared mean flow, decaying like  $x^{-4}$ .

$$\begin{aligned} \tilde{p}_0(x, r) = & -\tilde{p}_{in}(r, x) + \sum_{k_{2,n}} A_{2,n} \psi_1(k_{2,n}, r) e^{-ik_{2,n}x} - \sum_{\substack{\text{Re}(k_{2,n}) > \frac{\omega}{M} \\ \text{Im}(k_{2,n}) < 0}} A_{2,n} \psi_1(k_{2,n}, r) e^{-ik_{2,n}x} \\ & + \sum_{\text{Im}(k^+) < 0} A^+ \psi_1^+(k^+, r) e^{-ik^+x} + \bar{I}_{\frac{\omega}{M}} e^{-i\frac{\omega}{M}x} + \bar{I}_r e^{-ik_r x} H(r - 1 + h) \end{aligned} \quad (20.16a)$$

$$A_{2,n} = -\frac{i\omega}{Z} \frac{A_{in} K_-(k_{2,n}) \tilde{\psi}_1(k_{in}, 1)}{K_-(k_{in})(k_{2,n} - k_{in}) \left( \frac{\partial \tilde{\psi}'_1}{\partial k}(k_{2,n}, 1) + \frac{i\omega}{Z} \frac{\partial \tilde{\psi}_1}{\partial k}(k_{2,n}, 1) \right)} \quad (20.16b)$$

$$A^+ = -\frac{i\omega}{Z} \frac{A_{in} K_-(k^+) \tilde{\psi}_1(k_{in}, 1)}{K_-(k_{in})(k^+ - k_{in}) \left( \frac{\partial \tilde{\psi}'_1}{\partial k}(k^+, 1) + \frac{i\omega}{Z} \frac{\partial \tilde{\psi}_1}{\partial k}(k^+, 1) \right)} \quad (20.16c)$$

$$\bar{I}_{\frac{\omega}{M}} \sim A_{\frac{\omega}{M}}(r) x^{-\frac{7}{2}} \quad (20.16d)$$

$$\bar{I}_r \sim \frac{3iAD_1 K_-(k_r) x^{-4}}{\pi(\tilde{\psi}'_1(k_r, 1) + \frac{i\omega}{Z} \tilde{\psi}_1(k_r, 1) + 2\pi i AD_1 (\tilde{p}'_1(1) + \frac{i\omega}{Z} \tilde{p}_1(1)))(k_r - k_{in})} \quad (20.16e)$$

Note that a similar form for  $\bar{I}_{\frac{\omega}{M}}$  to that of  $\bar{I}_r$  has not been given, this is a result of our inability to express a closed form for the leading order terms of  $A_1$  and  $B_1$  with the closest expression given in (20.14).

## 21 Scattering of an Incoming Wave from a Non-Modal Pole

We will now repeat the same process for an incoming wave that takes the form of a non-modal pole. That is, we will assume that far up-stream there exists a point mass source in the region of sheared flow. This would lead to a non-modal pole located on the critical layer branch cut, whose residue has been isolated as our incoming wave. This is justified as when these modes exist they are neutrally stable, and so will propagate into the far-field, where other modal poles, including nearly cut-on modes, will no longer have an observable contribution. To this end we must first define the incoming wave, and its positive half range transform.

$$p_{in}(x, r) = A_{in} \tilde{\psi}_3(k_0, r) e^{-ik_0 x}, \quad (21.1a)$$

$$\tilde{\psi}_3(k, r) = \begin{cases} \frac{D_3}{D_1} \tilde{\psi}_1(k, r), & r < r_0, \\ C_3 \tilde{p}_1(k, r) + D_3 \tilde{p}_2(k, r), & r > r_0. \end{cases} \quad (21.1b)$$

$$k_0 \in \left(\frac{\omega}{M}, \infty\right), \quad (21.1c)$$

$$r_0 = 1 - h + h \sqrt{1 - \frac{\omega}{M k_0}} = 1 - h + Q_0, \quad (21.1d)$$

$$C_3 = \frac{\tilde{p}_2(k, 1)}{W(\tilde{p}_1, \tilde{p}_2; 1)} \quad (21.1e)$$

$$D_3 = \frac{-\tilde{p}_1(k, 1)}{W(\tilde{p}_1, \tilde{p}_2; 1)} \quad (21.1f)$$

$$\tilde{p}_{in+(k,r)} = \frac{i A_{in} \tilde{\psi}_3(k_0, r)}{(k - k_0)}. \quad (21.1g)$$

Since we are seeking  $p_{in}(x, r)$  to satisfy both the boundary condition at  $r = 0$  and  $r = 1$ .

From this construction it can be confirmed that  $p_{in}$  does indeed satisfy the boundary conditions at  $r = 0$  and  $r = 1$ . Further note that this form can in addition be extracted from the residue to the  $k_0$  non modal pole (8.7) for a point mass source. The remainder of the Wiener-Hopf problem can be derived as in section 19. It is only when retrieving the scattered field that we experience any distinctions, once again, we assume;

$$\tilde{p}_0 = A(k) \tilde{\psi}_1(k, r). \quad (21.2a)$$

which results in

$$K(k) = \frac{\tilde{\psi}'_1(k, 1) + \frac{i\omega}{Z}\tilde{\psi}_1(k, 1)}{\tilde{\psi}'_1(k, 1)}, \quad (21.2b)$$

and perform an additive decomposition on

$$S(k) = \frac{\tilde{p}_{in+}(k, 1)}{K_-(k)} \quad (21.2c)$$

$$\begin{aligned} &= S_+(k) \quad + S_-(k) \\ &= \frac{\tilde{p}_{in+}(k, 1)}{K_-(k_0)} \quad + \tilde{p}_{in+}(k, 1) \left( \frac{1}{K_-(k)} - \frac{1}{K_-(k_0)} \right) \end{aligned} \quad (21.2d)$$

And find

$$\tilde{p}_{0+}(k, 1) = -\tilde{p}_{in+}(k, 1) + \frac{\tilde{p}_{in+}(k, 1)}{K_-(k_0)K_+(k)} \quad (21.2e)$$

$$\tilde{p}_{0-}(k, 1) = \tilde{p}_{in+}(k, 1) - \frac{\tilde{p}_{in+}(k, 1)K_-(k)}{K_-(k_0)} \quad (21.2f)$$

and finally,

$$p_0(x, r) = \frac{1}{2\pi} \int_{\Gamma} \frac{iA_{in}}{(k - k_0)K_-(k_0)} \left( \frac{1}{K_+(k)} - K_-(k) \right) \frac{\tilde{\psi}_1(k, r)}{\tilde{\psi}'_1(k, 1)} e^{-ikx} dk \quad (21.2g)$$

When we close  $\Gamma$  in the upper half plane,  $x < 0$ , once again making use of  $K_+$  being non-zero and analytic, it can be found,

$$p_0(x, r) = \frac{1}{2\pi} \int_{\Gamma} \frac{iA_{in}}{(k - k_0)K_-(k_0)K_+(k)} \frac{-\frac{i\omega}{Z}\tilde{\psi}_1(k, r)}{\tilde{\psi}'_1(k, 1)} e^{-ikx} dk \quad (21.3a)$$

$$= \sum_{k_{1,n}} \frac{A_{in}}{(k_{1,n} - k_0)K_-(k_0)K_+(k_{1,n})} \frac{\frac{i\omega}{Z}\tilde{\psi}_1(k_{1,n}, r)}{\frac{\partial \tilde{\psi}'_1}{\partial k}(k_{1,n}, 1)} e^{-ik_{1,n}x} \quad (21.3b)$$

$$= \sum_{k_{1,n}} A_{1,n} \tilde{\psi}_1(k_{1,n}, r) e^{-ik_{1,n}x} \quad (21.3c)$$

$$A_{1,n} = \frac{i\omega}{Z} \frac{A_{in}}{(k_{1,n} - k_0)K_-(k_0)K_+(k_{1,n}) \frac{\partial \tilde{\psi}'_1}{\partial k}(k_{1,n}, 1)} \quad (21.3d)$$

For  $x > 0$ , we close in the lower half plane, and must account for the integration around the critical layer branch cut which now includes the  $k_0$  non-modal pole.

$$p_0(x, r) = \frac{1}{2\pi} \int_{\Gamma} \frac{iA_{in}K_-(k)}{(k - k_0)K_-(k_0)} \frac{-\frac{i\omega}{Z}\tilde{\psi}_1(k, r)}{\tilde{\psi}'_1(k, 1) + \frac{i\omega}{Z}\psi_1(k, 1)} e^{-ikx} dk \quad (21.4a)$$

$$= \sum_{k_{2,n}} A_{2,n} \tilde{\psi}_1(k_{2,n}, r) e^{-ik_{2,n}x} - I(x, r). \quad (21.4b)$$

$$A_{2,n} = -\frac{i\omega}{Z} \frac{A_{in}K_-(k_{2,n})}{(k_{2,n} - k_0)K_-(k_0)} \left( \frac{\partial \tilde{\psi}'_1}{\partial k}(k_{2,n}, 1) + \frac{i\omega}{Z} \frac{\partial \tilde{\psi}_1}{\partial k}(k_{2,n}, 1) \right). \quad (21.4c)$$

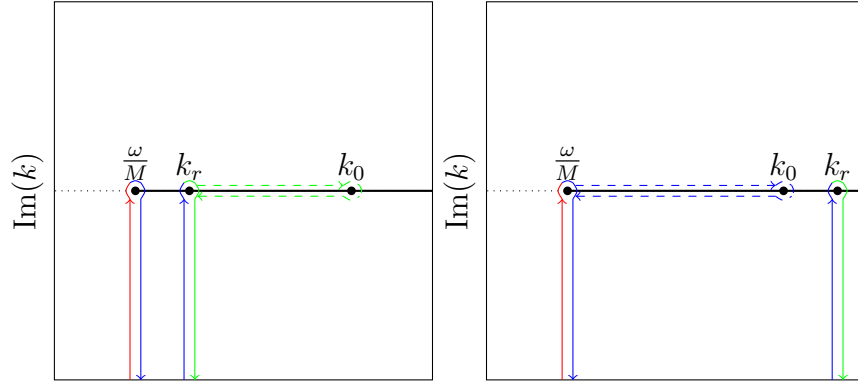


Figure 55: The steepest descent contours deformed for the Wiener-Hopf equation for an incoming wave from a non-modal pole at  $k = k_0$  as in figure 7, although no  $k^\pm$  pole have been included. (Left) For  $r < r_0$  we evaluate the integral around  $k_0$  as if we are above at  $1 - h$  and  $r$ , while for (Right)  $r > r_0$ , we evaluate as if we are above at  $1 - h$  but below at  $r$ .

$$I(x, r) = + \int_{\frac{\omega}{M}}^{\infty} \frac{\omega}{Z} \frac{A_{in} K_-(k) e^{-ikx}}{2\pi(k - k_0) K_-(k_0)} \Delta \left[ \frac{\psi_1(k, r)}{\psi_1'(k, 1) + \frac{i\omega}{Z} \psi_1(k, 1)} \right] dk, \quad (21.4d)$$

$$I(x, r) = I_{\frac{\omega}{M}}(x, r) + I_r(x, r) H(r - 1 + h) + R_0(x, r; r_0) \quad (21.4e)$$

Here we find the distinction between the modal and non-modal source; when considering a modal input this was exactly cancelled in the scattered field, this being due to mode associated with the incoming wave no longer being present, whereas in this case we actually continue to have a pole at  $k_0$ , and so we continue to find a neutrally stable mode travelling with the same phase velocity. The residue of this mode depends on the branch that sees the non-modal pole, this is depicted in figure 55, and results in;

$$R_0(x, r; r_0) = - \frac{i\omega}{Z} \frac{A_{in} e^{ik_0 x} \left( \tilde{\psi}_1(k_0, r) + 2\pi i A D_1 \tilde{p}_1(k_0, r) H(r - r_0) \right)}{\tilde{\psi}_1'(k_0, 1) + \frac{i\omega}{Z} \tilde{\psi}_1(k_0, 1) + 2\pi i A D_1 \left( \tilde{\psi}_1'(k_0, 1) + \frac{i\omega}{Z} \tilde{\psi}_1(k_0, 1) \right)}. \quad (21.5)$$

It can easily be observed that  $R_0(1, r_0)$  does not satisfy the boundary condition at  $r = 1$ , noting that there are no hidden dependencies on the wall impedance  $Z$ , but rather, will find,

$$p'_{in}(x, 1) + R'_0(x, 1; r_0) + \frac{i\omega}{Z} p_{in}(x, 1) + R_0(x, 1; r_0) = 0. \quad (21.6)$$

Additionally it should be observed that despite the presence of the Heaviside function in  $R_0(x, r; r_0)$ , the outgoing wave is in fact continuous, since  $\tilde{p}_1(k_0, r_0) = 0$ . Additionally we continue to have the contributions from the two integrals, which can then be transformed onto the steepest descent contour, revealing, or removing any  $k^\pm$  poles that may be present. These work exactly as given in section 8.3, with

the exception of when  $r = r_0$ . These are given below;

First note that in the both the  $r = r_0$  and  $r \neq r_0$  cases we have

$$I(x, r) = \bar{I}_{\frac{\omega}{M}}(x, r) + \bar{I}_r(x, r)H(r - 1 + h) + R_0(x, r; r_0) + \sum_{\text{Im}(k^+) < 0} A_+ \tilde{\psi}_1(k^+, r) e^{-ik^+x} - \sum_{\substack{\text{Re}(k_{2,n}) > \frac{\omega}{M} \\ \text{Im}(k_{2,n}) < 0}} A_{2,n} \tilde{\psi}_1(k_{2,n}, r) e^{-ik_{2,n}x} \quad (21.7a)$$

$$\bar{I}_{\frac{\omega}{M}}(x, r) = - \int_0^\infty \frac{\tilde{\psi}_1(r)(\tilde{p}'_1(1) + \frac{i\omega}{Z}\tilde{p}_1(1))}{\tilde{\psi}'_1(k, 1) + \frac{i\omega}{Z}\tilde{\psi}_1(k, 1) + 2\pi i A D_1(\tilde{p}'_1(k, 1) + \frac{i\omega}{Z}\tilde{p}_1(k, 1))} \times \frac{\omega}{Z} \frac{A_{in} K_-(k) e^{-i\frac{\omega}{M}x} e^{-\xi x} A D_1}{(k - k_0) K_-(k_0) (\tilde{\psi}'_1(k, 1) + \frac{i\omega}{Z}\tilde{\psi}_1(k, 1))} \Big|_{k=\frac{\omega}{M}-i\xi} d\xi \quad r < 1 - h \quad (21.7b)$$

$$\bar{I}_{\frac{\omega}{M}}(x, r) = \int_0^\infty \frac{\tilde{p}_1(r)(\tilde{p}'_2(1) + \frac{i\omega}{Z}\tilde{p}_2(1)) - \tilde{p}_2(r)(\tilde{p}'_1(1) + \frac{i\omega}{Z}\tilde{p}_1(1))}{\tilde{\psi}'_1(k, 1) + \frac{i\omega}{Z}\tilde{\psi}_1(k, 1) + 2\pi i A D_1(\tilde{p}'_1(k, 1) + \frac{i\omega}{Z}\tilde{p}_1(k, 1))} \times \frac{\omega}{Z} \frac{A_{in} K_-(k) e^{-i\frac{\omega}{M}x} e^{-\xi x} A D_1^2}{(k - k_0) K_-(k_0) (\tilde{\psi}'_1(k, 1) + \frac{i\omega}{Z}\tilde{\psi}_1(k, 1))} \Big|_{k=\frac{\omega}{M}-i\xi} d\xi \quad r > 1 - h \quad (21.7c)$$

$$\bar{I}_r(x, r) = - \int_0^\infty \frac{\tilde{p}_1(r)}{\tilde{\psi}'_1(k, 1) + \frac{i\omega}{Z}\tilde{\psi}_1(k, 1) + 2\pi i A D_1(\tilde{p}'_1(k, 1) + \frac{i\omega}{Z}\tilde{p}_1(k, 1))} \times \frac{\omega}{Z} \frac{A_{in} K_-(k) e^{-ik_r x} e^{-\xi x} A D_1}{(k - k_0) K_-(k_0) (\tilde{\psi}'_1(k, 1) + \frac{i\omega}{Z}\tilde{\psi}_1(k, 1))} \Big|_{k=k_r-i\xi} d\xi \quad (21.7d)$$

$$A^+ = - \frac{i\omega}{Z} \frac{A_{in} K_-(k^+)}{K_-(k_0)(k^+ - k_0) \left( \frac{\partial \tilde{\psi}'_1}{\partial k}(k^+, 1) + \frac{i\omega}{Z} \frac{\partial \tilde{\psi}_1}{\partial k}(k^+, 1) \right)} \quad (21.7e)$$

Once again this results in a wave that decays like  $x^{-\frac{7}{2}}$  at phase velocity equal to that of the mean flow,  $M$ , and a secondary wave that is only present when the observer is located in the sheared flow  $r > 1 - h$  that decays like  $x^{-4}$  and has phase velocity equal to the flow speed at the observer  $U(r)$ , with the exception of when the observer is located in the same position radially as the source,  $r = r_0$ . In this case we instead find that the wave decays slower, like  $x^{-3}$ . This is due to the  $k - k_0$  term in the denominator of  $\bar{I}_r$ , which is equal to  $(k - k_r)$  when  $r = r_0$ . These have been found once again through Watson's lemma, making note that for  $k \approx k_r$ ,  $\tilde{p}_1(r, k) = (k - k_r)^3 + O((k - k_r)^4)$ .

## 22 Scattering of a $k^+$ Modal Incoming Wave

In section 12.3 it was shown that for a hard walled duct under a quadratic shear flow profile a stable modal  $k^+$  pole located behind the branch cut will be present. And it was further suggested that this mode can in some cases be nearly cut-on,

representing a stabilised hydrodynamic instability. Its contribution from a point mass source was found to be discontinuous in the  $r$ , with an equal and opposite discontinuity in the  $I_r(x, r)$  integral.

In what follows we will assume an incoming modal solution from the hard walled region of the duct, including the discontinuity. This is due to the lack of a closed form of the waves coming from the steepest descent integrals for which we would be required to consider each in order to maintain a continuous incoming wave. This is due to the  $k^+$  hidden modal pole only contributing as part of the critical layer branch cut.

Assuming an incoming modal wave from a mode hidden behind the critical layer branch cut,  $k_{in}^+$ .

$$p_{in}(x, r) = A_{in}(\tilde{\psi}_1(k_{in}^+, r) + 2\pi i A D_1 \tilde{p}_1(k_{in}^+, r) H(r - \text{Re}(r_c^+))) e^{-ik_{in}^+ x} \quad (22.1)$$

$$p'_{in}(x, 1) = A_{in}(\tilde{\psi}'_1(k_{in}^+, r) + 2\pi i A D_1 \tilde{p}'_1(k_{in}^+, r) H(r - \text{Re}(r_c^+))) e^{-ik_{in}^+ x} = 0 \quad (22.2)$$

$$\tilde{p}_{in}(k, r) = \frac{i A_{in}(\tilde{\psi}_1(k_{in}^+, r) + 2\pi i A D_1 \tilde{p}_1(k_{in}^+, r) H(r - \text{Re}(r_c^+)))}{k - k_{in}^+} \quad (22.3)$$

The construction of the Wiener-Hopf problem and the half range solutions  $\tilde{p}_{0+}(k, 1)$  and  $\tilde{p}_{0-}(k, 1)$  follows exactly as in the previous two cases.

$$\tilde{p}_{0-}(k, 1) = \tilde{p}_{in}(k, 1) \left( 1 - \frac{K_-(k)}{K_-(k_{in}^+)} \right) \quad (22.4a)$$

$$\tilde{p}_{0+}(k, 1) = -\tilde{p}_{in}(k, 1) \left( 1 - \frac{1}{K_-(k_{in}^+) K_+(k)} \right) \quad (22.4b)$$

$$\begin{aligned} \tilde{p}_0(x, r) = \int_{\Gamma} \frac{i A_{in}(\tilde{\psi}_1(k_{in}^+, 1) + 2\pi i A(k_{in}^+) D_1(k_{in}^+) \tilde{p}_1(k_{in}^+, 1))}{2\pi(k - k_{in}^+) K_-(k_{in}^+)} \\ \times \frac{\tilde{\psi}_1(k, r) e^{-ikx}}{\tilde{\psi}_1(k, 1)} \left( \frac{1}{K_+(k)} - K_-(k) \right) dk \end{aligned} \quad (22.4c)$$

$$\tilde{p}_0(x, r) = \sum_{k_{1,n}} A_{1,n} \tilde{\psi}_1(k_{1,n}, r) e^{-ik_{1,n} x} \quad x < 0 \quad (22.4d)$$

$$A_{1,n} = \frac{i\omega A_{in}(\tilde{\psi}_1(k_{in}^+, 1) + 2\pi i A(k_{in}^+) D_1(k_{in}^+) \tilde{p}_1(k_{in}^+, 1))}{Z (k_{1,n} - k_{in}^+) K_-(k_{in}^+) K_+(k_{1,n}) \frac{\partial \tilde{\psi}'_1}{\partial k}(k_{1,n}, 1)} \quad (22.4e)$$

For  $x > 0$ , we must take careful consideration for how the pole at  $k = k_{in}^+$  contributes to the final solution. Firstly the pole will contribute similarly to the case of the modal incoming wave, being picked up by the closing of the integration contour and contributing along with the modal poles. The pole will then contribute again as part of the integral around the critical layer branch cut, which is apparent when transforming the integrals onto the steepest descent contours. In this way, the residue from the pole in the usual modal sum is removed, by the initial deformation, of the integral below the branch cut, and then a new residue is given by the the

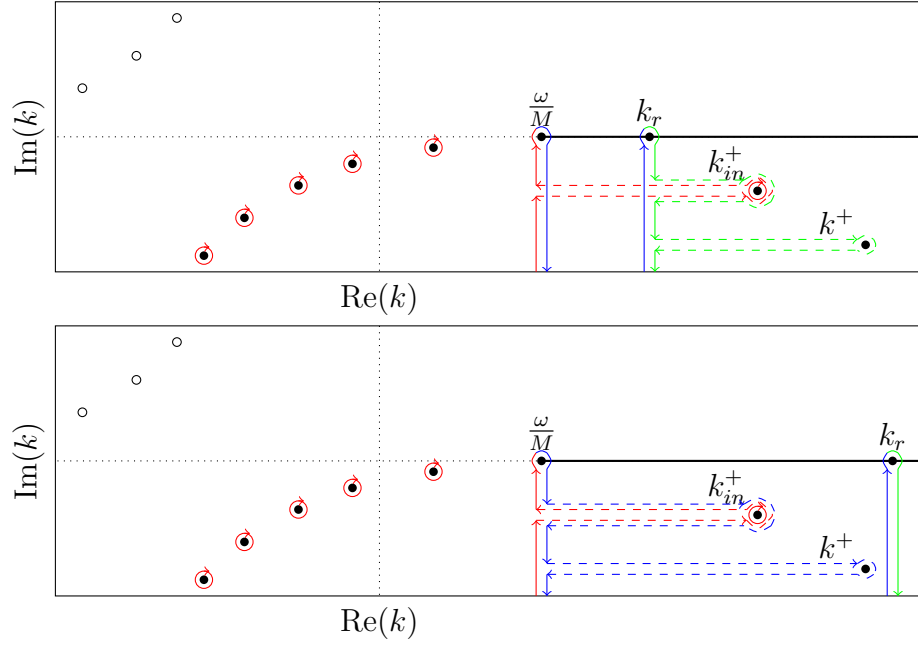


Figure 56: Illustration of the residues that contribute to the closure of  $\Gamma$  in the lower half plane. Red lines indicate evaluation as below the branch cut, blue lines as if above the branch cut at  $1 - h$ , but below at  $r$ , and green if above at both  $1 - h$  and  $r$ . Note that  $k_{in}^+$  is integrated around three times in each illustration, once as a usual pole, which is removed by the first steepest descent contour, and then a new contribution is given by either the blue ( $k_r > \text{Re}(k_{in}^+)$ , bottom) or green ( $k_r > \text{Re}(k_{in}^+)$ , top) steepest descent contour depending on the value of  $r$ , this cancels exactly with the incoming wave in the total pressure perturbation.

integration contour with the  $k_{in}^+$  closest to the right, just as a usual  $k^+$  modal pole. That is;

$$\tilde{p}_0(x, r) = \sum_{k_{2,n}} A_{2,n} \tilde{\psi}_1(k_{2,n}, r) e^{-ik_{2,n}x} + I(x, r) - \frac{i\omega A_{in}(\tilde{\psi}_1(k, 1) + 2\pi i A D_1 \tilde{p}_1(k, 1))}{Z \frac{i\omega}{Z} \tilde{\psi}_1(k, 1) - 2\pi i A D_1 \tilde{p}'(1)} \Bigg|_{k=k_{in}^+} \tilde{\psi}_1(k_{in}^+, r) e^{-ik_{in}^+x} \quad x > 0 \quad (22.4f)$$

$$A_{2,n} = - \frac{i\omega A_{in}(\tilde{\psi}_1(k_{in}^+, 1) + 2\pi i A(k_{in}^+) D_1(k_{in}^+) \tilde{p}_1(k_{in}^+, 1)) K_-(k_{2,n})}{Z (k_{2,n} - k_{in}^+) K_-(k_{in}^+) \left( \frac{\partial \tilde{\psi}_1}{\partial k}(k_{2,n}, 1) + \frac{i\omega}{Z} \frac{\partial \tilde{\psi}_1}{\partial k}(k_{2,n}, 1) \right)} \quad (22.4g)$$

with  $I(x)$  consisting of the steepest descent branch cuts, and the corresponding 'hidden' pole residues, and cancelling out the contribution of the  $k_{in}^+$  pole within

both the sum of residues and the incoming wave;

$$\begin{aligned}
I(x, r) = & \bar{I}_{\frac{\omega}{M}}(x, r) + \bar{I}_r(x, r) - \tilde{p}_{in}(x, r) \\
& + \sum_{\text{Im}(k^+) < 0} A_+ \tilde{\psi}_1(k^+, r) e^{-ik^+x} - \sum_{\substack{\text{Re}(k_{2,n}) > \frac{\omega}{M} \\ \text{Im}(k_{2,n}) < 0}} A_{2,n} \tilde{\psi}_1(k_{2,n}, r) e^{-ik_{2,n}x} \\
& + \frac{i\omega}{Z} \frac{A_{in}(\tilde{\psi}_1(k, 1) + 2\pi i A D_1 \tilde{p}_1(k, 1))}{\frac{i\omega}{Z} \tilde{\psi}_1(k, 1) - 2\pi i A D_1 \tilde{p}'(1)} \Big|_{k=k_{in}^+} \tilde{\psi}_1(k_{in}^+, r) e^{-ik_{in}^+x} \\
& - A_{in} (\tilde{p}_1(k, r) + 2\pi i A D_1 \tilde{p}_{k,r} H(r - \text{Re}(r_c^+))) e^{-ik_{in}^+x} \Big|_{k=k_{in}^+}, \quad (22.4h)
\end{aligned}$$

where

$$\begin{aligned}
\bar{I}_{\frac{\omega}{M}}(x, r) = & - \int_0^\infty \frac{\tilde{\psi}_1(r)(\tilde{p}'_1(1) + \frac{i\omega}{Z} \tilde{p}_1(1))}{\tilde{\psi}'_1(k, 1) + \frac{i\omega}{Z} \tilde{\psi}_1(k, 1) + 2\pi i A D_1 (\tilde{p}'_1(k, 1) + \frac{i\omega}{Z} \tilde{p}_1(k, 1))} \\
& \times \frac{\omega}{Z} \frac{A_{in} \tilde{\psi}_1^+(k_{in}^+, 1) K_-(k) e^{-i\frac{\omega}{M}x} e^{-\xi x} A D_1}{(k - k_{in}^+) K_-(k_{in}^+) (\tilde{\psi}'_1(k, 1) + \frac{i\omega}{Z} \tilde{\psi}_1(k, 1))} \Big|_{k=\frac{\omega}{M} - i\xi} d\xi \quad r < 1 - h \quad (22.4i)
\end{aligned}$$

$$\begin{aligned}
\bar{I}_{\frac{\omega}{M}}(x, r) = & \int_0^\infty \frac{\tilde{p}_1(r)(\tilde{p}'_2(1) + \frac{i\omega}{Z} \tilde{p}_2(1)) - \tilde{p}_2(r)(\tilde{p}'_1(1) + \frac{i\omega}{Z} \tilde{p}_1(1))}{\tilde{\psi}'_1(k, 1) + \frac{i\omega}{Z} \tilde{\psi}_1(k, 1) + 2\pi i A D_1 (\tilde{p}'_1(k, 1) + \frac{i\omega}{Z} \tilde{p}_1(k, 1))} \\
& \times \frac{\omega}{Z} \frac{A_{in} \tilde{\psi}_1^+(k_{in}^+, 1) K_-(k) e^{-i\frac{\omega}{M}x} e^{-\xi x} A D_1^2}{(k - k_{in}^+) K_-(k_{in}^+) (\tilde{\psi}'_1(k, 1) + \frac{i\omega}{Z} \tilde{\psi}_1(k, 1))} \Big|_{k=\frac{\omega}{M} - i\xi} d\xi \quad r > 1 - h \quad (22.4j)
\end{aligned}$$

$$\begin{aligned}
\bar{I}_r(x, r) = & - \int_0^\infty \frac{\tilde{p}_1(r)}{\tilde{\psi}'_1(k, 1) + \frac{i\omega}{Z} \tilde{\psi}_1(k, 1) + 2\pi i A D_1 (\tilde{p}'_1(k, 1) + \frac{i\omega}{Z} \tilde{p}_1(k, 1))} \\
& \times \frac{\omega}{Z} \frac{A_{in} \tilde{\psi}_1^+(k_{in}^+, 1) K_-(k) e^{-ik_r x} e^{-\xi x} A D_1}{(k - k_{in}^+) K_-(k_{in}^+)} \Big|_{k=k_r - i\xi} d\xi \quad (22.4k)
\end{aligned}$$

$$A^+ = - \frac{i\omega}{Z} \frac{A_{in} \tilde{\psi}_1^+(k_{in}^+, 1) K_-(k^+)}{K_-(k_{in}^+) (k^+ - k_{in}^+) \left( \frac{\partial \tilde{\psi}_1^+}{\partial k}(k^+, 1) + \frac{i\omega}{Z} \frac{\partial \tilde{\psi}_1^+}{\partial k}(k^+, 1) \right)} \quad (22.4l)$$

And so downstream we see the removal of the incoming wave, a modal scattering, including any new modes hidden behind the branch cut, a wave travelling with phase velocity equal to the centre line mach number  $M$  with decaying amplitude like  $x^{-\frac{7}{2}}$  in the far-field, and for  $r > 1 - h$ , a wave with phase velocity  $U(r)$  decaying like  $x^{-4}$  in the far-field.

## 23 Interpretation of Results

For each of the three incoming waves investigated, as motivated by a point-mass source solution for a lined duct investigated in part II, the total upstream  $x < 0$

pressure field caused by a change in boundary condition from a lined to a hard wall consists of; the incoming pressure wave, and scattered modal waves corresponding to the hard walled duct. The amplitudes of these waves are linearly proportional to both the incoming wave at the duct wall at the scattering point and contain the factor  $\frac{i\omega}{Z}$ , where  $Z$  is the impedance of the lined section. As would be expected this results in less scattering if the lined section is harder.

In the downstream direction,  $x > 0$  we similarly have the duct modes, now corresponding to the lined section. When the incoming wave is modal, including when it is hidden as part of the critical layer branch cut, the scattered field removes the incoming wave, resulting in this term no longer being present in the down stream direction. For the non-modal source however, instead of removing the incoming wave the amplitude is changed in order to retrieve the boundary condition at the duct wall for the lined section. The wave continues to propagate with the same phase velocity and radial ‘shape’ for  $r < r_0$ , although a new shape is followed for  $r > r_0$  in order to retrieve the boundary condition.

Also in the downstream direction we have the non-modal contributions from the two critical layer integrals, understood most easily by being transformed onto the contour of steepest descent. In each case a wave exists with phase velocity equal to the flow speed within the uniform flow section,  $M$ . In the far-field it can be seen that the amplitude is decaying like  $x^{-\frac{7}{2}}$ . This decay rate corresponds to the point mass source problem to a point mass source located within the uniform flow for the problem of the sheared mean flow profile within an infinite lined duct. We additionally have a second wave with phase velocity equal to the flow speed at the observer  $U(r)$  that decays like  $x^{-4}$  and is only present in for an observer in the sheared flow,  $r > 1 - h$ . This is exactly equivalent to the wave corresponding to this same phase velocity in the point-mass source case, with the exception of when a  $k_0$  non-modal source was considered, for which we found, when  $r = r_0$ , a decay like  $x^{-3}$ , corresponding to the wave with phase velocity  $U(r_0)$  within the infinite lined duct problem. Through transforming the integrals on the steepest descent contours any stabilised  $k^+$  poles corresponding to the lined region are also picked up. These contain a discontinuity which is once again cancelled exactly with a discontinuity in the wave decaying like  $x^{-4}$

Once again it is also observed that if any  $k^-$  modes did exist in the lower half plane, which was seen in the linear shear flow case for a point mass source, their contributions would also be removed by the critical layer branch cut. Although no evidence for these poles to be present has been seen for a quadratic shear flow profile, it may be that these can occur for other flow profiles. The scattering of these modes is expected to work similar to that of the usual modal poles

## 24 Construction of the Matrix Wiener-Hopf Problem

In order to solve the finite length lined wall case, as depicted previously in figure 53 we must define an offset half range transforms;

$$\int_L^\infty f(x)e^{ikx} dx = e^{ikL} \int_0^\infty f(x+L)e^{ikx} dx \quad (24.1a)$$

$$= e^{ikL} \tilde{f}_{+L}(k) \quad (24.1b)$$

$$\int_{-\infty}^L f(x)e^{ikx} dx = e^{ikL} \int_{-\infty}^0 f(x+L)e^{ikx} dx \quad (24.1c)$$

$$= e^{ikL} \tilde{f}_{-L}(k) \quad (24.1d)$$

In this way,

$$\tilde{f}(k) = e^{ikL} (\tilde{f}_{+L}(k) + \tilde{f}_{-L}(k)) \quad (24.1e)$$

and  $\tilde{f}_{+L}$  and  $\tilde{f}_{-L}$  have the same analytic properties as the half range transforms defined for  $L = 0$ .

It should be noted that  $e^{ikL} \tilde{f}_{-L}(k)$  is not a  $(-)$  function, since the exponential term is unbounded in the lower half plane.

Similarly to section 19 we construct the problem by considering the boundary conditions in the different regions of the duct.

We once again take a pressure field  $p(x, r; m)$ , considering a single wave mode following a Fourier series expansion, comprised of an incoming wave, which we will take to be modal,  $p_{in}(x, r; m)$  and a scattered field  $p_0(x, r; m)$ .

$$p(x, r) = p_{in}(x, r) + p_0(x, r) \quad (24.2)$$

We apply the hard and lined walled boundary conditions to the total pressure  $p(x, r)$ ;

$$p'(x, 1) = \begin{cases} 0 & 0 < x \\ -\frac{i\omega}{M} p(x, 1) & 0 < x < L \\ 0 & L < x \end{cases} \quad (24.3a)$$

$$p'_{in}(x, 1) = 0 \quad (24.3b)$$

$$p'_0(x, 1) = \begin{cases} 0 & 0 < x \\ -\frac{i\omega}{M} p_{in}(x, 1) - \frac{i\omega}{M} p_0(x, 1) & 0 < x < L \\ 0 & L < x \end{cases} \quad (24.3c)$$

As before, we take appropriate half range transforms in order to capture the various regions of the domain,

$$\tilde{p}_{in+}(k, r) = \frac{iA_{in}\tilde{\psi}_1(k_{in}, r)}{k - k_{in}} \quad (24.4a)$$

$$\tilde{p}_{in+L}(k, r) = \frac{iA_{in}\tilde{\psi}_1(k_{in}, r)e^{-ik_{in}L}}{k - k_{in}} \quad (24.4b)$$

$$\tilde{p}_0(k, r) = \tilde{p}_{0+}(k, r) + \tilde{p}_{0-}(k, r) \quad (24.4c)$$

$$= (\tilde{p}_{0+L}(k, r) + \tilde{p}_{0-L}(k, r))e^{ikL} \quad (24.4d)$$

$$\int_{-\infty}^0 p'_0(x, 1)e^{ikx} dx = \tilde{p}'_{0-}(k, 1) = 0 \quad (24.5a)$$

$$\int_L^{\infty} p'_0(x, 1)e^{ikx} dx = e^{ikL}\tilde{p}'_{0+L}(k, 1) = 0 \quad (24.5b)$$

$$\begin{aligned} \int_0^L p'_0(x, 1)e^{ikx} dx &= \tilde{p}'_{0+}(k, 1) - e^{ikL}\tilde{p}'_{0+L}(k, 1) \\ &= -\frac{i\omega}{Z}(\tilde{p}_{in+}(k, 1) - e^{ikL}\tilde{p}_{in+L}(k, 1) + \tilde{p}_{0+}(k, 1) - e^{ikL}\tilde{p}_{0+L}(k, 1)) \end{aligned} \quad (24.5c)$$

$$\begin{aligned} &= e^{ikL}\tilde{p}'_{0-L}(k, 1) - \tilde{p}'_{0+}(k, 1) \\ &= -\frac{i\omega}{Z}(\tilde{p}_{in+}(k, 1) - e^{ikL}\tilde{p}_{in+L}(k, 1) + e^{ikL}\tilde{p}_{0-L}(k, 1) - \tilde{p}_{0-}(k, 1)) \end{aligned} \quad (24.5d)$$

With these four equations we can make use of the assumed form of the scattered wave,  $\tilde{p}_0(k, r) = A(k)\tilde{\psi}_1(k, r)$ , to write;

$$A(k)\tilde{\psi}_1(k, 1)\tilde{\psi}'(k, 1) = (\tilde{p}_{0-}(k, 1) + \tilde{p}_{0+}(k, 1))\tilde{\psi}'_1(k, 1) \quad (24.6a)$$

$$= (\tilde{p}_{0-L}(k, 1) + \tilde{p}_{0+L}(k, 1))\tilde{\psi}'_1(k, 1)e^{ikL} \quad (24.6b)$$

$$\begin{aligned} &= (\tilde{p}'_{0-}(k, 1) + \tilde{p}'_{0+}(k, 1))\tilde{\psi}_1(k, 1) \\ &= -\frac{i\omega}{Z}(\tilde{p}_{in+}(k, 1) - e^{ikL}\tilde{p}_{in+L}(k, 1) \\ &\quad + \tilde{p}_{0+}(k, 1) - e^{ikL}\tilde{p}_{0+L}(k, 1))\tilde{\psi}_1(k, 1) \end{aligned} \quad (24.6c)$$

$$\begin{aligned} &= (\tilde{p}'_{0-L}(k, 1) + \tilde{p}'_{0+L}(k, 1))\tilde{\psi}_1(k, 1)e^{ikL} \\ &= -\frac{i\omega}{Z}(\tilde{p}_{in+}(k, 1) - e^{ikL}\tilde{p}_{in+L}(k, 1) \\ &\quad + e^{ikL}\tilde{p}_{0-L}(k, 1) - \tilde{p}_{0-}(k, 1))\tilde{\psi}_1(k, 1). \end{aligned} \quad (24.6d)$$

Which can then be formulated into a matrix equation;

$$\begin{aligned} & \begin{pmatrix} \tilde{\psi}'_1(k, 1) + \frac{i\omega}{Z}\tilde{\psi}_1(k, 1) & -\frac{i\omega}{Z}\tilde{\psi} - 1(k, 1)e^{ikx} \\ 0 & \tilde{\psi}'_1 \end{pmatrix} \begin{pmatrix} \tilde{p}_{0+}(k, 1) + \tilde{p}_{in+}(k, 1) \\ \tilde{p}_{0+L}(k, 1) + \tilde{p}_{in+L}(k, 1) \end{pmatrix} \\ &= - \begin{pmatrix} \tilde{\psi}'_1(k, 1) & 0 \\ -\frac{i\omega}{Z}\psi_1 e^{-ikx} & \tilde{\psi}'_1 + \frac{i\omega}{Z}\tilde{\psi}_1(k, 1) \end{pmatrix} \begin{pmatrix} \tilde{p}_{0-}(k, 1) - \tilde{p}_{in+}(k, 1) \\ \tilde{p}_{0-L}(k, 1) - \tilde{p}_{in+L}(k, 1) \end{pmatrix} \end{aligned} \quad (24.7)$$

and retrieve the matrix Wiener-Hopf problem;

$$\underline{K}(k) \begin{pmatrix} \tilde{p}_{0+}(k, 1) + \tilde{p}_{in+}(k, 1) \\ \tilde{p}_{0+L}(k, 1) + \tilde{p}_{in+L}(k, 1) \end{pmatrix} + \begin{pmatrix} \tilde{p}_{0-}(k, 1) \\ \tilde{p}_{0-L}(k, 1) \end{pmatrix} = \begin{pmatrix} \tilde{p}_{in+}(k, 1) \\ \tilde{p}_{in+L}(k, 1) \end{pmatrix} \quad (24.8)$$

$$\underline{K}(k) = \frac{1}{K(k)} \begin{pmatrix} K(k) & 0 \\ (K(k) - 1)e^{-ikL} & 1 \end{pmatrix} \begin{pmatrix} K(k) & -(K(k) - 1)e^{ikL} \\ 0 & 1 \end{pmatrix} \quad (24.9)$$

Where  $\underline{K}(k)$  is the matrix Wiener-Hopf kernel, and  $K(k)$  is the kernel of the scalar problem (19.15). We seek to decompose  $\underline{K}(k)$  into two matrices,  $\underline{K}_{\pm}(k)$ , where each matrix is comprised of functions that are analytic in the upper and lower half planes respectively with,

$$\underline{K}_-(k)\underline{K}_+(k) = \underline{K}(k) \quad (24.10)$$

We further require that these matrices are invertable and their inverses to also be  $(\pm)$  matrix functions respectively.

Unlike for the scalar Wiener-Hopf problem, exact conditions for such a decomposition to exist are not known. However a decomposition of the matrix may be given by making use of the scalar decomposition.

Decomposing the left matrix of  $\underline{K}(k)$  (24.9) it is found

$$\begin{pmatrix} K(k) & 0 \\ (K(k) - 1)e^{-ikL} & 1 \end{pmatrix} = \begin{pmatrix} 0 & K_-(k) \\ -e^{-ikL} & K_-(k)e^{-ikL} \end{pmatrix} \begin{pmatrix} 1 & -e^{ikL} \\ K_+(k) & 0 \end{pmatrix} \quad (24.11)$$

Note that the left matrix of (24.11) is comprised only of  $(-)$  functions, and the right matrix of  $(+)$  functions. We can do the same to the right matrix of  $\underline{K}(k)$  (24.9),

$$\begin{pmatrix} K(k) & -(K(k) - 1)e^{-ikL} \\ 0 & 1 \end{pmatrix} = \begin{pmatrix} 1 & K_-(k) \\ e^{-ikL} & 0 \end{pmatrix} \begin{pmatrix} 0 & e^{ikL} \\ K_+(k) & -K_+(k)e^{ikL} \end{pmatrix} \quad (24.12)$$

Note that we can now express  $\underline{K}(k)$  as the multiplication of four matrices, with  $(-)(+)(-)(+)$  analytic. Thus we will multiply together the two middle matrices

and decompose these further;

$$\begin{pmatrix} 1 & -e^{ikL} \\ K_+(k) & 0 \end{pmatrix} \begin{pmatrix} 1 & K_-(k) \\ e^{-ikL} & 0 \end{pmatrix} = \begin{pmatrix} 0 & K_-(k) \\ K_+(k) & K(k) \end{pmatrix} \quad (24.13)$$

$$\begin{pmatrix} 0 & K_-(k) \\ K_+(k) & K(k) \end{pmatrix} = \begin{pmatrix} K_-(k) & K_-(k) \\ \mathcal{K}_-(k) & 1 + \mathcal{K}_-(k) \end{pmatrix} \begin{pmatrix} -K_+(k) & -\mathcal{K}_+(k) \\ K_+(k) & 1 + \mathcal{K}_+(k) \end{pmatrix} \quad (24.14)$$

Where,

$$K(k) - 1 = \frac{i\omega \tilde{\psi}'_1(k, 1)}{Z \tilde{\psi}'_1(k, 1)} = \mathcal{K}(k) = \mathcal{K}_-(k) + \mathcal{K}_+(k) \quad (24.15)$$

Making use of the additive decomposition (18.3).

Finally we can write the decomposition of  $\underline{K}(k)$ , making use of being able to write the factor  $\frac{1}{K(k)} = \frac{1}{K_-(k)} \frac{1}{K_+(k)}$ ,

$$\underline{K}(k) = \begin{pmatrix} \mathcal{K}_-(k) & \mathcal{K}_-(k) + 1 \\ (\mathcal{K}_-(k) - 1)e^{-ikL} & \mathcal{K}_-(k)e^{-ikL} \end{pmatrix} \begin{pmatrix} -\mathcal{K}_+(k) & (\mathcal{K}_+(k) - 1)e^{ikL} \\ \mathcal{K}_+(k) + 1 & -\mathcal{K}_+(k)e^{ikL} \end{pmatrix} \quad (24.16)$$

Which have determinants  $e^{\mp ikL}$  respectively, and so are invertible, however their inverses are not  $(\pm)$  matrices. Despite this the matrix Wiener-Hopf equation can be written as;

$$\begin{aligned} & e^{-ikL} \begin{pmatrix} -\mathcal{K}_+(k) & (\mathcal{K}_+(k) - 1)e^{ikL} \\ \mathcal{K}_+(k) + 1 & -\mathcal{K}_+(k)e^{ikL} \end{pmatrix} \begin{pmatrix} \tilde{p}_{0+}(k, 1) + \tilde{p}_{in+}(k, 1) \\ \tilde{p}_{0+L}(k, 1) + \tilde{p}_{in+L}(k, 1) \end{pmatrix} \\ &= - \begin{pmatrix} \mathcal{K}_-(k)e^{-ikL} & -(\mathcal{K}_-(k) + 1) \\ -(\mathcal{K}_-(k) - 1)e^{-ikL} & \mathcal{K}_-(k) \end{pmatrix} \begin{pmatrix} \tilde{p}_{0-}(k, 1) \\ \tilde{p}_{0-L}(k, 1) \end{pmatrix} \\ &+ \begin{pmatrix} \mathcal{K}_-(k)e^{-ikL} & -(\mathcal{K}_-(k) + 1) \\ -(\mathcal{K}_-(k) - 1)e^{-ikL} & \mathcal{K}_-(k) \end{pmatrix} \begin{pmatrix} \tilde{p}_{in-}(k, 1) \\ \tilde{p}_{in-L}(k, 1) \end{pmatrix} \quad (24.17) \end{aligned}$$

and the remainder of the problem would follow similarly to that of the scalar Wiener-Hopf problem. Unfortunately, this is not a suitable matrix decomposition, as already highlighted. we have the incorrect exponential behaviour due to the determinants of  $(+)$  and  $(-)$  matrices. This was similarly observed for  $\tilde{p}_{in+L}e^{ikL}$  and  $\tilde{p}_{in-L}e^{ikL}$ . In that in order to have a left hand side which is a plus function, note that the current left hand side is unbounded in the upper half plane, we would be required to multiply our  $(-)$  matrix by an exponential unbounded in the lower half plane. Instead, we may be able to decompose the matrix based on differently in order to remove the exponential behaviours manually, accounting for the fact that we wish

to invert the matrices. Seeking,

$$\underline{K}(k)\underline{K}_+(k) = \underline{K}_-(k) \quad (24.18)$$

and

$$\underline{K}_-^{-1}(k)\underline{K}(k) = \underline{K}_+^{-1}(k). \quad (24.19)$$

This is then done manually with pole removal where appropriate. This is described fully within [Abrahams and Aitken, 2019]. The difference between our problem, and where similar methods are used, is in the presence of the semi infinite critical layer branch cut, as opposed to just simple poles or finite length branch cuts.

## Part V

# Conclusions

## 25 Summary of Key Results

In this thesis we have constructed three different problems for modelling sound within a lined cylindrical duct under an inviscid parallel mean flow. Firstly, solving the full Pridmore-Brown equation for a quadratic shear flow profile. Secondly, constructing a Brambley Boundary condition to account for the quadratic shear flow, which we have called the Quadratic-Brambley boundary condition. Finally, finding the scattered field under a change in boundary condition from hard to lined wall for a quadratic shear mean flow profile.

When examining the full solutions to the Pridmore-Brown equation it was observed that not only was the critical layer present but in fact it may be the dominant contribution in the far-field. This is a result of two interacting mechanisms; the previously predicted behaviour of the neutrally stable non-modal pole, which is only present for a sound source within the sheared flow; and the stabilisation of the hydrodynamic instability by the critical layer branch cut. This stabilisation was previously hypothesised not to occur [Brambley et al., 2012a], with the implications of such not commented upon in work where it had been observed since [Brambley and Gabard, 2016].

The critical layer in the case of a mean flow that has a quadratic shear boundary layer produces between one and three algebraically decaying waves just as previously observed when a linear shear boundary layer was investigated. The first of the waves has phase velocity equal to that of the mean flow velocity,  $M$ . When the sound source is within the uniform flow this wave has an amplitude that decays like  $x^{-\frac{5}{2}}$ , or like  $x^{-\frac{7}{2}}$  for a sound source in the sheared flow. This wave was previously predicted in Swinbanks and Brambley et al. although neither give an accurate prediction of the decay rate, likely due to the varying setting. Swinbanks predicting that this wave would decay at least as fast as  $x^{-2}$ , and Brambley et al. giving exact algebraic decay rates in their considered setting of the amplitude like  $x^{-4}$  and  $x^{-5}$  in the respective cases.

The second wave, which depends on the location of the observer within the duct, only being present when  $r > 1 - h$ , decays like  $x^{-4}$  and has phase velocity equal to the flow speed at the observer  $U(r)$ . This wave was correctly predicted by Brambley

et al. although was not commented upon by Swinbanks, although previously because the decay rate of this wave was equal or slower to that of the wave travelling with the mean flow its effects were comparable in the far-field to that of the wave with phase velocity  $M$ .

Finally, the third wave is only present when the sound source, which was taken to be a point mass source of amplitude  $\epsilon$ , is contained within the sheared flow,  $r_0 > 1 - h$ . This wave was correctly predicted in both previous works, producing the non-modal pole contribution which is neutrally stable, and a wave with algebraically decaying wave like  $x^{-3}$  and phase velocity equal to the flow speed at the source  $U(r_0)$ .

Although the predicted behaviours of the waves with phase velocity  $U(r)$  and  $U(r_0)$  were previously correctly predicted through this work, we have been able to more closely study their interaction when  $r = r_0$  and when  $r_0 = 1 - h$ . The latter of these was not previously possible for the linear shear flow profile, due to the discontinuity of the derivative of the flow profile. It is observed that as  $r$  crosses  $r_0$  both waves remain present without any cancellations occurring, likely due to the difference in how the  $k_r$  branch point and  $k_0$  non-modal pole occur within the Green's function. While at  $r_0 = 1 - h$ , we do not observe the non-modal pole, with the problem reducing to the case that  $r_0 < 1 - h$ . In addition to this it was observed numerically that as the source was taken closer to the duct wall the effects of the non-modal pole becomes stronger.

Previously the critical layer was thought to be negligible, as a result of Swinbanks predictions, and this was somewhat re-enforced by the work of Brambley et al.. Although it can be observed from Brambley et al. that the contribution of the critical layer branch cut is comparable in some cases to that of the modal sum. In the work given here, however, it is undeniable that the critical layer branch cut may not only be comparable in the near field but dominant in the far-field. This is mainly due in both cases to the behaviour of the hydrodynamic instability. With the work completed here in the quadratic shear flow the first time stabilisation of the hydrodynamic instability has been observed and studied in detail.

When the hydrodynamic instability is stabilised it does so by crossing the critical layer branch cut. When this occurs the hydrodynamic instability not only becomes stable, but also non-modal, only contributing to the the pressure field as part of the critical layer branch cut. Its contribution may be isolated by deforming the integration contour around the branch cut onto the one of steepest descent, and can be observed to contain a discontinuity as a result of the three different waves. A continuous version may be produced by taking a matching discontinuity within the wave with phase velocity  $U(r)$ , which is equivalent to always evaluating the residue

as if above the critical layer branch cut at  $r$ , although this has not been presented in this work.

Due to the hydrodynamic instability becoming stable, the far-field behaviour of the pressure perturbation changes. This results in three cases. The first is when we do not have stabilisation. In such a case the hydrodynamic instability mode will dominate the far-field with an exponentially growing contribution. This will lead to a break down of the linearisation of the Euler equations suggesting that the mean flow pressure and velocity will vary. The second case is for a stabilised flow with sound source within the region of uniform flow. In this case, all of the contributing terms will decay away from the sound source, and it may be observed that either the modal sum or the critical layer branch cut could be dominant in the far-field. Finally we have the case where we have both stability and the sound source within the sheared flow where the neutrally stable non-modal pole, which contributes as part of the critical layer branch cut, and will be the dominant contribution once the other terms decay away.

A fourth special case could be investigated at the point where the hydrodynamic instability is located exactly on the critical layer branch cut, where it would also produce a neutrally stable contribution. This has not been investigated here however since there will then exist a value of  $r_0$  such that non-modal pole is located on this mode, producing a pole of order 2 and complicating the resulting residues. It is our expectation however that the parameter sets required for this stability are of importance.

In particular as the contribution of the hydrodynamic instability grows, it may have an effect that thickens the boundary layer thickness. This can in turn be seen to have a stabilising effect of this mode and would eventually result in the system with boundary layer thickness equal to  $h_c$ , the critical boundary layer thickness such that the hydrodynamic instability is located exactly on the critical layer branch cut, and become neutrally stable. It is unknown at this time how the contribution of these modes would behave within the summation of the Fourier series in the azimuthal wave-number  $m$ , with a potentially different stability given for each. In general only a finite number of azimuthal wave-numbers are considered when summing the Fourier series, with the majority of wave-numbers having negligible contributions. Despite this if the dominant wave-numbers were stabilised while neglected wave-numbers were unstable, the resulting far-field behaviour would be that of the unstable hydrodynamic instabilities with neglected wave-numbers. How varying  $m$  effects stability is unknown.

To investigate this further we have tracked how the hydrodynamic instability moves

as each parameter is varied, and have observed what would have been otherwise expected behaviour. Firstly as already stated thickening the boundary layer results in a stable pressure perturbation, with the mode moving through the branch cut and then towards the branch point located at  $k = \frac{\omega}{M}$ .

Secondly as the Mach number is varied, slower flow profiles are seen to lead to stability. This could be important with the acknowledgement that in actual flights the flight speed, and the speed of sound, both vary. As a result, depending on the stage of flight, a different stability may be observed without having to consider a change in lining.

Thirdly we have the results of varying the frequency of the waves considered. First, when considering the frequency domain, it was observed that both higher and lower frequencies lead to stabilisation. This was true both independently and together with the variation felt by the wall impedance due to the frequency, which was taken to follow a Mass-Spring-Damper model. It was observed that a fixed intermediate frequency existed such that once the flow was stable for this particular frequency it would be stable for all other frequencies. Although no relationship between this frequency and the wall impedance was investigated. This may have implications for the time domain problem which has not been investigated here.

It is to be noted that for all considered systems, only one mode has been found to be hidden behind the branch cut, and in particular, prior to becoming stable, any other modes that may be unstable have joined the usual modal sum. This suggests that no absolute instabilities will be able to occur behind the critical layer branch cut. If this is the case then a boundary layer chosen suitably thick will not only lead to stability for any fixed frequency, but also no absolute instabilities in the time domain. This aligns with previous predictions that increasing the boundary layer thickness can remove absolute instabilities, while it was suggested this resulted in hydrodynamic instabilities, [Rienstra and Darau, 2011], which we have now observed to also be stabilised by a similar mechanism.

Finally if we vary the wall impedance it was observed that harder walls lead to a stable flow profile. It is expected that all hard walled ducts are stable, with the sketch of a proof given in the main text. This would be expected in reality however previous models, such as the linear shear flow or uniform flow under the Ingard-Myers, or Linear-Brambley boundary conditions, have not seen stability in this way. With the linear shear flow solution and boundary condition not observing any stability at all. Our results here are particularly important because it suggests that stability is also achieved for a sufficiently hard walled duct, irrespective if this is achieved with a Mass, Spring or Damper like wall with the mechanism for the stability is the same in each case. While, for example, the Ingard-Myers boundary condition, although observes this same stability, retrieves it in different ways depending on if the wall

is more Mass or Spring like, and in some cases is actually unstable except in the limit.

Extending the work from the full solution of the Pridmore-Brown equation for a flow profile that is uniform except within a boundary layer where it is sheared, we have also constructed a Myers-like boundary condition to account for this finite thickness boundary layer. This was built off the work of Brambley [2011b] which proposes the modified-Myers, or as it is more commonly known, Brambley, boundary condition. In Brambley [2011b], the boundary condition proposed is very general, accounting not just for the linear shear flow profile which it is most commonly associated with and has been referred to here as the Linear-Brambley boundary condition, but actually any flow profile with a finite thickness boundary layer. As such we have constructed and investigated the Quadratic-Brambley boundary condition which while following a very similar form to that of the Linear-Brambley boundary condition can be observed to include more features of the full solution including an effect from the critical layer branch cut, which was not present in the Linear-Brambley boundary condition.

It is believed that the reason for this the critical layer branch cut being present in the Quadratic-Brambley boundary condition and not the Linear-Brambley boundary condition is due to the acknowledgement that the boundary condition should not see the shape of the domain it is applied to. In the full linear shear flow solution it is known that the critical layer only occurs in the Pridmore-Brown equation due to the cylindrical geometry of the problem as a result of the second derivative of the mean flow profile  $U''(r)$  being zero everywhere except at  $r = 1 - h$  where it is undefined. On the other hand, since  $U''(r)$  is non-zero for the Quadratic shear flow profile the critical layer is observed from both the geometry of the problem and the flow profile itself. Thus the Quadratic-Brambley boundary condition more closely resembles the problem it is modelling.

Evaluating the contribution of the critical layer branch cut, it is found that there is only one branch point, and the resulting contribution, irrespective of the values of  $r$  and  $r_0$ , takes the form of a single wave with phase velocity equal to the mean flow velocity that decays algebraically like  $x^{-\frac{5}{2}}$ . This is the equivalent of a sound source and observer located within the region of uniform flow within the full problem, with no non-modal pole present on the critical layer branch cut, as may be expected.

In addition to this we also continue to observe the stabilisation of the hydrodynamic instability by the critical layer branch cut, with the mode passing through the branch cut following the same mechanisms as described for the full solution. With thicker boundary layers, lower Mach numbers, high and low frequencies and

hard walls leading to stability.

There are however some exceptions. It appears that for significantly thick boundary layers two different behaviours may be observed. Firstly the mode, which remains located behind the branch cut, may move to the left of the critical layer and stop contributing to the Fourier inversion as part of the steepest descent contour. Or, the mode may move back through the critical layer becoming unstable again. It is expected that both of these behaviours would be a result of a break down in the linearisation of the behaviour near the duct wall, with the  $O(h^2)$  terms being comparable in magnitude to the  $O(1)$  and  $O(h)$  terms of the expansions, and therefore being required to maintain accuracy.

When comparing the Quadratic-Brambley boundary condition to the Ingard-Myers and Linear-Brambley boundary conditions it was found that in each case the usual acoustic modes were well predicted and produced very similar modal sums as a part of the Fourier inversion. Additionally as the boundary layer thickness was decreased, both of the Brambley boundary condition retrieved the Ingard-Myers boundary condition, as would be anticipated since the Ingard-Myers considers a vanishing thin boundary layer thickness.

It is worth while once again reiterating that just as the full solution, the Quadratic-Brambley in the majority of cases observes stability in the hard walled limits for the wall impedance. With the only exceptions being when the hydrodynamic instability has destabilised by passing back through the critical layer branch cut due to a thick boundary layer. In fact when the hydrodynamic instability has been destabilised in this way it remains unstable for all wall impedance's. This further suggests that this destabilisation is due to the the boundary layer being too thick such that the  $O(h^2)$  terms may not be ignored. This is by noting that the wall impedance does not appear in either the  $h$  expansion for the pressure or the normal velocity, instead relating the two together, thus unlike the other parameters the asymptotic form is independent of the impedance  $Z$ .

In the cases where we do not have this destabilisation we once again observe that the pressure perturbation is stable for a range of wall impedance, being stabilised by the wall becoming either more, Mass, Spring or Damper like, and in some cases may be stable for all wall impedance values.

Finally, when considering the Fourier inversion we have observed how the contributions of each the modal sum, steepest descent contour and the hydrodynamic instability, stabilised or otherwise, compare within both the near and far-fields. In

particular while in the near field the flow profile is dominated between the modal sum and the potentially stabilised hydrodynamic instability, the far-field has been seen to be much more comparable between the modal sum and the contribution from the steepest descent contour when the hydrodynamic instability is stable. More-over, despite that the downstream Fourier inversion in the near field does appear to be dominated by the hydrodynamic instability, once again either stable or unstable, the downstream modal sum and the steepest descent contour may also be comparable, particularly near the duct wall, and for sound sources near the duct wall.

While it is suspected that the overall behaviour of the Fourier inverted pressure perturbation may be inaccurate due to errors within the numerical evaluation, the overall results would actually be expected to be of greater importance than are currently observed, once again particularly in the near field.

The third and final problem contained within the main body of this thesis is an exploration of the scattering problem constructed by considering the change in boundary condition from a hard to a lined duct wall. Making use of the solutions to the Pridmore-Brown equation for a quadratic shear flow profile the Wiener-Hopf technique has been utilised such that the effects of the critical layer branch cut may be observed.

This has been performed for three different incoming wave forms, coming from; a modal pole, a non-modal pole, and a stabilised hydrodynamic instability. In both the cases of the incoming modal pole and the stabilised hydrodynamic instability, this incoming wave is removed by the scattered field. While in the case of the non-modal pole this wave continues to propagate down the duct, but with an altered amplitude. In all three cases both upstream and downstream the scattered field also consists of contributions from a modal sum identical to those seen in the infinite lined duct, for the hard and lined walls respectively. Additionally, downstream we observe the contribution of the critical layer branch cut.

For this particular case the critical layer branch cut consists of up to two waves. Once again we have a wave with phase velocity equal to that of the mean flow velocity  $M$ , which in this case decays like  $O(x^{-7/2})$  and is equivalent to if we had a sound source located with the region of sheared flow for the infinite lined duct. Although the non-modal pole is not observed except in the case of an incoming wave from an equivalent non-modal pole. In addition to this in each case, we once again have a wave with phase velocity equal to the flow speed at the observer  $U(r)$  when  $r$  is located within the sheared flow region. This wave once again has a decaying contribution like  $x^{-4}$  as was the case for the equivalent wave within the infinite lined duct, however we do retrieve an exception when  $r = r_0$  associated with an incoming

wave from the non-modal pole of a point mass source, where instead a decay rate of  $x^{-3}$  is observed instead.

On top of the three incoming waves described here, one could also consider an incoming wave that takes the form of an integral around the critical layer branch cut. This can be done in two ways, firstly if the whole critical layer branch cut was considered; this would include the contributions of the both the  $k_0$  non-modal pole but also the hidden  $k^+$  modal pole. The advantage of this incoming wave would be that it is continuous, and any potential cancellations between the various phase velocities could be observed. The alternative would be to consider the integrals from  $I_{\frac{\omega}{M}}$  and  $I_r$ , and potential  $I_0$  separately. Although these would contain discontinuities, it would be expected each of these waves satisfy the boundary condition for the hard walled section separately, however showing this proves difficult.

This has not been done here due to a lack of a closed form for any of these integrals without assuming asymptotic behaviours, which are both inaccurate near  $x = 0$  and not integrable. It is expected however that each of these waves will result in a scattered field similar to that of the  $k_0$  non-modal poles incoming wave, with an upstream component that is purely modal, and a downstream component that is both modal, and non-modal, varying the incoming wave to satisfy the new boundary condition, and providing decaying waves with the two different phase velocities. It is not clear however that the decay rates of the amplitude would remain as given in the investigated cases.

In addition it is expected that since these waves decay algebraically in the lined duct for a point mass source, outside of the non-modal pole and the stabilised  $k^+$  pole, which is assumed to always be present for a hard walled duct, section 12.3, the contribution of the steepest descent contours will be observed to be small compared to both of these and the usual modal sum.

To complete the work on this topic, the production of numerical code for the evaluation of the Wiener-Hopf kernel decomposition will be required. Such code would allow this work to have greater impact and easier comparison between various parameter sets. It would also be the first step toward numerically evaluating the equivalent matrix Wiener-Hopf problem discussed in section 24, which has more direct applications in comparing to real experiments. Additionally, numerical code would allow for the confirmation some of the decay rates given for the steepest descent contours, and to be able to observe how the effects of the scattering manifest. This includes how comparing the amplitudes of the scattered waves compare to the incoming waves. It is useful to note that for each of the incoming waves the kernels are identical, and so when investigating each incoming wave the factorisation

will only need to be done once. The main difficulties of performing this numerical evaluation are; The construction of the correct contours,  $\Gamma^\pm$  such that the strip  $D$  correctly locates the  $k^+$  pole from the lined section, if it is present, and the critical layer branch cut below  $\Gamma^+$ . Secondly the evaluation of  $K(k)$  for large values of  $k$ , partially due to the oscillatory behaviour of the Bessel functions  $J_m(\alpha r)$  which are present within  $C_1$  and  $D_1$  of  $\tilde{\psi}_1(k, 1)$  and its derivative.

To resolve the first of these issues it may be possible to artificially move the  $k^+$  pole, when it is acting as a hydrodynamic instability, into the other half plane, meaning the contours need only be taken between the critical layer branch cut and this mode. This is similarly done in Rienstra [2007] and manifests in additional factors to  $K_\pm$ . It is found that this does impact the resulting behaviour of the entire function, introducing constants into the solutions for  $\tilde{p}_{0+}(k, 1)$  and  $\tilde{p}_{0-}(k, 1)$ .

When resolving the issue of highly oscillatory behaviour in the large  $|k|$  limit it may be possible to make use of the asymptotic forms given in section 19.1, to approximate the kernel where necessary.

It is worth observing that in addition to each of the scattered fields being constructed from the same terms, each of these are scale linearly with  $\frac{1}{Z}$  and  $A_{in}$ . That is, as would be expected, as the lined section becomes harder, there is less scattering caused by the change in boundary conditions. This may suggest initially that since the scattered field is always removed for the modal incoming wave a solution would then to seek near hard walls. However there is a converse effect of a factor of  $\frac{1}{(k-k_{in})}$  which will cancel out this removal by locating the modal pole near each other resulting in a scattered field that closely resembles the incoming field.

Additionally the factor of  $A_{in}$  indicates that the scattered field is linear in the amplitude of the incoming wave, thus a biggest incoming wave gives a larger scattered field, although the same behaviours will continue to be observed.

## 26 Extensions

Extending the work presented on the infinite lined ducts can be completed in several ways. Firstly, the proposition in section 12.3, that all hard walled ducts in a quadratic shear flow are stable. This could most easily be completed by proving that  $\tilde{p}'_1(1) \neq 0$  for  $k$  located on the critical layer branch cut. It is known that as  $k \rightarrow \infty$  we will have  $\tilde{p}'_1(1) \rightarrow 0$  like  $\left(\frac{\omega h}{2M}\right)^3 \frac{1}{k^3}$ , and for  $k$  on the critical layer branch cut each of the  $a_n$  are real.

If finite values of  $k$  on the critical layer branch cut such that  $\tilde{p}'_1(1) = 0$  do exist, then it would follow that there are cases for which hard walled duct is unstable and

cases where it is stable. In these instances it would be of interest to observe the parameters required to achieve this instability and to check if this behaviour would be expected for a physically relevant system. Assuming that the conjecture holds true, it would also be beneficial to show that as  $|Z| \rightarrow \infty$  we have  $h_c \rightarrow 1$ , and may be important to compare these limits.

In addition to this, we may also seek further understanding of the behaviour of  $h_c$ , by either constructing an exact or approximate form for  $h_c$  in terms of each of the other system parameters. This would allow for models to more easily select a boundary layer thickness in order to observe unstable, or stable behaviour. If an explicit formulation for  $h_c$  could be found this would also allow for the neutrally stable case to be explored in greater detail, which as previously suggested we suspect it may be important within applications.

Such a formulation would additionally allow for more direct study of the relationship between the impedance and the frequency, including other impedance models such as a Helmholtz resonator model, instead of just the Mass-Spring-Damper, or constant models used here, or observing the behaviours near ‘optimal’ impedance.

In addition, both the full solution and the Quadratic-Brambley boundary condition the work could be extended into the time domain. This would require the locating of double roots of the dispersion relations in  $\omega$  for real values of  $k$ . If for a particular parameter set these may occur for  $\text{Im}(\omega) < 0$  then we would have an absolute instability in the time domain, which we have observed evidence of in the main text when two  $k^+$  poles have been present, only one of which is the hydrodynamic instability. It is suspected that increasing the boundary layer thickness removes absolute instabilities reducing them to hydrodynamic instabilities which may be observed by the reduction of the two  $k^+$  pole case to the one pole equivalent, and here we suspect the hydrodynamic instability can then be stabilised by the critical layer branch cut.

Interest would arise if an otherwise stable mode could pass through the critical layer branch cut becoming unstable, with an absolute instability occurring ‘behind’ the branch cut. However, it is suspected that this will not occur as this would result in the critical layer having an upstream contributing component in order to cancel out the effect of this mode.

This may be made easier for the Quadratic-Brambley condition if we first investigate the surface mode dispersion relation, which would additionally allow us to more easily locate the surface modes, and know how many are present for any particular parameter set.

Finally this work may be extended in order to compare against experiments, this is likely through the numerical evaluation of the Matrix Wiener-Hopf problem with comparisons against impedance education experiments such as those described by [Spillere et al., 2020]. This could be used to tune the boundary layer thickness and observe the prominence of the non-modal effects. Varying the other parameters systems in order to retrieve cases where current computations are not observed to be accurate to the experiments may also be useful when making these comparisons to isolate, observing the difference between the results with and without the non-modal effects included.

## 26.1 Extension to Other Sheared Flow Profiles

Another extension of particular interest would be the similarities and differences from this work to what may be observed for other flow profiles. It is our understanding that this could be completed for other polynomial shear flow profiles and we lay out our predictions below.

### 26.1.1 Differences Between the Results for Linear and Quadratic Shear Flow Problems

We remind the reader that the only differences between the linear and quadratic shear flow problems were contained within the mean flow being considered, that is,

$$U(r) = \begin{cases} M & 0 \leq r \leq 1 - h \\ \frac{M(1-r)}{h} & 1 - h \leq r \leq 1 \end{cases} \quad (26.1)$$

for a linear shear flow, and,

$$U(r) = \begin{cases} M & 0 \leq r \leq 1 - h \\ M \left(1 - \left(1 - \frac{1-r}{h}\right)^2\right) & 1 - h \leq r \leq 1 \end{cases} \quad (26.2)$$

for a quadratic shear flow.

The approach to solving the Pridmore-Brown equation, although does not require matching between the  $\tilde{p}_c$  and  $\tilde{p}_1$  solution for a linear shear flow, and the finding the decay rates from the critical layer branch cut for each flow, given in part II, with the result of between one and three algebraically decaying waves. The first of the waves, called  $I_{\frac{\omega}{M}}$  in the main text, has phase velocity equal to the centre-line Mach number  $M$ , decaying like  $x^{-4}$  or  $x^{-5}$  if the sound source is located in the region of uniform flow or the shear flow respectively. For the Quadratic shear flow on the other hand these decay rates were  $x^{-\frac{5}{2}}$  and  $x^{-\frac{7}{2}}$  respectively. Each of these have a difference of

$x^{-\frac{3}{2}}$  between the two profiles. Despite this, when considering the other two waves,  $I_r$  and  $I_0$  these each have identical decay rates between the two problems, like  $x^{-4}$  and  $x^{-3}$  respectively.

The difference in the behaviour of the  $I_{\frac{\omega}{M}}$  integrals may be understood as having two causes. The first is the difference in behaviour of the constant  $A$ , given in general as

$$A = -\frac{1}{3} \left( \frac{\omega^2}{M^2} + \frac{m^2}{r_c^2} \right) \left( \frac{U''(r_c)}{U'(r_c)} - \frac{1}{r_c} \right) - \frac{2m^2}{3r_c^3}. \quad (26.3)$$

In the case of linear shear flow, the  $U''$  term is zero for  $k \neq \frac{\omega}{M}$  and the resulting expression is  $O(1)$  as  $k \rightarrow \frac{\omega}{M}$ . In the case of a quadratic shear boundary layer,  $U''$  is non zero and dominates  $A$  as  $k \rightarrow \frac{\omega}{M}$ , providing a factor of  $(k - \frac{\omega}{M})^{-\frac{1}{2}}$ . The remainder of the differences between the decay rates is explained, for  $I_{\frac{\omega}{M}}$ , by the fact that  $(r_c^+ - (1 - h)) \sim (k - \frac{\omega}{M})^{\frac{1}{2}}$  in the quadratic shear case, where as for linear shear  $(r_c - (1 - h)) \sim (k - \frac{\omega}{M})$ . These terms appear twice withing the evaluation of the Wronskian  $W(r)$  for the respective problems, providing the remaining factor of  $(k - \frac{\omega}{M})^{-1}$

For the  $I_0$  and  $I_r$  contributions, where we do not have  $r_c^+ \rightarrow 1 - h$ , all the other terms are equivalent between the linear and quadratic cases, therefore giving the same eventual asymptotic scalings, although the pre-factors may vary significantly.

### 26.1.2 Generalising the Decay Rates

Understanding this difference, and claims made by Swinbanks [1975], although not supported with any evidence, we give an argument to conjecture the behaviour of the critical layer contribution for large  $x$  for an  $n$ -polynomial flow profile given by

$$U(r) = \begin{cases} M & 0 \leq r \leq 1 - h \\ M \left(1 - \left(1 - \frac{1-r}{h}\right)^n\right) & 1 - h \leq r \leq 1 \end{cases}. \quad (26.4)$$

When considering these profiles the solutions will likely follow identically to what is given here in part II, with the upstream contributions given by a modal sum, and the downstream consisting of a modal sum, the critical layer branch cut, and any hydrodynamic instabilities. The critical layer branch cut will then continue to be able to be broken down further into up to three steepest descent contours, the removal of any any modal poles located below the critical layer branch cut, and the inclusion of any poles hidden behind the critical layer branch cut.

The three steepest descent contours will be analogous in form to those given in section 8.3 and we suggest their behaviour below. Setting  $r_C$  to be some solution of

$\omega - U(r_C)k = 0$ , the solutions for small  $|r - r_C|$  will take the form

$$\tilde{p}_1(r) = (r - r_C)^3 + O((r - r_C)^4) \quad (26.5a)$$

$$\tilde{p}_2(r) = A \log(r - r_C) \tilde{p}_1(r - r_C) + 1 + O((r - r_C)^2) \quad (26.5b)$$

$$\tilde{p}'_1(r) = 3(r - r_C)^2 + O((r - r_C)^3) \quad (26.5c)$$

$$\tilde{p}'_2(r) = b_2(r - r_C) + O((r - r_C)^2) \quad (26.5d)$$

for some coefficient  $b_2$ . The Wronskian will satisfy

$$\mathcal{W}(\tilde{p}_1, \tilde{p}_2; r) = W(r) \propto \frac{1}{r} \prod_{\omega - U(r_c)k=0} (r - r_c)^2. \quad (26.6)$$

For the solutions expanded around the particular critical point  $r_C$ , we therefore have

$$W(r) = -3 \frac{r_C}{r} \frac{\prod_{\omega - U(r_c)k=0} (r - r_c)^2}{\prod_{\substack{\omega - U(r_c)k=0 \\ r_c \neq r_C}} (r_C - r_c)^2}. \quad (26.7)$$

As  $k \rightarrow \frac{\omega}{M}$  we have

$$\begin{aligned} A &= -\frac{1}{3} \left( \frac{\omega^2}{M^2} + \frac{m^2}{r_C^2} \right) \left( \frac{U''(r_C)}{U'(r_C)} - \frac{1}{r_C} \right) - \frac{2m^2}{3r_C^3} \\ &\sim -\frac{1}{3} \left( \frac{\omega^2}{M^2} + \frac{m^2}{(1-h)^2} \right) \frac{n-1}{r_C - 1-h} + O(1), \end{aligned} \quad (26.8)$$

and also that

$$W(1-h) = O(1-h-r_C)^2, \quad W(r) = O((1-h-r_C)^{-2(n-1)}), \quad r > 1-h. \quad (26.9)$$

Because of the  $W(r)$  scalings and the  $\tilde{p}_1$  and  $\tilde{p}_2$  scalings, we also have that  $C_1 = O((1-h-r_C)^{-2})$  while  $D_1, \hat{C}_2, \hat{D}_2 = O(1)$ .

It then follows that

$$C_1 \hat{D}_2 - D_1 \hat{C}_2 = O((1-h-r_C)^{-2}) \quad (26.10a)$$

$$\text{and } \Delta(C_1 \hat{D}_2 - D_1 \hat{C}_2) = 2\pi i A D_1 \hat{D}_2 = O((1-h-r_C)^{-1}). \quad (26.10b)$$

We further know that as  $k \rightarrow \frac{\omega}{M}$  we have

$$\omega - U(1-h)k = M \left( k - \frac{\omega}{M} \right) \quad \text{and} \quad \psi_1(r), \psi_2(r) = O(1). \quad (26.11)$$

Noting also that  $(1-h-r_C) = O((k - \frac{\omega}{M})^{\frac{1}{n}})$ , we are finally ready to predict the

behaviour of  $I_{\frac{\omega}{M}}$ :

$$\Delta\tilde{G}_{\frac{\omega}{M}} \sim \frac{(\omega - U(r^*)k)A}{r^*W(r^*) \left( C_1\widehat{D}_2 - \widehat{C}_2D_1 \right) \left( C_1\widehat{D}_2 - \widehat{C}_2D_1 + 2i\pi AD_1\widehat{D}_2 \right)}$$

$$\sim \begin{cases} \frac{(k - \frac{\omega}{M})(1 - h - r_C)^{-1}}{(1 - h - r_C)^2(1 - h - r_C)^{-4}} \sim (k - \frac{\omega}{M})^{1+\frac{1}{n}} & r_0 \leq 1 - h \\ \frac{(1 - h - r_C)^{-1}}{(1 - h - r_C)^{-2(n-1)}(1 - h - r_C)^{-4}} \sim (k - \frac{\omega}{M})^{2+\frac{1}{n}} & r_0 > 1 - h, \end{cases} \quad (26.12)$$

and hence we predict that  $I_{\frac{\omega}{M}}$  decays like  $x^{-2-\frac{1}{n}}$  for  $r_0 \leq 1 - h$  and  $x^{-3-\frac{1}{n}}$  for  $r_0 > 1 - h$  following from Watson's lemma.

In order to do the same for  $I_r$  and  $I_0$ , we first note that, as  $k \rightarrow k_r$ , we have  $(r - r_C) = O(k - k_r)$ , and analogously for  $k \rightarrow k_0$ . Further we have  $C_1, D_1, \widehat{C}_2, \widehat{D}_2 = O(1)$  and that  $A = O(1)$ .

It is noticed that for  $r > 1 - h$ ,  $\tilde{p}_1(r) = O((r - r_C)^3)$  while  $\psi_1(r_0), \psi_2(r_0) = O(1)$ . Using the previously given results for  $\omega - U(r^*)k$  and noting that  $W(r_0) = O((r_0 - r_C)^2)$  for  $I_0$  only, and otherwise  $W(r_0) = O(1)$ , it follows  $I_0$  decays like  $x^{-3}$  while  $I_r$  decays like  $x^{-4}$ , exactly as for the quadratic and linear cases.

The validity of the above conjecture depends on the the assumed scalings for  $\tilde{p}_1(r)$  and  $\tilde{p}_2(r)$  at  $r = 1 - h$ ,  $1 - h < r < 1$  and  $r = 1$ , in the limits  $k \rightarrow \frac{\omega}{M}$ ,  $k \rightarrow k_r$  and  $k \rightarrow k_0 \neq k_r$ . Particular attention would be required for  $n \geq 6$ , where three sets of Frobenius expansions would be needed to cover the whole domain  $r \in [1 - h, 1]$ , whereas in this case only two have been required, resulting in  $\tilde{p}_{c1}, \tilde{p}_{c2}$  and  $\tilde{p}_{11}, \tilde{p}_{12}$ . This is due to the  $\omega - U(r)k$  having  $n$  solutions forming an regular-n-polygon with centre  $1 - h$ . For  $n \geq 6$  the distance between two critical values will be less than or equal to the distance between  $1 - h$  and any of these critical values.

It is worth noting that the decay rates given here actually align with the results of Swinbanks [1975] for a source located within the uniform flow, with the equivalent result for a source in the sheared flow being that the wave will decay at least as fast as  $x^{-3}$ .

### 26.1.3 Stabilisation of the Hydrodynamic Instability

It is anticipated that just as in the case of a Quadratic shear flow, a general n-polynomial shear flow will continue to observe stabilisation by the critical layer branch cut under the same mechanisms described here. With thicker boundary layers leading to stabilisation. Of particular interest would be how the values of  $h_c$

compare between different shear flow profiles as each of the other parameters are varied, and if this decreases for increasing values of  $n$ , resulting in stable pressure fields for thin boundary layers.

Indeed it may also be true that considering a smoother flow profile results in fewer cases where two  $k^+$  poles may be present, and so, considering these smoother profiles may remove absolute instabilities. This is however assuming that we continue to only observe one mode hidden behind the critical layer branch cut.

Also of interest will be how the location of any  $k^-$  poles varies, and if this mode can also move through the critical layer branch cut as was observed for the linear shear flow, but not for the Quadratic shear flow. In many cases this results in a contribution of the critical layer that is more closely comparable to that of the modal sum, being required to cancel out one such mode.

## 26.2 Extending the Brambley Boundary Condition

If we instead consider the Brambley-boundary condition for a uniform flow profile, accounting for a shear layer as described by (26.4) the problem once again reduces to describing  $hI_0$  and  $hI_1$  as discussed in section 14.1. In fact we can still express exact forms of  $hI_0$  and  $hI_1$  for these profiles as shown below.

Consider

$$\begin{aligned}
hI_0 &= \int_0^1 1 - \frac{(\omega - U(r)k)^2}{(\omega - Mk)^2} dr \\
&= - \int_{1-h}^1 \frac{2(M - U(r))k}{\omega - Mk} + \frac{(M - U(r))^2 k^2}{(\omega - Mk)^2} dr \\
M - U(r) &= \frac{M(r - (1 - h))^n}{h^n}
\end{aligned} \tag{26.13}$$

$$\begin{aligned}
hI_0 &= - \int_0^h \frac{2R^n Mk}{h^n(\omega - Mk)} + \frac{R^{2n} M^2 k^2}{h^{2n}(\omega - Mk)^2} dR \\
&= - \frac{2hMk}{(n+1)(\omega - Mk)} - \frac{hM^2 k^2}{(2n+1)(\omega - Mk)^2} \\
&= - \frac{hMk}{(\omega - Mk)^2} \frac{(4n+2)\omega - (3n+1)Mk}{(n+1)(2n+1)}.
\end{aligned} \tag{26.14}$$

$$\begin{aligned}
hI_1 &= \int_0^1 1 - \frac{(\omega - Mk)^2}{(\omega - U(r)k)^2} dr \\
&= h - \int_0^1 \frac{(\omega - Mk)^2}{(\omega - Mk + (M - U(r))k)^2} dr
\end{aligned}$$

$$\begin{aligned}
&= h - \int_0^h \frac{1}{\left(1 + \frac{Mk}{\omega - Mk} \frac{R^n}{h^n}\right)^2} dR \\
&= h - \frac{h}{n} \int_0^1 \frac{s^{\frac{1}{n}-1}}{\left(1 + \frac{Mk}{\omega - Mk} s\right)^2} ds \\
&= h - \frac{h}{n^2} {}_2F_1\left(2, \frac{1}{n}; \frac{1}{n} + 1; \frac{-Mk}{\omega - Mk}\right) \tag{26.15}
\end{aligned}$$

Where  ${}_2F_1((a, b; c; z)$  is the hypergeometric function. Making use of the properties of the hypergeometric function this can be seen to retrieve  $hI_1$  for the linear shear ( $n = 1$ ) case,

$${}_2F_1(a, b; c; z) = {}_2F_1(b, a; c; z) \tag{26.16a}$$

$${}_2F_1(a, b; b; z) = (1 - z)^{-a} \tag{26.16b}$$

$$hI_1 = h - h \left( {}_2F_1\left(1, 2; 2; \frac{-Mk}{\omega - Mk}\right) \right) = \frac{hMk}{\omega} \tag{26.16c}$$

For general  $n$  it is known that the hypergeometric function contains a branch cut along  $z \in [1, \infty)$ , which relates in our case exactly when  $k$  is on the critical layer branch cut.  $k \in [\frac{\omega}{M}, \infty)$ . The jump in  $hI_1$  for  $k$  crossing the branch cut can also be defined in terms of a hypergeometric function,

$$\Delta hI_1 = - \frac{h\Gamma(1 + \frac{1}{n})\Gamma(2 - \frac{1}{n})}{2n^2 \left(\frac{-Mk}{\omega - Mk}\right)^{\frac{1}{n}}} {}_2F_1\left(\frac{1}{n}, 0; \frac{1}{n} - 1; 1 - \frac{\omega}{Mk}\right) \left(e^{\frac{i\pi}{n}} - e^{-\frac{i\pi}{n}}\right) \tag{26.17}$$

This is found by evaluating the hypergeometric function using Barnes integral form and analytic continuations as given in [Bateman, 1953, section 2.1]. Thus with  $hI_0$ ,  $hI_1$  and  $\Delta hI_1$ , the Brambley boundary condition can be defined to account for any polynomial shear flow profile with finite but thin boundary layer thickness.

Just as in the case of the Quadratic-Brambley boundary condition, the Fourier inversion will consist of the stable modal poles, the steepest descent contour from the critical layer branch cut and any hydrodynamic instabilities that are either unstable, or have been stabilised by the critical layer branch cut and are located below the branch cut within the complex  $k$  plane.

While the stability of the hydrodynamic instability will dictate the overall far-field behaviour, with either a growing pressure perturbation, or one that decays, it is expected that the contribution from the modal sum will be comparable in size to the contribution of the steepest descent contour, particularly in the near field and near the duct wall.

Assuming that the form of the jump in the Green's function remains consistent with the definition in equation (16.14), then it would be anticipated that the decay rate of the contribution from the critical layer branch cuts steepest descent contour is

$x^{-2-\frac{1}{n}}$ , although no support for this is given at this time.

### 26.3 Other Flow Profiles

Apart from other polynomial shear flows there are various other flow profiles that may be of interest and worth studying.

Firstly understanding how different shear flows interact within their solutions could allow for easily expanding the analysis given above onto any flow profile with a sheared boundary layer that can be described by a finite or possibly infinite sum of polynomial shears, even if through approximation, such as an exponential [Campos and Serrão, 1998] or tanh boundary layer profile [Brambley, 2013], on which prior study has been performed and comparisons could be made.

Alternatively one could consider the case where there is no region of uniform flow. In this case although the same process may be applied to constructing the solutions to the mean flow, note this would not be applicable for the Brambley-Boundary condition. Careful consideration would have to be taken however for considering the various radii of convergence. By taking  $h = 1$  and removing the uniform flow region  $1 - h$  is located at  $r = 0$ , which is also a regular singularity of the Pridmore-Brown equation. It is likely therefore that three solutions would be required, the first around  $r = 0$ , the second around  $r = r_c$  and the third around  $r = 1$ . Although in practice only the expansions around  $r = 0$  and  $r = 1$  would actually be required. Including the expansion around  $r = r_c$  would allow for accuracy near this point, which was the main advantage of the Frobenius series solutions over taking a purely numerical approach. In addition we would no longer be required to match the solutions to the Pridmore-Brown equation to the Bessel functions, instead constructing the  $\tilde{\psi}_1$  solution by considering the boundary condition at  $r = 0$ .

A flow profile such as this was considered in Campos and Oliveira [2011], where the effect of the critical layer, referred to as critical levels, is observed to result in no single set of eigenvalues and eigenfunctions being able to describe the sound. This is a result of seeking a modal description of the sound field, and so the non-modal effects of the critical layer are not considered beyond this conclusion.

A second extension may be possible in the reduction of the number of assumptions within our problem, potentially removing the the assumption of constant mean density and sound speed. For a given mean density profile  $\rho_0(r)$  and sound speed profile  $c_0(r)$ , one could still construct a solution to the resulting Pridmore-Brown equation, taking careful notice of the potentially complex roots of  $c_0(r)$ . It would be possible

to construct a solution using the Frobenius series solutions still so long as these are not double roots or of higher order, and  $\frac{\rho'_0(r)}{\rho(r)}$  has at most regular singularities in the complex  $r$  plane. The exception to this would be in the case where these singularities occur at  $r = r_c^+$  then the critical layer branch cut will still occur in identical form to that seen in our work, although the resulting scaling in the various limits seen above may vary. When retrieving these, the work given here would provide a suitable outline for the approach to be taken and how to consider the various contributions, including the possible stabilisation of the hydrodynamic instability which will continue to be of importance [Brambley, 2011a].

Finally, the critical layer may be regularized by considering either viscosity or weak nonlinearity, and it would be interesting to investigate how the results presented here are recovered in the inviscid or small-amplitude limits. In particular, for viscous thin boundary layers, the critical layer is recovered as a caustic in the high-frequency limit.

## 26.4 Extensions to the Scattering Problem

In order to finish/extend the work completed on the Wiener-Hopf scattering problem numerical code for the evaluation of the Wiener-Hopf kernel and its multiplicative decomposition would be constructed. Packages, based on the work by Olver [2012] have been constructed in the Julia and Mathematica coding languages, making use of Chebyshev polynomials to approximate the kernel and more easily perform the factorisation, this is performed for Riemann-Hilbert problems, although the method is applicable for the evaluation of any problems that resemble the Cauchy-transform, such as Wiener-Hopf problems [Kisil, 2015]. The greatest difficulty in the process will be the locating and deformation around the critical layer branch cut and any hydrodynamic instabilities, with the code requiring a conformal mapping from the contour onto the unit disk [Olver, 2011]. Methods for more easily doing so are present within the literature, such as in the work of Rienstra [2007], where the hydrodynamic instability mode is tactfully considered within the incorrect half plane and suitable modifications are then made to correctly account for this. With this done we would only be required to deform above the critical layer branch cut which could be done by taking the inversion contour to have a small positive imaginary part for  $\text{Re}(k) > 0$ . With the scalar Wiener-Hopf kernel decomposition complete the remainder of the process for finding numerical results would be making use of the formula given in this work for the evaluation of the scattered field. In this way comparisons of the the magnitude of the critical layer branch cut, the modal sum and any stabilised hydrodynamic instabilities for each of the different incoming waves could be made.

Of particular interest would be an incoming non-modal pole hidden behind the branch cut with very small imaginary part, and examining the difference between a liner that produces a stable and an unstable pressure perturbation for  $x > 0$ .

Once the scalar problem has been completed the next extension would be to complete the Matrix problem described at the end of part IV. With the Matrix kernel undergoing a different factorisation in order to account for the exponential behaviour appropriately. From these the remainder of the problem could be solved analytically as we have done in the scalar case, and the far-field effects could be predicted. Note that for the finite length duct, if our proposition regarding the hard walled ducts in the quadratic shear flow case is indeed true, section 12.3, the far-field behaviour of this system will always be at worst neutrally stable, irrespective of the stability of the lined section. Observing how this stability over the lined section effects the near and far-fields however would be of interest particularly when comparing two similar parameter sets that lead to different stabilities, by for example varying the frequency, or the Mach number, both of which have physical relevance to observing different waves, or different stages of flight respectively.

In addition to this, the matrix problem may give insights into the scattering of the an incoming wave that comes from the critical layer branch cut steepest descent contours, with these waves being produced when the waves scatters at  $x = 0$ , and then are scattered themselves at  $x = L$ . This may provide the insights required to conclude the scalar problem with an incoming wave that is generally produced by the critical layer branch cut, and not just from the hidden modal pole, or the non-modal source pole.

The code provided by Olver [2012] is additionally able to approximate the decomposition of matrix kernels, allowing for numerical evaluation of the matrix problem in order to give support to the analysis provided for a larger audience. This would also allow for comparisons to be made more easily between the Wiener-Hopf approach and purely modal methods such as mode matching. Alternatively, comparisons between the analytic model and experimental data could be made. In particular we may be able to use these comparisons to identify where the critical layer may be observed within experiments, explaining the difficulty of modal methods to capture all of the behaviour. Other methods for the numerical evaluation of scalar and matrix Wiener-Hopf problems do exist and could also be considered, [e.g. Llewellyn Smith and Luca, 2019].

Additionally, discussion about the inclusion or exclusion of the hidden modal pole within mode matching techniques would be of interest and motivated by this work, particularly if it is observed that it is the hidden modal pole that dominates the missing effects of the critical layer within the comparisons described above. Specif-

ically this hidden mode was observed in many cases to be a comparable, or even dominant contribution within the infinite lined duct problem.

Progress may be made analytically by considering the methods highlighted in [Kisil et al., 2021, section 3.6], which focuses on matrix problems with exponential entries, suggesting further investigations into works such as [Abrahams and Wickham, 1990, Aktosun et al., 1992, Feldman et al., 2000].

Finally, the equivalent scattering problems with a uniform mean flow under the Quadratic-Brambley boundary condition could be considered and compared against the full solutions given in this work or proposed above. This could potentially reduce the computational cost of evaluating the solutions, with Frobenius series solutions not being required. However, a different kernel may be produced, which may be more complicated than that given in this work. This may allow for these models to be more amenable to comparisons, both between other boundary conditions and mode matching techniques, which are both modal. Additionally, this would not be required to account for a constant boundary layer thickness throughout the duct, with the ability to change the boundary layer being considered at each scattering point. Although this would not be able to model a slowly developing boundary layer as would be expected of reality, a change in the boundary layer thickness resulting in a stable or unstable flow profile may be of interest.

## References

- I David Abrahams and MG Aitken. A brief and gentle introduction to the wiener–hopf technique. *Lecture notes, Summer School “Bringing pure and applied analysis together via the Wiener–Hopf technique”*. [Cited on page 12.], 2019.
- ID Abrahams and GR Wickham. General wiener–hopf factorization of matrix kernels with exponential phase factors. *SIAM Journal on Applied Mathematics*, 50(3): 819–838, 1990.
- M Abramowitz and IA Stegun. *Handbook of Mathematical Functions*. US Government Printing Office, 10th edition, 1964.
- Tuncay Aktosun, Martin Klaus, and Cornelis van der Mee. Explicit wiener-hopf factorization for certain non-rational matrix functions. *Integral Equations and Operator Theory*, 15(6):879–900, 1992.
- Y Aurégan. On the use of a stress–impedance model to describe sound propagation in a lined duct with grazing flow. *J. Acoust. Soc. Am.*, 143(5):2975–2979, 2018. doi: 10.1121/1.5037585.
- Y. Aurégan and M. Leroux. Experimental evidence of an instability over an impedance wall in a duct with flow. *J. Sound Vib.*, 317:432–439, 2008. doi: 10.1016/j.jsv.2008.04.020.
- Harry Bateman. *Higher transcendental functions [volumes i-iii]*, volume 1. McGraw-Hill Book Company, 1953.
- A Bers. Space–time evolution of plasma instabilities — absolute and convective. In AA Galeev and RN Sudan, editors, *Basic plasma physics*, volume 1, pages 451–517. North-Holland, 1983.
- Edward Brambley. Viscous boundary layer effects on the myers impedance boundary condition. In *15th AIAA/CEAS Aeroacoustics Conference (30th AIAA Aeroacoustics Conference)*, page 3241, 2009a.
- EJ Brambley. Fundamental problems with the model of uniform flow over acoustic linings. *J. Sound Vib.*, 322(4-5):1026–1037, 2009b.
- EJ Brambley. Acoustic implications of a thin viscous boundary layer over a compliant surface or permeable liner. *Journal of Fluid Mechanics*, 678:348–378, 2011a.
- EJ Brambley. A well-posed boundary condition for acoustic liners in straight ducts with flow. *AIAA J.*, 49(6):1272–1282, 2011b.

- EJ Brambley. Surface modes in sheared boundary layers over impedance linings. *J. Sound Vib.*, 332(16):3750–3767, 2013. doi: 10.1016/j.jsv.2013.02.028.
- EJ Brambley and G Gabard. Time-domain implementation of an impedance boundary condition with boundary layer correction. *J. Comput. Phys.*, 321:755–775, 2016.
- EJ Brambley, M Darau, and SW Rienstra. The critical layer in linear-shear boundary layers over acoustic linings. *J. Fluid Mech.*, 710:545–568, 2012a.
- EJ Brambley, AMJ Davis, and N Peake. Eigenmodes of lined flow ducts with rigid splices. *J. Fluid Mech.*, 690:399–425, 2012b. doi: 10.1017/jfm.2011.445.
- RJ Briggs. *Electron-stream interaction with plasmas*, chapter 2. MIT, 1964.
- CJ Brooks and A McAlpine. Sound transmission in ducts with sheared mean flow. AIAA paper 2007-3545, 2007.
- LMBC Campos and MH Kobayashi. On the propagation of sound in a high-speed non-isothermal shear flow. *Int. J. Aeroacoustics*, 8(3):199–230, 2009.
- LMBC Campos and JMGS Oliveira. On the acoustic modes in a duct containing a parabolic shear flow. *J. Sound Vib.*, 330(6):1166–1195, 2011.
- LMBC Campos and PGTA Serrão. On the acoustics of an exponential boundary layer. *Philosophical Transactions of the Royal Society of London. Series A: Mathematical, Physical and Engineering Sciences*, 356(1746):2335–2378, 1998.
- KM Case. Stability of inviscid plane Couette flow. *Phys. of Fluids*, 3:143–148, 1960. doi: 10.1063/1.1706010.
- Chao Chen, Xiaodong Li, and Fangqiang Hu. On spatially varying acoustic impedance due to high sound intensity decay in a lined duct. *Journal of Sound and Vibration*, 483:115430, 2020.
- R. Courant, K. Friedrichs, and H. Lewy. On the partial difference equations of mathematical physics. *IBM Journal of Research and Development*, 11(2):215–234, 1967. doi: 10.1147/rd.112.0215.
- Yuanyuan Deng, Antoni Alomar, Didier Dagna, and Marie-Annick Galland. Characterization and suppression of the hydrodynamic instability in the time domain for acoustic propagation in a lined flow duct. *Journal of Sound and Vibration*, 500:115999, 2021.

- W Eversman and RJ Beckemeyer. Transmission of sound in ducts with thin shear layers — Convergence to the uniform flow case. *J. Acoust. Soc. Am.*, 52:216–220, 1972. doi: 10.1121/1.1913082.
- I Feldman, I Gohberg, and N Krupnik. Convolution equations on finite intervals and factorization of matrix functions. *Integral equations and operator theory*, 36(2):201–211, 2000.
- S Félix and V Pagneux. Acoustic and hydrodynamic modes generated by a point source in a duct carrying a parallel shear flow. In *Proc. 19th International Congress on Acoustics, Madrid, 2–7 September, 2007*. URL [http://www.sea-acustica.es/WEB\\_ICA\\_07/fchrs/papers/phy-08-005.pdf](http://www.sea-acustica.es/WEB_ICA_07/fchrs/papers/phy-08-005.pdf).
- G Gabard and RJ Astley. A computational mode-matching approach for sound propagation in three-dimensional ducts with flow. *Journal of Sound and Vibration*, 315(4-5):1103–1124, 2008.
- Gwénaél Gabard. A comparison of impedance boundary conditions for flow acoustics. *Journal of Sound and Vibration*, 332(4):714–724, 2013.
- VV Golubev and HM Atassi. Sound propagation in an annular duct with mean potential swirling flow. *J. Sound Vib.*, 198(5):601–616, 1996.
- CJ Heaton and N Peake. Algebraic and exponential instability of inviscid swirling flow. *J. Fluid Mech.*, 565:279–318, 2006.
- Fang Q Hu and Douglas M Nark. On the implementation and further validation of a time domain boundary element method broadband impedance boundary condition. In *28th AIAA/CEAS Aeroacoustics 2022 Conference*, page 2898, 2022.
- Uno Ingard. Influence of fluid motion past a plane boundary on sound reflection, absorption, and transmission. *J. Acoust. Soc. Am.*, 31(7):1035–1036, 1959.
- Hanbo Jiang, Alex Siu Hong Lau, and Xun Huang. An efficient algorithm of wiener-hopf method with graphics processing unit for duct acoustics. *Journal of Vibration and Acoustics*, 139(5), 2017.
- D Khamis and EJ Brambley. Acoustics in a two-deck viscothermal boundary layer over an impedance surface. *AIAA J.*, 55(10):3328–3345, 2017a. doi: 10.2514/1.J055598.
- Doran Khamis and Edward James Brambley. Acoustic boundary conditions at an impedance lining in inviscid shear flow. *Journal of Fluid Mechanics*, 796:386–416, 2016.

- Doran Khamis and Edward James Brambley. Viscous effects on the attenuation of a plane wave by an acoustic lining in shear flow. *The Journal of the Acoustical Society of America*, 141(4):2408–2417, 2017b.
- A Khavaran. Exhaust noise Green’s function in turbofan jet engines with an external centerbody. *AIAA J.*, 57(5):1914–1929, 2019. doi: 10.2514/1.J057723.
- Matthew J King and Edward J Brambley. Stabilisation of the hydrodynamic instability by the critical layer. In *28th AIAA/CEAS Aeroacoustics 2022 Conference*, page 3096, 2022.
- Matthew J King, Edward J Brambley, Renan Liupekevicius, Miren Radia, Paul Lafourcade, and Tauqeer H Shah. The critical layer in quadratic flow boundary layers over acoustic linings. *Journal of Fluid Mechanics*, 950:A8, 2022.
- Anastasia V Kisil. The relationship between a strip wiener–hopf problem and a line riemann–hilbert problem. *IMA Journal of Applied Mathematics*, 80(5):1569–1581, 2015.
- Anastasia V Kisil, I David Abrahams, Gennady Mishuris, and Sergei V Rogosin. The wiener–hopf technique, its generalizations and applications: constructive and approximate methods. *Proceedings of the Royal Society A*, 477(2254):20210533, 2021.
- S-H Ko. Sound attenuation in acoustically lined circular ducts in the presence of uniform flow and shear flow. *J. Sound Vib.*, 22(2):193–210, 1972. doi: 10.1016/0022-460X(72)90535-4.
- W Koch and W Mohring. Eigensolutions for liners in uniform mean flow ducts. *AIAA Journal*, 21(2):200–213, 1983.
- Stefan G Llewellyn Smith and Elena Luca. Numerical solution of scattering problems using a riemann–hilbert formulation. *Proceedings of the Royal Society A*, 475(2229):20190105, 2019.
- D. Marx and Y. Aurégan. Effect of turbulent eddy viscosity on the unstable surface mode above an acoustic liner. *J. Sound Vib.*, 332:3803–3820, 2013. doi: 10.1016/j.jsv.2013.02.005.
- JR Mathews and N Peake. The acoustic Green’s function for swirling flow in a lined duct. *J. Sound Vib.*, 395:294–316, 2017. doi: 10.1016/j.jsv.2017.02.015.
- J.R. Mathews and N. Peake. The acoustic green’s function for swirling flow with variable entropy in a lined duct. *Journal of Sound and Vibration*, 419:630–653, 2018a.

ISSN 0022-460X. doi: <https://doi.org/10.1016/j.jsv.2017.08.010>. URL <https://www.sciencedirect.com/science/article/pii/S0022460X17306119>.

- JR Mathews and N Peake. An analytically-based method for predicting the noise generated by the interaction between turbulence and a serrated leading edge. *J. Sound Vib.*, 422:506–525, 2018b. doi: 10.1016/j.jsv.2018.02.024.
- P Mungur and GML Gladwell. Acoustic wave propagation in a sheared fluid contained in a duct. *J. Sound Vib.*, 9:28–48, 1969. doi: 10.1016/0022-460X(69)90260-0.
- MK Myers. On the acoustic boundary condition in the presence of flow. *J. Sound Vib.*, 71(3):429–434, 1980.
- RT Nagel and RS Brand. Boundary layer effects on sound in a circular duct. *J. Sound Vib.*, 85:19–29, 1982.
- Peter Nørtoft, Jens Gravesen, and Morten Willatzen. Isogeometric analysis of sound propagation through laminar flow in 2-dimensional ducts. *Computer Methods in Applied Mechanics and Engineering*, 284:1098–1119, 2015.
- O Olivieri, A McAlpine, and RJ Astley. Determining the pressure modes at high frequencies in lined ducts with a shear flow. AIAA paper 2010-3944, 2010.
- Sheehan Olver. Computing the hilbert transform and its inverse. *Mathematics of computation*, 80(275):1745–1767, 2011.
- Sheehan Olver. A general framework for solving riemann–hilbert problems numerically. *Numerische Mathematik*, 122(2):305–340, 2012.
- M Oppeneer, SW Rienstra, and P Sijtsma. Efficient mode-matching based on closed form integrals of pridmore-brown modes. AIAA paper 2013-2172.
- M Oppeneer, SW Rienstra, and P Sijtsma. Efficient mode matching based on closed-form integrals of Pridmore-Brown modes. *AIAA J.*, 54(1):266–279, 2016. doi: 10.2514/1.J054167.
- H Posson and N Peake. The acoustic analogy in an annular duct with swirling mean flow. *J. Fluid Mech.*, 726:439–475, 2013. doi: 10.1017/jfm.2013.210.
- DC Pridmore-Brown. Sound propagation in a fluid flowing through an attenuating duct. *J. Fluid Mech.*, 4(4):393–406, 1958.
- Basil Regan and John Eaton. Modelling the influence of acoustic liner non-uniformities on duct modes. *Journal of Sound and Vibration*, 219(5):859–879, 1999.

- Y Renou and Y Aurégan. Failure of the Ingard–Myers boundary condition for a lined duct: An experimental investigation. *J. Acoust. Soc. Am.*, 130:52–60, 2011. doi: 10.1121/1.3586789.
- S. W. Rienstra. Numerical and asymptotic solutions of the Pridmore-Brown equation. *AIAA J.*, 58(7):3001–3018, 2020.
- Sjoerd Rienstra. Impedance models in time domain, including the extended helmholtz resonator model. In *12th AIAA/CEAS Aeroacoustics Conference (27th AIAA Aeroacoustics Conference)*, page 2686, 2006.
- Sjoerd Rienstra and Nigel Peake. Modal scattering at an impedance transition in a lined flow duct. In *11th AIAA/CEAS Aeroacoustics Conference*, page 2852, 2005.
- Sjoerd W Rienstra. Acoustic scattering at a hard–soft lining transition in a flow duct. *Journal of Engineering Mathematics*, 59(4):451–475, 2007.
- Sjoerd W Rienstra and Mirela Darau. Boundary-layer thickness effects of the hydrodynamic instability along an impedance wall. *J. Fluid Mech.*, 671:559–573, 2011.
- Sjoerd W Rienstra and Brian J Tester. An analytic green’s function for a lined circular duct containing uniform mean flow. *Journal of Sound and Vibration*, 317(3-5):994–1016, 2008.
- SW Rienstra. A classification of duct modes based on surface waves. *Wave Motion*, 37:119–135, 2003. doi: 10.1016/S0165-2125(02)00052-5.
- SW Rienstra. Slowly varying modes in a two-dimensional duct with shear flow and lined walls. *J. Fluid Mech.*, 906, 2021.
- SW Rienstra, M Darau, and EJ Brambley. The trailing vorticity field behind a line source in 2D incompressible linear shear flow. *J. Fluid Mech.*, 720:618–636, 2013. doi: 10.1017/jfm.2013.2.
- A Schulz, C Weng, F Bake, L Enghardt, and D Ronneberger. Modeling of liner impedance with grazing shear flow using a new momentum transfer boundary condition. AIAA paper 2017-3377, 2017.
- AF Sobolev and MA Yakovets. Application of the wiener–hopf method for describing the propagation of sound in cylindrical and rectangular channels with an impedance jump in the presence of a flow. *Acoustical Physics*, 63(6):625–636, 2017.

- AMN Spillere, LA Bonomo, JA Cordioli, and EJ Brambley. Experimentally testing impedance boundary conditions for acoustic liners with flow: Beyond upstream and downstream. *J. Sound Vib.*, 489:115676, 2020. doi: 10.1016/j.jsv.2020.115676.
- MA Swinbanks. The sound field generated by a source distribution in a long duct carrying sheared flow. *J. Sound Vib.*, 40(1):51–76, 1975.
- Christopher KW Tam and Konstantin A Kurbatskii. Microfluid dynamics and acoustics of resonant liners. *AIAA journal*, 38(8):1331–1339, 2000.
- Christopher KW Tam, Hongbin Ju, Michael G Jones, Willie R Watson, and Tony L Parrott. A computational and experimental study of resonators in three dimensions. *Journal of Sound and Vibration*, 329(24):5164–5193, 2010.
- CKW Tam and L Auriault. The wave modes in ducted swirling flows. *J. Fluid Mech.*, 371:1–20, 1998.
- G Teschl. *Ordinary differential equations and dynamical systems*, volume 140. American Mathematical Soc., 2012.
- BJ Tester. Some aspects of “sound” attenuation in lined ducts containing inviscid mean flows with boundary layers. *J. Sound Vib.*, 28:217–245, 1973. doi: 10.1016/S0022-460X(73)80104-X.
- GN Watson. The harmonic functions associated with the parabolic cylinder. *Proc. Lond. Math. Soc.*, 2(1):116–148, 1918.
- Willie R Watson, Michael G Jones, and Tony L Parrott. Validation of an impedance education method in flow. *AIAA journal*, 37(7):818–824, 1999.
- C Weng, A Schulz, D Ronneberger, L Enghardt, and F Bake. Flow and viscous effects on impedance education. *AIAA J.*, 56(3):1118–1132, 2017. doi: 10.2514/1.J055838.
- Cheng Yang, Yi Fang, Chao Zhao, and Xin Zhang. On modeling the sound propagation through a lined duct with a modified ingard-myers boundary condition. *Journal of Sound and Vibration*, 424:173–191, 2018.
- Qi Zhang and Daniel J Bodony. Numerical investigation of a honeycomb liner grazed by laminar and turbulent boundary layers. *Journal of Fluid Mechanics*, 792:936–980, 2016.